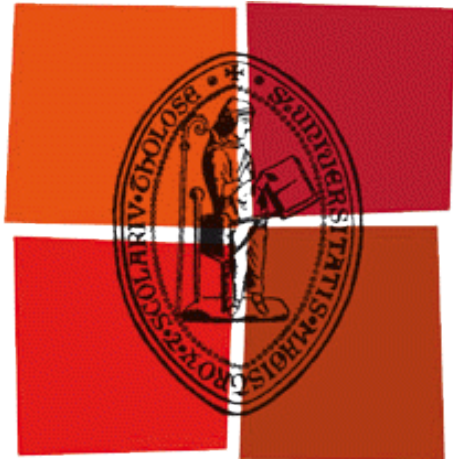


ON THE REACTIVITY OF MG-CARBONATES



Université
de Toulouse



Cotutelle-dissertation of
Université Toulouse 3 Paul Sabatier (UT3 Paul Sabatier)
and
Fakultät für Geowissenschaften of Ludwig-Maximilians-Universität München (LMU)

Submitted to Fakultät für Geowissenschaften of Ludwig-Maximilians-Universität München

June 7th, 2016

by

Ulf-Niklas Berninger

Supervisors: Prof. Dr. Eric H. Oelkers
(CNRS / Université Toulouse 3 Paul Sabatier,
University College London, and Háskóli Íslands)
Prof. Dr. Guntram Jordan
(Ludwig-Maximilians-Universität München)

Primary reviewer: Prof. Dr. Guntram Jordan
(Ludwig-Maximilians-Universität München)

Secondary reviewer: Prof. Dr. Martin Dietzel
(Technische Universität Graz)

Doctoral committee: Prof. Dr. José M. Astilleros García-Monge
(Universidad Complutense de Madrid)
Prof. Dr. Martin Dietzel
(Technische Universität Graz)
Prof. Dr. Guntram Jordan
(Ludwig-Maximilians-Universität München)
Prof. Dr. Eric H. Oelkers
(Université Toulouse 3 Paul Sabatier,
University College London, and Háskóli Íslands)
Prof. Dr. Wolfgang W. Schmahl
(Ludwig-Maximilians-Universität München)
Dr. Jacques Schott
(CNRS / Université Toulouse 3 Paul Sabatier)
Prof. Dr. Claudia A. Trepmann
(Ludwig-Maximilians-Universität München)
Prof. Dr. Jérôme Viers
(CNRS / Université Toulouse 3 Paul Sabatier)

Thesis defense: September 7th, 2016

EXTENDED ABSTRACT

This thesis presents a systematic study of Mg-carbonate reactivity, specifically dissolution and precipitation kinetics of hydromagnesite ($\text{Mg}_5(\text{CO}_3)_4(\text{OH})_2 \cdot 4\text{H}_2\text{O}$), magnesite (MgCO_3), and dolomite ($\text{CaMg}(\text{CO}_3)_2$). The hydrous Mg-carbonate mineral hydromagnesite readily dissolves and precipitates at ambient conditions and, therefore, provides an excellent case study to improve our understanding of the remarkable link between mineral dissolution and precipitation kinetics. The anhydrous Mg-carbonate minerals magnesite and dolomite readily dissolve at ambient conditions but due to the sluggish or inhibited kinetics of anhydrous Mg-carbonate precipitation (Lippmann, 1973; Land, 1998; Pokrovsky and Schott, 2002; Saldi *et al.*, 2009), hydrous Mg-carbonates tend to form at lower temperatures despite being thermodynamically disfavored (Lippmann, 1973; Hänchen *et al.*, 2008). This puzzling precipitation behavior of anhydrous Mg-carbonates is further complicated in the case of dolomite having two different cations interfering each other on the respective lattice sites. Focusing on the influence of these competing aqueous magnesium and calcium ions on the precipitation behavior of anhydrous Mg-carbonates, it is anticipated that the results of this thesis will help to illuminate this enigmatic precipitation behavior. Moreover, a detailed understanding of the reactivity of Mg-carbonates has been of recent interest since these minerals could provide a long-term storage host for anthropogenic CO_2 (*e.g.*, Giammar *et al.*, 2005; Oelkers and Schott, 2005; Hänchen *et al.*, 2008; Oelkers and Cole, 2008; Oelkers *et al.*, 2008; Dufaud *et al.*, 2009; Prigiobbe *et al.*, 2009).

A suite of closed-system reactor experiments were performed to characterize the dissolution and precipitation behavior of hydromagnesite as a function of temperature (22.5 to 75 °C) and pH (8.6 to 10.7). The equilibrium constants for the reaction



were determined by bracketing the final fluid compositions obtained from the dissolution and precipitation experiments. Surface area normalized precipitation rates were found to increase by a factor of about two with pH decreasing from pH 10.7 to 8.6. At ambient temperatures these precipitation rates are approximately two orders of magnitude faster than corresponding forsterite dissolution rates, suggesting that the overall rates of the low temperature carbonation of fluid-olivine systems are controlled by the relatively sluggish dissolution of the magnesium silicate mineral.

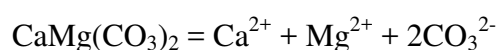
Moreover, the mechanism of hydromagnesite dissolution and precipitation was illuminated using a novel approach, the temporal evolution of isotope compositions during fluid-mineral interaction. Experiments tracking the magnesium isotopic signatures of aqueous fluids during hydromagnesite dissolution and precipitation and during fluid-hydromagnesite equilibrium at ambient temperatures over month-long timescales provided direct evidence of the rapid resetting of these isotopic signatures. All experiments were performed in batch reactors in aqueous sodium carbonate buffer solutions having a pH from 8 to 9. During hydromagnesite dissolution, the fluid first became enriched in isotopically light magnesium, but the magnesium isotope composition became heavier after the fluid attained chemical equilibrium with the mineral; the $\delta^{26}\text{Mg}$ composition of the fluid was up to $\sim 0.25\%$ heavier than the dissolving hydromagnesite at the end of the dissolution experiments. Hydromagnesite precipitation was provoked during one experiment by increasing the reaction temperature from 4 to 50 °C. The $\delta^{26}\text{Mg}$ composition of the fluid increased as hydromagnesite precipitated and continued to increase after the fluid attained bulk equilibrium with this phase, such that it was $\sim 0.25\%$ higher after one month of fluid-carbonate interaction. These observations are consistent with the theoretical hypothesis that fluid-mineral equilibrium is dynamic (*i.e.*, dissolution and precipitation occur at equal, non-zero rates at equilibrium). Moreover the results presented in this study confirm that 1) the isotopic transfer of material from the

hydromagnesite solid to the fluid phase is not conservative during dissolution and 2) the isotopic composition of hydromagnesite continues to equilibrate even when the mineral is in bulk chemical equilibrium with its coexisting fluid. This latter observation suggests that the preservation of isotopic signatures of carbonate minerals in the geological record requires some sort of combination of the isolation of fluid-mineral system from external chemical input and/or the existence of a yet to be defined dissolution/precipitation inhibition mechanism.

Magnesite precipitation behavior was investigated on the microscopic and macroscopic scale through a series of hydrothermal atomic force microscopy (HAFM) and hydrothermal mixed-flow reactor (HMFR) experiments. This complementary approach yielded a robust and validated rate equation which was tested up to higher degrees of fluid supersaturation with respect to magnesite than previous studies. The measured growth rates can be accurately described taking into account the combined effects of both mechanisms: spiral growth and two dimensional nucleation/growth. Furthermore, to assess how this precipitation may be influenced by the presence of cations, the effect of aqueous calcium on magnesite growth kinetics at 100 °C and pH ~ 7.7 was determined. Obtuse step velocities on (104) surfaces during magnesite growth were measured to be 4 ± 3 nm/s at fluid saturation states of 86 to 117. These step velocities do not vary systematically with aqueous calcium concentration up to 3×10^{-3} mol/kg. Consequently, magnesite growth rates determined by HAFM are found to be negligibly affected by the presence of aqueous calcium at these saturation states and are largely consistent with those previously reported in aqueous Ca-free systems by Saldi *et al.* (2009) and Gautier *et al.* (2015). Similarly, magnesite growth rates measured by HMFR exhibit no systematic variation on aqueous calcium concentrations. This result contrasts greatly with the observed effect of aqueous magnesium on calcite growth kinetics at ambient temperatures. Despite the lack of a clear effect of aqueous calcium on magnesite growth rates,

Raman spectroscopy confirmed the incorporation of up to 8 mole percent of Ca^{2+} into the growing magnesite structure.

The solubility of dolomite ($\text{CaMg}(\text{CO}_3)_2$) was investigated from 50 to 175 °C in 0.1 molal NaCl solutions by using a hydrogen electrode concentration cell (HECC). Attempts were made to attain fluid-dolomite equilibrium from both undersaturated and supersaturated conditions. Although dissolution readily led to a fluid-dolomite equilibrium state at all temperatures, an apparent equilibrium was obtained via precipitation only at temperatures at 150 and 175 °C. The obtained apparent solubility products for the reaction



were calculated to infinite dilution to generate the solubility product constants for this reaction ($K_{sp(Dol)}$). The retrieved equilibrium constants were fitted with a fixed heat capacity (retrieved from the literature) of the reaction above and can be accurately described using $\log_{10} K_{sp(Dol)} = a + b/T + cT$ with T referring to absolute temperature, $a = 18.1777$, $b = -4400.8736$ K, and $c_{(fixed)} = -0.06919$ 1/K. The value of dolomite solubility product derived in this study is nearly equal to that predicted by SUPCRT92 (Johnson *et al.*, 1992) at 200 °C, but about one order of magnitude higher at 50 °C, suggesting that dolomite is less stable than previously assumed.

Following up on these observations, suggesting that dolomite precipitation is possible at higher temperatures, microscopic experiments were performed to precipitate dolomite on dolomite seeds at elevated temperatures. Hydrothermal atomic force microscopy was applied to grow dolomite on its (104) surface at temperatures up to 100 °C, pH ranging from 4 to 8, and pressures up to 5 bars. Most of the growth experiments, however, led to the growth of one or two layers of a carbonate (each layer ~ 3 Å high), which morphologically reproduced the initial surface features, resembling a template effect as was previously described by Astilleros

et al. (2003, 2006) and Freij *et al.* (2004). Growth on top of these layers was strongly inhibited and did not show any systematic crystallographically orientated growth morphologies. As such, this study shows that, while dissolution can readily release material from the dolomite surface to great depths, growth becomes sparingly slow after the first monolayer has previously been precipitated on its surface.

RESUME ETENDU

Dans ce travail est présentée une étude systématique de la réactivité des carbonates de magnésium, plus précisément dissolution et précipitation, dans les environnements naturels. La dissolution à température ambiante des carbonates de magnésium a été étudiée depuis plus de quarante ans (*cf.*, Chou *et al.*, 1989; Pokrovsky and Schott, 1999; Morse and Arvidson, 2002; Duckworth and Martin, 2004; Pokrovsky *et al.*, 2005; Morse *et al.*, 2007). Plus récemment, un certain nombre d'études se sont concentrées sur la dissolution des carbonates à hautes températures et sous de fortes pressions partielles de CO₂ afin de mieux comprendre la réactivité de ces minéraux à des conditions correspondant à la séquestration géologique ou industrielle du CO₂ (*e.g.*, Talman *et al.*, 1990; Jordan *et al.*, 2001, 2007; Higgins *et al.*, 2002; Zhang *et al.*, 2007; Pokrovsky *et al.*, 2009; Saldi *et al.*, 2010).

De même, un certain nombre de travaux ont eu pour but de mieux comprendre la cinétique de précipitation des carbonates de magnésium (*e.g.*, Sayles and Fyfe, 1973; Saldi *et al.*, 2009, 2012, 2013; Case *et al.*, 2011; Felmy *et al.*, 2012, 2015; Pearce *et al.*, 2012; King *et al.*, 2013; Prigiobbe and Mazzotti, 2013; Xu *et al.*, 2013; Bracco *et al.*, 2014; Gautier *et al.*, 2015). Ces études ont montré que ces minéraux présentent une cinétique de précipitation complexe. A cause de la lenteur ou de l'inhibition de la cinétique de précipitation des carbonates de magnésium anhydres, les carbonates de magnésium hydratés tendent à précipiter aux températures ambiantes bien que leur formation soit thermodynamiquement moins favorable.

Une motivation pour cette thèse sur la réactivité des carbonates de magnésium est que ces minéraux peuvent permettre, en l'absence de calcium, le stockage à long terme du dioxyde de carbone (*cf.*, Oelkers and Schott, 2005; Hänchen *et al.*, 2008; Oelkers and Cole, 2008; Oelkers *et al.*, 2008). Par exemple, des nombreuses études se sont concentrées sur la transformation en

magnésite (MgCO_3) de silicates magnésiens afin de créer un processus industriel de stockage minéral du carbone (*e.g.*, Wolf *et al.*, 2004; Maroto-Valer *et al.*, 2005; Chen *et al.*, 2006; Alexander *et al.*, 2007; Gerdemann *et al.*, 2007; Oelkers *et al.*, 2008; Andreani *et al.*, 2009; Garcia *et al.*, 2010; King *et al.*, 2010; Case *et al.*, 2011; Saldi *et al.*, 2013; Sissmann *et al.*, 2014). L'optimisation de ces processus de carbonatation minérale est facilitée par la connaissance détaillée de la réactivité des carbonates magnésiens.

Une autre motivation pour cette étude est une meilleure connaissance du lien entre vitesse de dissolution et vitesse de précipitation des minéraux. L'application de la théorie de l'état transitoire (TST) a permis l'établissement d'équations qui décrivent avec précision les vitesses de dissolution des minéraux en fonction de la composition de la solution aqueuse et de son état de saturation par rapport au minéral étudié (*cf.*, Berger *et al.*, 1994; Oelkers *et al.*, 1994; Oelkers and Schott, 1995, 1999; Schott and Oelkers, 1995; Pokrovsky *et al.*, 2005; Schott *et al.*, 2009). Les équations dérivées de la TST ont été aussi utilisées pour prédire les vitesses de précipitation des minéraux lors des études de modélisation géochimique (*e.g.*, Zhu *et al.*, 2010; Liu *et al.*, 2011), cependant l'applicabilité de ces équations reste à vérifier en détail. A ce regard, les carbonates de magnésium fournissent un exemple unique pour étudier le lien entre cinétiques de dissolution et de précipitation. Le carbonate de magnésium hydraté hydromagnésite se dissout et précipite facilement à température ambiante. En revanche, bien que les carbonates anhydres de magnésium, magnésite et dolomite ($\text{CaMg}(\text{CO}_3)_2$), se dissolvent aisément aux conditions ambiantes, ces minéraux ne précipitent que difficilement ou même pas du tout aux mêmes conditions. La précipitation de la magnésite s'observe assez facilement aux températures supérieures à 80 °C mais, dans le cas de la dolomite, des températures supérieures pourraient être requises (Rodriguez-Blanco *et al.*, 2015). On s'attend à ce que les résultats de cette thèse permettent de fournir des éclaircissements sur ce comportement énigmatique.

Afin de faciliter sa lecture et sa publication, cette thèse se compose de 5 manuscrits (chapitres 2-6) distincts. Les chapitres sont résumés ci-dessous.

Chapitre 1: Ce chapitre contient une introduction générale.

Chapitre 2: Ce chapitre présente les résultats d'une suite d'expériences destinées à caractériser la dissolution et précipitation de l'hydromagnésite, le carbonate magnésien hydraté le plus abondant dans la nature. Des expériences de dissolution et précipitation d'hydromagnésite naturelle ($\text{Mg}_5(\text{CO}_3)_4(\text{OH})_2 \cdot 4\text{H}_2\text{O}$) ont été réalisées en réacteurs fermés en fonction de la température de 22,5 à 75 °C et à des pH compris entre 8,6 et 10,7. La constante d'équilibre de la réaction



a été déterminée à partir des compositions finales des fluides obtenues lors de ces expériences de dissolution et précipitation. Si les vitesses de dissolution étaient trop rapides pour être déterminées à partir de ces expériences, les vitesses de précipitation, plus lentes, ont pu être quantifiées. Les vitesses de précipitations normalisées à la surface BET du minéral augmentent d'un facteur ~ 2 lorsque le pH décroît de 10,7 à 8,6. Les vitesses de précipitation mesurées sont approximativement deux ordres de grandeur plus rapides que les vitesses de dissolution de la forstérite aux mêmes pH. Ceci suggère que les vitesses globales de carbonatation de l'olivine aux conditions ambiantes sont contrôlées par la dissolution relativement lente de ce minéral.

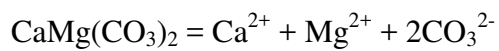
Chapitre 3: Ce chapitre décrit une tentative de caractérisation des mécanismes de dissolution et précipitation de l'hydromagnésite à partir de la mise en œuvre d'une approche nouvelle: l'évolution temporelle de la composition isotopique du magnésium lors des interactions fluide-minéral. Cette étude a fourni une preuve expérimentale directe d'un rapide renouvellement de la signature isotopique de magnésium de l'hydromagnésite lors de sa

dissolution congruente, précipitation et mise à l'équilibre en présence d'un fluide aqueux à températures ambiantes sur une durée mensuelle. Toutes les expériences ont été réalisées en réacteurs fermés dans des solutions tamponnées de carbonate de sodium ayant un pH de 8 à 9. Durant la dissolution stœchiométrique de l'hydromagnésite, le fluide s'enrichit d'abord en isotopes légers du magnésium mais la composition isotopique de magnésium devient plus lourde après que le fluide ait atteint l'équilibre chimique avec le minéral; la valeur du $\delta^{26}\text{Mg}$ du fluide à la fin des expériences de dissolution est ainsi jusqu'à $\sim 0,25$ ‰ plus lourde que celle de l'hydromagnésite qui se dissout. Lors d'une expérience, la précipitation de l'hydromagnésite a été provoquée par accroissement de la température de réaction de 4 à 50 °C. Le $\delta^{26}\text{Mg}$ du fluide s'accrût durant la précipitation de l'hydromagnésite et continua à augmenter après que l'équilibre chimique soit atteint entre le fluide et le solide si bien qu'il était $\sim 0,25$ ‰ plus élevé après 1 mois d'interaction fluide-solide. Ces observations sont en conformité avec l'hypothèse théorique que l'équilibre minéral-fluide est dynamique (*i.e.*, à l'équilibre dissolution et précipitation se produisent à des vitesses égales, différentes de zéro). De plus, les résultats présentés dans cette étude confirment que 1) le transfert de matière du solide vers la phase fluide durant la dissolution stœchiométrique de l'hydromagnésite n'est pas conservatif et 2) la composition isotopique de l'hydromagnésite continue d'évoluer vers l'équilibre, même après que le minéral ait atteint l'équilibre chimique avec le fluide à son contact. Cette dernière observation suggère que la préservation des signatures isotopiques des minéraux carbonatés dans les enregistrements géologiques nécessite que le système fluide-minéral reste isolé de possibles apports chimiques externes et/ou l'existence d'un mécanisme d'inhibition de la dissolution/précipitation qui reste à ce jour à définir.

Chapitre 4: Ce chapitre s'appuie sur des travaux antérieurs sur la précipitation de la magnésite menés au Laboratoire de Géosciences de l'Environnement de l'Université de Toulouse et au Département für Geo- und Umweltwissenschaften de la Ludwig-Maximilians-

Universität München. Grâce à une série d'expériences mettant en œuvre la microscopie à force atomique hydrothermale (HAFM) et des réacteurs hydrothermaux à circulation (HMFR), Saldi *et al.* (2009, 2012) et Gautier *et al.* (2015) ont démontré que la magnésite précipite au-dessus de 80 °C et en présence de ligands organiques. Afin d'établir comment ces vitesses de précipitations peuvent être influencées par la présence de cations inorganiques, nous avons déterminé l'effet de calcium aqueux sur la cinétique de croissance de la magnésite à 100 °C et pH ~ 7,7. On a mesuré des vitesses d'avancement des marches obtuses sur les plans de clivages (104) de 4 ± 3 nm/s pour des états de saturation du fluide de 86 à 117. Ces vitesses ne varient pas significativement avec la concentration en Ca^{2+} jusqu'à des concentrations de 3×10^{-3} mol/kg. Les vitesses de croissance de la magnésite déterminées par HAFM ne sont que très faiblement affectées par la présence de calcium aqueux pour les mêmes états de saturation et sont en accord avec les vitesses reportées antérieurement par Saldi *et al.* (2009) et Gautier *et al.* (2015) dans des systèmes sans calcium. De même, les vitesses de croissance de la magnésite déterminées dans des réacteurs hydrothermaux à circulation n'apparaissent pas varier significativement avec la concentration en calcium. Les vitesses de croissance de cette étude, cependant, ont été déterminées pour une gamme d'état de saturation du fluide vis-à-vis de la magnésite supérieur à ceux des études précédentes. Toutes les vitesses mesurées par HMFR peuvent être décrites avec précision en tenant compte des effets liés à la fois aux mécanismes de croissance en spirale et de nucléation/croissance bidimensionnelles. Les concentrations en calcium à l'état stationnaire lors des expériences en réacteur à circulation s'élevaient jusqu'à 3×10^{-3} mol/kg; cette limite a été fixée pour éviter la précipitation d'aragonite. Malgré l'absence d'un effet significatif du calcium dissous sur la vitesse de croissance de la magnésite, la spectroscopie Raman a confirmé l'incorporation de jusqu'à 8 mole pourcent de Ca^{2+} dans la structure de la magnésite lors de sa croissance.

Chapitre 5: Ce chapitre rend compte des résultats de nos efforts pour caractériser la solubilité d'une dolomite naturelle. La solubilité de ce minéral a été déterminée de 50 à 175 °C dans des solutions 0,1 mol/kg de NaCl en utilisant une cellule de concentration à électrode d'hydrogène (HECC). On a essayé d'atteindre l'équilibre dolomite-solution aqueuse à partir à la fois de solutions sous-saturées et sur-saturées par rapport à ce minéral. Bien que la dissolution du solide conduise aisément à un état d'équilibre fluide-dolomite à toutes les températures étudiées, un équilibre apparent n'a été obtenu via la précipitation du solide qu'à 150 et 175 °C. Les valeurs du produit de solubilité apparent correspondant à la réaction



ont été calculées à dilution infinie pour générer les constantes d'équilibre ($K_{sp(Dol)}$) de cette réaction. Une fonction $\log_{10} K_{sp(Dol)}$ de la forme $\log_{10} K_{sp(Dol)} = a + b/T(\text{K}) + cT(\text{K})$ a été ajustée aux valeurs ainsi extraites en utilisant une valeur constante de la capacité calorifique de la réaction issue de la littérature. Le meilleur ajustement aux données a été obtenu avec $a = 18,1777$, $b = -4400,8736 \text{ K}$ et $c_{(fixé)} = -0,06919 \text{ 1/K}$. La valeur du produit de solubilité de la dolomite générée dans cette étude est à peu près égale à celle prédite par SUPCRT92 (Johnson *et al.*, 1992) à 200 °C mais elle est environ d'un ordre de grandeur plus élevée à 50 °C, ce qui suggère que la dolomite est un peu moins stable que ce qui était supposé jusqu'à maintenant.

Chapitre 6: Faisant suite à nos observations du *Chapitre 5* qui suggèrent que la précipitation de la dolomite est possible aux températures hydrothermales, ce chapitre expose les résultats d'essais de précipitation de dolomite sur des cristaux de dolomites à ces températures. La croissance de dolomite sur sa surface (104) a été observée par microscopie à force atomique hydrothermale à des températures jusqu'à 100 °C, des pH compris entre 4 et 8 et des pressions jusqu'à 5 bars. La plupart des expériences de croissance, cependant, n'ont

abouti qu'à la formation d'une ou deux couches de carbonates (d'une épaisseur de $\sim 3 \text{ \AA}$) qui reproduisent les caractéristiques morphologiques initiales de la surface, ressemblant ainsi à un effet de gabarit. La croissance au sommet de ces couches est fortement inhibée et ne montre aucune morphologie de croissance présentant une orientation cristallographique systématique. Ainsi, cette étude montre que tandis que la dissolution peut aisément libérer de la matière de la surface de la dolomite jusqu'à de grandes profondeurs, la croissance devient très lente une fois que la première monocouche s'est formée à la surface du solide.

Chapitre 7: Ce chapitre contient un court résumé.

TABLE OF CONTENT

Preface	1
Contribution of authors	3
1 General introduction	5
2 The experimental determination of hydromagnesite precipitation rates at 22.5 to 75 °C	11
2.1 Introduction	12
2.2 Theoretical background	13
2.3 Materials and methods	14
2.4 Results	17
2.5 Discussion	22
2.5.1 The role of hydromagnesite precipitation rates in mineral carbonation	22
2.5.2 Comparison with hydromagnesite hydrolysis constants available in the literature	24
2.5.3 The variation of hydromagnesite precipitation rates as a function of temperature	25
2.6 Conclusion	27
3 Magnesium isotope fractionation during hydromagnesite dissolution, precipitation, and at equilibrium	28
3.1 Introduction	29
3.2 Theoretical considerations	32
3.3 Methods	36
3.3.1 Experimental design	36
3.3.2 Chemical analyses	39
3.3.3 Magnesium isotope analyses	40
3.4 Results	41
3.5 Discussion	50

3.5.1 Magnesium fractionation during hydromagnesite dissolution and at equilibrium	50
3.5.2 Isotopic evolution during hydromagnesite precipitation	54
3.5.3 Preservation of isotopic signatures in natural systems	55
3.6 Conclusion	56
4 On the effect of aqueous calcium on magnesite growth – insight into trace element inhibition of carbonate mineral precipitation	57
4.1 Introduction	58
4.2 Materials, chemical analysis, and experimental methods	59
4.2.1 Hydrothermal atomic force microscopy (HAFM) experiments	59
4.2.2 Hydrothermal mixed-flow reactor (HMFR) experiments	62
4.2.3 Reactive fluids and their analysis	66
4.2.4 Saturation state and growth rates	68
4.2.5 Raman spectroscopy	70
4.3 Results	70
4.4 Discussion	90
4.4.1 Comparison with past results and a description of measured rates as a function of saturation state	90
4.4.2 The incorporation of calcium into the magnesite structure	91
4.4.3 Raman spectroscopy	91
4.4.4 Why is there little effect of aqueous calcium on magnesite precipitation rates?	92
4.4.5 Consequences for mineral carbonation	94
4.5 Conclusion	94
5 Experimental determination of the solubility product of dolomite at 50 to 175 °C	96
5.1 Introduction	97
5.2 Summary of past work	98
5.3 Materials and methods	105
5.3.1 Dolomite sample	105

5.3.2 Hydrogen electrode concentration cell (HECC)	106
5.3.3 Fluid analyses	108
5.3.4 Solid analyses after experimental runs	110
5.4 Experimental results	111
5.4.1 Determination of dolomite solubility product	111
5.4.2 Solid phase analyses on retrieved material after the experiments	116
5.4.3 Determination of dolomite thermodynamic properties	121
5.5 Discussion	125
5.6 Conclusion	125
6 Assessing dolomite surface reactivity by hydrothermal atomic force microscopy	127
6.1 Introduction	127
6.2 Materials, chemical analysis, and experimental methods	129
6.2.1 Geochemical calculations	129
6.2.2 Hydrothermal atomic force microscopy (HAFM) experiments	130
6.2.3 Reactive fluids and their analysis	133
6.3 Results	136
6.4 Discussion	145
6.4.1 Comparison with past results	145
6.4.2 What inhibits dolomite precipitation at temperatures ≤ 100 °C?	146
6.4.3 Consequences for mineral carbonation	147
6.5 Conclusion	148
7 Conclusions	149
References	153

PREFACE

This dissertation is the result of the research carried out during the period 2012 to 2016 at the laboratories of Géosciences Environnement Toulouse (GET) and Department für Geo- und Umweltwissenschaften of Ludwig-Maximilians-Universität München (LMU). The experimental work performed within this joint research project combines the highly specialized experimental equipment and analytical facilities of both laboratories such as macroscopic-chemical and probe-microscopical experiments. A rigorous comparison of these complementary approaches would not have been possible without the input and guidance of many friends and colleagues. In particular, I am indebted to my advisors Eric Oelkers and Guntram Jordan who enabled me to combine these two research capacities. They have been very generous with their time and geochemical expertise. Their attention to detail, encouragement and patience is most sincerely appreciated.

Additionally, my work has greatly benefited from insightful discussions, precious advice and encouragement of Pascale Bénézeth, Vasileios Mavromatis, Oleg Pokrovsky, and Jacques Schott.

I thank the former and current graduate students of both research groups for their support, company, and good times spent together at work as well as abroad for symposiums and conferences: Alisson Akerman, Cristina Castillo, Ulf Gattermann, Quentin Gautier, Christian Grimm, Michael Lindner, Dirk Müller, Andrea Perez, Alexander Reul, Franziska Stamm, and Martin Voigt.

I am much obliged to the technicians Thierry Aigouy, Alain Castillo, Carole Causserand, Philippe de Parseval, and Michel Thibaut for their assistances with SEM, BET, wet-chemical analyses, electron microprobe, and XRD, respectively, and for constantly organizing supplies of chemicals and laboratory equipment.

Oleg Pokrovsky and Liudmila Shirokova are thanked for providing the hydromagnesite samples used in the studies reported in *Chapter 2* and *3*. Museum Reich der Kristalle in Munich, Germany, is thanked for providing the dolomite single crystals from Sunk, Austria, used in the study reported in *Chapter 6*.

All members of the European Marie Curie Initial Training Network on Mineral Scale Formation (MINSC) with its main industry partners Maersk Oil, Reykjavik Energy, and WEST Systems are cordially acknowledged for providing such a pleasant working environment for scientific exchange: Liane Benning, Bjørn Jamtveit, Luigi Marini, Eric Oelkers, Andrew and Christine Putnis, Andri Stefánsson, Susan Stipp, Claire Desplats, Thomas Rinder, Tomasz Stawski, Fernando Berro, Christopher Hawkins, Stanislav Jelavic, Diwaker Jha, Daniela Meier, Giulia Montanari, Prathap Moola, Mia Nielson, Jan Prikryl, Taher Rabizadeh, Cristina Ruiz-Agudo, Bi Yun Zhen-Wu.

Acknowledgement is made to the Donors of this research project. This study has been supported by the European Commission (through the project MINSC 290040), Centre National de la Recherche Scientifique (CNRS), Deutsche Forschungsgemeinschaft (DFG), and the French-German exchange program PROCOPE (Egide 28469SD / DAAD 55923335). The thesis defense has been supported by Deutsch-Französische Hochschule (DFH).

Last but not least, with my deepest gratitude I would like to thank Sylvia Eriksson for her invaluable assistance and support throughout this time.

CONTRIBUTION OF AUTHORS

This thesis is the synopsis of the author's Ph.D. research work. The Ph.D. was conducted as an equally entitled collaboration between Géosciences Environnement Toulouse (GET) and Department für Geo- und Umweltwissenschaften of Ludwig-Maximilians-Universität München (LMU). The thesis consists of seven chapters, five of which are scientific research manuscripts whereas the remaining two are the general introduction and conclusions. *Chapter 2* was published in *Mineralogical Magazine* and *Chapter 4* was published in *Geochimica et Cosmochimica Acta*. *Chapter 3* was submitted to *Geochimica et Cosmochimica Acta* and is in the review. *Chapter 5* will be submitted to the scientific journal *Chemical Geology*. *Chapter 6*, completed in manuscript form will be submitted to a still to be determined scientific journal following the defense of this thesis.

The research presented in this thesis was aided by the contribution of numerous friends and colleagues. All work was performed under the supervision of Prof. Dr. Eric H. Oelkers and Prof. Dr. Guntram Jordan. They provided constructive comments, criticisms, and suggestions on the interpretation of experimental data and modeling results as well as critically reviewed the scientific content and style of all the material presented in this thesis. Dr. Jacques Schott commented on data evaluation and interpretation, and critically reviewed the scientific content as well as providing references that helped improve the quality. Dr. Jérôme Chmeleff, Dr. Vasileios Mavromatis, and Andrea Pérez-Fernández contributed to *Chapter 3* with clean lab sample preparation and magnesium isotopic measurements at GET. Michael Lindner and Alexander Reul assisted the experimental work reported in *Chapter 4* which was performed in Toulouse and Munich using hydrothermal mixed-flow reactors, hydrothermal atomic force microscopy, and Raman spectroscopy. Dr. Pascale Bénézech designed and constructed the hydrogen electrode concentration cell which was used for the

experiments described in *Chapter 5*. Her experience and supervision on the experimental protocol as well as her guidance on thermodynamic calculations significantly contributed to this work. Dr. Nico Bovet performed the x-ray photoelectron spectroscopy in Copenhagen on the samples obtained from the experiments reported in *Chapter 5*. All experimental and analytical work other than that described above, as well as data acquisition, interpretation, speciation calculations, and experimental protocols were designed and carried out by the author. Consequently, the author is responsible for the content of this thesis and is the lead author of the five associated manuscripts.

Chapter 1

GENERAL INTRODUCTION

A systematic study of Mg-carbonate reactivity, specifically dissolution and precipitation kinetics, in natural environments is presented within this thesis. The low temperature dissolution behavior of Mg-carbonates has been studied for more than 40 years (*cf.*, Chou *et al.*, 1989; Pokrovsky and Schott, 1999; Morse and Arvidson, 2002; Duckworth and Martin, 2004; Pokrovsky *et al.*, 2005; Morse *et al.*, 2007). More recently a number of studies have focused on the dissolution behavior of carbonates at high temperature and elevated CO₂ partial pressures, mainly motivated to better understand the reactivity of these minerals at conditions relevant to CO₂ sequestration (Talman *et al.*, 1990; Jordan *et al.*, 2001, 2007; Higgins *et al.*, 2002; Zhang *et al.*, 2007; Pokrovsky *et al.*, 2009; Saldi *et al.*, 2010).

Similarly a number of studies have been aimed at an improved understanding of Mg-carbonate precipitation behavior (*e.g.*, Sayles and Fyfe, 1973; Saldi *et al.*, 2009, 2012; Case *et al.*, 2011; Pearce *et al.*, 2012; Felmy *et al.*, 2012; 2015; King *et al.*, 2013; Prigiobbe and Mazzotti, 2013; Xu *et al.*, 2013; Bracco *et al.*, 2014; Gautier *et al.*, 2015). Such studies have observed a complex precipitation behavior. Due to the sluggish or inhibited kinetics of anhydrous Mg-carbonate precipitation (Lippmann, 1973; Land, 1998; Pokrovsky and Schott, 2002; Saldi *et al.*, 2009), hydrous Mg-carbonates tend to form at lower temperatures despite being thermodynamically disfavored (Lippmann, 1973; Hänchen *et al.*, 2008).

One motivation of this thesis on the reactivity of Mg-carbonates is that these minerals could provide a long-term CO₂ storage host in the absence of calcium (*cf.*, Oelkers and Schott, 2005; Hänchen *et al.*, 2008; Oelkers and Cole, 2008; Oelkers *et al.*, 2008). For example,

numerous studies have focused on the transformation of Mg-rich silicate minerals to magnesite to generate an industrial process for carbon mineral storage (*e.g.*, Wolf *et al.*, 2004; Maroto-Valer *et al.*, 2005; Chen *et al.*, 2006; Alexander *et al.*, 2007; Gerdemann *et al.*, 2007; Oelkers *et al.*, 2008; Andreani *et al.*, 2009; Garcia *et al.*, 2010; King *et al.*, 2010; Case *et al.*, 2011; Saldi *et al.*, 2013; Sissmann *et al.*, 2014). The optimization of such mineral carbonation efforts is facilitated by the detailed understanding of Mg-carbonate reactivity.

Another motivation for this study of Mg-carbonate reactivity is an improved understanding of the link between mineral dissolution and precipitation rates. The application of transition state theory has led to equations that can accurately describe dissolution rates of minerals as a function of aqueous solution composition and saturation state (*cf.*, Berger *et al.*, 1994; Oelkers *et al.*, 1994; Oelkers and Schott, 1995, 1999; Schott and Oelkers, 1995; Pokrovsky *et al.*, 2005; Schott *et al.*, 2009). This theory has also been used to predict mineral precipitation rates in geochemical modeling studies (*e.g.*, Zhu *et al.*, 2010; Liu *et al.*, 2011), yet the applicability of these models has still to be verified in detail. In this regard the Mg-carbonates provide a unique case study of the link between dissolution and precipitation kinetics. The hydrous Mg-carbonate mineral hydromagnesite readily dissolves and precipitates at ambient conditions. In contrast, although the anhydrous Mg-carbonate minerals magnesite and dolomite readily dissolve at ambient conditions, these minerals are reluctant to precipitate at low temperature, if they precipitate at all. For the case of magnesite, precipitation has been readily observed at temperatures above 80 °C (Saldi *et al.*, 2009, 2012; Gautier *et al.*, 2015), but for the case of dolomite, higher temperatures may be required (*e.g.*, Graf and Goldsmith, 1956; Arvidson and Mackenzie, 1999; Kaczmarek and Sibley, 2014; Rodriguez-Blanco *et al.*, 2015). It is anticipated that the results of this thesis will help illuminate this enigmatic behavior.

To facilitate publication and readability, this thesis is comprised of 5 distinct manuscripts (*Chapters 2 to 6*). In the following, there will be a short introduction into these chapters:

Chapter 2: This chapter presents the results of a suite of experiments characterizing the dissolution and precipitation behavior of the most abundant natural hydrous Mg-carbonate phase, hydromagnesite ($\text{Mg}_5(\text{CO}_3)_4(\text{OH})_2 \cdot 4\text{H}_2\text{O}$). Natural hydromagnesite dissolution and precipitation experiments were performed in closed-system reactors as a function of temperature (22.5 to 75 °C) and pH (8.6 to 10.7). The equilibrium constants for the reaction



were determined by bracketing the final fluid compositions obtained from the dissolution and precipitation experiments. Whereas dissolution rates were too fast to be determined from the experiments, precipitation rates were slower and quantified. The resulting hydromagnesite precipitation rates normalized on BET surface area increase by a factor of ~ 2 with the pH decreasing from 10.7 to 8.6. Measured rates are approximately two orders of magnitude faster than corresponding forsterite dissolution rates. This suggests that the overall rates of the low temperature carbonation of olivine are controlled by the relatively sluggish dissolution of the magnesium silicate mineral.

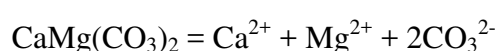
Chapter 3: This chapter describes attempts to illuminate the mechanism of hydromagnesite dissolution and precipitation using a novel approach, the temporal evolution of magnesium isotope compositions during fluid-mineral interaction. The study provides direct experimental evidence of the rapid resetting of the magnesium isotope signatures of hydromagnesite in the presence of an aqueous fluid during its congruent dissolution, precipitation, and at equilibrium at ambient temperatures over a period of several months. All experiments were performed in batch reactors in aqueous sodium carbonate buffer solutions having a pH from 8 to 9. During hydromagnesite dissolution, the fluid first became enriched in isotopically

light magnesium, but the magnesium isotope composition became heavier after the fluid attained chemical equilibrium with the mineral; the $\delta^{26}\text{Mg}$ composition of the fluid was up to ~ 0.25 ‰ heavier than the dissolving hydromagnesite at the end of the dissolution experiments. Hydromagnesite precipitation was triggered during one experiment by increasing the reaction temperature from 4 to 50 °C. The $\delta^{26}\text{Mg}$ composition of the fluid increased as hydromagnesite precipitated and continued to increase after the fluid attained bulk equilibrium with this phase, such that it was ~ 0.25 ‰ higher after one month of fluid-carbonate interaction. These observations are consistent with the theoretical hypothesis that fluid-mineral equilibrium is dynamic (*i.e.*, dissolution and precipitation occur at equal, non-zero rates at equilibrium). Moreover the results presented in this study confirm 1) that the transfer of material from the solid to the fluid phase is not isotopically conservative during stoichiometric dissolution and 2) that the isotopic compositions of carbonate minerals continue to equilibrate even when the mineral is in bulk chemical equilibrium with its coexisting fluid. This latter observation suggests that the preservation of isotopic signatures of carbonate minerals in the geological record requires some sort of combination of the isolation of fluid-mineral system from external chemical input and/or the existence of a yet to be defined dissolution/precipitation inhibition mechanism.

Chapter 4: This chapter builds upon past work at the GET laboratory on the precipitation behavior of magnesite (MgCO_3). Through a series of hydrothermal atomic force microscopy (HAFM) and hydrothermal mixed-flow reactor (HMFR) experiments Saldi *et al.* (2009, 2012) and Gautier *et al.* (2015) demonstrated that magnesite readily precipitates at temperatures in excess of 80 °C and in the presence of organic ligands. To assess how these rates may be influenced by the presence of inorganic cations, the effect aqueous calcium on magnesite growth kinetics at 100 °C and pH ~ 7.7 was determined. Obtuse step velocities on (104) surfaces during magnesite growth were measured to be 4 ± 3 nm/s at fluid saturation states of

86 to 117. These rates do not vary systematically with aqueous calcium concentration up to 3×10^{-3} mol/kg. Magnesite growth rates determined by HAFM are found to be negligibly affected by the presence of aqueous calcium at these saturation states and are largely consistent with those previously reported in aqueous Ca-free systems by Saldi *et al.* (2009) and Gautier *et al.* (2015). Similarly, magnesite growth rates measured by HMFR exhibit no systematic variation on aqueous calcium concentrations. Rates in this study, however, were extended to higher degrees of fluid supersaturation with respect to magnesite than previous studies. All measured HMFR rates can be accurately described taking into account the combined effects of both mechanisms spiral growth and two dimensional nucleation/growth. Steady-state fluid calcium concentrations of HMFR experiments ranged up to 3×10^{-5} mol/kg; this limit was chosen to avoid aragonite precipitation. Despite the lack of a clear effect of aqueous calcium on magnesite growth rates, Raman spectroscopy confirmed the incorporation of up to 8 mole percent of Ca^{2+} into the growing magnesite structure and, therefore, points to vast problems of dehydration of Mg^{2+} even at a temperature of 100 °C.

Chapter 5: This chapter is devoted to the quantitative characterization of the solubility of natural dolomite ($\text{CaMg}(\text{CO}_3)_2$) because in the literature there is a wide disparity in the values of dolomite solubility product and a scarcity of data at super-ambient conditions. In the present study, the solubility of dolomite was investigated from 50 to 175 °C in 0.1 molal NaCl solutions by using a hydrogen electrode concentration cell (HECC). Attempts were made to attain fluid-dolomite equilibrium from both undersaturated and supersaturated conditions. Although dissolution readily led to a fluid-dolomite equilibrium state at all temperatures, an apparent equilibrium was obtained via precipitation only at temperatures at 150 and 175 °C. The obtained apparent solubility products for the reaction



were calculated to infinite dilution to generate the solubility product constants for this reaction ($K_{sp(Dol)}$). The retrieved equilibrium constants were fitted with a fixed heat capacity (retrieved from the literature) of the reaction above and can be accurately described using $\log_{10} K_{sp(Dol)} = a + b/T + cT$ with T referring to absolute temperature, $a = 18.1777$, $b = -4400.8736$ K and $c_{(fixed)} = -0.06919$ 1/K. The value of dolomite solubility product derived in this study is nearly equal to that predicted by SUPCRT92 (Johnson *et al.*, 1992) at 200 °C, but about one order of magnitude higher at 50 °C, suggesting that dolomite is somewhat less stable than previously assumed.

Chapter 6: Following up on the observations in *Chapter 5*, which suggested that dolomite precipitation at high temperatures is possible, this chapter reports on attempts to precipitate dolomite on dolomite (104) surfaces using hydrothermal atomic force microscopy experiments at temperatures up to 100 °C, pH ranging from 4 to 8, and pressures up to 5 bars. Most of the growth experiments, however, led to growth of one or two layers of a carbonate (layer height ~ 3 Å), which morphologically reproduced the initial surface features, resembling a template effect which was previously also described on calcite surfaces (Astilleros *et al.*, 2003, 2006; Freij *et al.*, 2004). Growth on top of these layers was strongly inhibited and did not show any crystallographically orientated growth morphologies. As such, this study shows that, while dissolution can readily release material from the dolomite surface to great depths, growth becomes sparingly slow after the first monolayer has been precipitated on the surface.

Chapter 2

THE EXPERIMENTAL DETERMINATION OF HYDROMAGNESITE

PRECIPITATION RATES AT 22.5 TO 75 °C

Abstract

Natural hydromagnesite ($\text{Mg}_5(\text{CO}_3)_4(\text{OH})_2 \cdot 4\text{H}_2\text{O}$) dissolution and precipitation experiments were performed in closed-system reactors as a function of temperature from 22.5 to 75 °C and at $8.6 < \text{pH} < 10.7$. The equilibrium constants for the reaction



were determined by bracketing the final fluid compositions obtained from the dissolution and precipitation experiments. Resulting constants were found to be $10^{33.7 \pm 0.9}$, $10^{30.5 \pm 0.5}$ and $10^{26.5 \pm 0.5}$ at 22.5, 50, and 75 °C, respectively. Whereas dissolution rates were too fast to be determined from the experiments, precipitation rates were slower and quantified. The resulting BET surface area normalized hydromagnesite precipitation rates increase by a factor of ~ 2 with pH decreasing from pH 10.7 to 8.6. Measured rates are approximately two orders of magnitude faster than corresponding forsterite dissolution rates, suggesting that the overall rates of the low temperature carbonation of olivine are controlled by the relatively sluggish dissolution of the magnesium silicate mineral.

2.1 Introduction

The precipitation rates of carbonate minerals are of current interest due to their potential role in carbon storage (*e.g.*, Seifritz, 1990; Lackner *et al.*, 1995; Xu *et al.*, 2005; Marini, 2007; Flaathen *et al.*, 2011). Carbon storage via carbonate mineral precipitation appears to be particularly favored in basaltic and ultramafic rocks due to their high reactivity and their abundance in divalent cations such as Ca^{2+} and Mg^{2+} (McGrail *et al.*, 2006; Alfredsson *et al.*, 2008; Oelkers *et al.*, 2008; Matter *et al.*, 2009, 2011; Gislason *et al.*, 2010; Schaef *et al.*, 2010, 2011a; Aradóttir *et al.*, 2012; Gysi and Stefánsson, 2012; Oskierski *et al.*, 2013; Gislason and Oelkers, 2014). Whereas anhydrous Ca-carbonates such as calcite and aragonite readily precipitate at ambient temperatures (*e.g.*, Burton and Walter, 1987; Zuddas and Mucci, 1998; Teng *et al.*, 2000; Lakshtanov and Stipp, 2010; Rodriguez-Blanco *et al.*, 2011; Ruiz-Agudo *et al.*, 2013), the precipitation of the anhydrous Mg-carbonate mineral magnesite is apparently inhibited at temperatures lower than about 80 °C (*e.g.*, Saldi *et al.*, 2009, 2012). At these lower temperatures, the precipitation of hydrous Mg-carbonates, such as hydromagnesite and dypingite are favored (Mavromatis *et al.*, 2012; Shirokova *et al.*, 2013). The goal of this study is an improved understanding of the precipitation kinetics of hydrous Mg-carbonate minerals at temperatures below 80 °C, in part to assess their potential to store carbon at ambient temperatures. Towards this goal we measured hydromagnesite growth rates in closed system reactors at 22.5 to 75 °C. The purpose of this manuscript is to use the results of these experiments to evaluate the potential of hydrous Mg-carbonate minerals as a carbon storage host.

2.2 Theoretical background

The standard state adopted in this study for thermodynamic calculations is that of unit activity for pure minerals and H₂O at any temperature and pressure. For aqueous species other than H₂O, the standard state is unit activity of the species in a hypothetical 1 molal solution referenced to infinite dilution at any temperature and pressure. Hydromagnesite dissolution can be described using:



Taking account of this standard state, the law of mass action for *Reaction (1)* is given by:

$$K_{sp(Hmgs)} = \frac{a_{\text{Mg}^{2+}}^5 a_{\text{HCO}_3^-}^4}{a_{\text{H}^+}^6} \quad (2)$$

where $K_{sp(Hmgs)}$ stands for the equilibrium constant of *Reaction (1)* and a_i represents the activity of the subscripted aqueous species. The chemical affinity (A) of *Reaction (1)* can be expressed as:

$$A = -RT \ln \left(\frac{IAP_{Hmgs}}{K_{sp(Hmgs)}} \right) = -RT \ln \Omega_{Hmgs} \quad (3)$$

where R stands for the gas constant ($R = 8.3144 \text{ J/mol/K}$), T refers to absolute temperature, IAP_{Hmgs} signifies for the aqueous ion activity product, and Ω_{Hmgs} represents the saturation state of the aqueous phase with respect to hydromagnesite. All thermodynamic calculations in this study were performed using the PHREEQC *for Windows* (Version 2.18) computer code (Parkhurst and Appelo, 1999) together with its llnl database after adding the equilibrium constants for Mg²⁺ hydrolysis and the carbonic acid dissociation reported by Brown *et al.* (1996) and Millero *et al.* (2007), respectively.

2.3 Materials and methods

Natural hydromagnesite ($\text{Mg}_5(\text{CO}_3)_4(\text{OH})_2 \cdot 4\text{H}_2\text{O}$) was collected as stromatolite precipitates from Lake Salda in southwest Turkey (*cf.*, Shirokova *et al.*, 2011) then hand milled with an agate mortar and pestle. The resulting powder was cleaned with H_2O_2 to remove organics and oven dried at 50 °C for 24 h. The particles were not ultrasonically cleaned due to the fine nature of these natural grains. Scanning electron microscope (SEM) images, obtained using a JEOL JSM-6360 LV microscope, of the resulting hydromagnesite are shown in *Figure 1*. The prepared hydromagnesite powder consists of agglomerated crystals. The size of the individual hydromagnesite crystals ranges up to $\sim 5 \mu\text{m}$, the agglomerates range up to 50 μm . No other mineral phases were evident from SEM images nor were any detected using backscatter electron microscopy. The purity of this hydromagnesite was further verified via x-ray diffraction using an INEL CPS-120 diffractometer with Co K_α -radiation, $\lambda = 1.78897 \text{ \AA}$, and a graphite monochromator. X-ray diffraction was performed from 1 to 110° 2 θ at 0.09°/min and at a step size of 0.029°. This analysis revealed no phase other than hydromagnesite. The surface area of the prepared hydromagnesite was determined to be $8.5 \text{ m}^2/\text{g} \pm 10 \%$ by multipoint krypton adsorption according to the BET method (Brunauer *et al.*, 1938) using a Quantachrome Gas Sorption system.

Hydromagnesite dissolution and precipitation experiments were performed in closed system 0.5 L high-density polypropylene reactors. Approximately 1 g of hydromagnesite powder and 500 g of an aqueous sodium carbonate buffer solution having a 0.1 mol/kg ionic strength were placed into each reactor. The reactors were subsequently sealed and placed into temperature controlled shaking water baths. The initial solutions were composed of deionized H_2O and Merck reagent grade Na_2CO_3 and NaHCO_3 at varying ratios (*Table 1*); the resulting aqueous solutions had a pH ranging from 7.7 to 11.2. The original hydromagnesite was allowed to dissolve in this fluid for about five days until a steady-state aqueous magnesium

concentration was attained and validated. After this time, approximately 3 g of a 1.81 mol/kg aqueous MgCl_2 solution was added to each reactor to supersaturate the fluid with respect to hydromagnesite.

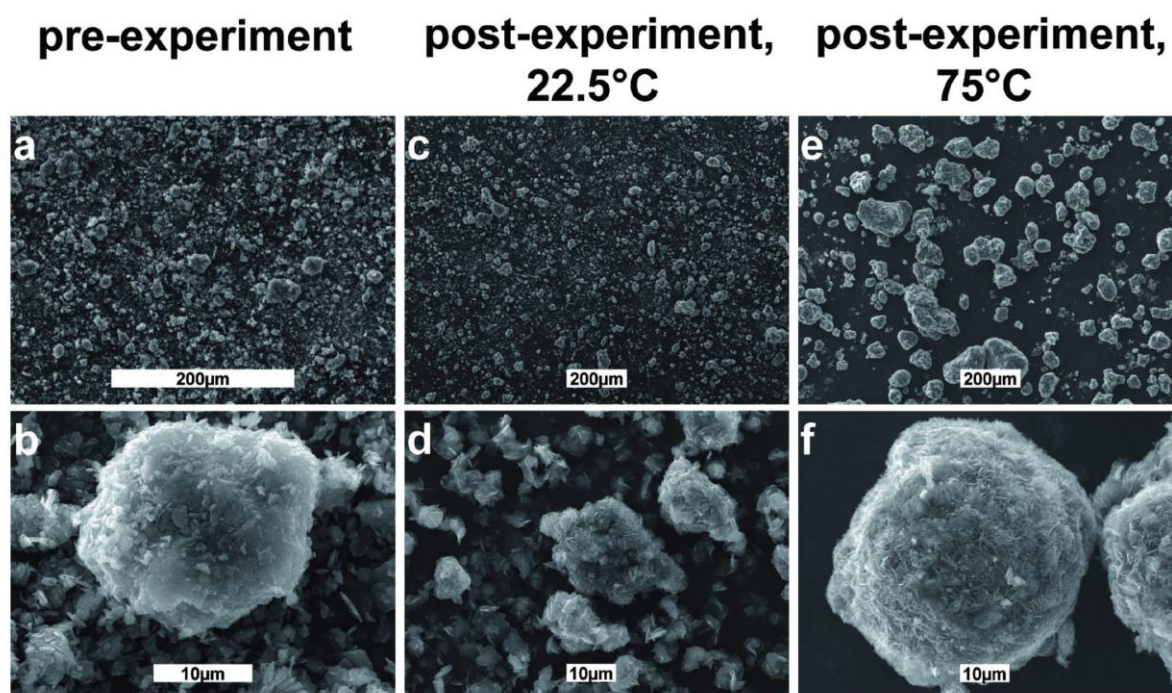


Figure 1: Scanning electron micrographs of the initial hydromagnesite seed material (a, b), after the precipitation experiment at 22.5 °C at pH 10.72 (c, d), and after the experiment performed at 75 °C at pH 9.75 (e, f).

The fluid in each reactor was sampled regularly to monitor reaction progress. Reactive fluid magnesium concentration was measured by flame atomic absorption spectroscopy using a Perkin Elmer Zeeman 5000 Atomic Absorption Spectrometer with an uncertainty of $\pm 2\%$ and a detection limit of 6×10^{-7} mol/kg. Alkalinity was determined by standard HCl titration using Schott TA 10plus with an uncertainty of $\pm 2\%$ and a detection limit of 5×10^{-5} eq/L. Fluid pH measurements were performed at 22.5 °C immediately after sampling using a standard glass electrode, previously calibrated with 4.01, 6.86, and 9.18 NIST pH buffers.

Table 1: Summary of experimental data on hydromagnesite dissolution and precipitation of *Chapter 2*.

Temp (°C)	Hmgs seeds (g)	Composition of buffer solution			Experimental parameters at the final state of the dissolution leg				Addition of aqueous MgCl ₂ (1.81 mol/kg)		Experimental parameters at the final state of the precipitation leg			
		NaHCO ₃ (g/L)	Na ₂ CO ₃ (g/L)	pH	Mg (mmol/kg)	Alkalinity (eq/L)	log <i>IAP</i> _{Hmgs}	(g)	pH	Mg (mmol/kg)	Alkalinity (eq/L)	log <i>IAP</i> _{Hmgs}	<i>k</i> _{Hmgs} (10 ⁻⁹ ·mol/m ² /s)	
22.5	0.9506	8.8990 ^a	0	8.75	5.19	0.114	32.94	2.89	8.59	14.6	0.105	34.47	1.0	
22.5	0.9515	8.8992	0	8.85	4.15	0.128	32.89	2.89	8.65	13.5	0.107	34.56	1.0	
22.5	0.9515	8.3166	0.2757	8.92	3.29	0.113	32.64	2.91	8.72	12.7	0.104	34.67	1.0	
22.5	0.9498	6.9732	0.8479	9.14	2.30	0.104	32.61	2.79	8.86	9.85	0.0944	34.72	0.90	
22.5	0.9503	4.6206	1.8020	9.53	1.30	0.0923	32.45	2.90	9.22	5.86	0.0757	34.85	0.80	
22.5	0.9491	2.3775	2.7238	9.90	0.85	0.0912	32.50	2.88	9.71	3.43	0.0621	35.01	0.70	
22.5	0.9493	0	3.7627	10.87	0.362	0.0720	32.52	2.77	10.72	2.81	0.0549	36.57	0.57	
50	0.9513	8.8990 ^a	0	8.59	1.88	0.115	29.34	2.98	8.37	6.59	0.0914	30.99	1.1	
50	0.9511	8.8992	0	8.68	1.51	0.119	29.19	2.90	8.42	5.44	0.0944	30.83	1.2	
50	0.9503	8.3166	0.2757	8.74	1.17	0.113	28.84	2.98	8.44	4.90	0.0902	30.71	1.2	
50	0.9491	6.9732	0.8479	8.96	0.928	0.108	29.02	3.00	8.51	4.72	0.0845	30.90	1.3	
50	0.9501	4.6206	1.8020	9.38	0.620	0.0989	29.20	3.00	8.90	2.20	0.0698	30.62	1.3	
50	0.9509	2.3775	2.7238	9.81	0.444	0.0879	29.39	2.96	9.46	1.28	0.0586	30.93	1.0	
50	0.9508	0	3.7627	10.62	0.335	0.0747	30.32	2.84	10.25	1.12	0.0506	31.95	0.90	
75	0.9530	8.8990 ^a	0	8.77	0.503	0.110	26.30	2.84	8.70	0.534	0.0804	26.15	1.2	
75	0.9415	8.8992	0	8.80	0.494	0.116	26.34	2.83	8.74	0.458	0.0791	25.95	1.2	
75	0.9473	8.3166	0.2757	8.84	0.437	0.113	26.18	2.84	8.74	0.475	0.0824	26.04	1.3	
75	0.9503	6.9732	0.8479	8.97	0.458	0.107	26.59	2.83	8.76	0.449	0.0773	25.97	1.3	
75	0.9492	4.6206	1.8020	9.30	0.304	0.0981	26.49	2.84	8.93	0.461	0.0672	26.52	1.4	
75	0.9524	2.3775	2.7238	9.71	0.224	0.0860	26.60	2.90	9.36	0.289	0.0571	26.53	1.3	
75	0.9478	0	3.7627	10.04	0.204	0.0772	27.05	2.84	9.75	0.242	0.0491	26.91	1.1	

^a In addition, 4.9 mL of 1N HCl was added to these initial reactive fluids.

2.4 Results

Aqueous magnesium concentrations as a function of time during a representative experiment are illustrated in *Figure 2*. It can be seen that an approximately constant magnesium concentration was obtained by dissolution within ~ 30 min. Following the addition of MgCl_2 to the fluid phase, the aqueous magnesium concentration decreased systematically with time. Note the near-constant aqueous magnesium concentration attained at the end of the dissolution leg is distinct from that attained at the end of the precipitation leg of the experiment, reflecting the different fluid pH present during these legs.

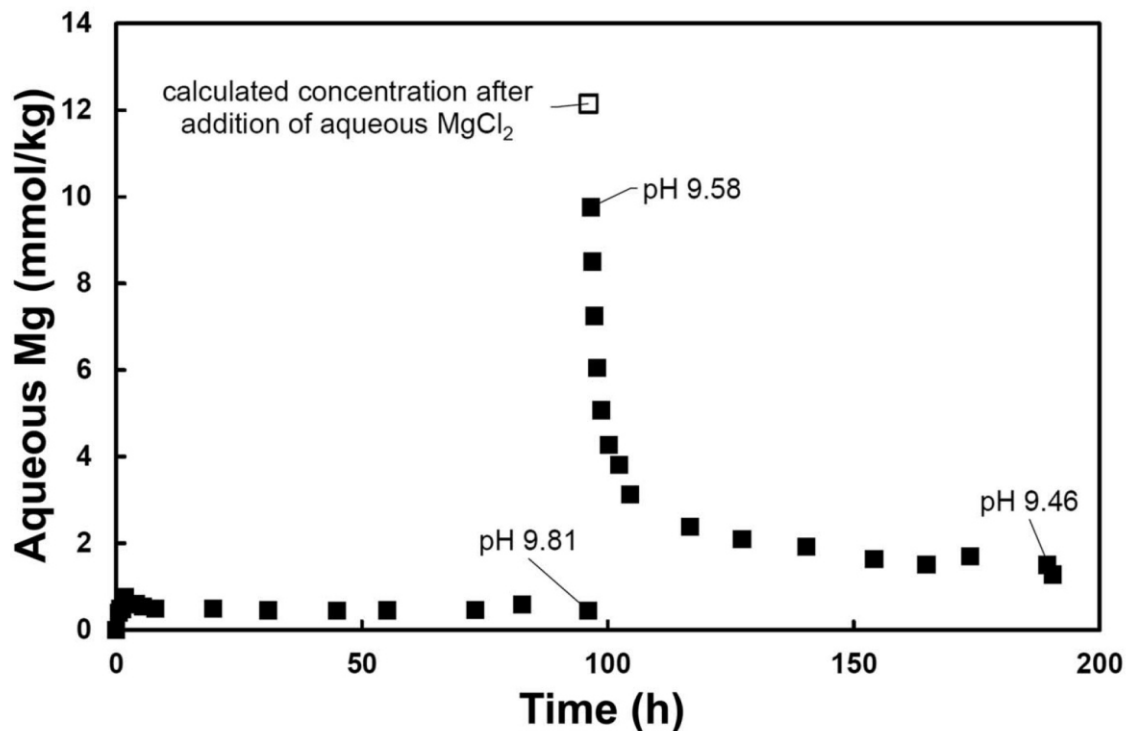


Figure 2: Temporal evolution of aqueous magnesium concentration for a representative experiment performed at 50 °C. This experiment began by the dissolution of hydromagnesite until a near stationary state was attained. After 100 h, additional magnesium was added to the aqueous fluid and precipitation began. Uncertainties of the concentration measurements are within the size of the symbols. Note that steady-state concentration aqueous magnesium during the dissolution leg is reached in < 30 min. The initial and final pH values of the fluid during the dissolution and precipitation leg of the experiment are shown.

The rate at which steady-state was attained during hydromagnesite dissolution was too rapid to obtain unambiguous dissolution rates from the temporal evolution of aqueous magnesium concentrations (see *Figure 2*). In contrast, the temporal evolution of aqueous magnesium concentrations during precipitation was sufficiently slow to fit these data to retrieve hydromagnesite rates. Surface area normalized hydromagnesite precipitation rates (r_{Hmgs}) were fit assuming they were consistent with surface growth in accord with:

$$r_{Hmgs} = k_{Hmgs} \left(\Omega_{Hmgs}^{1/\nu} - 1 \right)^n \quad (4)$$

where k_{Hmgs} refers to a rate constant, Ω_{Hmgs} signifies the saturation state of the aqueous phase with respect to the precipitating hydromagnesite, ν refers to the stoichiometric number of activated species in one mole of hydromagnesite (= 5; Gautier *et al.*, 2014) and n stands for the reaction order (= 1; Gautier *et al.*, 2014). Measured aqueous magnesium concentrations were fit following the method described by Harouiya *et al.* (2007) using *Equation (4)* and a trial and error method by varying k_{Hmgs} and comparing fluid concentrations calculated using an EXCEL spread sheet with measured aqueous magnesium concentrations. The results of this fit for all experiments are shown in *Figure 3*, where it can be seen that the calculated curves provide a close description of the temporal variation of the measured aqueous magnesium concentrations. Note that in some cases the first few measured magnesium concentrations during a precipitation leg plot below the curve. This observation may be due to the effects of hydromagnesite nucleation on aqueous fluid concentrations. Nucleation, which is favored in highly supersaturated fluids, is typically faster than growth and more strongly dependent on fluid saturation state. As such, aqueous magnesium concentrations in fluids experiencing hydromagnesite nucleation will decrease faster with time than magnesium concentrations in fluids experiencing only growth.

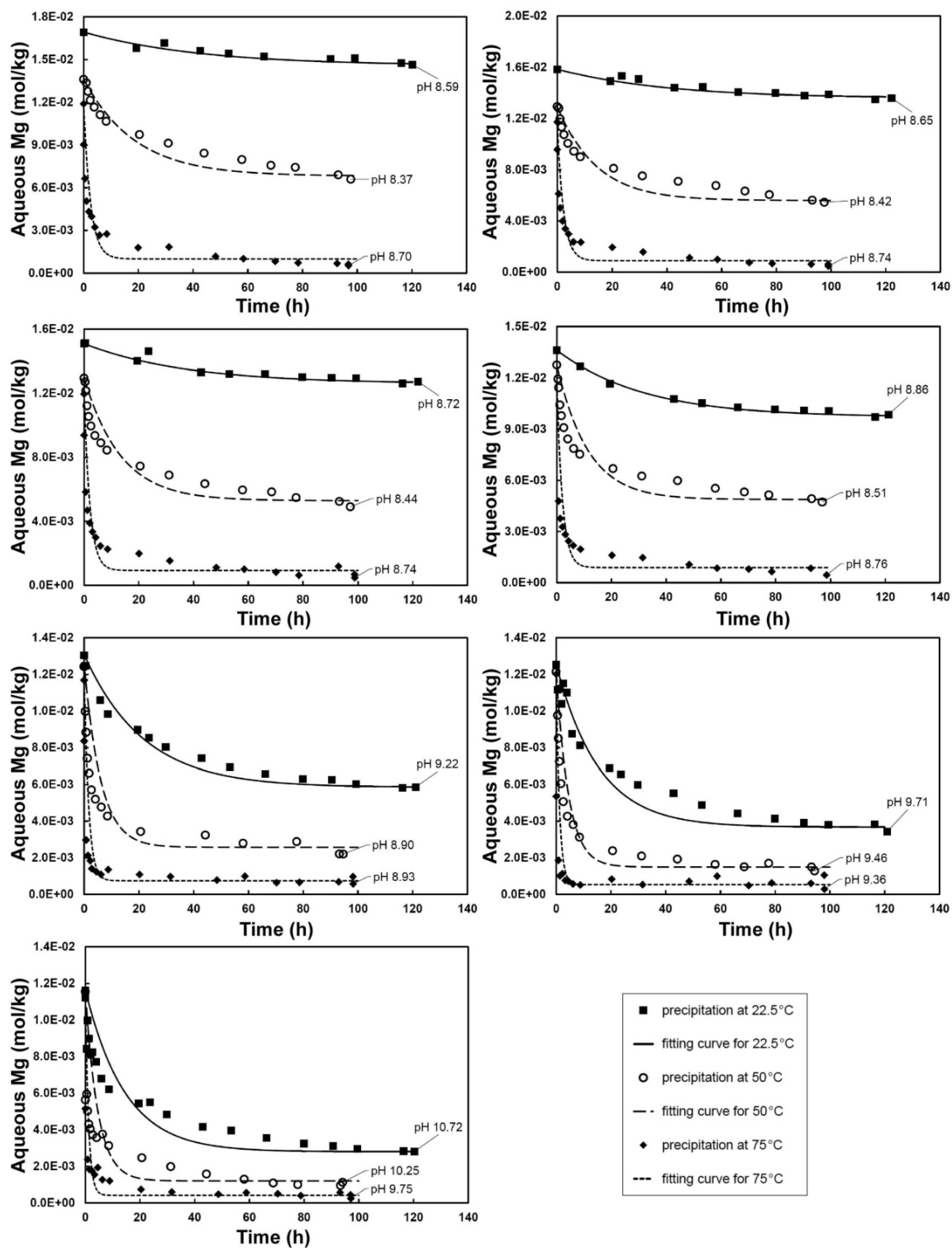


Figure 3: Temporal evolution of aqueous magnesium concentration during all precipitation experiments performed in this study. Results obtained at 22.5, 50, and 75 °C are represented by filled squares, hollow circles, and filled diamonds, respectively. Fits of these data at 22.5, 50, and 75 °C are depicted by the closed, dashed, and dotted curves, respectively (see text).

Hydromagnesite precipitation rate constants, consistent with the regression curves shown in *Figure 3* are provided as a function of pH in *Figure 4*. Two observations are evident in this *Figure 4*. First, hydromagnesite precipitation rate constants decrease by a factor of ~ 2 with increasing pH from 8.6 to 10.7 at 22.5 °C. A similar decrease in precipitation rates with pH was observed for the case of magnesite at 100 to 200 °C by Saldi *et al.* (2012). Second, hydromagnesite precipitation rate constants increase slightly with increasing temperature from 22.5 to 75 °C.

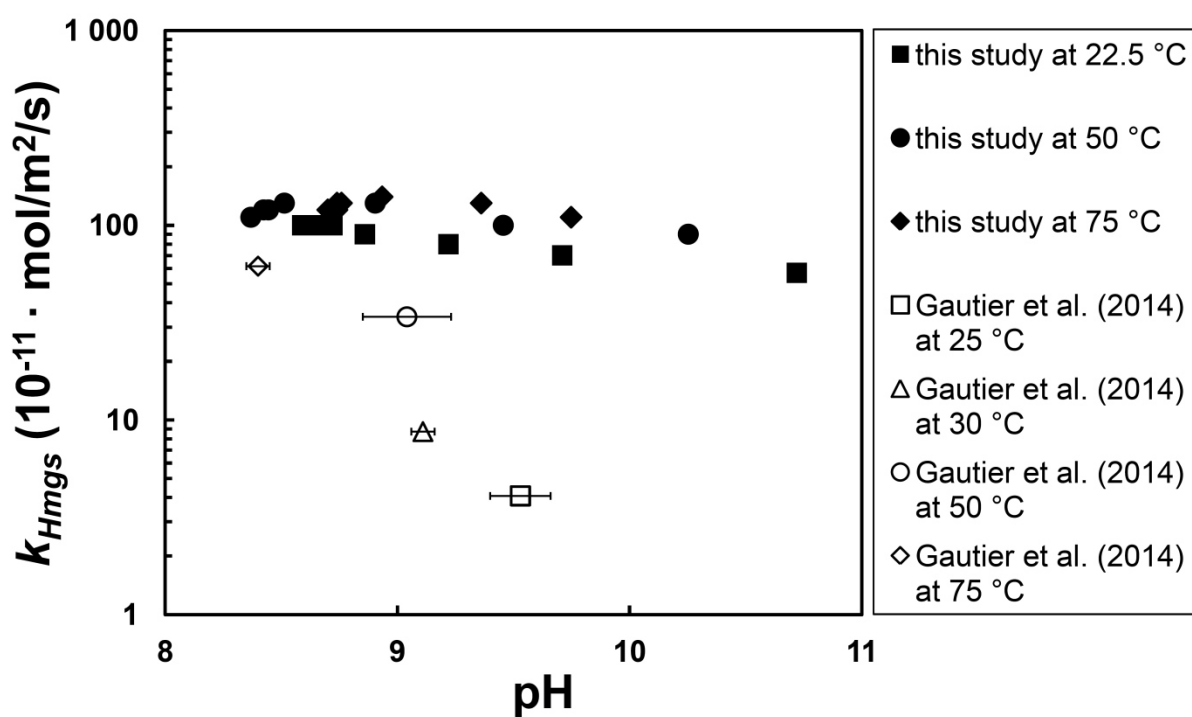


Figure 4: Hydromagnesite precipitation rate constants as a function of pH. Constants for 22.5, 50, and 75 °C are illustrated by filled squares, circles, and diamonds, respectively. Rate constants at different temperatures published by Gautier *et al.* (2014) as a function of pH are plotted for comparison.

The final steady-state aqueous magnesium concentrations during each dissolution and precipitation leg of each experiment were used together with corresponding pH and alkalinity values to determine the final ion activity product (IAP_{Hmgs}) of hydromagnesite. The resulting IAP_{Hmgs} values are illustrated as a function of pH in *Figure 5*. As these values were obtained from both dissolution and precipitation experiments, they bracket the equilibrium constant of the hydromagnesite hydrolysis *Reaction (1)*. The equilibrium IAP_{Hmgs} values shown in *Figure 5* were determined by the requirement that the equilibrium IAP_{Hmgs} be higher than those measured for dissolution and lower than those measured from precipitation. In each case, the equilibrium IAP_{Hmgs} was chosen to be the mean of the highest IAP_{Hmgs} determined from dissolution and the lowest determined from precipitation. There is some overlap among the measured IAP_{Hmgs} values for the 75 °C experiments. This observation could originate from uncertainties in the thermodynamic database adopted in this study. The logarithms of equilibrium constants for *Reaction (1)* generated by equating $K_{sp(Hmgs)}$ to this equilibrium IAP_{Hmgs} (see *Equation (3)*) are 33.7 ± 0.9 , 30.5 ± 0.5 , and 26.5 ± 0.5 for 22.5, 50, and 75 °C, respectively.

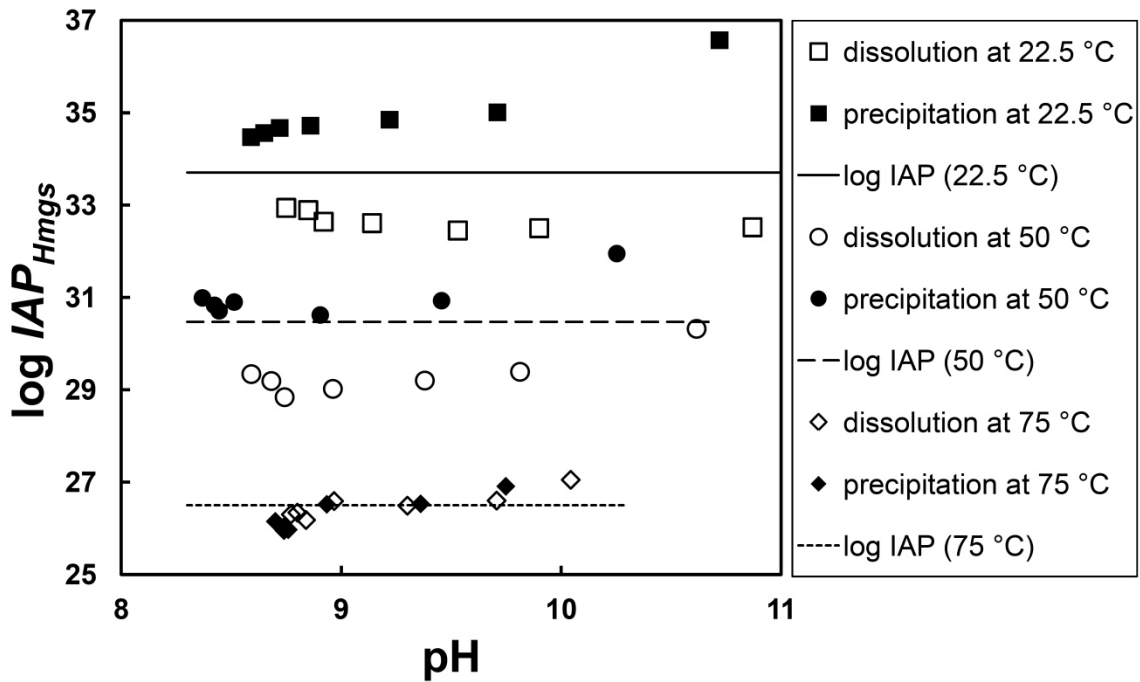
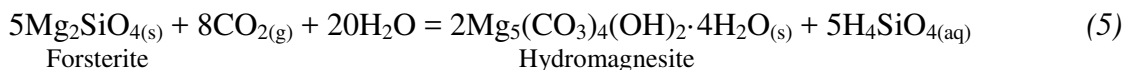


Figure 5: Hydromagnesite ion activity products (IAP_{Hmgs}) of the final fluid sampled of each experiment as a function of pH. Values of IAP_{Hmgs} determined from 22.5, 50, and 75 °C experiments are portrayed by squares, circles, and diamonds, respectively. Mean equilibrium IAP_{Hmgs} values are depicted by the lines indicated (see text).

2.5 Discussion

2.5.1 The role of hydromagnesite precipitation rates in mineral carbonation

The carbonation of Mg-rich olivine dissolution has been widely studied (*e.g.*, Béarat *et al.*, 2006; Andreani *et al.*, 2009; Prigiobbe *et al.*, 2009; King *et al.*, 2010; Daval *et al.*, 2011). Olivine is commonly thought to be the best source of the divalent metal cations required to create carbonate minerals due to its fast dissolution rates and worldwide abundance. The carbonation of Mg-enriched fluids due to forsterite dissolution at low temperatures, where magnesite precipitation is kinetically unfavored (*e.g.*, Saldi *et al.*, 2009), can proceed via:



Forsterite dissolution has been shown to follow a relatively simple dissolution mechanism (Pokrovsky and Schott, 2000; Oelkers, 2001a); dissolution rates of forsterite have been reported by Wogelius and Walther (1991), Pokrovsky and Schott (2000), Oelkers (2001a) and Hänchen *et al.* (2006) as function of reactive fluid pH. At steady-state, the stoichiometry of *Reaction (5)* requires:

$$5 r_{Fo} s_{Fo} = 2 r_{Hmgs} s_{Hmgs} \quad (6)$$

where r_{Fo} and s_{Fo} refer to the surface area normalized dissolution rate and surface area of forsterite, respectively, and s_{Hmgs} stands for the surface area of hydromagnesite. A comparison of surface area normalized forsterite dissolution rates and hydromagnesite precipitation rates is provided in *Figure 6*. Forsterite dissolution rates after normalization to its magnesium content are ~ 2 orders of magnitude slower than corresponding hydromagnesite precipitation rates. This observation indicates that, in contrast to the carbonation of forsterite to form magnesite (Saldi *et al.*, 2009), the limiting step of the carbonation process to form hydromagnesite from forsterite is the relatively slow dissolution of forsterite. As forsterite dissolution rates are not increased by changing saturation state at far-from-equilibrium conditions (*cf.*, Oelkers, 2001a) or substantially by the addition of organic ligands (Declercq *et al.*, 2013) it seems likely that the most efficient way of accelerating this overall process would be by increasing forsterite reactive surface areas (*e.g.*, by increased grinding leading to reduced particle sizes).

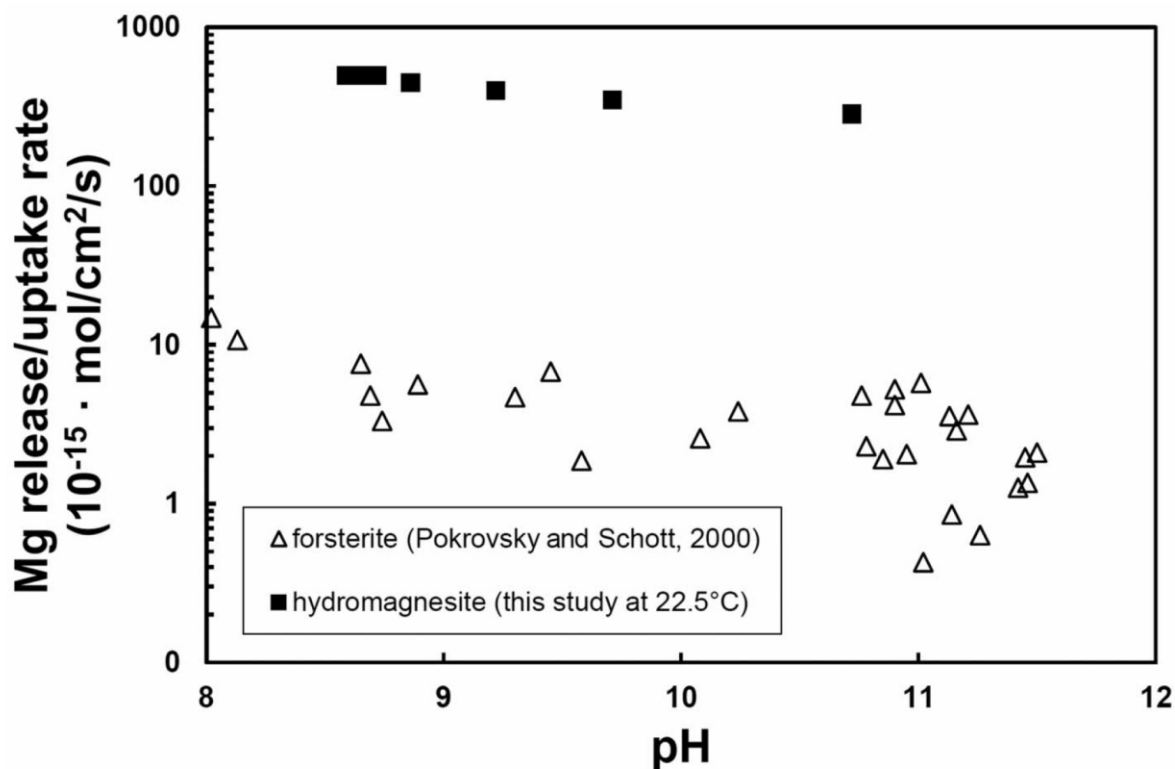


Figure 6: Comparison of forsterite dissolution rates (Pokrovsky and Schott, 2000) versus hydromagnesite precipitation rates (this study). All rates shown in this figure are normalized to magnesium release rather than to moles of mineral dissolved. These rates were obtained by multiplying reported mineral rates by the number of magnesium atoms in the formula of each mineral.

2.5.2 Comparison with hydromagnesite hydrolysis constants available in the literature

As experiments reported in this study bracket equilibrated hydromagnesite from both undersaturated and supersaturated conditions, the results presented above constrain strongly the equilibrium constant of *Reaction (1)*. There have been few reports of hydromagnesite solubility measurements in the literature. Data present in the Ilnl database of PHREEQC originates from SUPCRT92 (Johnson *et al.*, 1992), which takes account of the thermodynamic properties of hydromagnesite reported by Helgeson *et al.* (1978), which

themselves are based on the calorimetric measurements of Robie and Hemingway (1972, 1973). The equilibrium constants for *Reaction (1)* as calculated using PHREEQC and its Ilnl database as a function of temperature are plotted in *Figure 7*. Gautier *et al.* (2014) reported the hydromagnesite hydrolysis constants based on dissolution experiments performed on natural abiotic hydromagnesite. Measured equilibrium constants on natural biologically induced hydromagnesite, as determined in the present study, are one to three orders of magnitude higher than those generated from the Robie and Hemingway (1972, 1973) calorimetric data. Although these differences may be within the uncertainty of the calculations (*cf.*, Oelkers *et al.*, 2009) such differences may also result from the presence of small hydromagnesite grains. Hydrolysis constants generated in this study are less than an order of magnitude different from those reported by Gautier *et al.* (2014), confirming these previous results, and suggesting a similar stability of biotic versus abiotic hydromagnesite.

2.5.3 The variation of hydromagnesite precipitation rates as a function of temperature

The hydromagnesite precipitation rates illustrated in *Figure 4* suggest that there is little effect of increasing temperature on rates from 22.5 to 75 °C. This atypical observation can stem from a decrease in the number of active sites on the hydromagnesite surface in the higher temperature experiments. A potential mechanism for the decrease in reactive surface area with increasing temperature is the agglomeration of hydromagnesite particles during precipitation. Particle agglomeration decreases rates by decreasing the hydromagnesite surface area in contact with the reactive fluid. Indeed, SEM images taken after the 22.5 and 75 °C experiments can be compared in *Figure 1*, where it can be seen that the hydromagnesite recovered following the higher temperature experiments are larger, potentially reflecting the increased agglomeration of these grains. Note also that Pokrovsky *et al.* (2009) and Schott *et*

al. (2009) reported that carbonate mineral dissolution rates even decreased with increasing temperature from 100 to 150 °C. They attributed this atypical behavior to changes in the surface speciation of carbonate minerals with increasing temperature.

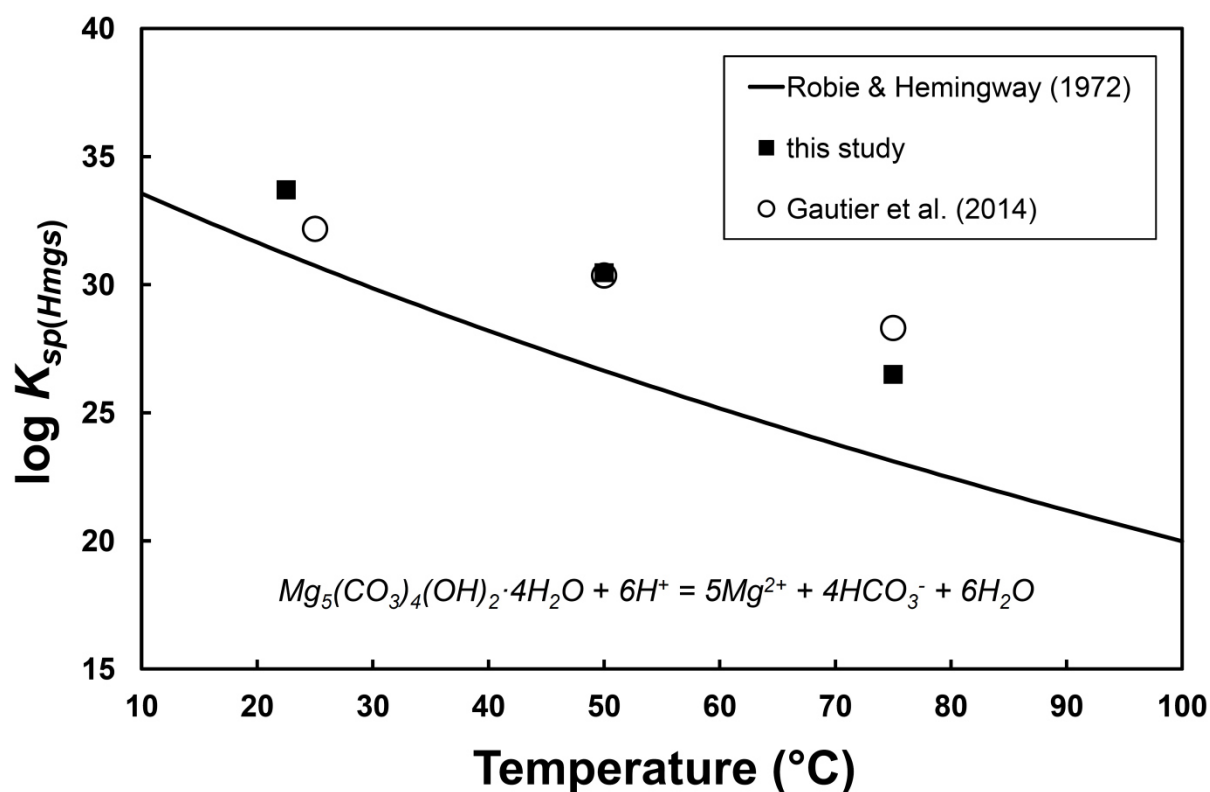


Figure 7: Equilibrium constants for the hydromagnesite hydrolysis reaction (*Reaction (1)*) as a function of temperature. Results of this study are represented by filled squares and can be compared to corresponding values reported by Gautier *et al.* (2014) and those generated by thermodynamic measurements of Robie and Hemingway (1972). Note that the solubility constant at 75 °C reported by Gautier *et al.* (2014) was extrapolated rather than measured directly.

A comparison between hydromagnesite precipitation rate constants generated in the present study and those of Gautier *et al.* (2014) is also provided in *Figure 4*. Rate constants generated in the present study on biogenic hydromagnesite are approximately 20-times faster than corresponding rate constants reported by Gautier *et al.* (2014) on abiotic hydromagnesite.

This difference suggests that biogenic hydromagnesite has far more active sites per unit surface area than its abiotic counterpart. Comparison of photomicrographs presented by Gautier *et al.* (2014) and in this study shows the abiotic hydromagnesite to consist of euhedral and larger crystals. Note that rates at 75 °C reported for the biotic and abiotic hydromagnesite are similar in value, but as mentioned above rates generated at this temperature in the present study may have been lowered due to agglomeration.

2.6 Conclusion

The results summarized above confirm the rapid dissolution and precipitation kinetics of hydromagnesite. Hydromagnesite dissolution rates were so rapid that they could not be accurately quantified from the closed system reactor experiments performed in this study. Due to its rapid reaction rates, hydromagnesite should quickly equilibrate with low and ambient temperature natural fluids. The fast precipitation rates of hydromagnesite suggest it could be an efficient product phase for the *ex-situ* and *in-situ* sequestration of CO₂.

Chapter 3

MAGNESIUM ISOTOPE FRACTIONATION DURING HYDROMAGNESITE DISSOLUTION, PRECIPITATION, AND AT EQUILIBRIUM

Abstract

This study provides direct experimental evidence of the rapid resetting of the magnesium isotope signatures of hydromagnesite ($\text{Mg}_5(\text{CO}_3)_4(\text{OH})_2 \cdot 4\text{H}_2\text{O}$) in the presence of an aqueous fluid during its congruent dissolution, precipitation, and at equilibrium at ambient temperatures over month-long timescales. All experiments were performed in batch reactors in aqueous sodium carbonate buffer solutions having a pH from 8 to 9. During congruent hydromagnesite dissolution, the fluid first became enriched in isotopically light magnesium, but the magnesium isotope composition became heavier after the fluid attained chemical equilibrium with the mineral; the $\delta^{26}\text{Mg}$ composition of the fluid was up to ~ 0.25 ‰ heavier than the dissolving hydromagnesite at the end of the dissolution experiments. Hydromagnesite precipitation was provoked during one experiment by increasing the reaction temperature from 4 to 50 °C. The $\delta^{26}\text{Mg}$ composition of the fluid increased as hydromagnesite precipitated and continued to increase after the fluid attained bulk equilibrium with this phase, such that it was ~ 0.25 ‰ higher after one month of fluid-carbonate interaction. These observations are consistent with the theoretical hypothesis that fluid-mineral equilibrium is dynamic (*i.e.*, dissolution and precipitation occur at equal, non-zero rates at equilibrium). Moreover the results presented in this study confirm 1) that the transfer of material from the solid to the

fluid phase is not conservative with respect to isotopic compositions during stoichiometric dissolution and 2) that the isotopic compositions of carbonate minerals continue to equilibrate even when the mineral is in bulk chemical equilibrium with its coexisting fluid. This latter observation suggests that the preservation of isotopic signatures of carbonate minerals in the geological record requires some sort of combination of the isolation of fluid-mineral system from external chemical input and/or the existence of a yet to be defined dissolution/precipitation inhibition mechanism.

3.1 Introduction

The isotopic signatures preserved in the geologic record have been applied by the Earth science community to characterize a plethora of natural processes and environments. For example, magnesium isotopes have been used in an attempt to constrain magnesium cycling in marine sediments (Higgins and Shrag, 2010), to provide insight into past and present continental weathering processes (Pogge von Strandmann *et al.*, 2008; Tipper *et al.*, 2008; Pokrovsky *et al.*, 2011; Wimpenny *et al.*, 2011; Mavromatis *et al.*, 2014b), to quantify carbonate diagenesis (Fantel and Higgins, 2014), to define ancient climatic events (Kasemann *et al.*, 2014), and as paleoenvironmental proxies (Pogge von Strandmann *et al.*, 2014; Saenger and Wang, 2014; Geske *et al.*, 2015). Critical to most of these applications is that mineral isotopic signatures are preserved over significant and in some cases over geologic timeframes. The preservation of stable isotopic signatures in minerals, however, has been questioned by a number of recent studies. For example, Pearce *et al.* (2012) observed that magnesium isotopic signatures continued to evolve between a fluid phase and coexisting magnesite at 150 and 200 °C after bulk equilibrium was attained between the mineral and solid. Mavromatis *et al.* (2012) and Shirokova *et al.* (2013) observed a continuous re-equilibration of magnesium

isotopes between the hydrous Mg-carbonate minerals nesquehonite and dypingite, and its co-existing aqueous fluid at ambient temperatures during experiments that lasted no more than 4 weeks. In a follow-up study, Mavromatis *et al.* (2015) reported the continuous re-equilibration of carbon isotopes between nesquehonite and dypingite and its co-existing aqueous fluid at the same conditions. Oelkers *et al.* (submitted) reported that the calcium isotopic composition of calcite can be reset over the course of a week when the mineral and fluid are at bulk chemical equilibrium. A significant number of observations also suggest that carbonate isotopic signatures can be reset in natural systems over geological timeframes (Fantle and DePaolo, 2007; Fantle *et al.*, 2010; Druhan *et al.*, 2013). Similar isotopic signature resetting was reported at ambient temperature during water-barite interaction by Curti *et al.* (2010), during water-epsomite interaction by Li *et al.* (2011), and during water-brucite interaction by Li *et al.* (2014). Building upon these past works, the present study provides further insight into the resetting of isotopic compositions through observations of the temporal evolution of magnesium isotopic composition of fluids and coexisting hydromagnesite during its dissolution, precipitation, and at equilibrium.

This study is centered on the reactivity of hydromagnesite, the most common hydrous Mg-carbonate on the Earth's surface. Despite the fact that the formation of anhydrous Mg-carbonates is thermodynamically favored (Hänchen *et al.*, 2008; Bénézeth *et al.*, 2011), the formation of these minerals such as magnesite is unlikely to occur at ambient temperatures due to the strong hydration of aqueous magnesium (*i.e.*, Lippmann, 1973; Saldi *et al.*, 2009, 2012; Mavromatis *et al.*, 2013; Gautier *et al.*, 2014). As such, hydrous magnesium carbonate minerals, like hydromagnesite and nesquehonite form in Earth's surface environments like alkaline lakes (Shirokova *et al.*, 2011, 2013; Mavromatis *et al.*, 2012, 2015; Power *et al.*, 2014). The formation of these minerals has been shown to be catalyzed by bacterial activity (Power *et al.*, 2007, 2009, 2014; Shirokova *et al.*, 2013).

The formation of hydrous Mg-carbonates like hydromagnesite and nesquehonite has recently attracted interest due to their potential use in geological CO₂ storage, particularly at low temperature conditions where magnesite does not form. Notably, field observations have shown that passive CO₂ storage may occur in ultramafic mine tailings through the weathering of Mg-silicates and precipitation of hydrous Mg-carbonates (Wilson *et al.*, 2009; Pronost *et al.*, 2011). Such observations have motivated a number of experimental studies characterizing the formation conditions, reactivity, and thermal stability of hydrous Mg-carbonates (Frost *et al.*, 2008; Hänchen *et al.*, 2008; Ballirano *et al.*, 2010; Berninger *et al.*, 2014; Gautier *et al.*, 2014). Other studies have investigated the mechanisms of hydromagnesite or nesquehonite formation during the carbonation of serpentine (Park and Fan, 2004; Teir *et al.*, 2007, 2009) and brucite (Zhao *et al.*, 2009; Schaef *et al.*, 2011b; Loring *et al.*, 2012).

Numerous studies have focused on characterizing magnesium fractionation among anhydrous carbonate minerals and their co-existing fluids. For example, magnesium isotope fractionation between fluids and co-existing magnesite and dolomite at elevated temperatures have been reported by Pearce *et al.* (2012) and Li *et al.* (2015). Corresponding fractionation has been measured for magnesium in calcite at ambient temperatures (Li *et al.*, 2012; Mavromatis *et al.*, 2013). Work on magnesium fractionation during hydrous Mg-carbonate water interaction include that of Mavromatis *et al.* (2012) on dypingite at ambient temperatures and that of Shirokova *et al.* (2013) on hydromagnesite stromatolites of Lake Salda, Turkey. This study is aimed to assess how rapidly such magnesium isotopic signatures may be reset through a study of magnesium isotope fractionation during batch reactor experiments performed under strictly defined physicochemical conditions for up to 575 days. The purpose of this manuscript is to report the results of this experimental study and use these to illuminate the potential for the resetting of isotopic signatures in natural systems.

3.2 Theoretical considerations

The variation of fluid isotopic signatures during stoichiometric dissolution and at equilibrium can be quantified through the application of transition state theory (Aagaard and Helgeson, 1982; Oelkers *et al.*, 1994, Schott and Oelkers, 1995; Oelkers, 2001b; Schott *et al.*, 2009). Within transition state theory, dissolution proceeds by the two way transfer of mass to and from the mineral surface. By symbolizing the detachment rate of mass from the surface (*e.g.*, ‘forward dissolution’) as r_+ and the return rate of mass to the surface (*e.g.*, ‘reverse precipitation’) as r_- , the overall dissolution rate (r) can be expressed as

$$r = r_+ - r_- = r_+ \left(1 - \frac{r_-}{r_+} \right) \quad (7)$$

For mineral dissolution, the forward dissolution rate is assumed proportional to its reactive surface area such that

$$r_+ = k_+ s \quad (8)$$

where k_+ and s refer to a rate constant and the reactive surface area, respectively. The reverse precipitation rate is given by

$$r_- = k_+ s \left(\frac{Q}{K_{eq}} \right)^{\frac{1}{\beta}} \quad (9)$$

where Q stands for the reaction quotient of the overall dissolution reaction and K_{eq} corresponds to its equilibrium constant. The symbol β in *Equation (9)* designates Temkin's average stoichiometric number equal to the ratio of the rate of destruction of the activated or precursor complex relative to the overall rate (Temkin, 1963), which is 5 for hydromagnesite

dissolution (Gautier *et al.*, 2014). Note that at equilibrium $\left(\frac{Q}{K_{eq}}\right)$ equals one and thus the overall dissolution rate equals zero at equilibrium.

The temporal change in isotopic composition of an element M in the fluid phase during closed-system dissolution of a single phase can be calculated from mass balance considerations according to

$$\frac{d\delta^n M_{fluid}}{dt} = \frac{v_M (r_+ \delta^n M_+ - r_- \delta^n M_-)}{V} \quad (10)$$

where t refers to time, V denotes the mass of fluid in the system, v_M symbolizes the number of moles of M in one mole of the mineral, and $\delta^n M_{fluid}$, $\delta^n M_+$, and $\delta^n M_-$ designates the isotopic composition of the M^{th} element in the fluid phase, the mass released from the solid by forward dissolution, and that removed from the fluid by reverse precipitation. In cases where there is no specific kinetic contribution to isotopic fractionation (*e.g.*, the differences in transport rates of distinct isotopes does not affect fractionation), $\delta^n M_-$, the isotopic composition of M removed from the fluid by reverse precipitation is given by

$$\delta^n M_- = \delta^n M_{fluid} - \Delta^n M_{fluid-mineral} \quad (11)$$

where $\Delta^n M_{fluid-mineral}$ symbolizes the equilibrium fluid-mineral fractionation factor of the M^{th} element. Material released from the mineral during its forward dissolution will consist of some original mineral and some of the material returned from the fluid phase via reverse precipitation. Note that the material returned to the mineral surface by reverse precipitation will have a strong tendency to be re-dissolved as this precipitation will tend to occur at the reactive sites on the mineral surface. Consequently, the isotopic composition of M added to the fluid via forward dissolution will be the weighted average of that of the original mineral

and that part of the reverse precipitation that is re-dissolved. If the original mineral was isotopically homogeneous, the composition of M added via forward dissolution is given by

$$\delta^n M_+ = \delta^n M_{original\ mineral} \left(1 - \frac{(1-X)r_-}{r_+}\right) + \delta^n M_+ \frac{(1-X)r_-}{r_+} \quad (12)$$

where X is the fraction of the precipitated material that is incorporated into the mineral and not re-dissolved. A representative example of the chemical and isotopic evolution of the fluid phase during closed-system dissolution of a mineral into originally pure water is shown in *Figure 8*. For this illustrative example, the mineral solubility product was set to 10^{-4} , its rate constant set to 10^{-8} mol/m²/s, and its total surface area set to 1 m². The $\delta^n M_{original\ mineral}$ was -1 and the $\Delta^n M_{fluid-mineral}$ was 0.5. The curves in *Figure 8* were generated by numerically integrating *Equations (7) to (12)* using an EXCEL spread sheet. In this example, the concentration of the fluid in M increases and attains bulk chemical equilibrium with the mineral after approximately 5 days. The temporal isotopic evolution of the fluid phase, however, depends greatly on the parameter X . If all the re-precipitated material is fixed into the mineral, $X = 1$ and isotopic equilibrium is attained at approximately the same time as bulk chemical equilibrium. When a small fraction of the re-precipitated material is fixed in the mineral phase the attainment of isotopic equilibrium is far slower than the attainment of bulk chemical equilibrium. If none of the re-precipitated material is fixed in the mineral, $X = 0$ and the isotopic composition of the fluid remains constant and is equal to that of the dissolving mineral. Such would result in a behavior consistent with the common assumption that isotopes are conservatively released by minerals during their stoichiometric dissolution. *Equations (7) to (12)* will be used below to model the isotopic evolution of magnesium during the dissolution of hydromagnesite.

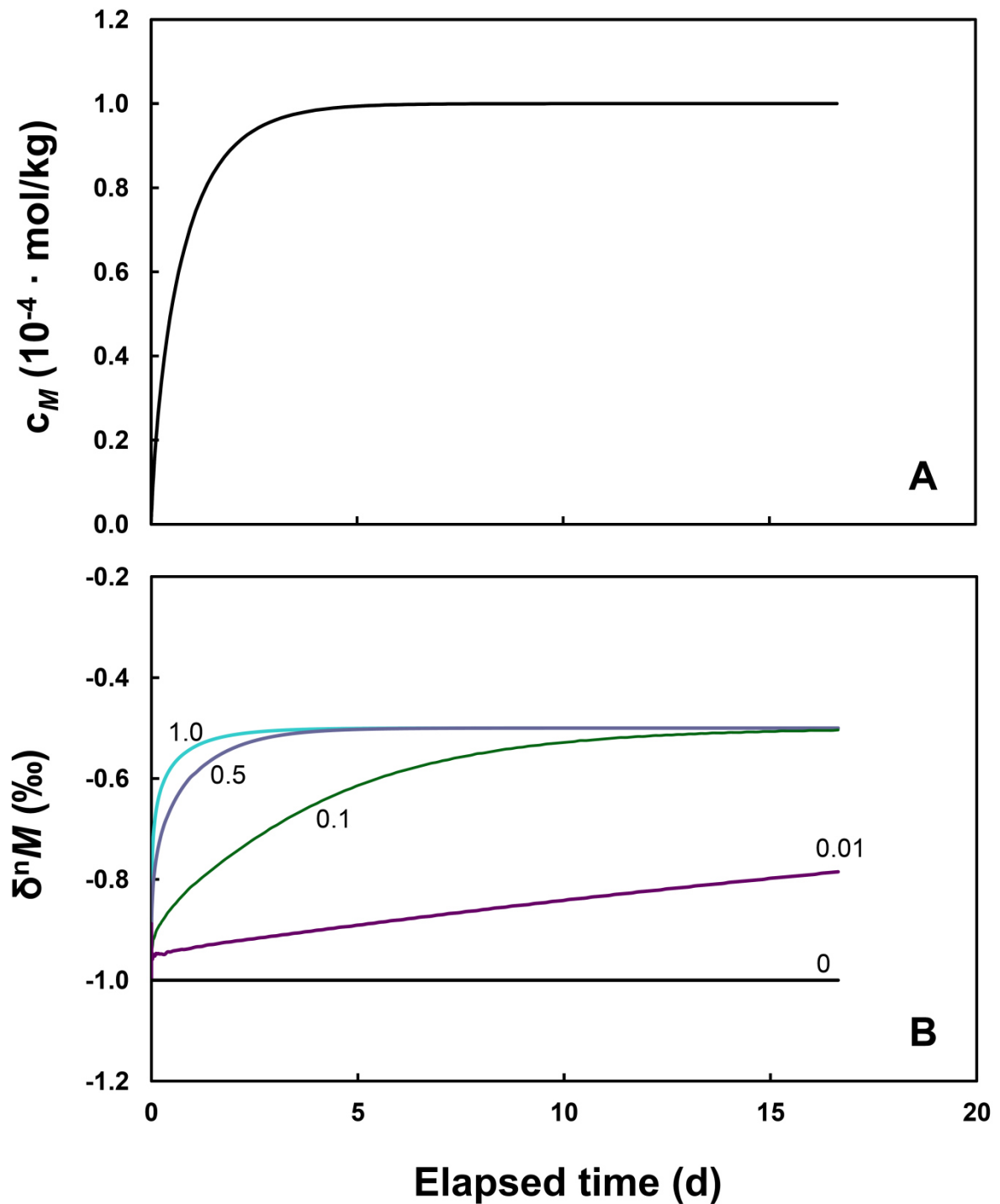


Figure 8: Temporal variation of fluid chemical and isotopic composition of a single component mineral dissolving into 1 kg of initially pure water in a closed-system reactor. The mineral solubility product was set to 10^{-4} , its rate constant set to 10^{-8} mol/m²/s, and its total surface area set to 1 m². The initial $\delta^n M$ of the mineral was -1 and the $\Delta^n M_{fluid-mineral}$ was 0.5: A) temporal fluid concentration, B) temporal $\delta^n M$ composition of the fluid for values of X , the fraction of reprecipitated metal M reincorporated into the mineral of 1, 0.5, 0.1, 0.01, and 0.

3.3 Methods

All thermodynamic calculations in this study were performed using the PHREEQC (Version 2.18) computer code (Parkhurst and Appelo, 1999) together with its Ilnl database after adding the equilibrium constants for Mg^{2+} hydrolysis and the carbonic acid dissociation reported by Brown *et al.* (1996) and Millero *et al.* (2007), respectively, and the equilibrium constant for the hydromagnesite hydrolysis reaction and the solubility product of hydromagnesite reported by Gautier *et al.* (2014).

3.3.1 Experimental design

All experiments in this study were performed using natural hydromagnesite collected from stromatolite precipitates in Lake Salda in southwest Turkey. These solids and their sampling methods have been described by Shirokova *et al.* (2011, 2013). Prior to their use in the experiments, these solids were handmilled with an agate mortar and pestle. The resulting powder was cleaned with 10 % H_2O_2 to remove organics and oven dried at 50 °C for 24 h. The particles were not cleaned ultrasonically due to the fine nature of these natural grains. Scanning electron microscope (SEM) images, obtained using a JEOL JSM-6360 LV microscope, of the resulting hydromagnesite are shown in *Figure 9*. The hydromagnesite powder consists of agglomerated crystals; the agglomerates range up to 50 μm in size, and the size of the individual hydromagnesite crystals is $\sim 5 \mu\text{m}$. No other mineral phases were evident from SEM images nor were any detected using backscattered electron microscopy. The purity of this hydromagnesite, was verified via x-ray diffraction using an INEL CPS-120 diffractometer with Co $\text{K}\alpha$ -radiation, $\lambda = 1.78897 \text{ \AA}$, and a graphite monochromator. X-ray diffraction was performed from 1 to $110^\circ 2\theta$ at $0.09^\circ/\text{min}$. This analysis revealed no phase other than hydromagnesite. The surface area of the cleaned hydromagnesite was determined

using a Quantachrome Gas Sorption system to be $8.5 \text{ m}^2/\text{g} \pm 10 \%$ according to the BET method (Brunauer *et al.*, 1938).

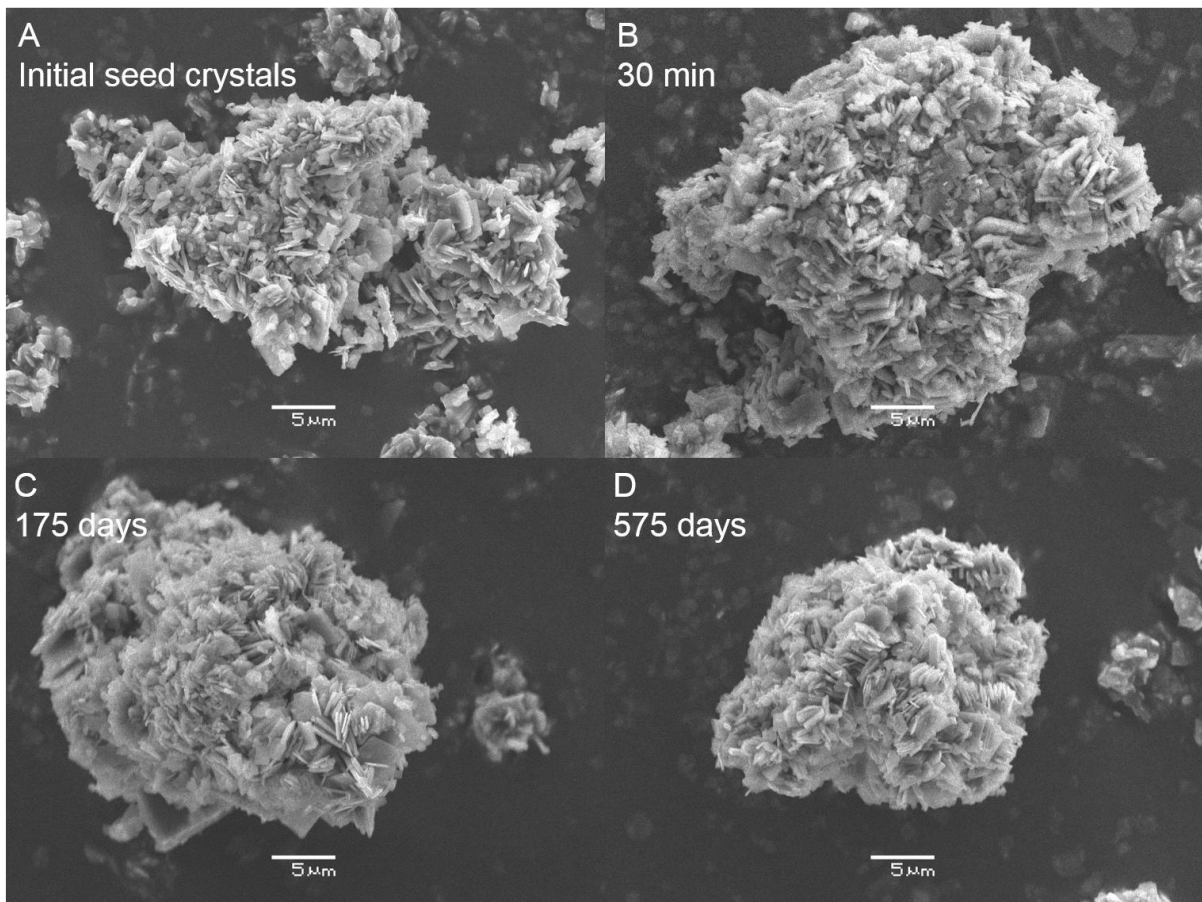


Figure 9: Scanning electron micrographs of (A) the initial hydromagnesite seed material, (B) after dissolution experiment Hmgs-2.1, (C) after dissolution experiment Hmgs-2.8, and (D) after dissolution experiment Hmgs-4.7. No change in morphology or grain size is observed during the experiments.

Two different types of batch experiments were performed in this study to illuminate the behavior of magnesium fractionation during dissolution, precipitation and at equilibrium. Experiments Hmgs-1, Hmgs-3, Hmgs-4, and Hmgs-5 were single batch reactor experiments; the protocol for these experiments was presented in further detail by Berninger *et al.* (2014). Experiment Hmgs-2 consisted of a series of 13 individual batch experiments each ran for a

selected elapsed time before being stopped. Experiments Hmgs-1, Hmgs-2, Hmgs-3, and Hmgs-4 were performed in 0.5 L high-density polypropylene reactors while experiment Hmgs-5 was performed in a 1 L high-density polypropylene reactor. Experiments Hmgs-1 to Hmgs-4 were initiated by placing ~ 1 g of hydromagnesite powder and 500 g of the initial reactive fluid into the reactor. Experiment Hmgs-5 was started by adding 10 g of hydromagnesite powder and 1 kg of initial reactive fluid to the reactor. The initial reactive fluids were composed of deionized H₂O and Merck reagent grade Na₂CO₃ and NaHCO₃, and had a pH of ~ 9.0; the composition of all initial fluids is provided in *Table 2*. Note some minor magnesium was present in the initial reactive fluids; it was likely present as a trace component of the carbonate salts used to make these fluids. Hydromagnesite was allowed to dissolve in this fluid for time periods of up to 575 days. Fluids were sampled regularly from the traditional batch reactors, and at the end of each individual batch reactor using Millipore 0.22 µm cellulose acetate filters while sampling. All but one experiment was maintained at 25 ± 1 °C. The initial temperature during the final experiment (Hmgs-5) was set to 4 ± 1 °C for the first 33 days then raised to 50 ± 1 °C. Due to the retrograde solubility of hydromagnesite, increasing temperature led the reactor fluid to be supersaturated with respect to this phase, provoking its precipitation. At the end of each experiment the fluids were separated from solids using suction filtration through these 0.22 µm filters. The solids were oven dried at 50 °C for 24 h then stored at ambient temperature prior to chemical and isotopic analyses. All sampled fluids were stored at 4 °C prior to analysis.

Table 2: Initial solutions and parameters of experiments reported in *Chapter 3*.

Experiment	Hmgs seeds (g)	Composition of buffer solution		pH	c _{Mg} ($\mu\text{mol/kg}$)	Alkalinity (eq/L)
		NaHCO ₃ (g/kg)	Na ₂ CO ₃ (g/kg)			
Hmgs-1	0.9506	8.8990 ^a	0	7.77	7.8 \pm 0.4	0.105 \pm 0.001
Hmgs-2.1	0.9995	6.9731	0.8478	9.02	5.1 \pm 0.3	0.096 \pm 0.001
Hmgs-2.2	1.0005	6.9731	0.8478	9.02	5.1 \pm 0.3	0.096 \pm 0.001
Hmgs-2.3	0.9993	6.9731	0.8478	9.02	5.1 \pm 0.3	0.096 \pm 0.001
Hmgs-2.4	0.9996	6.9731	0.8478	9.02	5.1 \pm 0.3	0.096 \pm 0.001
Hmgs-2.5	0.9989	6.9731	0.8478	9.02	5.1 \pm 0.3	0.096 \pm 0.001
Hmgs-2.6	0.9997	6.9731	0.8478	9.02	5.1 \pm 0.3	0.096 \pm 0.001
Hmgs-2.7	0.9988	6.9731	0.8478	9.02	5.1 \pm 0.3	0.096 \pm 0.001
Hmgs-2.8	1.0001	6.9725	0.8479	9.22	6.4 \pm 0.3	0.097 \pm 0.001
Hmgs-2.9	1.0017	6.9725	0.8479	9.22	6.4 \pm 0.3	0.097 \pm 0.001
Hmgs-2.10	1.0001	6.9725	0.8479	9.22	6.4 \pm 0.3	0.097 \pm 0.001
Hmgs-2.11	1.0007	6.9725	0.8479	9.22	6.4 \pm 0.3	0.097 \pm 0.001
Hmgs-2.12	1.0003	6.9725	0.8479	9.22	6.4 \pm 0.3	0.097 \pm 0.001
Hmgs-2.13	1.0011	6.9725	0.8479	9.22	6.4 \pm 0.3	0.097 \pm 0.001
Hmgs-3	0.9994	6.9725	0.8479	9.22	6.4 \pm 0.3	0.097 \pm 0.001
Hmgs-4	1.0012	6.9725	0.8479	9.22	6.4 \pm 0.3	0.097 \pm 0.001
Hmgs-5	10.00	6.9731	0.8478	9.02	5.1 \pm 0.3	0.096 \pm 0.001

^a In addition, 4.9 mL of 1N HCl was added to 1 L of this initial reactive fluid.

3.3.2 Chemical analyses

Aqueous fluid magnesium concentrations were measured by flame atomic absorption spectroscopy (AAS) using a Perkin Elmer AAnalyst 400 with an uncertainty of $\pm 2\%$ and a detection limit of 6×10^{-7} mol/kg. Alkalinity was determined following a standard HCl titration procedure using an automatic Schott TitroLine alpha TA10plus titrator with an un-

certainty of $\pm 2\%$ and a detection limit of 5×10^{-5} eq/L. Fluid pH was measured using a Metrohm 713 pH Meter combined electrode on the activity scale with NIST buffers (pH = 4.006, 6.865, and 9.183 at 25 °C). Solids were analyzed by SEM and XRD to verify their compositions following the experiments.

3.3.3 Magnesium isotope analyses

Prior to stable magnesium isotope analyses, liquid and solid samples were chemically purified by cation exchange chromatography following a protocol similar to that reported earlier by our group (*e.g.*, Mavromatis *et al.* 2012, 2013; Pearce *et al.* 2012; Shirokova *et al.* 2013). Fluid samples were evaporated to dryness and re-dissolved in aqueous 1 molal HNO₃ prior to loading onto columns for chromatographic separation. Hydromagnesite samples, were dissolved in concentrated aqueous HNO₃ before being evaporated to dryness, and then dissolved again in aqueous 1 molal HNO₃. Aliquots of these solution samples were loaded onto 10 mL Bio-Rad poly-prop columns containing AG-50W-X12 resin (200-400 mesh) for separation of Mg²⁺ from Na⁺. Magnesium recovery after chromatographic separation was > 99.5 %. The magnesium isotopes were measured with a Thermo-Finnigan ‘Neptune’ Multi Collector Inductively Coupled Plasma Mass Spectrometer (MC-ICP-MS) at the GET laboratory (Toulouse, France). All the solutions were prepared in 0.3 molal HNO₃ and were introduced into the Ar plasma with a standard spray chamber. The instrumental mass fractionation effects were corrected via sample-standard bracketing using the DSM3 standard and all data are presented in delta notation values with respect to the DSM3 ($\delta^x\text{Mg} = ((^x\text{Mg}/^{24}\text{Mg})_{\text{sample}} / (^x\text{Mg}/^{24}\text{Mg})_{\text{DSM3}} - 1) \times 1000$) where *x* refers to the Mg-mass of interest. All sample analyses were run in triplicate, with the mean value being presented in the tables below. All results are consistent with mass dependent fractionation. The reproducibility

of the isotopic analyses was assessed by replicate of three magnesium reference liquid standards (DSM3, CAM-1 and OUMg) and the dolomite carbonate standard JDo-1, yielding precisions better than 0.07 ‰; these measurements were in agreement with the previously published values (*e.g.*, Bolou-Bi *et al.*, 2009; Wombacher *et al.*, 2009, Beinlich *et al.*, 2014; Mavromatis *et al.*, 2014a, b).

3.4 Results

Representative photomicrographs of hydromagnesite recovered after the single batch experiments stopped after 30 min, 175 days, and 575 days are shown in *Figure 9*. Mass balance calculations indicate that as much as 10 % of the hydromagnesite dissolved into the fluid phase during these experiments. Only hydromagnesite is evident in the images consistent with the stoichiometric dissolution of this mineral; similarly XRD analysis of the solids following the experiments reveals only the presence of hydromagnesite. There is no evidence on this scale of hydromagnesite recrystallization, as the size of the individual crystals and the agglomerates recovered from these experiments appear to be identically sized as the initial hydromagnesite seed grains. The lack of secondary mineral precipitation is also consistent with geochemical calculations indicating that all secondary solids besides magnesite were undersaturated in the reactive fluids throughout the experiments.

The chemical and isotopic evolution of the fluid and solid phases during all experiments is presented in *Table 3* and shown in *Figures 10* to *13*. The magnesium isotope composition of solid hydromagnesite used in the experimental runs is -1.1 ± 0.1 ‰, which is identical to that reported for this hydromagnesite by Shirokova *et al.* (2011, 2013). Owing to the carbonate-rich reactive fluids, the alkalinity and pH remained close to constant during the

experiments, other than in experiment Hmgs-1 during which the pH increased by ~ 0.8 units. Chemical equilibrium between the fluid and the hydromagnesite is rapidly attained in all experiments consistent with the results reported by Berninger *et al.* (2014). For example, chemical equilibration was attained after ~ 5 h during experiment Hmgs-1 and after ~ 2 days during experiment Hmgs-2. This difference in equilibration times of the 25°C experiments may reflect the different pH of the initial reactive fluids. Note as well, that unlike Hmgs-1 the experimental series Hmgs-2 was not primarily designed to track the kinetics of hydromagnesite dissolution but to investigate the long-term evolution of the isotopic signatures. The equilibration of the fluids required that $\sim 25\%$ and $\sim 10\%$ of the hydromagnesite dissolved during these experiments, respectively. Notably, the isotopic composition of the fluid phase during the experiments evolves continuously and is distinct from that of the hydromagnesite seed crystals. During Hmgs-1 the $\delta^{26}\text{Mg}_{\text{fluid}}$ evolves from -1.0‰ consistent with the original seed material to -0.65‰ (see *Figure 10B*); during Hmgs-2 the reactive fluid becomes initially enriched in ^{24}Mg achieving a $\delta^{26}\text{Mg}_{\text{fluid}}$ of -1.33‰ but it is then progressively depleted in ^{24}Mg achieving an isotopic steady-state value of $0.87 \pm 0.04\text{‰}$ after 16 days of reaction time (*Figure 11B*). Note that isotopic analyses in replicate experiments performed during Hmgs-3 and Hmgs-4 resulted in identical, within analytical uncertainty, compositions of the reactive fluids (*Figure 12B*).

Table 3: Summary of experimental data of *Chapter 3*.

Experiment	Time (days)	Temp (°C)	pH	c_{Mg} (mmol/kg)	Alkalinity (eq/L)	$\delta^{25}Mg$	$\delta^{26}Mg$	$\log \Omega_{Hmgs}$	a_{Mg+2}/a_{CO_3-2}	Reactive fluid (g)	%Mg in fluid
Hmgs-1.1	0.01	23	8.34	2.9±0.1	0.109±0.001	-0.51±0.04	-1.01±0.07	-2.9	1.02	499.99	13.4
Hmgs-1.2	0.02	23	8.43	3.9±0.2	0.110±0.001			-1.8	1.08	494.58	18.0
Hmgs-1.3	0.04	23	8.47	4.2±0.2	0.111±0.001			-1.5	1.06	490.20	19.4
Hmgs-1.4	0.06	23	8.51	5.1±0.3	0.113±0.001	-0.38±0.05	-0.77±0.01	-0.9	1.12	486.09	23.1
Hmgs-1.5	0.12	23	8.56	5.5±0.3	0.113±0.001			-0.5	1.06	481.75	24.6
Hmgs-1.6	0.16	23	8.58	5.9±0.3	0.114±0.001	-0.40±0.02	-0.78±0.03	-0.1	1.06	477.46	26.4
Hmgs-1.7	0.22	23	8.60	7.1±0.4	0.115±0.001			0.3	1.20	473.54	31.3
Hmgs-1.8	0.27	23	8.63	6.0±0.3	0.114±0.001			0.1	0.94	470.39	26.2
Hmgs-1.9	0.32	23	8.65	6.0±0.3	0.115±0.001			0.2	0.89	467.72	26.3
Hmgs-1.10	0.47	23	8.64	6.3±0.3	0.115±0.001			0.3	0.96	465.26	27.4
Hmgs-1.11	0.90	23	8.68	6.7±0.3	0.116±0.001			0.5	0.92	461.73	28.7
Hmgs-1.12	1.29	23	8.70	5.7±0.3	0.115±0.001			0.3	0.74	459.19	24.5
Hmgs-1.13	1.91	22	8.71	5.3±0.3	0.113±0.001			0.1	0.70	456.85	22.6
Hmgs-1.14	2.36	23	8.71	5.3±0.3	0.114±0.001			0.2	0.66	453.80	22.3
Hmgs-1.15	2.92	23	8.71	5.6±0.3	0.114±0.001	-0.33±0.01	-0.65±0.03	0.2	0.72	451.21	23.7
Hmgs-1.16	3.39	23	8.71	6.4±0.3	0.116±0.001			0.5	0.81	448.19	26.7
Hmgs-1.17	4.17	23	8.75	5.2±0.3	0.114±0.001			0.2	0.60	445.88	21.7
Hmgs-2.1	0.03	26	9.04	0.92±0.05	0.098±0.001	-0.60±0.04	-1.22±0.06	-2.0	0.05	539.82	4.7
Hmgs-2.2	0.07	26	9.05	1.16±0.06	0.098±0.001	-0.67±0.04	-1.33±0.04	-1.5	0.06	542.05	5.9
Hmgs-2.3	0.28	26	9.05	1.55±0.08	0.098±0.001			-0.9	0.09	538.66	7.8
Hmgs-2.4	0.99	26	9.09	1.9±0.1	0.098±0.001	-0.57±0.03	-1.19±0.02	-0.3	0.10	540.99	9.7
Hmgs-2.5	6.81	24	9.13	2.3±0.1	0.100±0.001	-0.52±0.03	-1.06±0.06	0.1	0.11	538.56	11.6

Table 3: continued

Experiment	Time (days)	Temp (°C)	pH	c_{Mg} (mmol/kg)	Alkalinity (eq/L)	$\delta^{25}Mg$	$\delta^{26}Mg$	$\log \Omega_{Hmgs}$	a_{Mg+2}/a_{CO3-2}	Reactive fluid (g)	%Mg in fluid
Hmgs-2.6	16.22	25	9.17	2.2±0.1	0.103±0.001	-0.42±0.04	-0.87±0.04	0.2	0.09	542.65	11.3
Hmgs-2.7	33.14	25	9.09	2.2±0.1	0.103±0.001			-0.1	0.11	534.84	10.9
Hmgs-2.8	174.63	21	9.09	2.4±0.1	0.103±0.001			-0.4	0.13	540.38	12.1
Hmgs-2.9	205.48	22	9.15	2.3±0.1	0.102±0.001			-0.2	0.10	540.78	11.5
Hmgs-2.10	239.87	22	9.17	2.3±0.1	0.103±0.001			-0.2	0.10	540.83	11.4
Hmgs-2.11	359.78	24	9.20	2.0±0.1	0.103±0.001			-0.1	0.08	540.64	10.3
Hmgs-2.12	490.71	21	9.20	2.1±0.1	0.103±0.001			-0.3	0.09	541.00	10.7
Hmgs-2.13	545.65	22	9.15	2.1±0.1	0.102±0.001			-0.4	0.10	540.38	10.5
Hmgs-3.1	174.63	21	9.09	2.4±0.1	0.102±0.001	-0.49±0.02	-0.97±0.02	-0.4	0.13	540.29	12.1
Hmgs-3.2	205.49	22	9.15	2.3±0.1	0.102±0.001			-0.2	0.11	533.63	11.4
Hmgs-3.3	239.87	22	9.16	2.2±0.1	0.102±0.001	-0.47±0.02	-0.94±0.03	-0.2	0.10	527.34	10.9
Hmgs-3.4	359.78	24	9.20	2.0±0.1	0.100±0.001	-0.45±0.02	-0.92±0.03	-0.1	0.08	520.99	9.9
Hmgs-3.5	490.73	21	9.18	2.1±0.1	0.101±0.001			-0.4	0.09	514.54	10.1
Hmgs-3.6	545.66	22	9.16	2.1±0.1	0.102±0.001			-0.4	0.09	507.83	9.9
Hmgs-3.7	574.71	24	9.16	2.1±0.1	0.102±0.001			0.0	0.09	501.40	10.0
Hmgs-4.1	174.63	21	9.09	2.4±0.1	0.102±0.001	-0.49±0.03	-0.98±0.06	-0.4	0.13	540.19	12.1
Hmgs-4.2	205.50	22	9.15	2.3±0.1	0.102±0.001			-0.2	0.11	533.46	11.4
Hmgs-4.3	239.87	22	9.17	2.2±0.1	0.102±0.001			-0.2	0.10	526.95	10.9
Hmgs-4.4	359.78	24	9.21	2.0±0.1	0.101±0.001	-0.45±0.01	-0.92±0.03	0.0	0.08	520.65	9.9
Hmgs-4.5	490.73	21	9.19	2.1±0.1	0.102±0.001			-0.3	0.09	514.11	10.1
Hmgs-4.6	545.65	22	9.16	2.1±0.1	0.102±0.001			-0.4	0.09	507.29	9.8
Hmgs-4.7	574.71	24	9.16	2.2±0.1	0.103±0.001			0.0	0.09	500.80	10.1

Table 3: continued

Experiment	Time (days)	Temp (°C)	pH	c_{Mg} (mmol/kg)	Alkalinity (eq/L)	$\delta^{25}Mg$	$\delta^{26}Mg$	$\log \Omega_{Hmgs}$	a_{Mg+2}/a_{CO3-2}	Reactive fluid (g)	%Mg in fluid
Hmgs-5.1	8.01	4	9.30	3.3±0.2	0.099±0.001			-1.1	0.21	1181.82	36.6
Hmgs-5.2	14.04	4	9.41	3.4±0.2	0.102±0.001			-0.7	0.16	1175.55	37.1
Hmgs-5.3	22.07	4	9.48	3.5±0.2	0.103±0.001			-0.4	0.14	1169.70	38.2
Hmgs-5.4	32.89	4 / 50	9.30 / 8.89	3.8±0.2	0.103±0.001	-0.68±0.13	-1.32±0.13	-0.7 / 3.5	0.23 / 0.16	1163.57	41.2
Hmgs-5.5	38.68	50	8.92	2.1±0.1	0.100±0.001	-0.52±0.15	-1.02±0.15	2.3	0.09	1157.73	23.3
Hmgs-5.6	49.60	50	9.02	0.86±0.04	0.098±0.001			0.6	0.03	1151.64	9.2
Hmgs-5.7	57.80	50	8.90	0.79±0.04	0.097±0.001			0.1	0.03	1145.76	8.5
Hmgs-5.8	63.55	50	8.94	0.80±0.04	0.098±0.001			0.2	0.03	1139.52	8.5
Hmgs-5.9	71.75	50	9.04	0.80±0.04	0.098±0.001			0.5	0.02	1133.45	8.4
Hmgs-5.10	78.76	50	9.01	0.79±0.04	0.097±0.001	-0.48±0.06	-0.97±0.06	0.4	0.03	1127.48	8.4
Hmgs-5.11	133.12	50	9.10	0.92±0.05	0.096±0.001	-0.43±0.05	-0.82±0.11	1.0	0.02	1121.38	9.6
Hmgs-5.12	307.79	50	8.98	0.68±0.03	0.098±0.001	-0.43±0.04	-0.82±0.04	0.0	0.02	1113.72	7.1
Hmgs-5.13	316.63	50	9.06	0.75±0.04	0.100±0.001			0.4	0.02	1101.80	7.7

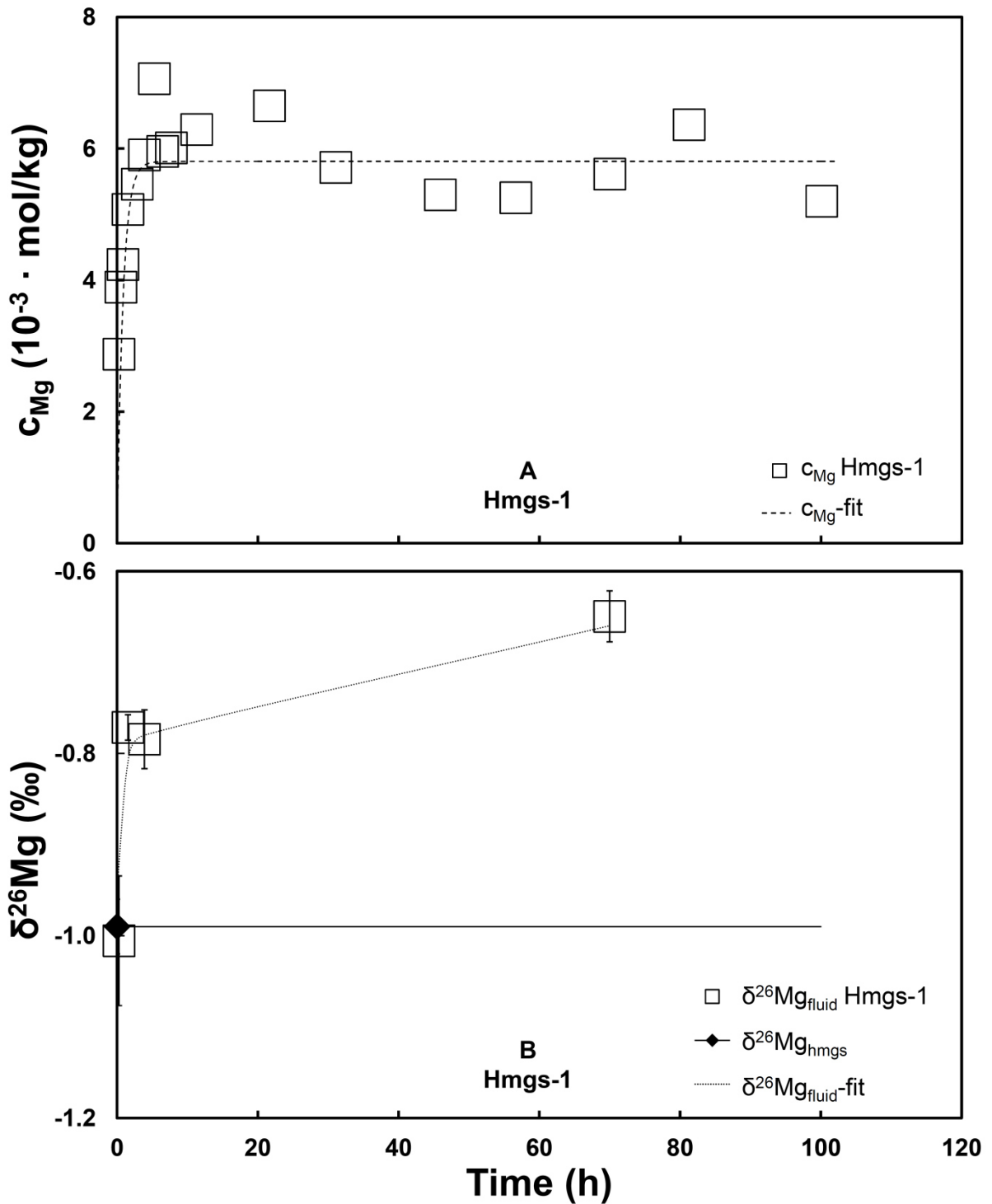


Figure 10: Temporal evolution of aqueous magnesium concentration and isotopic composition during batch reactor experiment Hmgs-1. Uncertainties of the concentration measurements are within the size of the symbols. Note that near constant aqueous magnesium concentrations are attained in ~ 1 h. The curves through the data in this figure were generated from a fit using *Equations (7) to (12)* together with the parameters provided in *Table 4*.

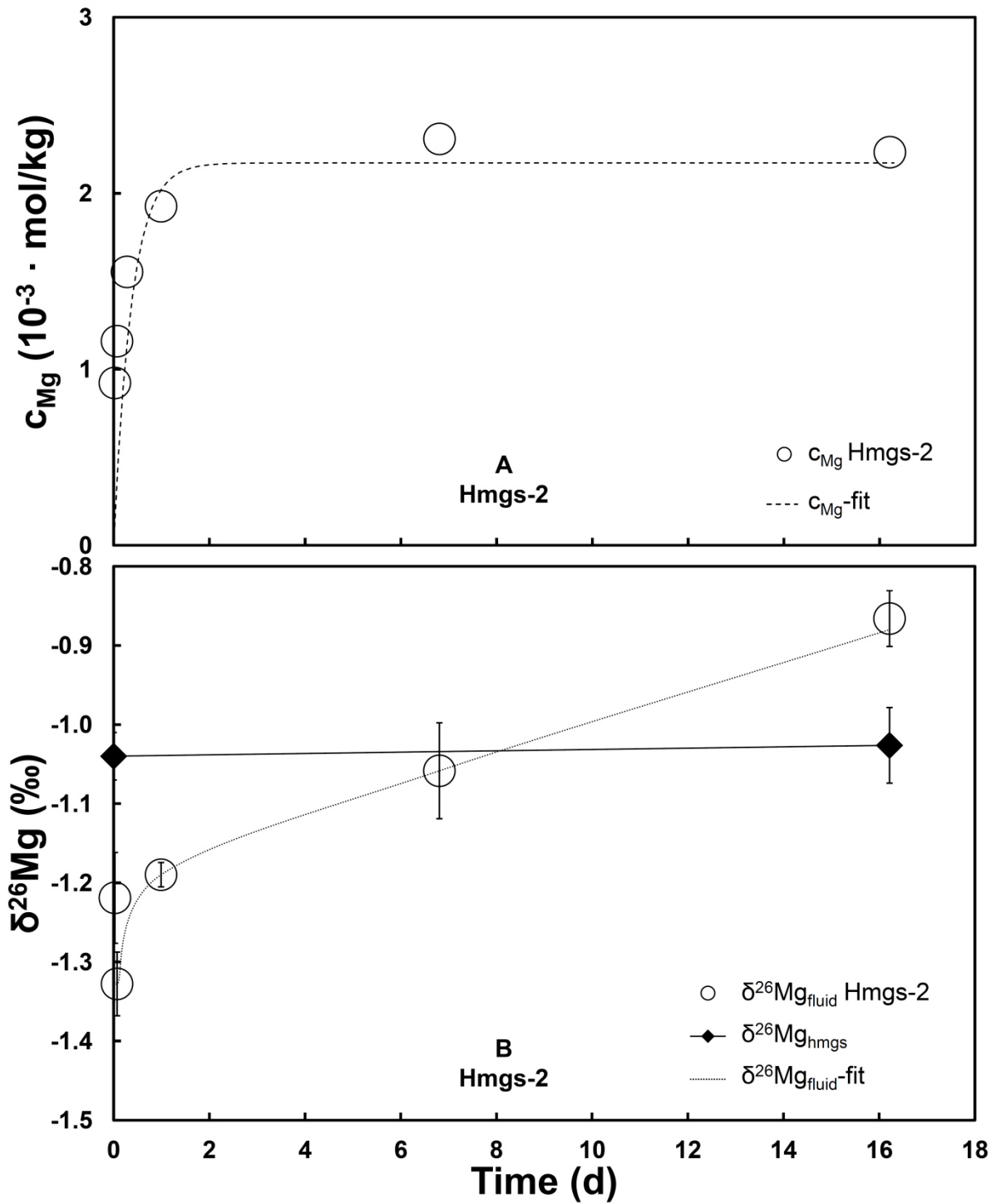


Figure 11: Temporal evolution of aqueous magnesium concentration and isotopic composition during the first 16 days of the individual batch reactor experiments Hmgs-2. The curves through the data in this figure were generated from a fit using *Equations (7) to (12)* together with the parameters provided in *Table 4*.

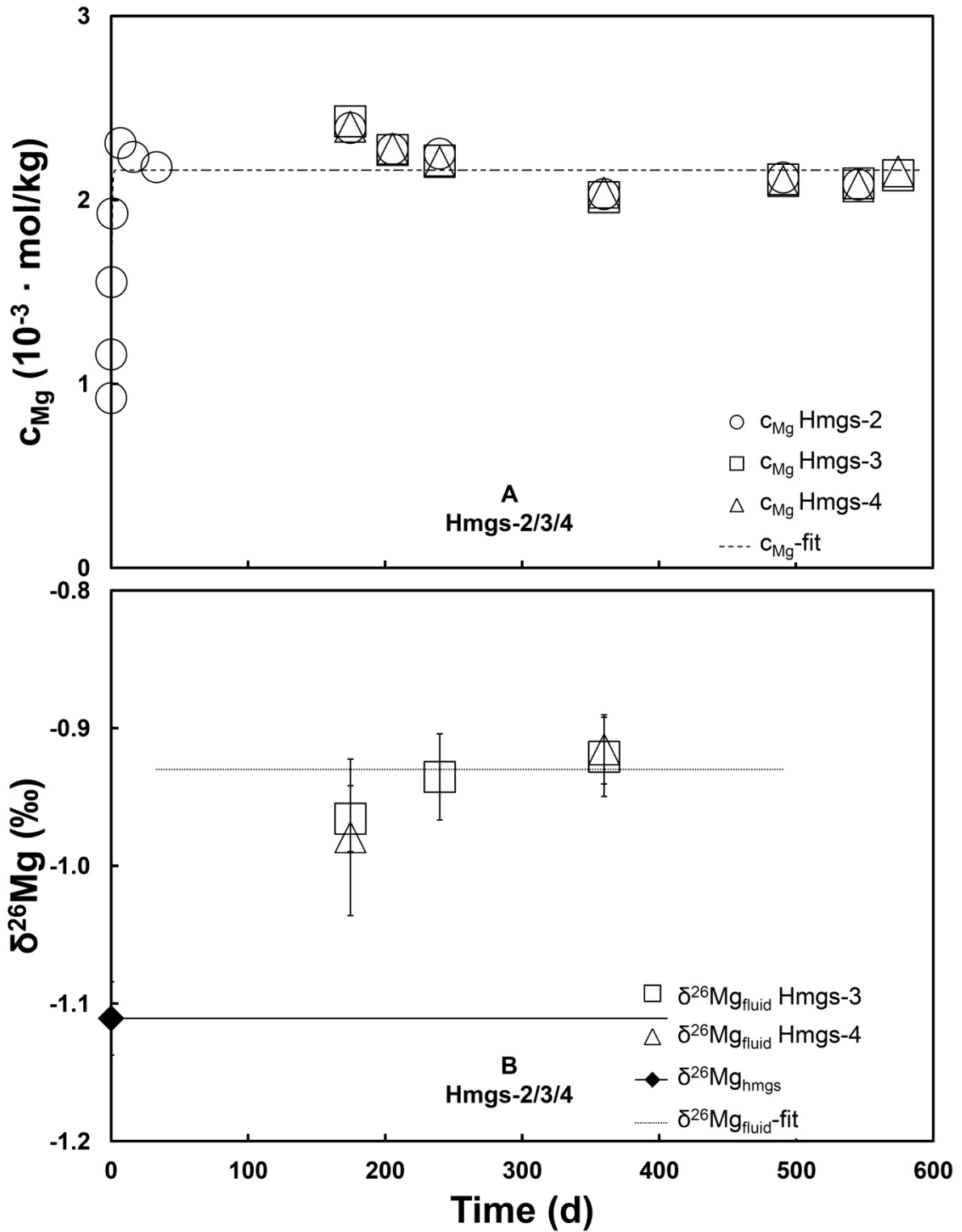


Figure 12: Temporal evolution of aqueous magnesium concentration and isotopic composition during ~ 1.5 years of the individual batch reactor experiments Hmgs-2, Hmgs-3, and Hmgs-4. Note the very good reproducibility of the experiments. The curves through the data in this figure were generated from a fit using *Equations (7) to (12)* together with the parameters provided in *Table 4*.

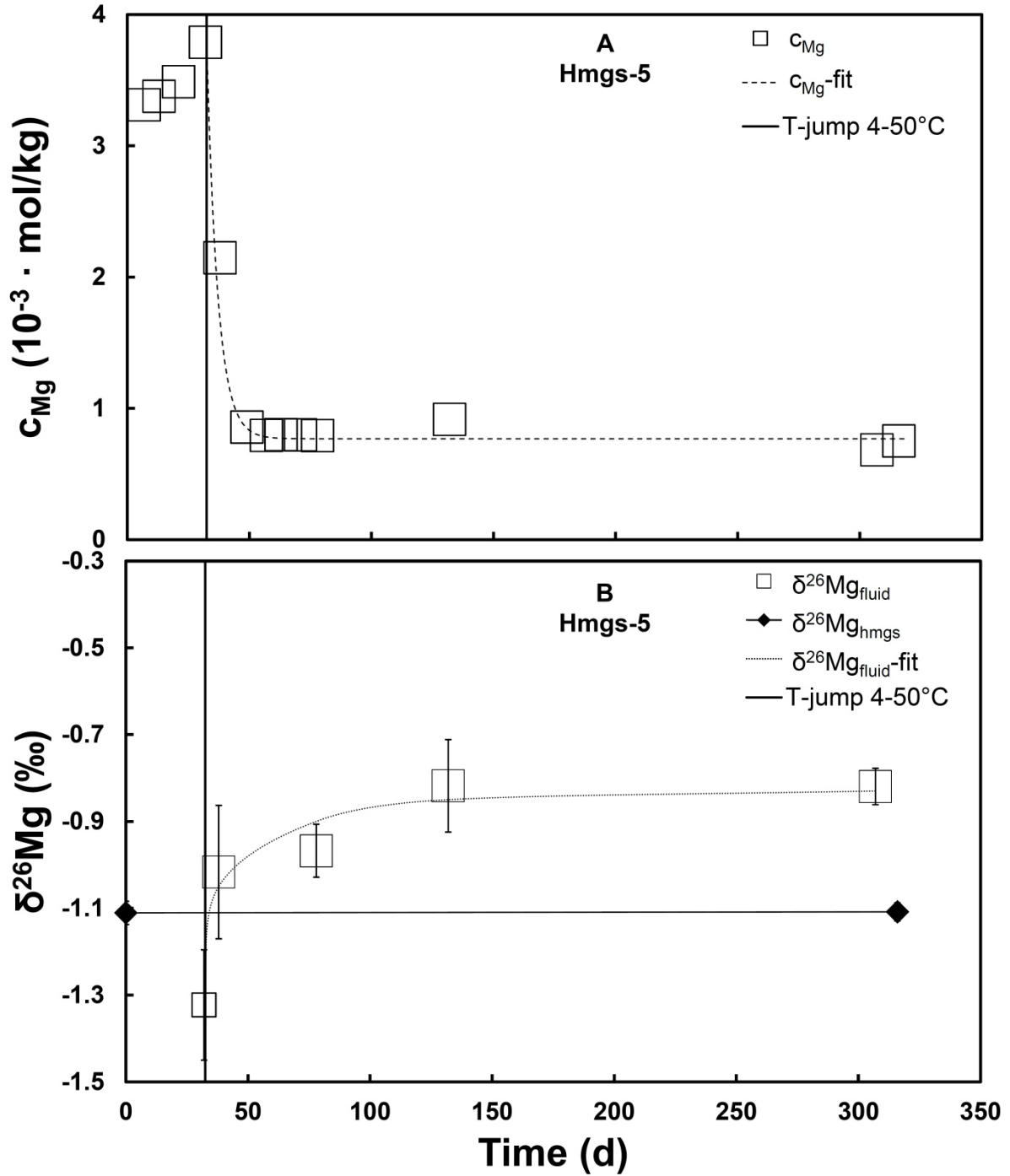


Figure 13: Temporal evolution of aqueous magnesium concentration and isotopic composition during experiment Hmgs-5. Note that the reactor temperature was increased from 4 to 50 °C at day 33 provoking hydromagnesite precipitation. The curves through the data in this figure were generated from a fit using *Equations (7) to (12)* together with the parameters provided in *Table 4*.

The evolution of the magnesium concentration and isotopic composition of experiment Hmgs-5 is shown in *Figure 13*. The reaction temperature of this experiment was 4 °C for the first 33 days. During this time the aqueous magnesium concentration increased to 3.8×10^{-3} mol/kg, corresponding to the dissolution of ~ 3.7 % of the original hydromagnesite seeds. During this time, the fluid became enriched in light magnesium compared to the dissolving solid; the $\delta^{26}\text{Mg}_{\text{fluid}}$ was -1.3 ± 0.1 ‰ after 33 days of dissolution compared to a $\delta^{26}\text{Mg}_{\text{hmgss}}$ of -1.1 ‰ for the solid. After 33 days the reactor temperature was increased to 50 °C. The retrograde solubility led to the precipitation of hydromagnesite and the decrease in fluid magnesium concentration to less than 1×10^{-3} mol/kg. During this time the isotopic composition of the fluid became heavier than the original hydromagnesite attaining a value of $\delta^{26}\text{Mg}_{\text{fluid}}$ of -0.97 ± 0.06 ‰ at approximately 100 days after the temperature increase. Note that the isotopic composition of magnesium in the fluid phase appears to continue to evolve after the fluid attained bulk chemical equilibrium with the precipitating hydromagnesite. Consistent with the small quantity of hydromagnesite dissolved, the magnesium isotopic composition of the solid recovered from the reactor following the experiment is identical within uncertainty to that of the initial hydromagnesite powder.

3.5 Discussion

3.5.1 Magnesium fractionation during hydromagnesite dissolution and at equilibrium

The magnesium isotopic composition of the fluid phase exhibits a complex behavior during hydromagnesite dissolution. The fluid phase of experiment Hmgs-2 becomes enriched in ^{24}Mg after 1.5 h of elapsed time with the $\delta^{26}\text{Mg}_{\text{fluid}}$ to obtain a value of -1.33 ‰, which is about 0.3 ‰ lighter compared to the original hydromagnesite material (see *Figure 11*). Then, the $\delta^{26}\text{Mg}_{\text{fluid}}$ approaches that of the original material within 6 days, and eventually becomes

isotopically heavy compared to this original material. A similar temporal increase in $\delta^{26}\text{Mg}_{\text{fluid}}$ is seen during experiment Hmgs-1. Although it is quite similar within uncertainty to the original hydromagnesite seeds, the first magnesium isotopic analysis shows this fluid to be slightly enriched in ^{24}Mg compared to the seed material. The fluid then becomes progressively heavier and is about 0.3 ‰ heavier compared to the original hydromagnesite at the end of the experiment. Experiments Hmgs-3 and Hmgs-4 were run longer-term and no fluid phase samples were collected during the first 170 days of the experiments. Although the magnesium isotopic analyses of these experiments suggest the fluids may become isotopically heavier between 170 and 300 days, these values are identical within uncertainty, and ~ 0.2 ‰ heavier than the original hydromagnesite. Similar to the fluid magnesium isotopic composition of these experiments, the fluid phase after 33 days of dissolution at 4 °C during experiment Hmgs-5 resulted in a fluid that was ~ 0.2 ‰ lighter than the dissolving solid.

The chemical and isotopic composition of the fluid phase during hydromagnesite dissolution presented above is consistent with two distinct processes. First, during the initial stages of dissolution, ^{24}Mg owing to its lighter mass is transported in the aqueous fluid rapidly relative to subsequent to its heavier magnesium isotopomers (*i.e.*, ^{25}Mg and ^{26}Mg). Second, there may be a tendency to break more rapidly $^{24}\text{Mg-O}$ compared to $^{26}\text{Mg-O}$ in the hydromagnesite structure (*cf.*, Hoefs, 1973; Criss, 1999). Note that at these initial stages of dissolution in the batch reactors adopted in this study, the fluid phase tends to be strongly undersaturated, such that mass transfer is dominated by the net removal of magnesium from the solid to the aqueous phase (*e.g.*, the forward reaction dominates over the reverse reaction – see Aagaard and Helgeson, 1982; Oelkers *et al.*, 1994; Schott and Oelkers, 1995; Oelkers, 2001b; Schott *et al.*, 2009). As such during the early stages of these experiments the signal of the preferential initial release of light magnesium is still evident in the fluid phase.

The preferential enrichment of the reactive fluid with ^{24}Mg during the initial stages of the experiments reported in this study contrasts with that observed for calcium isotopes released during calcite dissolution (Oelkers *et al.*, submitted). This difference in behavior may stem from the strong hydration of aqueous Mg^{2+} , which is a major limiting factor for the nucleation/growth of anhydrous Mg-carbonates such as magnesite and dolomite (Lippmann, 1973; Saldi *et al.*, 2009). Indeed, the strong hydration of aqueous magnesium is exemplified by the relatively slow exchange of water molecules in the magnesium hydration sphere compared to that of the other alkali earths (10^5 s^{-1} ; Lincoln and Merbach, 1995; Pokrovsky and Schott, 2002).

The tendency for the fluid phase to become increasingly heavy after this initial stage likely stems from the effect of back reaction – as bulk chemical equilibrium is approached between the fluid and the dissolving hydromagnesite, the rate of the reverse reaction (*e.g.*, reverse precipitation) increases to equal that of the forward reaction (*e.g.*, forward dissolution) consistent with the concept of dynamic equilibrium. The importance of the reverse precipitation reaction is such that the fluid-solid system evolves towards isotopic equilibrium even after bulk chemical equilibrium has been attained. This observation is consistent with the modeling calculations reported by Steefel *et al.* (2014), which predicts the isotopic equilibration of a fluid-mineral system in the absence of bulk chemical disequilibrium based on a transition state theory. Note that at the end of each experiment the magnesium isotopic composition of the fluid phase in this study is $\sim 0.25 \text{ ‰}$ heavier than the dissolving solid. Galy *et al.* (2002), Young and Galy (2004), and Tipper *et al.* (2006) also concluded that carbonate minerals tend to favor incorporation of lighter magnesium into their structures.

The temporal evolution of the chemical and isotopic composition of the fluid phase during the closed-system dissolution of hydromagnesite can be can be quantified using *Equations (7) to (12)*. These equations were integrated numerically using an EXCEL spread

sheet, and the results are shown as the curves in *Figures 10 to 12*. In each case the best fit was obtained by a trial and error adjustment of the model parameters. Note that the modeling of the isotopic evolution of these fluids was initiated from the minimum $\delta^{26}\text{Mg}_{fluid}$ measured during each experiment; as described above, the initial decrease observed in $\delta^{26}\text{Mg}_{fluid}$ is attributed to the preferential rapid release of isotopically light magnesium from the mineral. A close correspondence can be seen between the calculated curves and the measured reactive fluid isotopic compositions. The rate constants generated from this fitting effort are listed in *Table 4* and they are similar to those previously reported by Berninger *et al.* (2014). The fraction of magnesium re-precipitated from the fluid that is fixed in the mineral is calculated to be less than 25 % in all experiments. This result suggests that the vast majority of re-precipitated material is again rapidly returned to the fluid phase by forward dissolution. The equilibrium fractionation factor, $\Delta^{26}\text{Mg}_{fluid-hmgs}$, for all the dissolution experiments is equal to 0.25 ± 0.1 %.

Table 4: Model parameters used to describe the variation of reactive fluid isotopic composition using *Equations (7) to (12)*.

Experiment	k (mol/m ² /s ¹)	$\Delta^{26}\text{Mg}_{fluid-hmgs}$	X
Hmgs-1	1.19×10^{-7}	0.35	0.25
Hmgs-2	1.76×10^{-9}	0.25	0.12
Hmgs-3	-	0.20	-
Hmgs-4	-	0.20	-
Hmgs-5	2.35×10^{-11}	0.30	0 ^a

^a Fraction of original material re-dissolved during hydromagnesite precipitation.

3.5.2 Isotopic evolution during hydromagnesite precipitation

The results of experiment Hmgs-5 demonstrate that the precipitation of hydromagnesite at 50 °C favors the incorporation of isotopically light magnesium into the solid phase. The average composition of the precipitated hydromagnesite can be determined from mass balance considerations. Prior to the precipitation of hydromagnesite, the reactive fluid contained 3.8×10^{-3} mol/kg of magnesium with a $\delta^{26}\text{Mg}_{\text{fluid}}$ of -1.35 ‰; following precipitation, the reactive fluid contained 0.8×10^{-3} mol/kg of magnesium with a $\delta^{26}\text{Mg}_{\text{fluid}}$ of -0.82 ‰. Mass balance thus requires that hydromagnesite precipitation removed 3.0×10^{-3} mol/kg of magnesium having a $\delta^{26}\text{Mg}_{\text{hmgs}}$ of -1.49 ‰. A simple Rayleigh fraction model, if based on the one-way transfer from the fluid to the solid phase would require a $\Delta^{26}\text{Mg}_{\text{fluid-hmgs}} = \delta^{26}\text{Mg}_{\text{fluid}} - \delta^{26}\text{Mg}_{\text{hmgs}}$ of 0.31 ‰. In contrast, as the fluid phase magnesium isotopic composition evolves after the fluid-solid system in the experiment attained bulk chemical equilibrium, it is clear that chemical transfer from the fluid to the solid is not unidirectional. Nevertheless, taking account of the forward and reverse reactions, modeling the isotopic composition of the fluid using *Equations (7) to (12)* yields an equilibrium fractionation factor, $\Delta^{26}\text{Mg}_{\text{fluid-hmgs}}$, of ~ 0.3 ‰ (see *Figure 13* and *Table 4*), which is similar to that obtained from the fitting of the fluid composition of the dissolution experiments performed at 25 °C.

This equilibrium fractionation factor between the hydromagnesite and the aqueous fluid ($\Delta^{26}\text{Mg}_{\text{fluid-hmgs}}$) estimated from both the dissolution and precipitation experiments is -0.25 ± 0.1 ‰. This small fractionation likely stems from the small differences in Mg-O bonding between these two phases. For aqueous Mg^{2+} , the Mg-O bond has been reported to be 2.08 Å in length (Pavlov *et al.*, 1998) whereas for hydromagnesite this length is 2.06 ± 0.02 Å (Akao *et al.*, 1974; Politi *et al.*, 2010). Note however that this fractionation may be influenced by the presence of aqueous carbonate in the reactive fluid leading to the formation of Mg-

carbonate aqueous complexes; chemical speciation calculations indicate that ~ 39 % of aqueous magnesium is present as aqueous Mg^{2+} in the reactive fluid of the 25 °C experiments, whereas the sum of the MgCO_3^0 and MgHCO_3^+ aqueous species count for ~ 61 % of aqueous magnesium. As shown by Di Tommaso and de Leeuw (2010) using molecular dynamic simulations, the formation of MgCO_3^0 and MgHCO_3^+ aqueous species, shortens the Mg-O bond to 2.06 Å. Thus the presence of aqueous carbonate might be expected to alter this equilibrium fractionation factor somewhat (see Criss, 1999).

3.5.3 Preservation of isotopic signatures in natural systems

The results reported in this study illustrate that transfer of isotopic signatures 1) are not conservatively transferred to the fluid phase during hydromagnesite dissolution and 2) can evolve towards isotopic equilibrium after bulk equilibrium has been obtained in the fluid-carbonate system. These results are coherent with similar observations reported for other carbonate systems including calcium isotope fractionation during calcite dissolution and precipitation (Oelkers *et al.*, submitted), magnesium isotopic fractionation during the dissolution and precipitation of magnesite, nesquehonite, and dypingite (Pearce *et al.*, 2012; Mavromatis *et al.*, 2012; Shirokova *et al.*, 2013), and carbon isotope fractionation during nesquehonite and dypingite precipitation (Mavromatis *et al.*, 2015). Similar observations have also been reported for epsomite (Li *et al.*, 2011) and brucite (Li *et al.*, 2014). These studies all indicate that isotopic signatures continue to evolve towards an equilibrium state after apparent bulk fluid-mineral equilibrium has been attained. Such observations appear to contravene the commonly held assumption that carbonate minerals can preserve their isotopic signatures over geological timeframes. As emphasized by Oelkers *et al.* (submitted) isotopic preservation in natural systems would require either the isolation of the carbonate fluid-mineral system from

external chemical input, potentially by lowering rock permeability or a dramatic slowing of the coupled mineral dissolution/precipitation reactions. Turchyn and DePaolo (2011) suggested that such processes may play a role in isotopic preservation in some natural systems.

3.6 Conclusion

The results summarized above provide further evidence for the rapid and efficient re-equilibration of isotopic signatures during water-rock interaction. Such observations indicate that the accurate interpretation of the isotopic signals recorded in the geological record cannot be assumed to be fixed during their original precipitation, and may likely reflect at least some resetting during deposition and burial. This appears to be particularly the case for carbonate minerals, which tend to react rapidly at ambient conditions. Similarly, as the isotopic composition of the fluid phase is clearly influenced significantly and rapidly by its interaction with its coexisting rocks, it seems unlikely that natural fluids preserve pristine records of the origin of these fluids.

Chapter 4

ON THE EFFECT OF AQUEOUS CALCIUM ON MAGNESITE GROWTH – INSIGHT INTO TRACE ELEMENT INHIBITION OF CARBONATE MINERAL PRECIPITATION

Abstract

Motivated by the strong effect of aqueous magnesium on calcite growth rates, this study used hydrothermal atomic force microscopy (HAFM) and hydrothermal mixed-flow reactor (HMFR) experiments to explore the effect of aqueous calcium on magnesite growth kinetics at 100 °C and pH ~ 7.7. Obtuse step velocities on (104) surfaces during magnesite growth were measured to be 4 ± 3 nm/s at fluid saturation states, equal to the ion activity quotient divided by the equilibrium constant for the magnesite hydrolysis reaction, of 86 to 117. These rates do not vary systematically with aqueous calcium concentration up to 3×10^{-3} mol/kg. Magnesite growth rates determined by HAFM are found to be negligibly affected by the presence of aqueous calcium at these saturation states and are largely consistent with those previously reported in aqueous Ca-free systems by Saldi *et al.* (2009) and Gautier *et al.* (2015). Similarly, magnesite growth rates measured by HMFR exhibit no systematic variation on aqueous calcium concentrations. Rates in this study, however, were extended to higher degrees of fluid supersaturation with respect to magnesite than previous studies. All measured HMFR rates can be accurately described taking account the combined effects of both the spiral growth and two dimensional nucleation/growth mechanisms. Despite the lack of a clear effect of aqueous calcium on magnesite growth rates, Raman spectroscopy confirmed the incorporation of up to 8 mole percent of Ca^{2+} into the growing magnesite structure.

4.1 Introduction

Due to the presence of the substantial and varying concentration of magnesium in seawater over geological time (*e.g.*, Zimmermann, 2000; Dickson, 2002; Coggon *et al.*, 2010; Müller *et al.*, 2011; Mackenzie and Andersson, 2013), and the use of Mg/Ca ratios as a paleo-temperature proxy (*e.g.*, Lea *et al.*, 1999; Lear *et al.*, 2002; Elderfield *et al.*, 2006; Bryan and Marchitto, 2008; Healey *et al.*, 2008; Higgins and Schrag, 2010, 2015) a large number of studies have been focused on the effect of aqueous magnesium on calcite reactivity. Notably, there is a considerable amount of literature on the effect of the presence of aqueous magnesium on calcite dissolution (Compton and Brown, 1994; Gutjahr *et al.*, 1996; Alkattan *et al.*, 2002; Gledhill and Morse, 2006; Pina and Jordan, 2010; Xu and Higgins, 2011; Zhang *et al.*, 2013) and precipitation rates (Mucci and Morse, 1983; Arvidson and Mackenzie, 2000; Davis *et al.*, 2000, 2004; Zhang and Dawe, 2000; Wasylenki *et al.*, 2005; Lin and Singer, 2009; Astilleros *et al.*, 2010; Pina and Jordan, 2010; Sethmann *et al.*, 2010; Bracco *et al.*, 2012; Nielsen *et al.*, 2013). These studies have noted that there is a substantial slowing of calcite precipitation rates in the presence of aqueous magnesium. The present work has been designed to provide further insight into carbonate precipitation rates in the presence of aqueous divalent cations by applying hydrothermal atomic force microscopy (HAFM), hydrothermal mixed-flow reactors (HMFR), and Raman spectroscopy to quantify the influence of aqueous calcium on magnesite growth. The purpose of this study is to 1) report on how the presence of aqueous calcium influences magnesite precipitation rates, 2) use these results for a better understanding how trace element incorporation may influence carbonate growth rates, and 3) gain insight into the competing interactions of aqueous calcium and magnesium for lattice positions in rhombohedral carbonates.

There has been much recent interest in magnesite precipitation rates as this process has the potential to ‘permanently’ store anthropogenic carbon-dioxide within carbonate minerals (*e.g.*, Giammar *et al.*, 2005; Oelkers and Schott, 2005; Oelkers and Cole, 2008; Dufaud *et al.*, 2009; Prigiobbe *et al.*, 2009). For example, numerous studies have focused on the transformation of Mg-rich silicate minerals to magnesite to generate an industrial process for carbon mineral storage (*e.g.*, Wolf *et al.*, 2004; Maroto-Valer *et al.*, 2005; Chen *et al.*, 2006; Alexander *et al.*, 2007; Gerdemann *et al.*, 2007; Oelkers *et al.*, 2008; Andreani *et al.*, 2009; Garcia *et al.*, 2010; King *et al.*, 2010; Case *et al.*, 2011; Saldi *et al.*, 2013; Sissmann *et al.*, 2014). The optimization of such mineral carbonation efforts is facilitated by the detailed understanding of Mg-carbonate growth reactions. As such a number of studies have focused on an improved understanding of magnesite precipitation rates (*e.g.*, Sayles and Fyfe, 1973; Saldi *et al.*, 2009, 2012, 2013; Case *et al.*, 2011; Felmy *et al.*, 2012, 2015; Pearce *et al.*, 2012; King *et al.*, 2013; Prigiobbe and Mazzotti, 2013; Xu *et al.*, 2013; Bracco *et al.*, 2014; Gautier *et al.*, 2015). This study continues our efforts to quantitatively describe magnesite growth rates as a function of fluid composition, saturation state, and temperature. Saldi *et al.* (2009, 2012) reported magnesite growth rates as a function of saturation state at temperatures ranging from 80 to 200 °C. Gautier *et al.* (2015) focused on the influence of organic ligands on these growth rates. This study builds upon these past efforts by determining the effect of dissolved calcium, an ubiquitous and potentially competing cation, on magnesite growth rates.

4.2 Materials, chemical analysis, and experimental methods

4.2.1 Hydrothermal atomic force microscopy (HAFM) experiments

Hydrothermal atomic force microscopy growth experiments were performed using an in-house constructed continuous-flow HAFM operating in contact mode fitted with uncoated

silicon cantilevers from Nanosensors. The system allows for *in-situ* investigation of mineral surfaces at temperatures up to 150 °C and pressures up to 50 bars (*cf.*, Higgins *et al.*, 1998; Aldushin *et al.*, 2004; Jordan and Astilleros, 2006). The experiments in this study were performed at 100 °C with confining pressures of less than 3 bars. Pressure was applied by nitrogen gas separated from the magnesite/reactive fluid experimental system using an impermeable Kalrez membrane. Inlet fluids were placed in three Viton containers above the HAFM cell allowing gravitational fluid feed. Fluid flow rates were approximately 10 µg/s allowing the rapid renewal of the fluid within the ~ 500 µL reaction cell. Due to rapid fluid renewal and a mineral surface area of only a few mm², the chemical composition of the fluid was negligibly affected by mineral reactions occurring in the reaction cell. Experiments were performed on the (104) cleavage surface of transparent magnesite single crystals from Brumado, Bahia, Brazil. Electron microprobe analysis of the crystals revealed the presence of minor amounts of Ca = 0.08 % and Fe = 0.03 % (Saldi *et al.*, 2009). The crystals were cleaved with a scalpel immediately before being fixed in the HAFM cell via a titanium wire. The system was then pressurized and the cell heated to the desired temperature.

Step velocities during magnesite growth were obtained by measuring the step advancement rates perpendicular to the step orientation on images taken during the same scanning direction using a fix reference point. These step propagation measurements were corrected for the differences of scan times across each image (see *Figure 14*). To improve data accuracy, reported step velocities are the average of measurements taken on several steps, and different scanning directions. Magnesite growth rates, r_{HAFM} , were determined from the layer formation frequency F using:

$$r_{HAFM} = F \frac{d_{104}}{V_M} \quad (13)$$

where d_{104} stands for the lattice distance (2.74 Å), V_M refers to the magnesite molar volume (28.1 cm³/mol), and F denotes the layer formation frequency, which can be determined by counting steps generated at a particular step generation point, or by counting steps passing a fixed reference point during a selected time interval (Higgins *et al.*, 2002). Although the substitution of calcium for magnesium in the magnesite structure will change slightly the lattice parameters of the mineral, there are no resolvable step height differences detectable by the HAFM system used in this study. As such, these minor differences have been neglected.

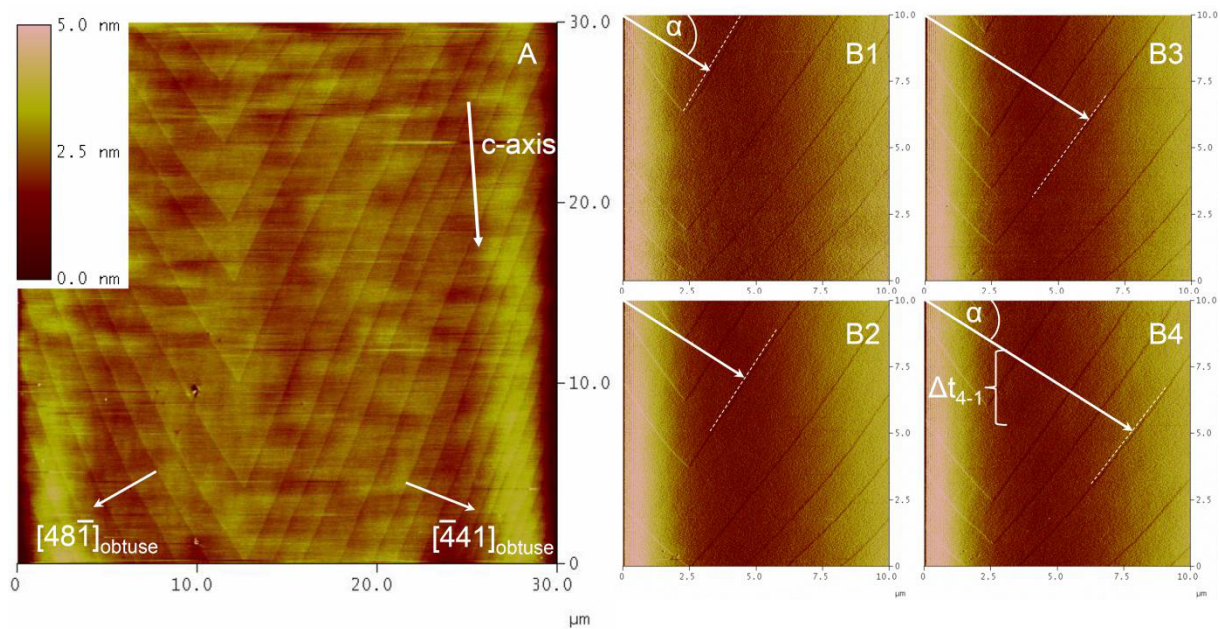


Figure 14: Hydrothermal atomic force microscopy (HAFM) images illustrating (104) magnesite obtuse step propagation at 100 °C and at a saturation state Ω_{Mgs} 100. Height image (A) recorded with downward scanning direction showing the topography control of a growth mechanism with the step formation located outside the scan area. Crystallographic directions on the (104) surface and the trajectory of the c -axis are indicated by white arrows. A series of deflection images (B1-4) of the central area shown in A, recorded with an upward scanning direction.

4.2.2 Hydrothermal mixed-flow reactor (HMFR) experiments

The 200 and 300 mL titanium hydrothermal mixed-flow reactors used in this study were previously described by Saldi *et al.* (2012). Inlet solutions were stored in collapsible polyethylene containers and injected into the reactor by a high pressure liquid chromatography (HPLC) pump allowing flow rates ranging from 0.1 to 10 mL/min. The reactive fluid inside the reactor was stirred at 300 rpm with a Parr magnetic stirrer and kept at 100 °C by a Parr furnace. The fluid left the reactor through a 2 µm Ti-filter and was cooled before passing through a back-pressure regulator that maintained a constant pressure throughout the system; this pressure was typically 15-35 bars. There was no evidence that stirring led to either fragmentation or other damage to the magnesite seed crystals.

The magnesite used during these growth experiments consisted of 1) a freshly cleaved magnesite single crystal (Brumado, Bahia, Brazil), which was fixed with a 0.2 µm nylon net directly underneath the stirrer and 2) synthesized 5 to 40 µm magnesite seed crystals. The larger crystal was added to the reactor for subsequent Raman spectroscopy analysis (see below). The smaller seed crystals were synthesized in a rocking 400 mL Ti-autoclave. These crystals were subsequently cleaned ultrasonically and oven dried at 60 °C for ~ 30 h. Scanning electron microscope (SEM) images of the resulting magnesite seed crystals were obtained with a JEOL JSM-6360 LV microscope as shown in *Figures 15A* and *15B*. The synthesized magnesite consists of single, twinned, and agglomerated crystals. No other mineral phases were evident in SEM images or by electron backscattering. The purity of the synthesized magnesite was further verified by x-ray diffraction using an INEL CPS-120 diffractometer with Co K_α-radiation, $\lambda = 1.78897 \text{ \AA}$, and a graphite monochromator. X-ray diffraction was performed from 1 to 110° 2 θ at 0.09°/min and at a step size of 0.029°. This

analysis revealed no phase other than magnesite. The specific surface area of the magnesite powder was determined to be $0.016 \text{ m}^2/\text{g} \pm 10 \%$ by multipoint krypton adsorption according to the BET method (Brunauer *et al.*, 1938) using a Quantachrome Gas Sorption system. Note that assuming rhombohedra with an edge length of $20 \mu\text{m}$ the geometrically estimated specific surface area of this seed material is about four times bigger than the value of the reproducible BET measurements.

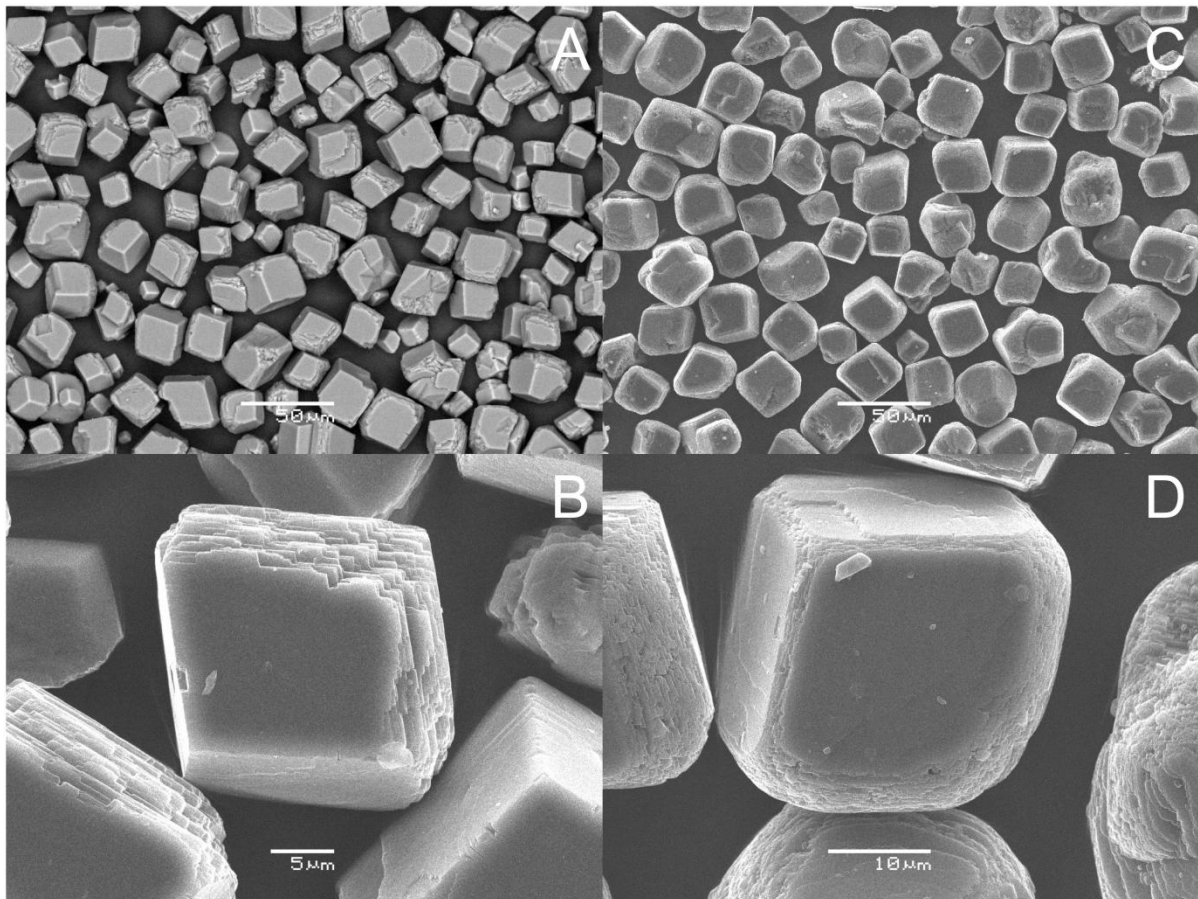


Figure 15: Scanning electron micrographs of (A, B) the initial magnesite seed material and (C, D) this material retrieved from the reactor after experiment mgs15 (performed for ~ 10 days in the presence of $> 2 \times 10^{-5} \text{ mol/kg}$ aqueous calcium at saturation states, Ω_{Mgs} , between 110 to 210). Note that the crystals grew significantly while maintaining their rhombohedral appearance.

HMFR-experiments were usually run in series. Each series consisted of experiments with several distinct fluid flow rates and/or several distinct inlet fluid compositions with a single magnesite powder. Each experiment in the series was run until a steady-state outlet fluid composition was obtained. A steady-state outlet composition was defined as a composition that did not change within analytical uncertainty for at least 3 residence times; a residence time is equal to the reactor volume divided by the fluid flow rate. Each experimental series is noted by a distinct prefix in *Table 5*. Steady-state precipitation rates, r_{HMFR} , were calculated using (Saldi *et al.*, 2012)

$$r_{HMFR} = \frac{\Delta[M^{2+}] \cdot q}{m \cdot s_{BET}} \quad (14)$$

where q represents the fluid flow rate, $\Delta[M^{2+}]$ stands for the difference between the inlet and outlet fluid divalent cation concentration (Mg^{2+} and Ca^{2+}), m denotes the mass of seed crystals, and s_{BET} refers to the mineral specific BET surface area of the initial seeds. The mass of magnesite in the reactor increased by as much as 30 % during each experimental series due to precipitation. To account for this mass change it was assumed in *Equation (14)*, to a first approximation, that the mass of magnesite in the reactor increased linearly with time from its initial value to its measured final value; these initial and final magnesite masses are listed in *Table 5*. It is estimated that this correction imparts no more than a 5 % uncertainty on the rates reported in this study.

Table 5: Conditions of hydrothermal mixed-flow reactor (HMFR) experiments reported in *Chapter 4* including initial fluid compositions and precipitated magnesite mass.

Experiment	m_{mgs} initial (g)	m_{mgs} final- recovered (g)	Reactor volume (mL)	Duration (days)	Temp (°C)	pH	inlet c_{Mg} ($\times 10^{-3}$) (mol/kg)	inlet c_{Ca} ($\times 10^{-6}$) (mol/kg)	Alkalinity ($\times 10^{-3}$) (eq/L)	NaCl (g/kg)	Calc. growth thickness ^a (μm)
mgs10.1	1.2698		200	7.3	21.5	8.23	3.48	5.78	24.8	4.208	9 \pm 2
mgs10.2		1.7912	200	13.3	20.5	8.22	3.52	6.83	24.8	4.208	
mgs9.1	1.7473	2.3332	300	13.1	22.0	8.18	3.44	41.6	24.7	4.208	7 \pm 1
mgs12.1	1.7414		300	3.2	22.0	8.18	3.42	40.9	24.8	4.208	6 \pm 1
mgs12.2		2.1992	300	4.9	22.0	8.19	3.49	41.2	24.8	4.208	
mgs13.1	1.3954	1.9493	200	12.3	23.0	8.27	3.44	41.2	24.7	4.208	7 \pm 1
mgs14.1	1.7521	2.5071	300	12.0	23.0	8.26	3.88	41.2	34.6	4.208	7 \pm 1
mgs15.1	1.3993	1.7596	200	10.3	23.0	8.37	3.43	85.2	24.7	4.208	6 \pm 1
mgs16.1	4.5085		300	5.9	23.0	8.19	3.96	84.3	34.6	4.091	6 \pm 3
mgs16.2		5.8735	300	9.2	22.5	8.28	3.48	78.1	34.8	4.090	
mgs11.1	1.7359	1.7673	300	6.9	22.0	8.18	3.44	121.1	24.7	4.208	5.0 \pm 0.5

^a Thickness of precipitated layer was calculated using the experimentally determined growth rates.

4.2.3 Reactive fluids and their analysis

The inlet fluids of all experiments consisted of high purity deionized water (resistivity 18.2 M Ω cm), and reagent grade NaCl, MgCl₂·6H₂O, NaHCO₃, and CaCl₂·2H₂O. The NaCl concentration was adjusted for a constant ionic strength of 0.1 molal. The inlet fluid compositions for all experiments are summarized in *Tables 5* and *6*.

Aqueous magnesium and calcium concentrations were measured by flame atomic absorption spectroscopy using a Perkin Elmer AAnalyst 400 Atomic Absorption Spectrometer with an uncertainty of $\pm 2\%$ and detection limits of 1×10^{-7} and 2×10^{-7} molal, respectively. Alkalinity was determined by standard HCl titration using Schott TA 10plus a with an uncertainty of $\pm 1\%$ and a detection limit of 2×10^{-5} eq/L. Reactive fluid pH measurements were performed at room temperature immediately after sampling using a standard glass electrode, previously calibrated with 4.01, 6.86, and 9.18 NIST pH buffers. The uncertainty of these measurements is estimated to be ± 0.05 pH units.

Table 6: Summary of the results of hydrothermal atomic force microscopy (HAFM) experiments reported in *Chapter 4*. All experiments were performed at 100 °C.

Experiment	pH ^a	outlet c _{Mg} (x 10 ⁻³) (mol/kg)	outlet c _{Ca} (x 10 ⁻⁶) (mol/kg)	Alkalinity (x 10 ⁻³) (eq/L)	NaCl (g/kg)	pH _{calc}	Obtuse step velocity (nm/s)	Growth rate (x 10 ⁻⁷) (mol/m ² /s)	Ω _{Mgs}	Ω _{Arag}	a _{Mg+2} (x 10 ⁻³)	a _{Ca+2} (x 10 ⁻⁷)	a _{CO3-2} (x 10 ⁻⁵)
AFM 1	8.43	0.80	6.25	20.0	4.734	8.13	4.2±0.5	0.64±0.3	98	0.3	0.22	0.3	13.8
AFM 2_1	8.10	3.05	2.51	8.72	4.675	7.80	n.d.	n.d.	95	0.0	1.04	7.4	2.83
AFM 2_3	8.10	2.97	3.76	8.59	4.675	7.80	n.d.	n.d.	92	0.0	1.02	11.1	2.79
AFM 3_1	8.13	3.10	2.66	8.69	4.675	7.81	3.2±0.3	0.21±0.02	99	0.0	1.06	7.8	2.90
AFM 3_3	8.14	3.11	3.47	8.64	4.675	7.81	3.1±0.6	0.65±0.05	100	0.0	1.06	10.2	2.91
AFM 4_1	8.11	3.02	2.54	8.77	4.676	7.80	4.0±0.7	0.61±0.05	96	0.0	1.03	7.5	2.88
AFM 4_3	8.10	3.07	20.5	8.62	4.676	7.79	6.7±0.8	0.38±0.03	94	0.3	1.05	60.6	2.77
AFM 5_1	8.15	2.95	2.79	8.64	4.676	7.82	4.6±1.0	0.51±0.04	97	0.0	1.01	8.2	2.98
AFM 5_3	8.15	3.10	105	8.71	4.676	7.81	3.9±0.5	0.36±0.03	100	1.4	1.06	307.8	2.91
AFM 6_1	8.14	2.98	5.10	8.80	4.674	7.82	4.8±0.7	1.10±0.09	99	0.1	1.01	15.0	3.00
AFM 6_3	8.14	3.09	1207	9.09	4.674	7.75	1.1±0.3	0.27±0.02	86	13.9	1.05	3558.8	2.53
AFM 7_1	8.05	3.00	5.20	8.83	4.673	7.82	n.d.	n.d.	101	0.1	1.02	15.1	3.04
AFM 7_3	8.15	3.11	2741	7.61	4.673	7.68	n.d.	n.d.	61	22.5	1.07	8358.0	1.75
AFM 8_1	8.16	3.04	6.30	8.71	4.674	7.83	4.2±0.2	0.35±0.03	101	0.1	1.03	18.3	3.02
AFM 8_3	8.16	3.09	16.0	8.83	4.674	7.83	n.d.	2.3±0.2	104	0.2	1.03	46.6	3.05
AFM 10_1	8.10	3.07	5.28	10.0	4.676	7.80	3.8±0.6	n.d.	109	0.1	1.04	0.4	3.26
AFM 11_1	8.09	3.16	4.88	9.89	4.675	7.79	4.4±0.4	n.d.	109	0.1	1.07	0.4	3.16
AFM 11_3	8.09	3.10	16.00	9.88	4.676	7.79	5±1	n.d.	107	0.2	1.05	1.2	3.16
AFM 12_3	8.16	3.22	16.76	9.68	4.674	7.82	4.0±0.4	n.d.	117	0.2	1.10	1.2	3.31
AFM 17_3	8.10	2.98	506	9.50	4.675	7.76	3.8±0.7	n.d.	93	6.4	1.02	36.3	2.82
AFM 18_3	8.12	2.98	613	9.70	4.675	7.76	1.8±0.6	n.d.	95	7.9	1.02	43.7	2.88

n.d.= not determined

^a Measured at 22 ± 1 °C

4.2.4 Saturation state and growth rates

The standard state adopted in this study for thermodynamic calculations is that of unit activity for pure minerals and H₂O at any temperature and pressure. For aqueous species other than H₂O, the standard state is unit activity of the species in a hypothetical 1 molal solution referenced to infinite dilution at any temperature and pressure. The results of this study are reported as a function of the saturation state, Ω_{Mgs} , of the fluid with respect to magnesite, defined as:

$$\Omega_{Mgs} = \frac{a_{Mg^{2+}} a_{CO_3^{2-}}}{K_{sp(Mgs)}} \quad (15)$$

where $K_{sp(Mgs)}$ stands for the equilibrium constant of the magnesite hydrolysis reaction and a_i represents the activity of the subscripted aqueous species. All thermodynamic calculations including chemical activities, pH, and fluid saturation states were computed using the computer code PHREEQC (Version 2.18) (Parkhurst and Appelo, 1999) together with its llnl database after the minor additions described below. The b-dot activity model (Helgeson, 1969) was used to compute the activity coefficients. Much of the thermodynamic data present in the llnl database of PHREEQC originates from SUPCRT92 (Johnson *et al.*, 1992). The llnl database was modified to include the equilibrium constants for Mg²⁺ hydrolysis and the carbonic acid dissociation reported by Brown *et al.* (1996) and Millero *et al.* (2007), respectively. The magnesite solubility product of the llnl.dat database is consistent with those of Bénézeth *et al.* (2011).

At relatively low saturation states, magnesite precipitation rates (r_{Mgs}) have been assumed to be consistent with their control by spiral growth mechanism (Saldi *et al.*, 2009, 2012) in accord with:

$$r_{Mgs} = k_{Mgs} (\Omega_{Mgs} - 1)^n \quad (16)$$

where k_{Mgs} refers to a rate constant and n equals 2. The form of *Equation (16)* is similar to transition state theory based mineral dissolution and precipitation rate equations (Aagaard and Helgeson, 1982; Oelkers *et al.*, 1994; Schott and Oelkers, 1995; Oelkers, 2001b; Oelkers and Schott, 2001; Schott *et al.*, 2009):

$$r_{Mgs} = r_{+Mgs} (\Omega_{Mgs}^{n'} - 1) \quad (17)$$

where r_{Mgs} and r_{+Mgs} refer to the overall and forward rate respectively. The parameter n' in *Equation (17)* is the product of the Temkin's stoichiometric number and a reaction order that depends on the precipitation mechanism. Temkin's stoichiometric number equals the ratio of the rate of destruction of the activated or precursor complex relative to the overall rate (Temkin, 1963), which is 1 for magnesite dissolution and precipitation (Saldi *et al.*, 2009; 2010). Note that the magnesite precipitation experiments performed in this study and those reported by Saldi *et al.* (2009; 2012) and Gautier *et al.* (2015) were performed at $\Omega_{Mgs} > 20$ such that $n \approx n'$.

At higher degrees of supersaturation, two dimensional nucleation and growth may dominate magnesite precipitation (Nielsen, 1984; Schott *et al.*, 2012). The variation of precipitation rates consistent with this mechanism is given by (Nielsen, 1984)

$$r_{Mgs} = k_c S^{\frac{7}{6}} (S - 1)^{\frac{2}{3}} (\ln(S))^{\frac{1}{6}} \exp\left(\frac{-K_c}{\ln(S)}\right) \quad (18)$$

where k_c and K_c represent constants, and S is defined as

$$S = \Omega_{Mgs}^{\frac{1}{v}} \quad (19)$$

and ν stands for the number of aqueous species in the mineral precipitation reaction, equal to 2 for magnesite. If spiral growth and two-dimensional nucleation and growth are occurring in parallel, which might be expected at elevated degrees of supersaturation, the overall magnesite precipitation rate would be given by the sum of *Equations (16) and (18)* such that

$$r_{Mgs} = k_{Mgs}(\Omega_{Mgs} - 1)^n + k_c S^{\frac{7}{6}}(S - 1)^{\frac{2}{3}}(\ln(S))^{\frac{1}{6}} \exp\left(\frac{-K_c}{\ln(S)}\right) \quad (20)$$

This equation will be used below to describe measured magnesite precipitation rates at both near- and far-to-equilibrium conditions.

4.2.5 Raman spectroscopy

Raman spectra of growth layers on the (104) magnesite surface were collected by vertical line mapping from the surface down to 30 μm in depth with a 1 μm step length using a confocal Horiba XploRaTM Jobin Yvon Raman spectrometer with an Olympus BX51 microscope. A 100 x objective with a numerical aperture of 0.8 was used for all measurements. Confocal hole and slit widths were set to 100 μm . Samples were excited using a 532 nm LASER with a spot size of 0.7 μm and an output power of 20 mW. The neutral density filter was set to 50 % and a 2400 spectral grating per mm was applied. Raman spectra were collected in a range of 50 cm^{-1} to 2000 cm^{-1} with an acquisition time of 2 x 60 s.

4.3 Results

The advancement of obtuse steps on the growing (104) magnesite surface, as imaged by HAFM, is illustrated in *Figure 14*. An overview of the magnesite surface is provided in

Figure 14A. This surface exhibits numerous linear obtuse growth steps. Changing the reactor fluid calcium concentration changed neither the appearance of these steps nor their height. Note, that the slight difference in the concave and convex appearance of obtuse steps during downwards and upwards scanning directions is an artifact resulting due to piezo calibration. The location of the step generation site was located outside the scanning area of *Figure 14*, as was the case for most of the experiments. *Figure 14B* shows 4 sequential images of the surface shown in *Figure 14A* taken 4 min apart. The white arrows in *Figure 14B* show the progression of an obtuse step across the image. As indicated by the regular step density, a constantly active generation site for new steps is evidenced.

The obtuse step velocities were measured as a function of the aqueous calcium concentrations of the reactive fluid; these velocities are shown in *Figure 16*. Measured velocities are 4 ± 3 nm/s and do not exhibit a systematic variation with dissolved calcium concentration. Note that the low velocity at $\text{Ca} = 1.2 \times 10^{-3}$ mol/kg was obtained from a solution with the lowest degree of supersaturation. Measured step advancement rates are in close agreement with previously measured step velocities between Ω_{Mgs} 91 to 113 as reported by Saldi *et al.* (2009). This previous study also performed these experiments at 100 °C, pH ~ 7.7, and at 0.1 molal ionic strength. Note, however, that the aqueous calcium concentration was not measured by Saldi *et al.* (2009), yet it is likely less than 10^{-6} mol/kg; as calcium was not added to the reactive fluids by Saldi *et al.* (2009), the only calcium that might be present would originate from the trace impurities in the bicarbonate salts used to make these fluids.

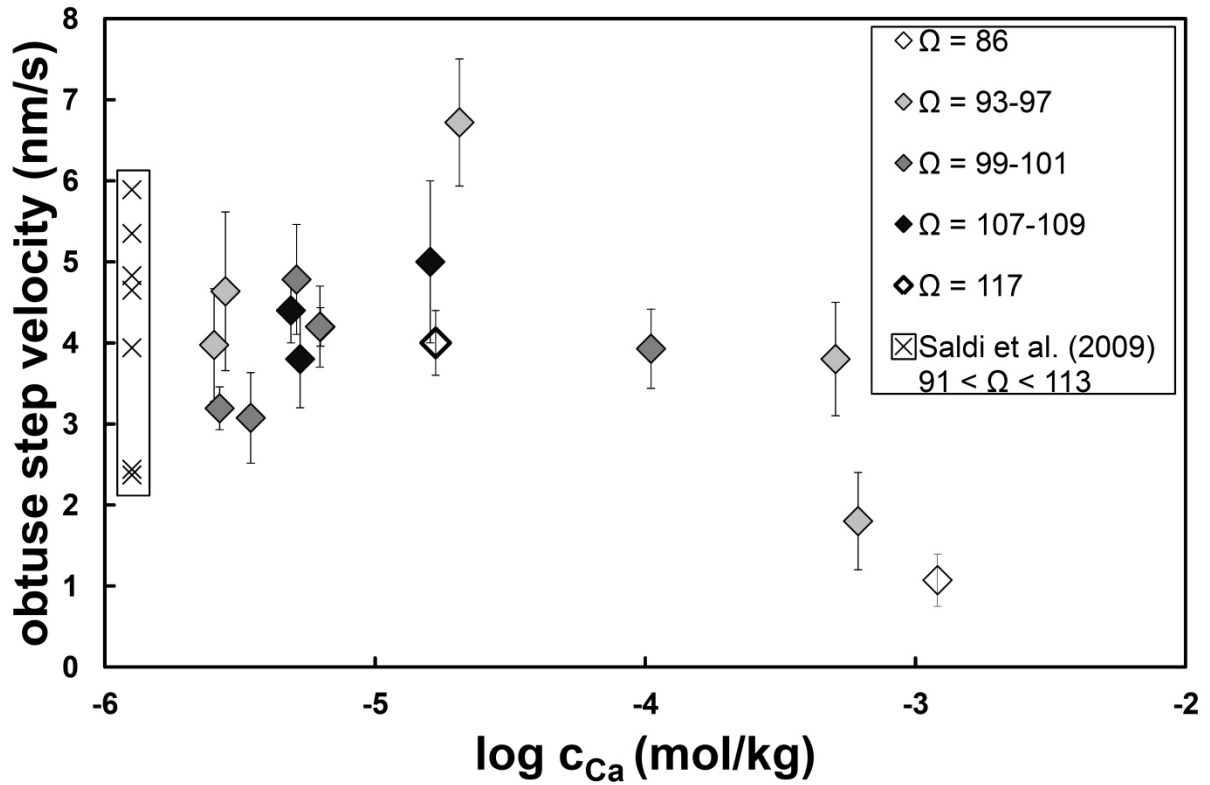


Figure 16: HAFM obtuse step advancement rates on the (104) surface of magnesite at 100 °C plotted versus the aqueous calcium concentration of the reactive fluid. Saturation states with respect to magnesite were kept near 100. Step advancement rates between Ω_{Mgs} 91 to 113 published by Saldi *et al.* (2009) are plotted for comparison. Note that while no aqueous calcium concentrations were reported by Saldi *et al.* (2009), these are likely to be smaller than 10^{-6} mol/kg.

A summary of the magnesite growth rates on the (104) surfaces obtained in this study from HAFM measurements are shown as a function of fluid saturation state in *Figure 17*. The rates were calculated using *Equation (13)* and based on the number of steps passing a fixed reference point on the magnesite surface. Although in this study HAFM rates were obtained only within a limited range of supersaturation (Ω_{Mgs}), they closely match corresponding rates reported by Saldi *et al.* (2009) and Gautier *et al.* (2015). Note that similarly to Saldi *et al.* (2009), Gautier *et al.* (2015) performed experiments in the absence of aqueous calcium other

than that unintentionally added due to the fluids via the presence of trace impurities in the used chemical reagents.

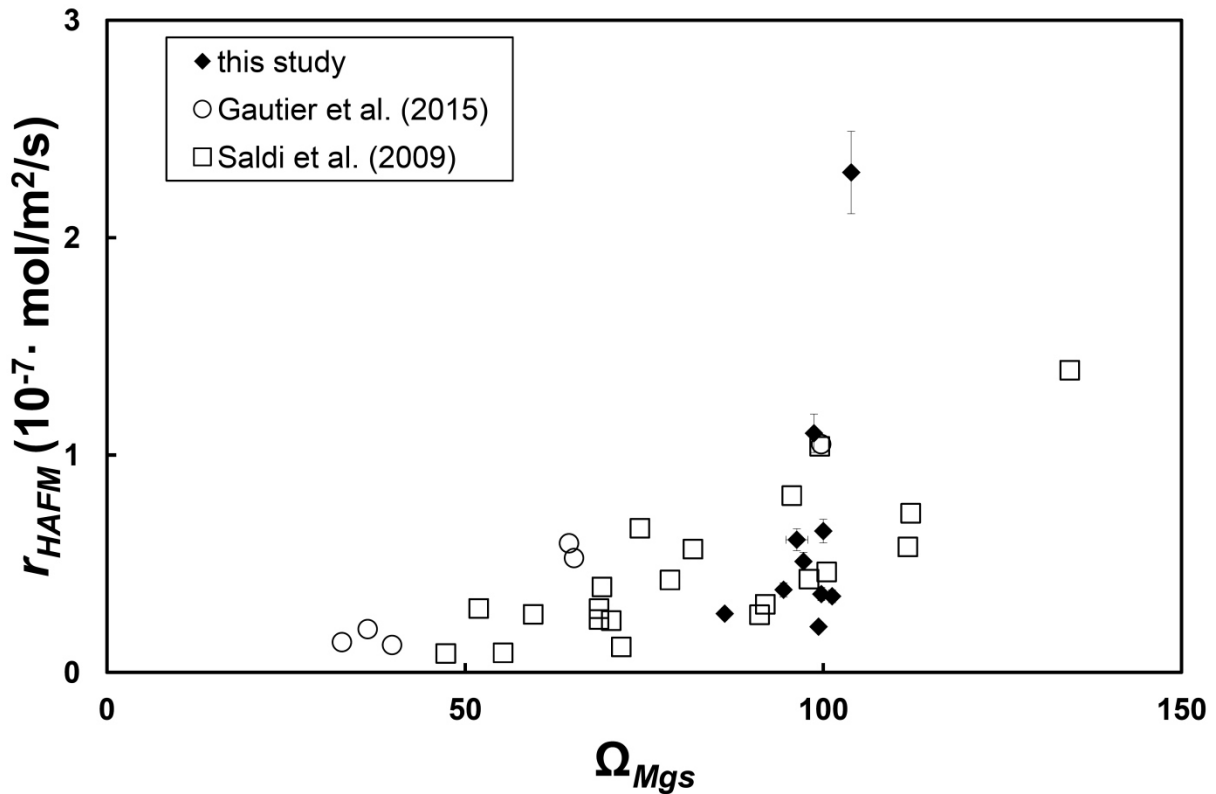


Figure 17: HAFM growth rates at 100 °C as a function of magnesite saturation state Ω_{Mgs} . Growth rates are in close agreement with previously published HAFM rates reported by Saldi *et al.* (2009) and Gautier *et al.* (2015) which are shown for comparison.

Representative photomicrographs of the magnesite powder recovered from HMFR experiment mgs15 are shown in *Figures 15C* and *15D*. Although this experiment was performed in fluids containing the highest aqueous calcium concentration, no signs of the formation of aragonite or other secondary minerals are evident. Comparison of the images shown in *Figures 15A* and *15B* with *15C* and *15D* show that the crystals grew significantly while maintaining their rhombohedral crystal form; no grains smaller than 10 μm are apparent in the magnesite powder. As the mass of magnesite precipitated from the fluid was ap-

proximately 25 % of that originally present in the seed crystals, these images confirm that magnesite growth on the original seed crystals dominated precipitation.

The temporal evolution of all steady-state outlet fluids collected from HMFR experiments performed in this study are provided in *Table 7*. Summarized steady-state magnesite growth rates obtained from these outlet fluid compositions are listed in *Table 8* and shown as a function of fluid saturation state in *Figure 18*. Although the reactive fluid aqueous calcium concentrations ranged up to 3×10^{-5} mol/kg, all measured growth rates plot as a single function of fluid saturation state within the uncertainty of the data. Note that inlet fluid calcium concentrations above 10^{-4} mol/kg were not considered as these led to the co-precipitation of aragonite during the experiments.

The mole fraction of calcium in the magnesium site of the magnesite precipitated during all HMFR experiments are shown as a function of the corresponding molar ratio of the fluid phase in *Figure 19*. Note the solid compositions shown in this figure were calculated from the difference in composition of the inlet and outlet fluids collected during the experiments together with mass balance considerations. The calcium concentration of the precipitated magnesite increases systematically with that of the fluid phase. The slope of the solid regression line in this figure is consistent with a distribution coefficient, K_D , of 6.9 ± 0.9 .

Information about the incorporation of calcium into the magnesite structure was obtained by Raman spectroscopy. The Raman spectra of Ca-free magnesite and magnesite produced with the highest aqueous calcium concentration (experiment mgs15) are compared in *Figure 20*. Data for 3 different depths below the magnesite surface are presented. An effect of the presence of Ca^{2+} on carbonate vibration modes is evident for both the translational ‘ T_v ’ and librational ‘ L_v ’ bands leading to a pronounced peak asymmetry at the low vibrational frequency side of these bands. Subtraction of the Ca-free reference spectrum from the Ca-rich

sample indicates the presence of secondary T^* and L^* bands at Raman shifts up to 8 cm^{-1} lower than the respective T_v and L_v bands. The other carbonate vibration modes revealed no significant changes due to the presence of calcium (Table 9).

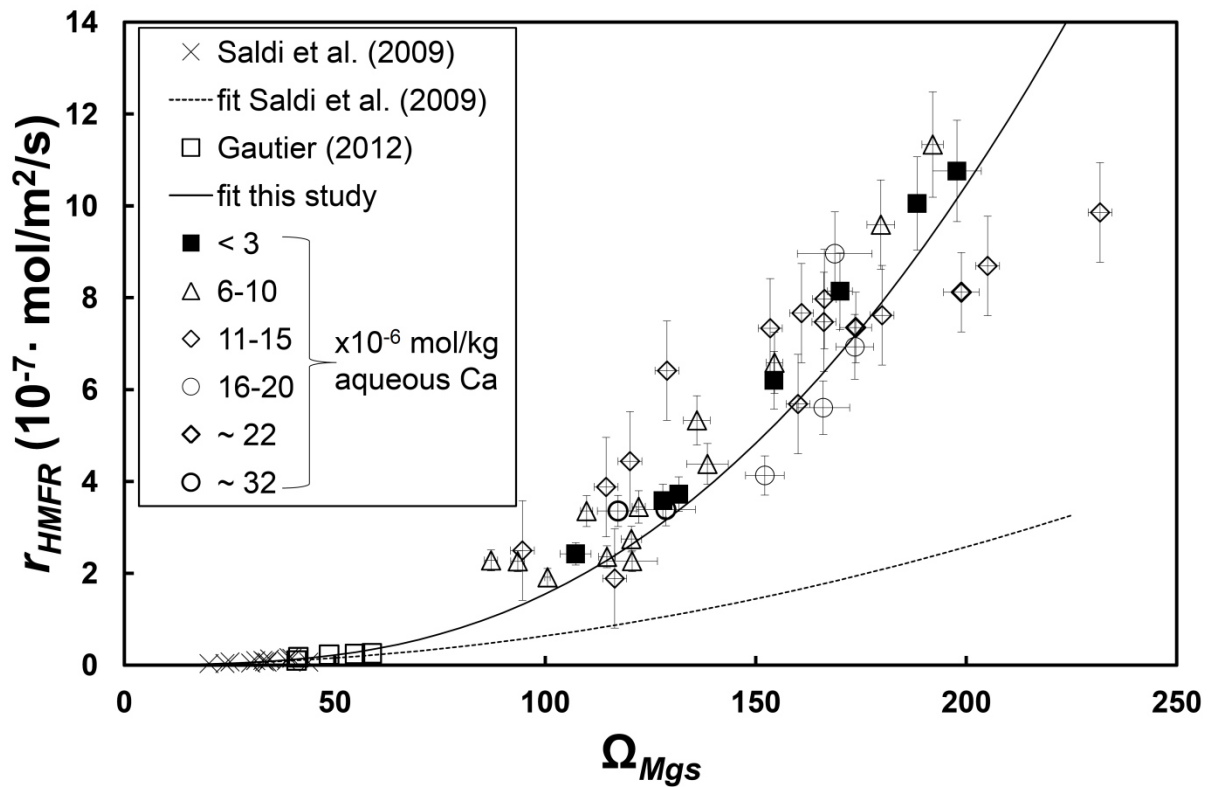


Figure 18: Magnesite growth rates determined by hydrothermal mixed-flow reactor (HMFR) experiments at $100\text{ }^\circ\text{C}$ as a function of magnesite saturation state Ω_{Mgs} . HMFR growth rates reveal no significant dependency on aqueous calcium concentration of the reactive fluid and are consistent with previously published HMFR rates by Saldi *et al.* (2009) and Gautier (2012). The fit of Saldi *et al.* (2009) based on Equation (16) is shown as a dashed curve, whereas the fit of the present study using Equation (20) is shown as a solid curve – see text. The error bars shown in this figure correspond to the range of rates and saturation states determined from the individual samples collected at steady-state during each experiment, whereas the symbols represent their median value.

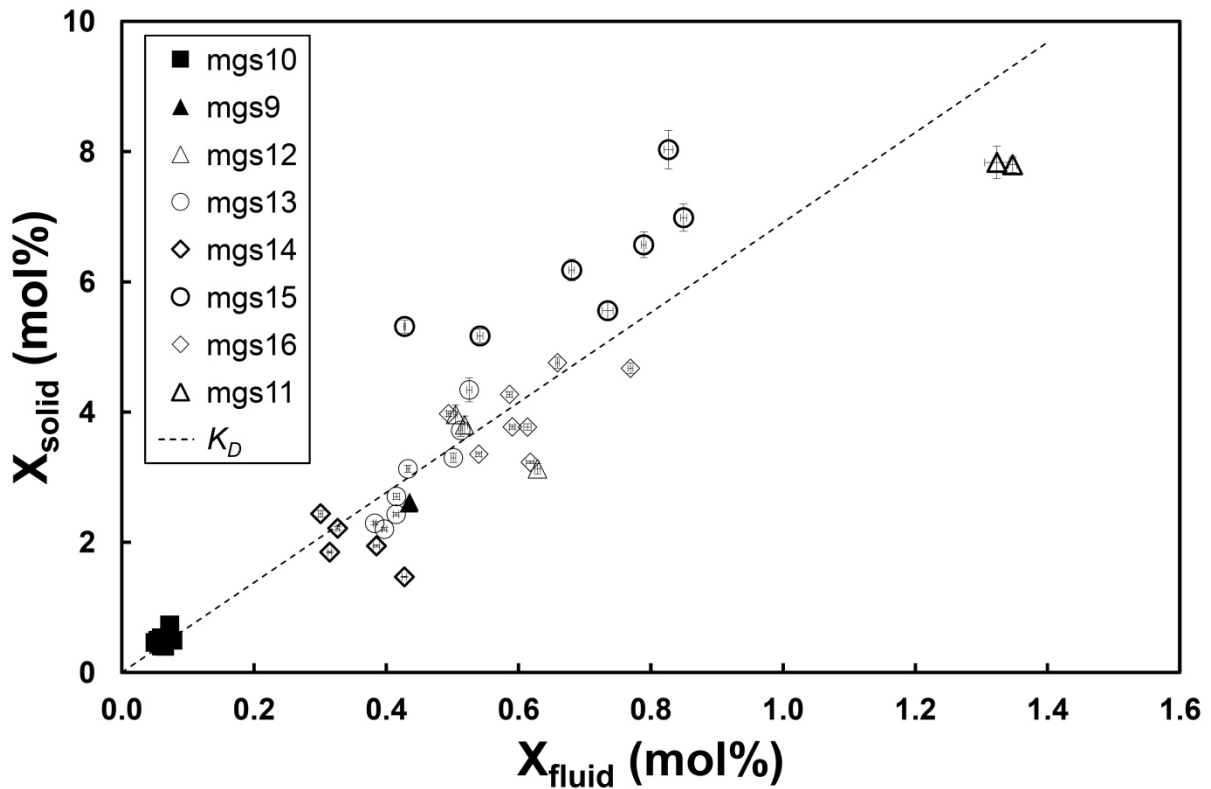


Figure 19: Composition of the precipitated calcium to the sum of divalent cation molar ratio ($X_{\text{solid}} = \Delta c_{\text{Ca}} / [\Delta c_{\text{Ca}} + \Delta c_{\text{Mg}}] \times 100$) as a function of the corresponding molar fluid ratio ($X_{\text{fluid}} = \text{outlet } c_{\text{Ca}} / [\text{outlet } c_{\text{Ca}} + \text{outlet } c_{\text{Mg}}] \times 100$) during HMFR experiments. Data show the preferential incorporation of Ca^{2+} in the growing magnesite at 100 °C. Assuming similar activity coefficients of Mg^{2+} and Ca^{2+} and an activity of the solid that equals its mole fraction, a distribution coefficient K_D of 6.9 ± 0.9 is obtained.

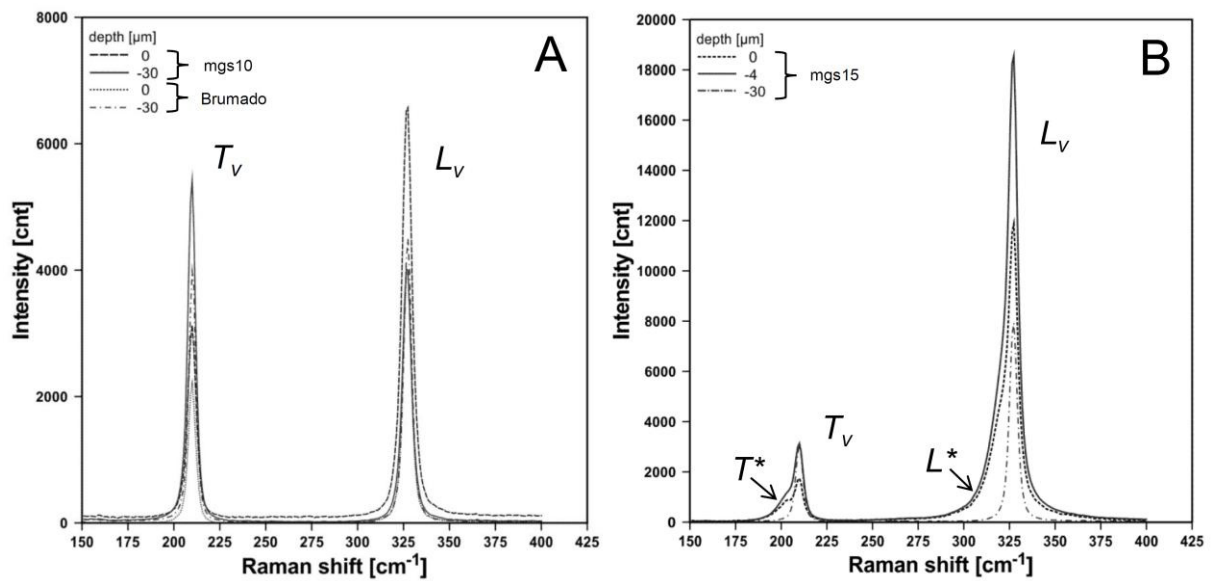


Figure 20: Confocal Raman spectra showing transitional T_V and librational L_V bands of carbonates measured on (104) magnesite single crystals as a function of depth. The vertical line mapping down to 30 μm of the reference spectra of experiment mgs10 and unreacted magnesite from Brumado, Brazil, consist of symmetric bands at all depths (A). Within the precipitated growth layers (B) the spectra of experiment mgs15 demonstrate the development of secondary T^* and L^* bands at frequencies about $8 \pm 1 \text{ cm}^{-1}$ lower due to the substitution of Ca^{2+} for Mg^{2+} . The unreacted crystal core is free of this effect.

Table 7: Summary of temporal evolution of the reactive fluid composition in all hydrothermal mixed-flow reactor (HMFR) experiments performed in this study. All experiments were performed at 100 °C.

Experiment	pH ^a	Fluid flow rate (g/min)	pH _{calc} (at 100 °C)	outlet c _{Mg} (x 10 ⁻³) (mol/kg)	outlet c _{Ca} (x 10 ⁻⁶) (mol/kg)	Alkalinity (x 10 ⁻³) (eq/L)	Growth rate (x 10 ⁻⁷) (mol/m ² /s)	Ω _{Mgs}	Ω _{Arag}	a _{Mg+2} (x 10 ⁻⁴)	a _{Ca+2} (x 10 ⁻⁷)	a _{CO3-2} (x 10 ⁻⁵)
mgs10.1-4	7.81	0.485	7.68	2.49	1.54	22.6	3.7±0.4	136	0.04	7.24	4.79	5.75
mgs10.1-5	7.79	0.486	7.67	2.49	2.00	22.6	3.7±0.4	132	0.04	7.24	4.79	5.62
mgs10.1-6	7.81	0.485	7.69	2.42	1.60	22.6	4.0±0.4	132	0.04	7.08	4.79	5.75
mgs10.1-7	7.78	0.486	7.67	2.47	1.80	22.6	3.7±0.4	131	0.04	7.24	4.79	5.62
mgs10.1-8	7.78	0.487	7.67	2.45	1.53	22.6	3.8±0.4	130	0.04	7.24	4.79	5.62
mgs10.1-9	7.78	0.487	7.67	2.48	1.59	22.6	3.6±0.4	131	0.04	7.24	4.79	5.62
mgs10.1-10	7.86	1.031	7.71	2.64	1.74	22.9	6.4±0.7	154	0.04	7.59	4.68	6.17
mgs10.1-11	7.86	0.920	7.71	2.57	1.53	22.9	6.1±0.6	151	0.04	7.41	4.68	6.17
mgs10.1-12	7.85	0.958	7.71	2.60	1.29	22.9	6.2±0.7	152	0.02	7.59	2.34	6.17
mgs10.1-13	7.86	0.973	7.72	2.61	1.32	22.9	6.2±0.6	154	0.02	7.59	2.34	6.31
mgs10.1-14	7.87	0.957	7.72	2.58	1.22	23.0	6.3±0.6	155	0.02	7.41	2.29	6.46
mgs10.1-15	7.86	0.970	7.72	2.61	1.81	23.0	6.2±0.6	155	0.05	7.59	4.68	6.31
mgs10.1-16	7.92	1.447	7.74	2.67	1.40	23.2	8.5±0.8	167	0.02	7.59	2.29	6.76
mgs10.1-17	7.91	1.412	7.74	2.67	1.40	23.2	8.3±0.8	168	0.02	7.59	2.29	6.76
mgs10.1-18	7.94	1.441	7.76	2.69	1.97	23.2	8.1±0.8	176	0.05	7.76	4.57	7.08
mgs10.1-19	7.91	1.439	7.74	2.70	1.62	23.2	8.0±0.8	170	0.05	7.76	4.57	6.76
mgs10.1-20	7.92	1.437	7.75	2.68	2.65	23.2	8.1±0.8	171	0.07	7.76	6.92	6.76
mgs10.1-21	7.97	1.991	7.77	2.80	2.95	23.4	10±1	188	0.08	7.94	6.76	7.24
mgs10.1-22	7.97	2.019	7.77	2.80	1.93	23.4	10±1	188	0.05	7.94	4.47	7.24
mgs10.1-23	7.99	1.999	7.79	2.76	1.89	23.4	10±1	190	0.05	7.94	4.47	7.41

Table 7: continued

Experiment	pH ^a	Fluid flow rate (g/min)	pH _{calc} (at 100 °C)	outlet c _{Mg} (x 10 ⁻³) (mol/kg)	outlet c _{Ca} (x 10 ⁻⁶) (mol/kg)	Alkalinity (x 10 ⁻³) (eq/L)	Growth rate (x 10 ⁻⁷) (mol/m ² /s)	Ω _{Mgs}	Ω _{Arag}	a _{Mg+2} (x 10 ⁻⁴)	a _{Ca+2} (x 10 ⁻⁷)	a _{CO3-2} (x 10 ⁻⁵)
mgs10.1-24	7.99	1.997	7.79	2.74	2.15	23.4	10±1	189	0.05	7.76	4.47	7.41
mgs10.1-25	7.98	1.975	7.78	2.74	2.37	23.4	10±1	187	0.05	7.76	4.47	7.41
mgs10.1-26	8.00	1.997	7.79	2.73	2.08	23.4	10±1	190	0.05	7.76	4.47	7.59
mgs10.2-27	7.99	2.484	7.79	2.87	2.08	23.7	11±1	199	0.05	8.13	4.47	7.59
mgs10.2-28	8.00	2.507	7.79	2.92	1.96	23.8	10±1	205	0.05	8.32	4.47	7.59
mgs10.2-29	7.99	2.480	7.79	2.85	2.11	23.7	11±1	198	0.05	8.13	4.47	7.59
mgs10.2-30	7.97	2.489	7.77	2.89	2.24	23.7	10±1	196	0.05	8.32	4.47	7.24
mgs10.2-31	7.94	2.489	7.76	2.87	1.95	23.7	11±1	187	0.05	8.13	4.47	7.08
mgs10.2-32	7.71	0.286	7.63	2.17	1.30	22.2	2.4±0.2	104	0.02	6.46	2.45	5.01
mgs10.2-33	7.74	0.286	7.65	2.13	0.94	22.2	2.5±0.2	107	0.02	6.31	2.40	5.25
mgs10.2-34	7.77	0.288	7.67	2.16	2.39	22.2	2.4±0.2	113	0.04	6.31	4.79	5.50
mgs10.2-35	7.82	0.496	7.70	2.28	1.20	22.5	3.7±0.4	128	0.02	6.61	2.34	5.89
mgs10.2-36	7.80	0.497	7.68	2.34	1.15	22.5	3.5±0.4	128	0.02	6.92	2.34	5.75
mgs10.2-37	7.80	0.493	7.69	2.30	1.16	22.6	3.6±0.4	126	0.02	6.76	2.34	5.75
mgs9.1-1	7.86	0.496	7.72	2.26	9.89	20.6	3.6±0.4	125	0.21	6.76	23.99	5.75
mgs9.1-2	7.80	0.501	7.68	2.27	9.71	22.3	3.4±0.3	122	0.21	6.61	23.99	5.62
mgs9.1-3	7.80	0.496	7.68	2.25	10.91	22.3	3.4±0.4	121	0.23	6.61	26.30	5.62
mgs9.1-4	7.73	0.496	7.64	2.25	9.53	22.3	3.4±0.3	110	0.19	6.61	23.99	5.13
mgs9.1-5	7.75	0.494	7.65	2.25	10.00	22.3	3.4±0.3	113	0.20	6.61	23.99	5.25
mgs9.1-6	7.72	0.494	7.63	2.26	9.67	22.2	3.3±0.3	110	0.19	6.76	24.55	5.01
mgs9.1-7	7.73	0.494	7.64	2.23	10.18	22.2	3.3±0.3	110	0.19	6.61	23.99	5.13
mgs12.1-1	7.88	1.984	7.72	2.77	14.61	23.3	8.0±0.8	166	0.34	7.94	34.67	6.46
mgs12.1-2	7.88	1.960	7.72	2.74	12.67	23.2	8.2±0.9	165	0.30	7.94	30.20	6.46
mgs12.1-3	7.88	2.044	7.72	2.79	14.14	23.3	7.9±0.8	168	0.32	8.13	32.36	6.46

Table 7: continued

Experiment	pH ^a	Fluid flow rate (g/min)	pH _{calc} (at 100 °C)	outlet c _{Mg} (x 10 ⁻³) (mol/kg)	outlet c _{Ca} (x 10 ⁻⁶) (mol/kg)	Alkalinity (eq/L)	Growth rate (x 10 ⁻⁷) (mol/m ² /s)	Ω _{Mgs}	Ω _{Arag}	a _{Mg+2} (x 10 ⁻⁴)	a _{Ca+2} (x 10 ⁻⁷)	a _{CO3-2} (x 10 ⁻⁵)
mgs12.1-4	7.85	1.992	7.70	2.70	12.45	23.1	8.4±0.9	156	0.26	7.76	28.18	6.17
mgs12.1-5	7.86	2.007	7.71	2.79	15.0	23.3	7.4±0.8	163	0.33	8.13	34.67	6.31
mgs12.1-6	7.90	1.970	7.74	2.73	14.19	23.2	7.6±0.8	169	0.33	7.94	32.36	6.61
mgs12.1-7	7.90	1.978	7.74	2.75	14.34	23.3	7.4±0.8	170	0.33	7.94	32.36	6.61
mgs12.2-8	7.91	1.994	7.74	2.70	16.67	23.4	8.4±0.9	169	0.40	7.76	38.90	6.76
mgs12.2-9	7.87	1.995	7.72	2.81	18.16	23.5	7.1±0.7	169	0.41	8.13	41.69	6.46
mgs12.2-10	7.91	2.005	7.74	2.82	20.8	23.4	6.8±0.7	178	0.50	8.13	47.86	6.76
mgs12.2-11	7.91	1.980	7.74	2.83	16.62	23.5	6.6±0.7	178	0.40	8.13	38.90	6.76
mgs13.1-1	7.85	0.289	7.72	2.16	10.13	21.3	2.8±0.3	123	0.22	6.31	23.99	5.89
mgs13.1-2	7.85	0.293	7.72	2.19	11.45	21.6	2.7±0.3	126	0.25	6.46	26.92	6.03
mgs13.1-3	7.82	0.289	7.70	2.16	8.98	21.9	2.7±0.3	121	0.19	6.31	21.38	5.89
mgs13.1-4	7.81	0.291	7.70	2.18	8.9	21.9	2.7±0.3	120	0.19	6.46	21.38	5.75
mgs13.1-5	7.82	0.290	7.70	2.13	8.7	22.0	2.8±0.3	119	0.19	6.31	20.89	5.89
mgs13.1-6	7.81	0.291	7.70	2.14	8.84	21.9	2.8±0.3	118	0.19	6.31	20.89	5.75
mgs13.1-7	7.82	0.290	7.70	2.15	9.08	22.0	2.7±0.3	120	0.20	6.31	21.38	5.89
mgs13.1-8	7.77	0.191	7.67	1.96	7.72	21.8	1.9±0.2	102	0.16	5.75	18.62	5.50
mgs13.1-9	7.76	0.191	7.67	1.95	7.78	21.9	1.9±0.2	101	0.16	5.75	18.62	5.37
mgs13.1-10	7.76	0.191	7.67	1.95	7.31	21.8	1.9±0.2	100	0.15	5.75	17.78	5.37
mgs13.1-11	7.77	0.192	7.67	1.92	8.02	21.9	1.9±0.2	101	0.16	5.62	19.50	5.50
mgs13.1-12	7.78	0.194	7.68	1.91	7.8	21.8	2.0±0.2	101	0.16	5.62	19.05	5.50
mgs13.1-13	7.86	0.598	7.72	2.30	9.59	22.6	4.4±0.4	136	0.22	6.76	22.39	6.31
mgs13.1-14	7.86	0.599	7.72	2.30	9.60	22.5	4.4±0.5	136	0.22	6.76	22.39	6.31
mgs13.1-15	7.90	0.593	7.75	2.29	9.75	22.5	4.4±0.4	143	0.23	6.61	22.39	6.61
mgs13.1-16	7.86	0.598	7.73	2.32	9.5	22.5	4.3±0.4	139	0.21	6.76	21.88	6.31

Table 7: continued

Experiment	pH ^a	Fluid flow rate (g/min)	pH _{calc} (at 100 °C)	outlet c _{Mg} (x 10 ⁻³) (mol/kg)	outlet c _{Ca} (x 10 ⁻⁶) (mol/kg)	Alkalinity (x 10 ⁻³) (eq/L)	Growth rate (x 10 ⁻⁷) (mol/m ² /s)	Ω _{Mgs}	Ω _{Arag}	a _{Mg+2} (x 10 ⁻⁴)	a _{Ca+2} (x 10 ⁻⁷)	a _{CO3-2} (x 10 ⁻⁵)
mgs13.1-17	7.93	0.598	7.77	2.28	10.44	22.5	4.4±0.4	149	0.26	6.61	23.99	6.92
mgs13.1-18	7.99	0.997	7.80	2.61	11.32	22.9	5.2±0.5	181	0.29	7.41	25.70	7.41
mgs13.1-19	7.92	0.998	7.76	2.43	10.79	22.9	6.3±0.6	157	0.26	7.08	24.55	6.92
mgs13.1-20	7.92	0.997	7.76	2.44	10.60	22.9	6.3±0.6	157	0.26	7.08	23.99	6.92
mgs13.1-21	7.91	0.996	7.75	2.53	10.89	22.9	5.7±0.6	160	0.26	7.24	25.12	6.76
mgs13.1-22	7.92	0.997	7.76	2.54	12.11	22.9	5.7±0.6	162	0.29	7.24	27.54	6.76
mgs13.1-23	7.98	1.495	7.79	2.62	13.36	23.1	7.6±0.8	182	0.34	7.59	30.20	7.41
mgs13.1-24	7.98	1.492	7.79	2.68	13.47	23.1	7.1±0.7	185	0.35	7.59	30.20	7.41
mgs13.1-25	7.97	1.507	7.78	2.61	13.1	23.1	7.8±0.8	175	0.33	7.41	29.51	7.24
mgs13.1-26	7.97	1.493	7.78	2.61	13.33	23.1	7.7±0.8	176	0.34	7.41	30.20	7.24
mgs13.1-27	7.98	1.494	7.79	2.62	13.02	23.1	7.5±0.8	180	0.33	7.59	29.51	7.41
mgs13.1-28	8.03	1.996	7.82	2.69	13.97	23.3	9.1±0.9	199	0.38	7.59	30.90	7.94
mgs13.1-29	8.05	1.995	7.83	2.72	14.29	23.3	8.8±0.9	205	0.39	7.76	31.62	8.13
mgs13.1-30	8.07	1.994	7.84	2.74	14.13	23.3	8.5±0.9	211	0.40	7.76	30.90	8.32
mgs13.1-31	8.02	1.999	7.81	2.73	13.88	23.3	8.7±0.9	199	0.37	7.76	30.90	7.94
mgs13.1-32	8.04	1.989	7.82	2.77	13.93	23.3	8.2±0.9	206	0.38	7.94	30.90	8.13
mgs13.1-33	7.84	0.291	7.72	2.01	7.87	21.9	2.4±0.2	116	0.17	5.89	18.62	6.03
mgs13.1-34	7.83	0.290	7.71	2.01	7.80	21.9	2.4±0.2	115	0.17	5.89	18.62	6.03
mgs13.1-35	7.81	0.288	7.70	2.01	7.61	21.9	2.3±0.2	111	0.16	5.89	18.20	5.75
mgs13.1-36	7.84	0.290	7.72	2.03	7.61	21.6	2.3±0.2	115	0.17	6.03	18.20	5.89
mgs13.1-37	8.14	2.992	7.88	2.87	15.27	23.5	10±1	237	0.45	8.13	32.36	9.12
mgs13.1-38	8.12	3.001	7.86	2.87	15.20	23.5	10±1	232	0.44	8.13	32.36	8.91
mgs13.1-39	8.12	2.967	7.86	2.83	14.94	23.5	10±1	229	0.44	7.94	32.36	8.91
mgs13.1-40	8.12	3.003	7.87	2.85	14.9	23.5	10±1	232	0.44	7.94	31.62	8.91

Table 7: continued

Experiment	pH ^a	Fluid flow rate (g/min)	pH _{calc} (at 100 °C)	outlet c _{Mg} (x 10 ⁻³) (mol/kg)	outlet c _{Ca} (x 10 ⁻⁶) (mol/kg)	Alkalinity (x 10 ⁻³) (eq/L)	Growth rate (x 10 ⁻⁷) (mol/m ² /s)	Ω _{Mgs}	Ω _{Arag}	a _{Mg+2} (x 10 ⁻⁴)	a _{Ca+2} (x 10 ⁻⁷)	a _{CO3-2} (x 10 ⁻⁵)
mgs14.1-1	7.83	0.496	7.72	2.05	6.36	28.0	5.4±0.5	141	0.16	5.62	13.49	7.76
mgs14.1-2	7.81	0.493	7.71	2.02	6.05	29.3	5.4±0.5	140	0.16	5.50	12.88	7.94
mgs14.1-3	7.76	0.485	7.68	2.00	6.27	30.3	5.3±0.5	131	0.15	5.37	13.18	7.59
mgs14.1-4	7.77	0.501	7.68	2.04	6.23	30.4	5.4±0.5	137	0.16	5.50	13.18	7.76
mgs14.1-5	7.75	0.496	7.67	2.04	6.63	30.6	5.3±0.5	134	0.16	5.50	14.13	7.59
mgs14.1-6	7.76	0.498	7.68	2.06	6.85	30.4	5.2±0.5	136	0.17	5.50	14.45	7.59
mgs14.1-7	7.75	0.497	7.67	2.04	8.18	30.5	5.3±0.5	133	0.20	5.50	17.38	7.59
mgs14.1-8	7.70	0.199	7.64	1.59	6.32	30.0	2.3±0.2	97	0.15	4.27	13.80	6.92
mgs14.1-9	7.67	0.198	7.62	1.58	6.37	30.0	2.3±0.2	92	0.14	4.27	13.80	6.61
mgs14.1-10	7.68	0.198	7.62	1.58	6.29	30.0	2.3±0.2	93	0.14	4.27	13.80	6.76
mgs14.1-11	7.68	0.198	7.62	1.57	6.73	30.3	2.3±0.2	93	0.15	4.27	14.45	6.76
mgs14.1-12	7.69	0.199	7.63	1.56	20.11	30.0	2.3±0.2	93	0.46	4.27	43.65	6.76
mgs14.1-13	7.69	0.199	7.63	1.53	6.30	30.0	2.3±0.2	92	0.14	4.17	13.80	6.76
mgs14.1-14	7.71	0.198	7.65	1.53	6.62	30.0	2.2±0.2	95	0.16	4.17	14.13	7.08
mgs14.1-15	7.69	0.199	7.63	1.58	6.87	30.0	2.2±0.2	95	0.16	4.27	14.79	6.92
mgs14.1-16	7.69	0.198	7.63	1.58	7.59	29.9	2.2±0.2	96	0.17	4.27	16.60	6.92
mgs14.1-17	7.78	0.879	7.69	2.25	9.37	31.2	6.6±0.7	155	0.24	6.03	19.50	7.94
mgs14.1-18	7.77	0.877	7.68	2.23	8.5	31.2	6.7±0.7	151	0.21	5.89	17.78	7.94
mgs14.1-19	7.79	0.878	7.69	2.26	8.48	31.2	6.5±0.7	157	0.22	6.03	17.78	8.13
mgs14.1-20	7.78	0.874	7.69	2.25	8.7	31.2	6.5±0.7	154	0.22	6.03	18.20	7.94
mgs14.1-21	7.78	0.895	7.69	2.24	8.85	31.2	6.7±0.7	154	0.23	5.89	18.62	7.94
mgs14.1-22	7.85	1.467	7.73	2.42	8.11	31.6	10±1	183	0.22	6.31	16.60	8.91
mgs14.1-23	7.86	1.494	7.74	2.39	8.07	31.7	10±1	184	0.23	6.31	16.22	9.12
mgs14.1-24	7.83	1.467	7.72	2.44	8.00	31.6	9.4±0.9	180	0.22	6.46	16.22	8.51

Table 7: continued

Experiment	pH ^a	Fluid flow rate (g/min)	pH _{cat} (at 100 °C)	outlet c _{Mg} (x 10 ⁻³) (mol/kg)	outlet c _{Ca} (x 10 ⁻⁶) (mol/kg)	Alkalinity (x 10 ⁻³) (eq/L)	Growth rate (x 10 ⁻⁷) (mol/m ² /s)	Ω _{Mgs}	Ω _{Arag}	a _{Mg+2} (x 10 ⁻⁴)	a _{Ca+2} (x 10 ⁻⁷)	a _{CO3-2} (x 10 ⁻⁵)
mgs14.1-25	7.83	1.472	7.72	2.42	7.72	31.6	10±1	178	0.21	6.31	15.85	8.51
mgs14.1-26	7.82	1.478	7.71	2.41	7.82	31.5	10±1	175	0.21	6.31	15.85	8.51
mgs14.1-27	7.86	1.936	7.73	2.54	7.94	31.8	11±1	192	0.22	6.61	16.22	8.91
mgs14.1-28	7.87	1.953	7.74	2.55	7.91	31.8	11±1	196	0.22	6.76	15.85	9.12
mgs14.1-29	7.86	1.952	7.73	2.53	7.64	31.8	11±1	192	0.21	6.61	15.49	8.91
mgs14.1-30	7.86	1.949	7.73	2.57	7.54	31.8	11±1	194	0.21	6.76	15.14	8.91
mgs14.1-31	7.85	1.931	7.72	2.52	7.12	31.8	11±1	188	0.20	6.61	14.45	8.71
mgs15.1-1	8.00	0.286	7.81	2.24	24.15	19.7	2.7±0.3	142	0.58	6.61	57.54	6.61
mgs15.1-2	7.93	0.293	7.77	2.26	19.81	20.6	2.7±0.3	137	0.46	6.76	46.77	6.31
mgs15.1-3	7.88	0.285	7.74	2.27	16.6	21.7	2.6±0.3	135	0.37	6.61	38.90	6.31
mgs15.1-4	7.86	0.290	7.73	2.30	17.0	21.7	2.6±0.3	133	0.38	6.76	39.81	6.03
mgs15.1-5	7.86	0.289	7.73	2.25	17.3	21.9	2.7±0.3	132	0.39	6.61	40.74	6.17
mgs15.1-6	7.86	0.289	7.73	2.29	16.4	21.9	2.6±0.3	133	0.37	6.76	38.90	6.17
mgs15.1-7	7.87	0.287	7.73	2.27	16.12	21.9	2.6±0.3	134	0.36	6.61	38.02	6.31
mgs15.1-8	7.81	0.193	7.70	2.08	11.32	21.9	1.9±0.2	114	0.24	6.17	26.92	5.75
mgs15.1-9	7.83	0.193	7.71	2.07	10.67	22.0	1.9±0.2	116	0.23	6.03	25.12	5.89
mgs15.1-10	7.84	0.191	7.71	2.07	12.24	21.9	1.9±0.2	118	0.27	6.03	28.84	6.03
mgs15.1-11	7.92	0.561	7.76	2.39	16.49	22.6	4.1±0.4	152	0.39	6.92	38.02	6.76
mgs15.1-12	7.89	0.559	7.74	2.38	16.31	22.6	4.2±0.4	146	0.38	6.92	38.02	6.46
mgs15.1-13	7.93	0.559	7.77	2.38	16.28	22.6	4.2±0.4	154	0.40	6.92	37.15	6.92
mgs15.1-14	7.89	0.555	7.74	2.39	16.18	22.6	4.1±0.4	148	0.38	6.92	37.15	6.61
mgs15.1-15	7.94	0.557	7.77	2.42	14.9	22.6	4.0±0.4	159	0.37	7.08	33.88	7.08
mgs15.1-16	8.02	0.889	7.82	2.47	20.09	22.8	5.9±0.6	178	0.54	7.08	44.67	7.76
mgs15.1-17	7.94	0.890	7.77	2.54	19.3	22.8	5.5±0.6	166	0.47	7.41	43.65	6.92

Table 7: continued

Experiment	pH ^a	Fluid flow rate (g/min)	pH _{calc} (at 100 °C)	outlet c _{Mg} (x 10 ⁻³) (mol/kg)	outlet c _{Ca} (x 10 ⁻⁶) (mol/kg)	Alkalinity (x 10 ⁻³) (eq/L)	Growth rate (x 10 ⁻⁷) (mol/m ² /s)	Ω _{Mgs}	Ω _{Arug}	a _{Mg+2} (x 10 ⁻⁴)	a _{Cr+2} (x 10 ⁻⁷)	a _{CO3-2} (x 10 ⁻⁵)
mgs15.1-18	7.94	0.888	7.77	2.55	26.51	22.8	5.4±0.6	167	0.65	7.41	60.26	6.92
mgs15.1-19	7.92	0.889	7.76	2.51	19.93	22.8	5.7±0.6	160	0.48	7.24	45.71	6.76
mgs15.1-20	7.93	0.882	7.76	2.52	19.79	22.8	5.6±0.6	163	0.48	7.24	45.71	6.92
mgs15.1-21	7.97	1.270	7.79	2.57	22.20	23.0	7.6±0.8	176	0.56	7.41	50.12	7.41
mgs15.1-22	7.97	1.267	7.79	2.59	21.92	23.0	7.4±0.8	177	0.56	7.41	48.98	7.41
mgs15.1-23	7.95	1.255	7.77	2.54	21.74	22.9	7.7±0.8	166	0.53	7.24	48.98	7.08
mgs15.1-24	7.95	1.261	7.77	2.60	22.5	23.0	7.2±0.8	171	0.55	7.41	51.29	7.08
mgs15.1-25	7.95	1.244	7.77	2.64	21.49	22.9	6.8±0.7	174	0.53	7.59	48.98	7.08
mgs15.1-26	8.03	1.626	7.82	2.70	22.83	23.1	8.2±0.9	197	0.61	7.76	50.12	7.94
mgs15.1-27	8.05	1.598	7.83	2.72	22.7	23.1	7.8±0.8	203	0.62	7.76	50.12	8.13
mgs15.1-28	8.06	1.634	7.84	2.75	23.0	23.1	7.7±0.8	208	0.64	7.76	50.12	8.13
mgs15.1-29	8.02	1.647	7.81	2.72	22.44	23.2	8.1±0.9	197	0.60	7.76	50.12	7.76
mgs15.1-30	8.04	1.616	7.83	2.69	22.3	23.1	8.3±0.9	199	0.61	7.59	48.98	7.94
mgs15.1-31	7.85	0.261	7.72	2.08	8.91	21.9	2.3±0.2	121	0.20	6.03	20.89	6.17
mgs16.1-1	7.64	0.990	7.59	2.14	13.30	30.9	4.4±0.4	120	0.29	5.75	28.84	6.31
mgs16.1-2	7.65	0.987	7.60	2.12	12.29	30.9	4.4±0.4	120	0.27	5.75	26.92	6.46
mgs16.1-3	7.66	0.986	7.60	2.13	13.0	31.0	4.4±0.4	123	0.29	5.75	28.18	6.61
mgs16.1-4	7.67	0.996	7.61	2.13	12.7	31.0	4.4±0.4	126	0.28	5.75	27.54	6.76
mgs16.1-5	7.65	0.988	7.60	2.08	10.91	30.9	4.5±0.5	119	0.24	5.62	23.99	6.46
mgs16.1-6	7.62	0.461	7.58	1.76	11.43	30.3	2.5±0.2	95	0.24	4.79	25.12	6.03
mgs16.1-7	7.62	0.475	7.57	1.79	11.98	30.3	2.5±0.3	96	0.25	4.90	26.30	6.03
mgs16.1-8	7.61	0.463	7.57	1.75	10.68	30.3	2.5±0.3	92	0.22	4.79	23.99	6.03
mgs16.1-9	7.62	0.453	7.58	1.75	10.6	30.3	2.4±0.2	94	0.22	4.79	23.44	6.03
mgs16.1-10	7.64	0.476	7.59	1.76	11.0	30.3	2.5±0.3	97	0.23	4.79	23.99	6.17

Table 7: continued

Experiment	pH ^a	Fluid flow rate (g/min)	pH _{calc} (at 100 °C)	outlet c _{Mg} (x 10 ⁻³) (mol/kg)	outlet c _{Ca} (x 10 ⁻⁶) (mol/kg)	Alkalinity (x 10 ⁻³) (eq/L)	Growth rate (x 10 ⁻⁷) (mol/m ² /s)	Ω _{Mgs}	Ω _{Arag}	a _{Mg+2} (x 10 ⁻⁴)	a _{Ca+2} (x 10 ⁻⁷)	a _{CO3-2} (x 10 ⁻⁵)
mgs16.1-11	7.72	1.493	7.64	2.26	14.81	31.4	6.2±0.6	142	0.35	6.03	31.62	7.24
mgs16.1-12	7.70	1.469	7.63	2.22	12.03	31.2	6.3±0.6	135	0.28	6.03	25.70	6.92
mgs16.1-13	7.67	1.488	7.61	2.14	10.62	31.1	6.6±0.7	125	0.24	5.75	22.91	6.61
mgs16.1-14	7.68	1.476	7.61	2.19	10.80	31.1	6.4±0.6	129	0.24	5.89	23.44	6.76
mgs16.1-15	7.67	1.494	7.60	2.17	10.58	31.1	6.5±0.7	126	0.23	5.89	22.91	6.61
mgs16.1-16	7.77	1.858	7.68	2.45	17.30	31.8	6.9±0.7	168	0.44	6.46	36.31	7.94
mgs16.1-17	7.76	1.987	7.67	2.46	17.8	31.8	7.3±0.7	166	0.45	6.61	37.15	7.76
mgs16.1-18	7.76	1.985	7.67	2.39	14.08	31.7	7.7±0.8	161	0.35	6.31	29.51	7.76
mgs16.1-19	7.73	1.982	7.65	2.36	12.65	31.4	7.8±0.8	152	0.31	6.31	26.92	7.41
mgs16.1-20	7.72	1.984	7.65	2.26	12.15	31.3	8.3±0.8	143	0.29	6.03	25.70	7.24
mgs16.1-21	7.75	2.333	7.66	2.30	13.48	31.5	10±1	152	0.33	6.17	28.18	7.59
mgs16.2-23	7.75	2.406	7.66	2.35	14.77	31.6	6.8±0.7	155	0.36	6.31	30.90	7.59
mgs16.2-24	7.76	2.386	7.67	2.30	16.25	31.7	7.0±0.7	155	0.41	6.17	33.88	7.76
mgs16.2-25	7.76	2.348	7.67	2.16	15.10	31.7	7.7±0.8	146	0.38	5.75	31.62	7.76
mgs16.2-26	7.84	2.904	7.73	2.34	21.30	32.4	8.2±0.8	179	0.59	6.17	42.66	8.91
mgs16.2-27	7.82	2.842	7.71	2.30	20.00	32.4	8.3±0.8	171	0.55	6.03	40.74	8.71
mgs16.2-28	7.83	2.896	7.72	2.23	17.30	32.2	9.0±0.9	169	0.48	5.89	34.67	8.91
mgs16.2-29	7.81	2.900	7.71	2.23	15.52	32.1	9.0±0.9	164	0.42	5.89	31.62	8.51
mgs16.2-30	7.78	2.853	7.69	2.16	14.48	32.0	9.3±0.9	153	0.38	5.75	30.20	8.13
mgs16.2-31	7.68	0.462	7.63	1.46	7.94	30.5	2.3±0.2	88	0.18	3.98	16.98	6.92
mgs16.2-32	7.67	0.474	7.62	1.47	8.47	30.6	2.3±0.2	87	0.19	3.98	18.20	6.76
mgs16.2-33	7.67	0.455	7.62	1.43	7.45	30.5	2.3±0.2	85	0.17	3.89	16.22	6.76
mgs16.2-34	7.68	0.473	7.63	1.49	8.68	30.5	2.3±0.2	90	0.20	4.07	18.62	6.92
mgs16.2-35	7.67	0.456	7.62	1.46	7.62	30.5	2.3±0.2	87	0.17	3.98	16.60	6.76

Table 7: continued

Experiment	pH ^a	Fluid flow rate (g/min)	pH _{calc} (at 100 °C)	outlet c _{Mg} (x 10 ⁻³) (mol/kg)	outlet c _{Ca} (x 10 ⁻⁶) (mol/kg)	Alkalinity (x 10 ⁻³) (eq/L)	Growth rate (x 10 ⁻⁷) (mol/m ² /s)	Ω _{Mgs}	Ω _{Arug}	a _{Mg+2} (x 10 ⁻⁴)	a _{Ca+2} (x 10 ⁻⁷)	a _{CO3-2} (x 10 ⁻⁵)
mgs16.2-36	7.74	0.915	7.66	1.67	8.93	31.0	4.1±0.4	110	0.22	4.47	19.05	7.59
mgs16.2-37	7.71	0.938	7.64	1.81	11.98	31.2	3.8±0.4	114	0.28	4.90	25.70	7.24
mgs16.2-38	7.73	0.941	7.66	1.80	11.12	31.2	3.9±0.4	117	0.27	4.79	23.44	7.41
mgs16.2-39	7.71	0.943	7.65	1.73	9.45	31.0	4.0±0.4	110	0.23	4.68	19.95	7.24
mgs16.2-40	7.73	0.936	7.66	1.80	12.27	31.2	3.9±0.4	118	0.30	4.79	25.70	7.59
mgs11.1-1	7.85	0.489	7.71	2.40	32.14	20.8	3.4±0.4	129	0.66	7.08	77.62	5.62
mgs11.1-4	7.71	0.488	7.62	2.42	34.84	22.4	3.3±0.3	114	0.64	7.08	85.11	4.90
mgs11.1-5	7.76	0.494	7.65	2.45	35.78	22.4	3.2±0.3	125	0.71	7.24	85.11	5.37
mgs11.1-6	7.77	0.496	7.65	2.38	30.69	22.3	3.4±0.3	121	0.60	7.08	74.13	5.37
mgs11.1-7	7.73	0.493	7.64	2.31	27.60	22.3	3.6±0.4	113	0.53	6.76	67.61	5.13

^a Measured at 22 ± 1 °C.

Table 8: Results of steady state hydrothermal mixed-flow reactor (HMFR) experiments at 100 °C.

Experiment	pH _{calc} (at 100 °C)	outlet c _{Mg} (x 10 ⁻³) (mol/kg)	outlet c _{Ca} (x 10 ⁻⁶) (mol/kg)	Δc _{Mg} (x 10 ⁻⁴) (mol/kg)	Δc _{Ca} (x 10 ⁻⁶) (mol/kg)	Growth rate (x 10 ⁻⁷) (mol/m ² /s)	X _{solid} ^a (mol%)	X _{liquid} ^a (mol%)	Ω _{Mgs}	a _{Mg+2} / a _{CO3-2}	a _{Ca+2} / a _{CO3-2}
mgs10.1-4/9	7.67	2.48	1.59	10.0	4.19	3.7±0.4	0.403	0.0650	132±2	12.9	0.009
mgs10.1-10/15	7.72	2.60	1.42	8.7	4.36	6.2±0.6	0.494	0.0548	154±2	12.0	0.006
mgs10.1-16/20	7.74	2.68	1.62	7.9	4.17	8.1±0.8	0.531	0.0599	170±3	11.2	0.006
mgs10.1-21/26	7.78	2.75	2.12	7.2	3.67	10±1	0.495	0.077	188±1	10.6	0.006
mgs10.2-27/31	7.79	2.87	2.08	6.5	4.75	11±1	0.73	0.0724	198±6	11.0	0.006
mgs10.2-32/34	7.65	2.16	1.30	13.6	5.53	2.4±0.2	0.408	0.0600	107±4	12.0	0.005
mgs10.2-35/37	7.69	2.30	1.16	12.2	5.67	3.6±0.4	0.463	0.0504	128±1	11.7	0.004
mgs9.1-1/3	7.68	2.26	9.89	11.8	31.7	3.4±0.4	2.62	0.435	122±2	11.7	0.043
mgs9.1-4/7	7.64	2.25	9.83	11.9	31.8	3.4±0.3	2.60	0.434	110±1	12.9	0.047
mgs12.1-1/3	7.72	2.76	14.14	6.5	26.73	8.0±0.8	4.0	0.505	166±1	12.3	0.050
mgs12.1-4/7	7.72	2.74	14.27	6.8	26.60	7.5±0.8	3.8	0.519	166±6	12.3	0.049
mgs12.2-8/11	7.74	2.81	17.41	6.7	23.74	6.9±0.7	3.13	0.629	174±4	12.0	0.061
mgs13.1-1/7	7.70	2.16	8.98	12.8	32.2	2.7±0.3	2.43	0.415	120±2	10.7	0.036
mgs13.1-8/12	7.67	1.95	7.78	14.9	33.44	1.9±0.2	2.20	0.397	101±1	10.5	0.035
mgs13.1-13/17	7.73	2.30	9.60	11.4	31.6	4.4±0.4	2.70	0.415	139±5	10.7	0.035
mgs13.1-18/22	7.76	2.53	10.89	9.1	30.33	5.7±0.6	3.13	0.433	160±9	10.2	0.035
mgs13.1-23/27	7.79	2.62	13.33	8.2	27.89	7.6±0.8	3.30	0.501	180±3	10.2	0.041
mgs13.1-28/32	7.82	2.73	13.97	7.1	27.3	8.7±0.9	3.7	0.513	205±5	9.5	0.039
mgs13.1-33/36	7.71	2.01	7.71	14.3	33.51	2.4±0.2	2.29	0.382	115±2	10.0	0.031
mgs13.1-37/40	7.87	2.86	15.07	5.8	26.2	10±1	4.3	0.525	232±3	8.9	0.036
mgs14.1-1/7	7.68	2.04	6.36	18.4	34.83	5.3±0.5	1.85	0.314	136±3	7.2	0.017
mgs14.1-8/16	7.63	1.58	6.62	23.0	34.58	2.3±0.2	1.47	0.427	93±2	6.2	0.021
mgs14.1-17/21	7.69	2.25	8.69	16.3	32.5	6.6±0.7	1.94	0.385	154±2	7.4	0.023

Table 8: continued

Experiment	pH _{calc} (at 100 °C)	outlet c _{Mg} (x 10 ⁻³) (mol/kg)	outlet c _{Ca} (x 10 ⁻⁶) (mol/kg)	Δc _{Mg} (x 10 ⁻⁴) (mol/kg)	Δc _{Ca} (x 10 ⁻⁶) (mol/kg)	Growth rate (x 10 ⁻⁷) (mol/m ² /s)	X _{solid} ^a (mol%)	X _{liquid} ^a (mol%)	Ω _{Mgs}	a _{Mg+2} / a _{CO3-2}	a _{Ca+2} / a _{CO3-2}
mgs14.1-22/26	7.72	2.42	8.00	14.6	33.19	10±1	2.21	0.326	180±3	7.4	0.019
mgs14.1-27/31	7.73	2.54	7.64	13.4	33.56	11±1	2.44	0.301	192±3	7.4	0.017
mgs15.1-1/7	7.73	2.27	17.0	11.7	68.2	2.6±0.3	5.6	0.735	134±3	10.7	0.066
mgs15.1-8/10	7.71	2.07	11.32	13.6	73.88	1.9±0.2	5.2	0.542	116±2	10.2	0.047
mgs15.1-11/15	7.76	2.39	16.28	10.4	68.92	4.1±0.4	6.2	0.680	152±5	10.2	0.056
mgs15.1-16/20	7.77	2.52	19.93	9.2	65.27	5.6±0.6	6.6	0.789	166±6	10.7	0.066
mgs15.1-21/25	7.77	2.59	21.92	8.4	63.28	7.4±0.8	7.0	0.850	174±4	10.2	0.069
mgs15.1-26/30	7.83	2.72	22.7	7.2	62.5	8.1±0.9	8.0	0.827	199±4	9.5	0.062
mgs15.1-31	7.72	2.08	8.91	13.6	76.29	2.3±0.2	5.3	0.427	121±6	9.8	0.034
mgs16.1-1/5	7.60	2.13	12.68	18.3	71.7	4.4±0.4	3.77	0.591	120±3	8.7	0.042
mgs16.1-6/10	7.58	1.76	10.95	22.0	73.4	2.5±0.3	3.23	0.618	95±2	7.9	0.040
mgs16.1-11/15	7.61	2.19	10.80	17.7	73.5	6.4±0.6	3.97	0.494	129±7	8.7	0.035
mgs16.1-16/20	7.67	2.39	14.08	15.7	70.3	7.7±0.8	4.27	0.586	161±9	8.3	0.038
mgs16.1/2-21/25	7.67	2.30	14.92	12.5	63.2	7.3±0.7	4.76	0.659	153±4	8.0	0.041
mgs16.2-26/30	7.71	2.23	17.30	12.5	60.8	9.0±0.9	4.67	0.769	169±9	6.9	0.039
mgs16.2-31/35	7.62	1.46	7.94	20.2	70.2	2.3±0.2	3.35	0.540	87±2	5.9	0.025
mgs16.2-36/40	7.66	1.80	11.12	16.8	67.0	3.9±0.4	3.77	0.614	114±4	6.5	0.032
mgs11.1-1	7.71	2.40	32.14	10.5	89.0	3.4±0.4	7.8	1.32	129±7	12.6	0.138
mgs11.1-4/7	7.64	2.40	32.77	10.4	88.3	3.4±0.3	7.8	1.35	117±5	13.3	0.148

^a Molar fraction of calcium versus Ca+Mg in the solid or fluid phase – see caption of Figure 19.

Table 9: Results of Raman spectra measurements as a function of depth on (104) magnesite single crystals. The parameters T , L , ν_1 , ν_2 , ν_3 , and ν_4 stand for the Raman active vibrational modes of carbonate in magnesite and are reported together with their full width half maximum (FWHM) values.

Experiment	Depth (μm)	T_r (cm^{-1})	FWHM (cm^{-1})	T^* (cm^{-1})	L_r (cm^{-1})	FWHM (cm^{-1})	L^* (cm^{-1})	ν_4 (cm^{-1})	FWHM (cm^{-1})	ν_1 (cm^{-1})	FWHM (cm^{-1})	ν_3 (cm^{-1})	FWHM (cm^{-1})	$2 \times \nu_2$ (cm^{-1})	FWHM (cm^{-1})
unreacted	0	209.9	5.5	-	327.0	5.5	-	737.1	16.6	1092.3	12.9	1444.9	7.4	1762.2	9.2
Brumado	-30	210.1	5.5	-	327.3	5.5	-	737.3	16.6	1092.4	12.9	1445.2	7.4	1762.2	9.2
mgs10	0	209.8	5.5	-	327.0	7.4	-	737.3	16.6	1092.4	12.9	1444.8	9.2	1762.2	11.1
	-30	209.7	5.5	-	326.9	5.5	-	737.2	16.6	1092.4	12.9	1444.8	7.4	1762.1	9.2
mgs9	0	209.3	7.4	203.2	327.4	7.4	320.2	736.3	14.8	1092.9	14.8	1444.5	9.2	1762.1	11.1
	-4	209.6	7.4	203.0	327.7	7.4	320.3	736.5	14.8	1092.8	14.8	1444.7	11.1	1762.0	9.2
	-30	209.7	5.5	-	327.4	5.5	-	736.9	16.6	1092.4	14.8	1444.8	7.4	1761.9	9.2
mgs12	0	209.9	5.5	203.4	327.8	7.4	320.2	737.4	16.6	1093.3	14.8	1446.0	-	1762.5	11.1
	-4	210.4	7.4	203.2	328.0	7.4	320.0	737.8	16.6	1093.3	14.8	1445.8	12.9	1762.7	11.1
	-30	211.3	5.5	-	328.5	5.5	-	738.7	14.8	1093.7	14.8	1446.1	9.2	1763.0	11.1
mgs15	0	209.7	5.5	201.5	326.9	5.5	318.7	736.4	16.6	1092.1	14.8	1444.6	7.4	1761.4	11.1
	-4	209.7	5.5	201.4	326.9	5.5	318.5	736.5	18.5	1092.3	12.9	1444.9	9.2	1761.6	11.1
	-30	209.9	5.5	-	327.2	5.5	-	737.0	16.6	1092.5	12.9	1445.0	9.2	1761.9	11.1

4.4 Discussion

4.4.1 Comparison with past results and a description of measured rates as a function of saturation state

This study builds upon those of Saldi *et al.* (2009) and Gautier (2012), who reported magnesite precipitation rates as a function of temperature and fluid saturation states (up to ~ 60 at $100\text{ }^{\circ}\text{C}$). The current study extended the range of measured fluid saturation state up to 190. Magnesite precipitation rates were fit in the previous studies to *Equation (16)* and a reaction order of 2, consistent with a spiral growth model (Shiraki and Brantley, 1995). The rate constants, k_{Mgs} , reported in these studies at $100\text{ }^{\circ}\text{C}$ were 6.5×10^{-12} and 1.07×10^{-11} mol/m²/s by Saldi *et al.* (2009) and Gautier (2012) respectively. These rates previously generated from HMFR experiments are compared with those generated in the present study in *Figure 18*. Also shown in this figure is the fit of the original Saldi *et al.* (2009) study. It can be seen that the Saldi *et al.* (2009) fit underestimates substantially the rates generated in this study at higher saturation states. Indeed, attempts to fit the rates obtained in this study using the spiral growth model adopted by Saldi *et al.* (2009) required a rate constant approximately six times higher than that obtained in this previous study and generated estimates inconsistent with that original study. It seems likely such inconsistencies stem from the influence of a two dimensional nucleation and growth mechanism which dominates growth strongly in supersaturated fluids (Nielsen, 1984). Indeed, the formation of growth steps by two dimensional nucleation was observed during two HAFM experiments performed at $100\text{ }^{\circ}\text{C}$ and $\Omega_{Mgs} > 100$ by Saldi *et al.* (2009). As such, the rates obtained in this study were fit using *Equation (20)* adopting the spiral growth mechanism rate constant of 6.5×10^{-12} mol/m²/s reported by Saldi *et al.* (2009). Data regression yielded values of k_c and K_c in *Equation (20)* of 10^{-4} mol/m²/s and 26, respectively. The results of this regression are shown as the solid curve in *Figure 18*; a close correspondence between the curve and all three

sets of magnesite precipitation rate measurements are apparent, demonstrating that *Equation (20)* can accurately describe magnesite precipitation rates from $15 < \Omega < 200$.

4.4.2 The incorporation of calcium into the magnesite structure

The results described above found that calcium is preferentially incorporated into the magnesite structure with a distribution coefficient, K_D , of 6.9 ± 0.9 . The distribution coefficients of metals into carbonate minerals have been demonstrated to be a strong function of the mineral precipitation rate (Lorens, 1981; Tesoriero and Pankow, 1996; Watson, 2004). Such was not observed in the present study likely due to the small range of measured magnesite precipitation rates, which ranged over less than one order of magnitude. The observation that calcium is preferentially incorporated into magnesite contrasts with the behavior of magnesium incorporation into calcite, which has been found to be preferentially excluded (Mavromatis *et al.*, 2013). This contrasting behavior is consistent with the affinity of magnesium for the aqueous phase and the growth/entrapment model of Watson (2004).

4.4.3 Raman spectroscopy

The measured Raman spectra confirmed the incorporation of Ca^{2+} into the growing magnesite by the observation of significant changes in the carbonate translational T_v and librational L_v vibration modes. Substitution of Ca^{2+} for Mg^{2+} places a larger cation into the divalent metal site, increasing the interatomic distances and decreasing the carbonate-metal vibrational frequencies (Krishnamurti, 1956; White, 1974). These lower frequency bands mirror the observed Raman shifts to higher carbonate-metal vibrational frequencies stemming from the substitution of Mg^{2+} for Ca^{2+} in magnesian calcites (Bischoff *et al.*, 1985). No

correlation is seen in this study, however, between incorporated calcium concentration and band halfwidths.

4.4.4 Why is there little effect of aqueous calcium on magnesite precipitation rates?

The results presented above indicate that there is little effect of the presence of aqueous calcium on magnesite precipitation rates at the conditions considered in this study. This observation contrasts with the frequently cited observations that aqueous magnesium has a large inhibiting effect on calcite precipitation rates (Gutjahr *et al.*, 1996; Davis *et al.*, 2000, 2004; Zhang and Dawe, 2000; Wasylenki *et al.*, 2005; Lin and Singer, 2009; Astilleros *et al.*, 2010; Pina and Jordan, 2010; Sethmann *et al.*, 2010; Bracco *et al.*, 2012; Nielsen *et al.*, 2013). Two models have been advocated to explain this inhibition. The first is the ‘step pinning’ model (*e.g.*, Pina and Jordan, 2010). This model assumes that the adsorption of hydrated magnesium at kink sites causes the pinning of steps, which hinders further advancement of this step. The second is the ‘impurity incorporation’ model (*e.g.*, De Yoreo and Vekilov, 2003). This model assumes that Mg^{2+} incorporates in the calcite structure forming a solid solution, which is more soluble than the pure phase, thus lowering the supersaturation state of the fluid at constant fluid composition. This latter model has been championed by Berner (1975) and Davis *et al.* (2000). Nevertheless, Astilleros *et al.* (2010) - using atomic force microscopy - observed a clear change in calcite growth morphology in the presence of as little as 5×10^{-5} mol/kg aqueous Mg^{2+} . Based on such observations they concluded that both factors play a role in slowing calcite precipitation rates.

There are several possibilities why there is no corresponding effect of aqueous calcium on magnesite precipitation rates observed in this study. First, all experiments in this study were performed at fluid saturation states with respect to pure magnesite in excess of 100. It

seems likely that the incorporation of small amounts of calcium into the magnesite structure will only negligibly affect overall saturation states at these conditions. Moreover, this high degree of supersaturation may be sufficient to overcome any step pinning inhibition effects. Indeed no change in growth step morphology was observed in the study due to the presence of aqueous calcium. In addition, one factor that may be critical to the inhibition of calcite precipitation by aqueous magnesium is its strong hydration in aqueous solution at ambient conditions (Bock, 1994; Katz *et al.*, 1996; Pavlov *et al.*, 1998). The incorporation of aqueous magnesium onto the calcite surface may occur without the complete removal of its hydration shell (Astilleros *et al.*, 2010), which contrasts with aqueous calcium, which is far less strongly hydrated. Note also that the strength of aqueous cation hydration shells weakens with increasing temperature; this temperature effect has been used to explain the favored precipitation of hydrous magnesium carbonate phases rather than magnesite at temperatures lower than ~ 80 °C (Lippman, 1973; Saldi *et al.*, 2009, 2012; Berninger *et al.*, 2014; Gautier *et al.*, 2014). As such one might expect that the inhibiting effect of aqueous magnesium on calcite precipitation might diminish with increasing temperature. Nevertheless, Deleuze and Brantley (1997) reported that the presence of Mg-rich aqueous solutions, having Mg/Ca ratios of 1/3 or more inhibit strongly calcite surface nucleation at 100 °C and 100 bars of pressure at near to equilibrium conditions, but little to no effect was observed in the parabolic growth regime, such as considered in this study of magnesite growth. Taken together, these observations suggest that the reasons for the negligible effect of aqueous calcium on magnesite precipitation rates in this study include 1) the high saturation state of the reactive fluid and 2) the still significant difference in the strength of the aqueous magnesium versus calcium hydration shells at 100 °C.

4.4.5 Consequences for mineral carbonation

Magnesite precipitation has been favored for mineral carbonation as this mineral is stable down to upper mantle conditions (Fiquet and Reynard, 1999; Isshiki *et al.*, 2004; Skorodumova *et al.*, 2005). As such, the injection of CO₂ into Mg-bearing rocks such as basalt and ultramafic rocks has been extensively explored and advocated (*e.g.*, Oelkers *et al.*, 2008; Gislason and Oelkers, 2014). The dissolution of these host rocks provides the dissolved magnesium needed to form magnesite, but also liberates significant quantities of other divalent cations including calcium and iron. The results of this study suggest that the presence of aqueous calcium will negligibly affect magnesite growth confirming the suitability of these rocks for mineral carbonation. In contrast, other studies suggested that the presence of minor quantities of aqueous divalent cations including iron and cobalt promote magnesite precipitation (Saldi *et al.*, 2013; Sissmann *et al.*, 2014; Felmy *et al.*, 2015) further favoring mineral carbonation in basaltic and ultramafic rocks.

4.5 Conclusion

HMFR experiments and Raman spectroscopy investigations show that Ca²⁺ preferably incorporates into the magnesite structure despite high saturation states with respect to pure magnesite. This incorporation, however, does not affect significantly measured magnesite growth rates. This result contrasts greatly with the observed effect of aqueous magnesium on calcite growth kinetics at ambient temperatures. Such differences may stem from a number of factors including the high saturation state of the reactive fluid in this study, differences in the strength of the hydration shells of aqueous Mg²⁺ and Ca²⁺, and the effect of increased temperature on the water exchange rate of these hydration shells. Nevertheless, the fact that the ubiquitous presence of aqueous calcium in geological settings does not substantially affect

magnesite precipitation rates suggests that the presence of this cation and other analogous aqueous divalent metal ions will not affect significantly mineral carbonation efforts in mafic or ultramafic rocks.

Chapter 5

EXPERIMENTAL DETERMINATION OF THE SOLUBILITY PRODUCT OF DOLOMITE AT 50 TO 175 °C

Abstract

The solubility of natural dolomite ($\text{CaMg}(\text{CO}_3)_2$) was investigated from 50 to 175 °C in 0.1 molal NaCl solutions by using a hydrogen electrode concentration cell (HECC). The obtained apparent solubility products ($Q_{sp(Dol)}$), for the reaction: $\text{CaMg}(\text{CO}_3)_2 = \text{Ca}^{2+} + \text{Mg}^{2+} + 2\text{CO}_3^{2-}$, were calculated to infinite dilution to generate the solubility product constants for this reaction ($K_{sp(Dol)}$). The retrieved equilibrium constants were fitted with a fixed heat capacity (retrieved from the literature) of the reaction above, $\Delta_r C_p^\circ$, of -789.832 J/mol/K at 298.15 K and can be accurately described using $\log_{10} K_{sp(Dol)} = a + b/T + cT$ with T referring to absolute temperature, $a = 18.1777$, $b = -4400.8736$ K and $c_{(fixed)} = -0.06919$ 1/K. This equation and its first and second derivatives with respect to T were used together with corresponding properties for aqueous species to calculate revised standard state thermodynamic properties of dolomite at 25 °C and 1 bar: Gibbs energy of formation: $\Delta_f G_{298.15}^\circ = (-2161 \pm 2)$ kJ/mol ($\log_{10} K_{sp(Dol)} = -17.2 \pm 0.4$); enthalpy of formation: $\Delta_f H_{298.15}^\circ = (-2324 \pm 2)$ kJ/mol; entropy: $S_{298.15}^\circ = (152 \pm 2)$ J/mol/K with a fixed heat capacity of dolomite: $C_{p,298.15}^\circ = (158 \pm 2)$ J/mol/K (uncertainties are 3σ). The value of dolomite solubility product derived in this study is nearly equal to that predicted by SUPCRT92 (Johnson *et al.*, 1992) at 200 °C, but about one order of magnitude higher at 50 °C, suggesting that dolomite is somewhat less stable than previously assumed.

5.1 Introduction

Dolomite, $\text{CaMg}(\text{CO}_3)_2$, is a double carbonate in which Mg^{2+} and Ca^{2+} are segregated into separate planes of the crystal structure (Lippmann, 1973; Antao *et al.*, 2004) as shown in *Figure 21* (after Warren, 2000).

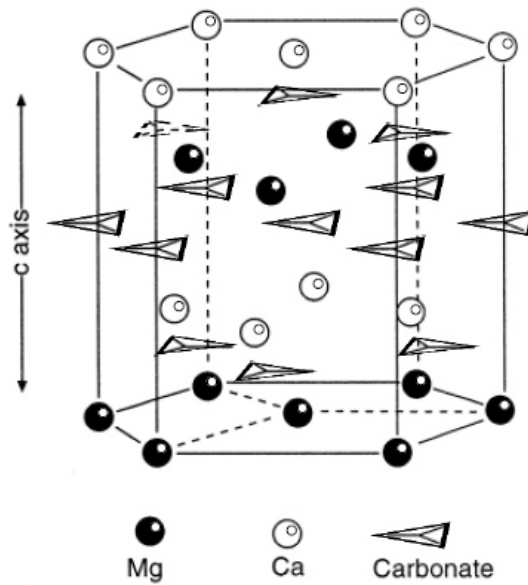


Figure 21: Stoichiometric dolomite crystal structure showing the layers of carbonate separated by alternating layers of calcium and magnesium ions (after Warren, 2000).

Dolomite is a common mineral in sedimentary rocks, ubiquitous in the past, yet rarely found in modern environments (Arvidson and Mackenzie, 1999; Mackenzie and Andersson 2013). Cation ordered dolomite is challenging to synthesize under laboratory conditions (Usdowski, 1994; Land, 1998) and its behavior, occurrence, and uncertainties about its origin, a conundrum known as the “dolomite problem”, have attracted the attention of scientists for more than a century (see Lippmann, 1973; Land, 1998; Arvidson and Mackenzie, 1999; Warren, 2000; Machel, 2004).

Due to the difficulty of precipitating dolomite in the laboratory, its relatively slow carbonate dissolution rate (Pokrovsky and Schott, 2001; Pokrovsky *et al.*, 2005), questions surrounding its crystallinity, and other experimental challenges including controlling experimental CO₂ partial pressure and the measurement of pH and alkalinity above ambient temperatures, there is a wide disparity in the values of dolomite solubility product available in the literature. To resolve this disparity and owing to the scarcity of data at super ambient temperatures, this study has been aimed at 1) measuring the solubility of natural dolomite from 50 to 175 °C, 2) verifying its congruent/incongruent dissolution and reversible equilibrium, 3) generating a revised set of consistent thermodynamic properties, and 4) assessing the quality of currently existing dolomite solubility data and estimates.

5.2 Summary of past work

Dolomite dissolution can be described by the reaction:



The law of mass action for *Reaction (21)* can be written as:

$$K_{sp(Dol)} = a_{eqCa^{2+}} a_{eqMg^{2+}} a_{eqCO_3^{2-}}^2 \quad (22)$$

where $K_{sp(Dol)}$ denotes the solubility product of dolomite and a_{eqi} refers to the activity of the subscripted aqueous species i at equilibrium. Due to a variety of experimental challenges, mentioned in the previous section, previous studies of dolomite solubility do not yield consistent and reliable solubility products. For example, the $\log_{10} K_{sp(Dol)}$ values obtained at 25 °C range from -16.5 to -19.3 (see *Table 10*, Yanat'eva, 1952; Garrels *et al.*, 1960; Halla and Van Tassel, 1965). Yanat'eva (1952) reported a $\log_{10} K_{sp(Dol)}$ of -18.37 at 25 °C, measured

from dolomite dissolution experiments performed in pure water over 100 days. Garrels *et al.* (1960) performed dissolution experiments with dolomite in pure water at 25 °C and 1 atm pCO₂ for 18 h. The pH at equilibrium between solution and < 0.1 mm sized dolomite grains was measured as 5.68 ± 0.02. These results yield a log₁₀ $K_{sp(Dol)}$ value of -19.34. However, Garrels *et al.* (1960) reported that adding well-ground dolomite powder to their experimental solutions when they were close to the equilibrium pH of ~ 5.6 resulted in a rapid increase of pH to 6.2. This latter result yields a log₁₀ $K_{sp(Dol)}$ value of -16.44, which may indicate a failure of having reached equilibrium. Langmuir (1964) performed dolomite dissolution experiments in distilled water and dilute MgCl₂ solutions and reported a value of -17.0, whereas Halla and Van Tassel (1965) reported a log₁₀ $K_{sp(Dol)}$ of -17.76 at 21 °C from experiments performed in pure water and 1 bar pCO₂. More recently, Sherman and Barak (2000) performed dolomite dissolution experiments at 25 °C and in Ca-Mg-HCO₃/CO₃ solutions for almost 2 years and derived a mean log₁₀ $K_{sp(Dol)}$ value of -17.2 ± 0.2, which is in agreement with the value (log₁₀ $K_{sp(Dol)}$ = -17.12) that can be calculated using the thermodynamic properties of dolomite reported by Robie *et al.* (1978) combined with the thermodynamic data of the aqueous species involved in *Reaction (21)* reported in *Table 11*. Most of the log₁₀ $K_{sp(Dol)}$ values gathered in *Table 10* are plotted as a function of the reciprocal temperature in *Figure 22* including the values generated from SUPCRT92 (Johnson *et al.*, 1992). It can be seen from this figure that the log₁₀ $K_{sp(Dol)}$ values reported by Halla and Van Tassel (1965) and Yanat'eva (1952) fall between a group of values near -17.00 (Kramer, 1959; Langmuir, 1964; Robie *et al.*, 1978; Sherman and Barak 2000) and the one generated from SUPCRT92 (Johnson *et al.*, 1992: log₁₀ $K_{sp(Dol)}$ = -18.15) or by Navrotsky and Capobianco (1987) from HCl solution calorimetry experiments performed at 85 °C (log₁₀ $K_{sp(Dol)}$ = -18.2 at 25 °C). The SUPCRT92 database uses dolomite thermodynamic data from Helgeson *et al.* (1978) to calculate this equilibrium constant. These data are based on the phase equilibrium for the reaction:



at $P = 2$ kbar and temperatures ranging from 400 to 600 °C, and yield quite different solubility products from the ones calculated with the data from Robie *et al.* (1978) (one log unit in the $K_{sp(Dol)}$).

Table 10: Literature values of dolomite solubility product obtained experimentally and/or thermodynamic calculations reported in the literature.

Temp (°C)	$\log_{10} K_{sp(Dol)}$	Conditions	Reference
25	-18.37	dissolution in pure water, 1 atm p_{CO_2} for 100 days	Yanat'eva (1952)
25	-16.8	dissolution in artificial seawater (35‰) atmospheric CO_2	Kramer (1959)
25	-19.34	dissolution in pure water and 1 atm p_{CO_2} for 18 hours	Garrels <i>et al.</i> (1960)
25	-16.44	added well-grounded dolomite to the above experiment	Garrels <i>et al.</i> (1960)
22-27	-16.70	groundwater assumed to be in equilibrium with dolomite	Hsu (1963)
25	-18.2	calculated with data of Graf and Goldsmith (1956), see text	Stout and Robie (1963)
25	-16.54	groundwater assumed to be in equilibrium with dolomite	Barnes and Back (1964)
25	-17.0	dissolution in distilled water and dilute MgCl_2 solutions	Langmuir (1964)
21	-17.76	dissolution in pure water, 1 atm p_{CO_2} for 546 days	Halla and Van Tassel (1965)
25	-17.12	calculated (see text)	Robie <i>et al.</i> (1978)
25	-18.15	calculated based on phase equilibria by Helgeson <i>et al.</i> (1978)	Johnson <i>et al.</i> (1992) (SUPCRT92)
25	-17.09 ± 0.37	calculated from HCl solution calorimetry at 300.15 K	Hemingway and Robie (1994)
25	-17.20	dissolution in Ca-Mg- HCO_3/CO_3 solutions for ~ 2 years	Sherman and Barak (2000)
80	-17.95	dissolution in HCl- NaHCO_3 solutions	Gautelier <i>et al.</i> (2007)

Table 11: Values of standard state properties of dolomite and aqueous species involved and used in *Reaction (21)* at 25 °C and 1 bar reported in the literature.

Solid phase	$\Delta_f G_{298.15}^{\circ}$ (kJ/mol)	$S_{298.15}^{\circ}$ (J/mol/K)	$\Delta_f H_{298.15}^{\circ}$ (kJ/mol)	C_p° _{298.15} (J/mol/K)	Reference
CaMg(CO ₃) ₂	-2161.7				Garrels <i>et al.</i> (1960)
		155.18		157.53	Stout and Robie (1963)
	-2166		-2331		Calculated (see text) from Graf and Goldsmith (1956)
	-2121.9				Naumov <i>et al.</i> (1974)
	-2162.35	154.89	-2325.25		Berman (1988)
	-2161.7 ± 1.1		-2324.5 ± 1.1		Hemingway and Robie (1994)
	-2163.4				Wagman <i>et al.</i> (1982)
	-2166.31	155.2	-2328.9	157.32	Johnson <i>et al.</i> (1992) from Helgeson <i>et al.</i> (1978)
	-2161.3	155.2	-2324.5	157.51	Values given in Robie and Hemingway (1995)
			-2332 ± 3		Chai and Navrotsky (1993)
	-2161.51	156.0	-2324.56		Holland and Powell (1990)
-2147.82 ± 2.2				Rock <i>et al.</i> (2001)	
Aqueous species	$\Delta_f G_{298.15}^{\circ}$ (kJ/mol)	$S_{298.15}^{\circ}$ (J/mol/K)	$\Delta_f H_{298.15}^{\circ}$ (kJ/mol)	C_p° _{298.15} (J/mol/K)	Reference
Mg ²⁺	-454.0	-138.1	-466.0	-22.3	Shock and Helgeson (1988) / Shock <i>et al.</i> (1997)
Ca ²⁺	-552.79	-56.48	-543.083	-30.96	Shock and Helgeson (1988) / Shock <i>et al.</i> (1997)
CO ₃ ²⁻	-527.98	-50.00	-675.24	-289.53	Shock and Helgeson (1988)

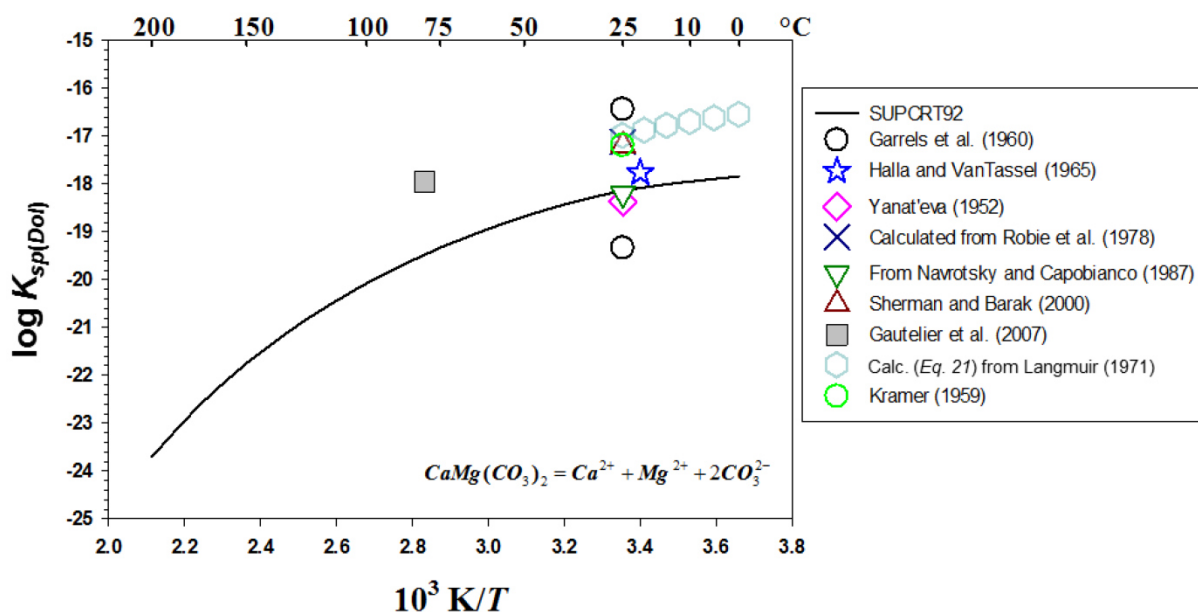


Figure 22: Summary of dolomite solubility product constants reported in the literature as a function of reciprocal absolute temperature.

Note that with the exception of the value reported by Gautelier *et al.* (2007) at 80 °C, a value about 1.5 log unit higher than the one derived from the SUPCRT92 (see *Figure 22* and *Table 10*), no dolomite solubility products have been reported for temperatures greater than 25 °C. Like for magnesite (see Bénézech *et al.*, 2011), the existing discordance at 25 °C about dolomite solubility, including its possible incongruent dissolution (see below), may have led to the belief that a reliable determination of its solubility product by classical solubility experiments, is almost impossible at higher temperatures.

Also shown in *Figure 22* are dolomite solubility products calculated using the equation provided by Langmuir (1971), which assumes that the heat capacity $\Delta_r C_{p,298.15}^{\circ}$ of *Reaction (21)* is constant below 25 °C and equals to 937.843 J/mol/K calculated from corresponding heat capacities ($C_{p,298.15}^{\circ}$) of the ions at 25 °C as reported by Criss and Coble (1964) and the dolomite heat capacity reported by Stout and Robie (1963). The latter value is

reported in *Table 11* along with other dolomite thermodynamic data from various literature sources. Stout and Robie (1963) determined the standard heat capacity from low temperature heat capacity measurements from which the entropy of dolomite has been derived as reported in *Table 11*. Based on the analysis of the data reported by Graf and Goldschmidt (1956) for the reaction:



Stout and Robie (1963) also recommended values for the enthalpy and free energy of *Reaction (24)* at 25 °C equal to 12.3 and 11.3 kJ/mol, respectively.

Combining these values with those for the Gibbs free energy and enthalpy of formation of calcite and magnesite from Robie and Hemingway (1995) and Bénézech *et al.*, (2011), respectively, yields values of dolomite Gibbs free energy and enthalpy of formation equal to -2166 and -2331 kJ/mol at 25 °C, respectively (*Table 11*). Subsequently, a $\log_{10} K_{sp(Dol)}$ value of -18.2 can be derived using $\text{Ca}^{2+}_{(aq)}$, $\text{Mg}^{2+}_{(aq)}$ and $\text{CO}_3^{2-}_{(aq)}$ standard partial molal Gibbs free energy of formation from SUPCRT92. Krupka *et al.* (1985) measured the heat capacity of dolomite at high temperature by differential scanning calorimetry (DSC) and combined this value with existing low temperature heat capacity reported by Stout and Robie (1963) and the high temperature relative enthalpy ($H^\circ_T - H^\circ_{298}$) reported by Southard (1941) and White (1919) to generate the heat capacity of dolomite as a function of absolute temperature:

$$C_p^\circ(298-650) = 547.88 - 0.16759 \times T + 2.840 \times 10^{-6} \times T^2 - 6547.9 \times T^{-0.5} + 7.7076 \times 10^{-5} \times T^2,$$

where C_p° is in units of J/mol/K. This equation yields a $C_p^\circ_{298.15}$ value of 157.51 J/mol/K. Hemingway and Robie (1994) reported a value of the enthalpy of formation of dolomite determined by HCl solution calorimetry at 25 °C (2324.5 ± 1.1 kJ/mol) acknowledging some problems that occurred during the experiments such as liberation of CO₂ in the calorimeter and a questionable degree of crystallinity of the reference materials, which was assumed to be

identical with the solid used to determine the enthalpies of formation. Moreover, using molten oxide drop solution calorimetry at 704 °C, Chai and Navrotsky (1993) determined the enthalpy of dolomite formation reaction from calcite and magnesite (-11.1 kJ/mol), which is in excellent agreement (-11.5 kJ/mol) with their previous measurements using acid brine solution calorimetry at 85 °C (Navrotsky and Capobianco, 1987). If these values are in good agreement with Graf and Goldsmith (1956) and Helgeson *et al.* (1978) (-10.2 kJ/mol), they are significantly different from that of Robie *et al.* (1978) (-3.8 kJ/mol) calculated using the values of the enthalpy of formation of dolomite (-2324.48 kJ/mol) from calcite (-1207.37 kJ/mol) and magnesite (-1113.28 kJ/mol), reported by these authors. According to Chai and Navrotsky (1993), the discrepancy between high temperature calorimetry and phase equilibrium experiments can be due to a difference in ordering state of the materials used in each study. The value of -2332 kJ/mol assigned to Chai and Navrotsky (1993) in *Table 11* has been calculated using various thermodynamic values and sources as in the case of the Graf and Goldsmith (1956) and Stout and Robie (1963) calculated data explained above.

Initial non-stoichiometric release of calcium and magnesium has been reported in many dolomite dissolution experiments with a molar Ca/Mg ratio in solution ranging between 2 and 6 (Pokrovsky and Schott, 2001; Pokrovsky *et al.*, 2005; Zhang *et al.*, 2007; Debure *et al.*, 2013). The lower hydration energy of Ca^{2+} and the much higher rate of exchange of water molecules in its hydration sphere compared to Mg^{2+} and the lower stability of Ca^{2+} at the water-dolomite interface could explain this preferential calcium release (Plummer and Busenberg, 1982; Pokrovsky and Schott, 2001; Zhang *et al.*, 2007; Schott *et al.*, 2009).

5.3 Materials and methods

5.3.1 Dolomite sample

Dolomite crystals from Sainte Colombe (Aude, France; hydrothermal origin) were hand crushed with mortar and pestle, dry sieved, and ultrasonically cleaned in pure ethanol to obtain a 50 to 100 μm size fraction. A magnetic separation of the resulting material was performed to remove minor amounts of magnetite. Scanning electron microscope (SEM) images, obtained using a JEOL JSM-6360 LV microscope, of the resulting dolomite are shown in *Figure 23*. The image shows that the powder consists only of dolomite without any adhering fine particles. The specific surface area of the prepared dolomite was determined to be $0.080 \text{ m}^2/\text{g} \pm 10 \%$ by multipoint krypton adsorption according to the BET method (Brunauer *et al.*, 1938) using a Quantachrome Gas Sorption system.

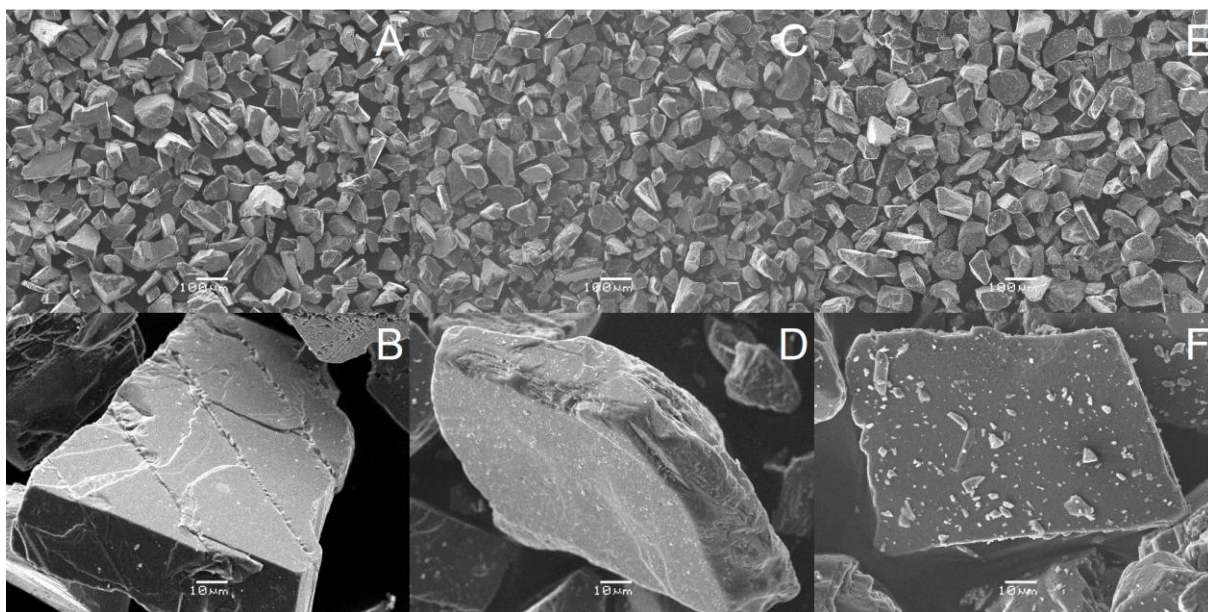


Figure 23: Scanning electron micrographs of (A, B) the initial Sainte Colombe dolomite seed material, (C,D) this material after its use in dissolution experimental series 3, and (E, F) this material after its use in the dissolution-reprecipitation experimental series 5.

The mineralogical composition of the dolomite seed material was determined by electron microprobe analysis using a CAMECA SXfive and is reported in *Table 12*. The purity of this dolomite was verified via x-ray diffraction using an INEL CPS-120 diffractometer with Co K α -radiation, $\lambda = 1.78897 \text{ \AA}$, and a graphite monochromator. Scans were performed from 1 to 110° 2 θ at 0.09°/min and a step size of 0.029°. This analysis demonstrated the cation ordered structure of this dolomite.

Table 12: Chemical composition of the initial Sainte Colombe dolomite seeds before the experiments and after selected experimental series.

	Initial Sainte Colombe dolomite seeds	Dolomite recovered from experimental series 2	Dolomite recovered from experimental series 5
CaO	34.35	34.40	34.60
MgO	22.72	22.86	23.00
FeO	0.0122	0.0101	0.0126
MnO	0.0075	0.0088	0.0090
TiO₂	0.0092	0.0071	0.0083
Cr₂O₃	0.0026	0.0039	0.0053
Al₂O₃	0.0033	0.0070	0.0061
SiO₂	0.0122	0.0064	0.0040
Na₂O	0.0037	0.0063	0.0051
K₂O	0.0017	0.0034	0.0034
calculated CO₂	42.89	42.69	42.35
chem. formula	Ca _{1.04} Mg _{0.96} (CO ₃) ₂	Ca _{1.04} Mg _{0.96} (CO ₃) ₂	Ca _{1.04} Mg _{0.96} (CO ₃) ₂

5.3.2 Hydrogen electrode concentration cell (HECC)

Dolomite solubility was measured from 50 to 175 °C in 0.1 molal NaCl solutions using a hydrogen electrode concentration cell (HECC) following previous studies on carbonate

stability measurements (Bénézeth *et al.*, 2007, 2009 and 2011). This cell is unique in its ability to measure the pH *in-situ* at a very high precision and at temperatures up to ~ 290 °C, a crucial parameter to define carbonate speciation and thus its solubility constants. Additionally the cell design avoids any potential for the fluid to be in contact and equilibrate with atmospheric CO₂.

Experiments in this study were performed in several series on a single dolomite seed material. Each series was initiated by placing the initial fluid, with a starting $\text{pH}_m = -\log_{10} [\text{H}^+]$ of ~ 3, and ~ 3 g of the initial dolomite seeds into the cell. These series are noted by a distinct prefix and are listed in *Table 13* with their corresponding equilibration temperatures. For all experiments carried out in this study, the same stoichiometric molal compositions (in mol/kg) of the starting reference and test solutions has been used, that is 2.5001 x 10⁻³ molal HCl and 0.0975 molal NaCl. In each run, once the cell attained thermal equilibrium, solution samples were withdrawn from the test solution over time. During each sampling approximately 5 mL of test solution was withdrawn via an Hastelloy valve through a platinum dip tube provided at its bottom with a porous Teflon frit (3 µm), and then through a polyvinylidene Acrodisc LC13 with a 0.2 µm mesh size. Fractions of each fluid sample were devoted to analysis of dissolved magnesium and calcium, as well as to determine the total dissolved inorganic carbon (TDIC). Steady-state fluid compositions were attained within few weeks (at temperature ≥ 100 °C); nevertheless samples were taken during longer time intervals to verify attainment of equilibrium (see *Table 13*). The cell temperature was subsequently decreased allowing the system to again approach equilibrium from undersaturation. During the course of some experimental runs (5 and 6), the temperature was raised (from 100 to 150 °C and from 125 to 175 °C, respectively) allowing the system to approach equilibrium from oversaturation.

Table 13: Results of dolomite solubility experiments performed in NaCl media using the HECC.

Experiment	Temp (°C)	$-\log[\text{H}^+]^{\text{a}}$ measured <i>in-situ</i>	$\log[\text{Mg}^{2+}]^{\text{a}}$	$\log[\text{Ca}^{2+}]^{\text{a}}$	$[\text{TDIC}]^{\text{a}}$ $\times 10^3$	$[\text{CO}_3^{2-}]^{\text{a}}$ $\times 10^7$	Equilibrium time (hours)
2.1	100.8	7.024	-3.042	-2.932	1.430	37.67	744
2.2*	125.7	6.641	-3.128	-2.951	0.946	8.124	936
2.3*	150.8	6.107	-3.219	-2.926	0.763	0.829	720
2.4**	101.4	6.258	-3.051	-2.842	1.750	5.161	624
3.1	175.5	6.443	-3.189	-3.025	0.658	1.674	281
3.2	148.6	6.460	-3.141	-2.999	0.755	2.996	498
3.3	125.1	6.532	-3.078	-2.971	1.061	6.578	427
3.4	99.8	6.666	-2.992	-2.942	1.454	14.76	664
3.5	75.9	6.845	-2.925	-2.885	2.044	32.35	760
3.6	50.6	7.197	-2.814	-2.818	2.957	92.44	1128
4	174.6	6.537	-3.212	-3.026	0.525	1.908	144
5.1	152.1	6.416	-3.145	-3.007	1.072	3.508	384
5.2	100.5	6.626	-2.964	-2.878	2.225	20.20	528
5.3*	152.2	6.260	-3.127	-3.013	0.984	1.849	432
6.1	124.7	6.721	-3.134	-2.999	0.781	8.468	1320
6.2*	175.1	6.425	-3.237	-3.029	0.413	0.997	300
6.3**	125.0	6.583	-3.176	-2.984	0.691	4.994	227
6.4	74.7	7.001	-3.013	-2.879	1.632	38.23	656
6.5	50.6	7.253	-2.774	-2.991	2.522	89.93	1169

^a Measured molal concentrations in the experimental solutions.

* Increasing temperature, approaching equilibrium from supersaturation.

** Re-decreasing temperature.

In *italic*: a run that did not behave correctly, not included in the fit.

5.3.3 Fluid analyses

Fluid samples were analyzed for magnesium, calcium, and total dissolved inorganic carbon (TDIC). Magnesium and calcium were analyzed using a Perkin Elmer AAnalyst 400 Atomic Absorption Spectrometer (AAS) with an uncertainty of $\pm 2\%$ and a detection limit of 1×10^{-7} and 2×10^{-7} mol/kg, respectively. These analyses were calibrated using magnesium

and calcium standard solutions having concentrations of 0.1 to 0.6 ppm and 0.5 to 5 ppm, respectively; the standard solutions were prepared with the same matrixes as the experiments.

TDIC was analyzed using a LI-820 (LICOR Inc.) non dispersive infrared (NDIR) CO₂ gas analyzer. This method is based on the measurement of the IR energy absorbed by the CO₂ extracted from a sample by acidification along an optical path, with respect to a reference signal (see Bénézeth *et al.*, 2011 for the details of the technique). The TDIC concentration is calculated using calibration curves obtained by analyzing standard solutions prepared from dried reagent grade Na₂CO₃ and NaHCO₃. Combining this TDIC with *in-situ* pH measurements allows the calculation of the aqueous carbonate speciation at the temperature of the experiment using the apparent dissociation constants (*D*) of the following reactions:



and



at the ionic strength of interest, in the present case 0.1 molal NaCl. The values of *D* for *Reactions* (25) and (26) were taken from Patterson *et al.* (1982 and 1984, respectively). The uncertainty of the TDIC analyses in this study is generally lower than 5 % with a detection limit of 10⁻⁵ mol/kg using an optical bench of 14 cm.

The standard state adopted in this study for thermodynamic calculations is that of unit activity for pure minerals and H₂O at any temperature and pressure. For aqueous species other than H₂O, the standard state is unit activity of the species in a hypothetical 1 molal solution referenced to infinite dilution at any temperature and pressure.

5.3.4 Solid analyses after experimental runs

Solids retrieved after the experimental runs were investigated by several analytical techniques. X-ray diffraction - using the above described INEL CPS-120 diffractometer - was applied to verify the purity of all experimental products. No changes concerning the degree of cation ordering of the dolomite seeds were detected. Precipitation on these seeds was too little to have any influence on the diffraction pattern. Scanning electron microscopy using a JEOL JSM-6360 LV microscope was used to visually investigate changes in surface appearance due to dissolution and/or precipitation processes. Changes concerning the mineralogical composition of the dolomite seed material were tracked by electron microprobe analysis using a CAMECA SXfive (*Table 12*). Exclusive investigations of the composition and structure of precipitated material on top of the seed material were performed using x-ray photoelectron spectroscopy (XPS). These experiments were performed with a Kratos AXIS UltraDLD fitted with a monochromatic Al K α -radiation source (with a power 150 W) and a charge neutralizer system. Pass energies of 160 eV for wide spectra and 20 eV for high resolution spectra were used, and the same acquisition time was used for all samples. The analysis area was 700 x 300 μm . We used the CasaXPS software and its associated relative sensitivity factor library for analysis of the data. The binding energy calibration was done using the C 1s peak fix at 285 eV.

5.4 Experimental results

5.4.1 Determination of dolomite solubility product

Solubility measurements were performed in experimental series. A representative temporal evolution of such a series is depicted in *Figure 24* showing the continuous dissolution from 175 down to 50 °C of the experimental series 3. Initial higher aqueous calcium concentrations compared to aqueous magnesium is observed for this experimental series. Similarly, all experiments in this study show reactive fluid compositions with aqueous calcium to magnesium ratios > 1 and are never reflecting exactly dolomitic stoichiometry at the initial experimental leg. This initial incongruent dolomite dissolution most likely stems from a preferential release of Ca^{2+} due to the faster aquo-ion exchange rate of calcium than magnesium (Pokrovsky and Schott, 2002; Schott *et al.*, 2009). The only experiment mirroring dolomite stoichiometry in the aqueous phase is experiment 3.6 at 50 °C (*Figure 24*). During the continuous dissolution of experimental series 3 by stepwise reduction of the temperature a small but steady development towards dolomitic stoichiometry is observed. The fluid stoichiometry is also developed with respect to the carbonate concentration. As for all other experiments in this study the carbonate concentration in the fluid phase stayed below the divalent cation concentrations but only reached unity with molal calcium to magnesium ratios at 50 °C in experiment 3.6. Note that fluid stoichiometry stayed rather constant during the several hundreds of hours lasting equilibrium times (*Table 13*).

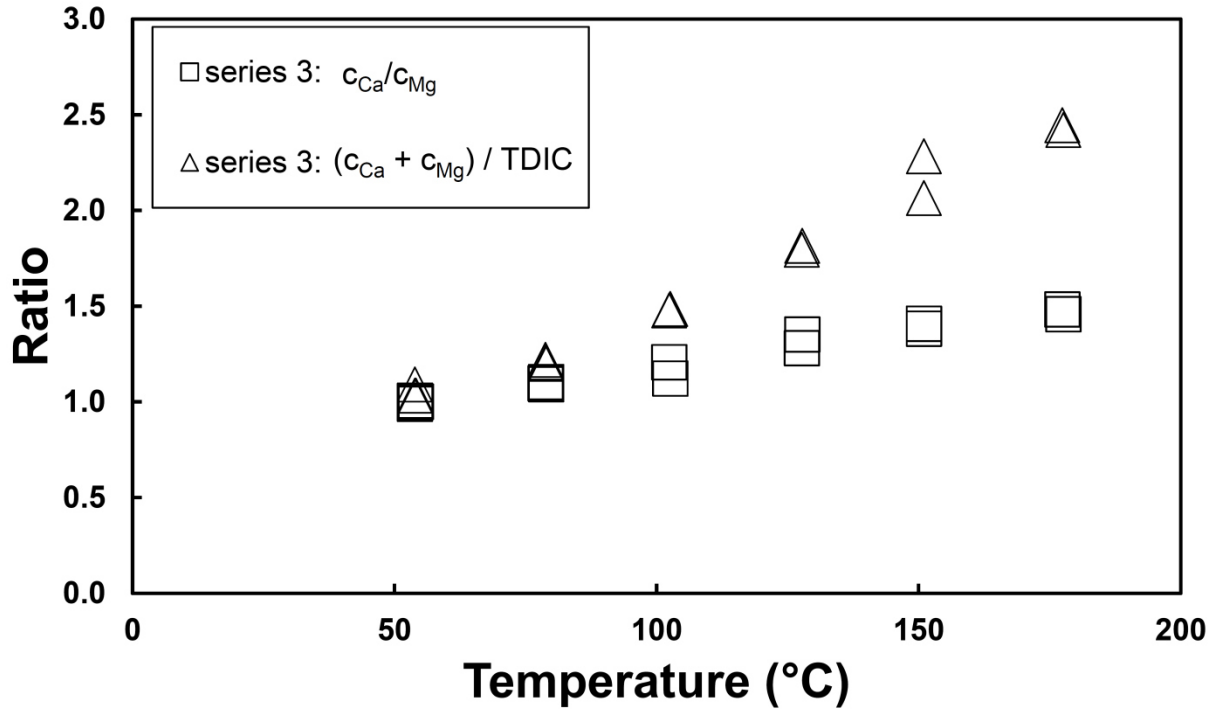


Figure 24: Evolution of reactive fluid stoichiometry for experiment series 3 as a function of temperature. Note that the experiment started at 175 °C and was then cooled by 25 °C stepwise.

The results of the solubility experiments performed in the HECC are summarized in *Table 13* showing for each experiment the measured temperature, measured *in-situ* pH_m , the logarithm of the magnesium and calcium concentrations, the values of TDIC obtained from NDIR analysis, and the corresponding calculated aqueous CO_3^{2-} concentrations. The apparent solubility products for *Reaction (21)*, defined as $Q_{sp(Dol)} = [Mg^{2+}] \cdot [Ca^{2+}] \cdot [CO_3^{2-}]^2$, are reported as their logarithms in *Table 14* with the corresponding ionic strength I . The ionic strength and the carbonate speciation were calculated iteratively from the measured pH_m , total magnesium, total calcium, and TDIC concentrations reported in *Table 13*.

The solubility product (at infinite dilution), $K_{sp(Dol)}$, can then be expressed as:

$$K_{sp(Dol)} = Q_{sp(Dol)} (\gamma_{Mg^{2+}}) (\gamma_{Ca^{2+}}) (\gamma_{CO_3^{2-}})^2 \quad (27)$$

where γ_i defines the activity coefficient of the i^{th} aqueous species.

The γ_i values were derived from the value of NaCl mean stoichiometric activity coefficient at the same ionic strength using $\gamma_I = \gamma_{\pm(\text{NaCl})}^{z^2}$. The values of $\gamma_{\pm(\text{NaCl})}^{z^2}$ calculated from Archer (1992), are reported in *Table 14* together with the ionic strength and the calculated dolomite solubility product at infinite dilution ($K_{sp(\text{Dol})}$).

Table 14: Dolomite apparent solubility products, $Q_{sp(\text{Dol})}$, at $I \approx 0.1$ molal NaCl, ionic strengths, I , activity coefficients, $\gamma_{\pm(\text{NaCl})}$, and dolomite solubility products, $K_{sp(\text{Dol})}$, calculated for all experiments performed in this study.

Experiment	Temp (°C)	$\log_{10} Q_{sp(\text{Dol})}$	I (mol/kg)	$\gamma_{\pm(\text{NaCl})}$	$\log_{10} K_{sp(\text{Dol})}^a$
2.1	100.8	-16.82	0.1038	0.7430	-18.89 ± 0.3
2.2*	125.7	-18.26	0.1036	0.7278	-20.47 ± 0.3
2.3*	150.8	-20.31	0.1035	0.7091	-22.69 ± 0.3
2.4	101.4	-18.47	0.1046	0.7420	-20.54 ± 0.3
3.1	175.5	-19.77	0.1019	0.6895	-22.35 ± 0.3
3.2	148.6	-19.19	0.1030	0.7114	-21.55 ± 0.3
3.3	125.2	-18.41	0.1034	0.7099	-20.62 ± 0.3
3.4	99.8	-17.60	0.1041	0.7436	-19.66 ± 0.3
3.5	75.9	-16.79	0.1051	0.7555	-18.74 ± 0.4
3.6	50.6	-15.70	0.1067	0.7654	-17.56 ± 0.4
4	174.6	-19.68	0.1025	0.6898	-22.26 ± 0.3
5.1	152.1	-19.06	0.1029	0.7086	-21.46 ± 0.3
5.2	100.5	-17.23	0.1048	0.7426	-19.30 ± 0.3
5.3*	152.2	-19.61	0.1031	0.7085	-22.00 ± 0.3
6.1	125.7	-18.28	0.1029	0.7287	-20.48 ± 0.3
6.2*	175.1	-20.27	0.1027	0.6891	-22.86 ± 0.3
6.3	125.0	-18.76	0.1029	0.7284	-20.96 ± 0.3
6.4	74.7	-16.73	0.1045	0.7573	-18.66 ± 0.4
6.5	50.6	-15.86	0.1056	0.7648	-17.72 ± 0.4

^a Uncertainties estimated from the combined experimental uncertainties.

* Equilibrium approached from supersaturation.

In *italic*: a run that did not behave correctly, not included in the fit.

The logarithms of the solubility products listed in *Table 14* are shown in *Figure 25* as a function of reciprocal temperature. Note that all solubilities determined during experimental series 3 which are shown as pink triangles in *Figure 25* were approached only from undersaturation, by first starting at 175 °C and then decreasing the temperature successively to 50 °C. This experimental series took 6 months to be completed. Experimental series 4 was performed only at 175 °C; the solubilities obtained in this series are shown as blue triangles in *Figure 25*. The first two experiments in series 5 determined dolomite solubilities at 150 and 100 °C from undersaturation; these solubilities are shown as green circles in *Figure 25*. Once steady-state was attained at 100 °C, the temperature was raised back to 150 °C, allowing the approach of equilibrium from supersaturation. Steady-state was achieved in 18 days in this experiment noted as experiment 5.3 in *Tables 13* and *14* and shown as a green circle/hourglass symbol in *Figure 25*. The close match between the measured solubilities obtained at 150 °C from both under- and supersaturated conditions might indicate that the reversibility of equilibrium was achieved in this experimental series, even though the $\log_{10} K_{sp(Dol)}$ obtained from supersaturated solution is slightly lower than that acquired from undersaturated solutions in experiments 5.1 and 3.2.

The results of experimental series 6 are shown as cyan squares in *Figure 25*. Experiment 6.1 approached equilibrium from undersaturation at 125 °C and matches nicely with the obtained $\log_{10} K_{sp(Dol)}$ from experiment 3.3 at 125 °C. Afterwards, experiment 6.2 was approaching equilibrium from supersaturation conditions at 175 °C. As for experiment 5.3, the $\log_{10} K_{sp(Dol)}$ obtained from experiment 6.2 is ~ 0.5 log units lower than that obtained by approaching equilibrium from undersaturation. This again might indicate a successfully reversed equilibrium at 175 °C. The $\log_{10} K_{sp(Dol)}$ obtained afterwards from undersaturation by decreasing the temperature from 175 back to 125 °C (step 6.2 to 6.3) is 0.34 and 0.48 lower than those obtained from undersaturation for experiments 6.1 and 3.3, respectively. Note these

lower $\log_{10} K_{sp(Dol)}$ values suggest that the dolomite, which precipitated during the supersaturated experiments, is more stable than the initial dolomite being dissolved during the undersaturated experiments.

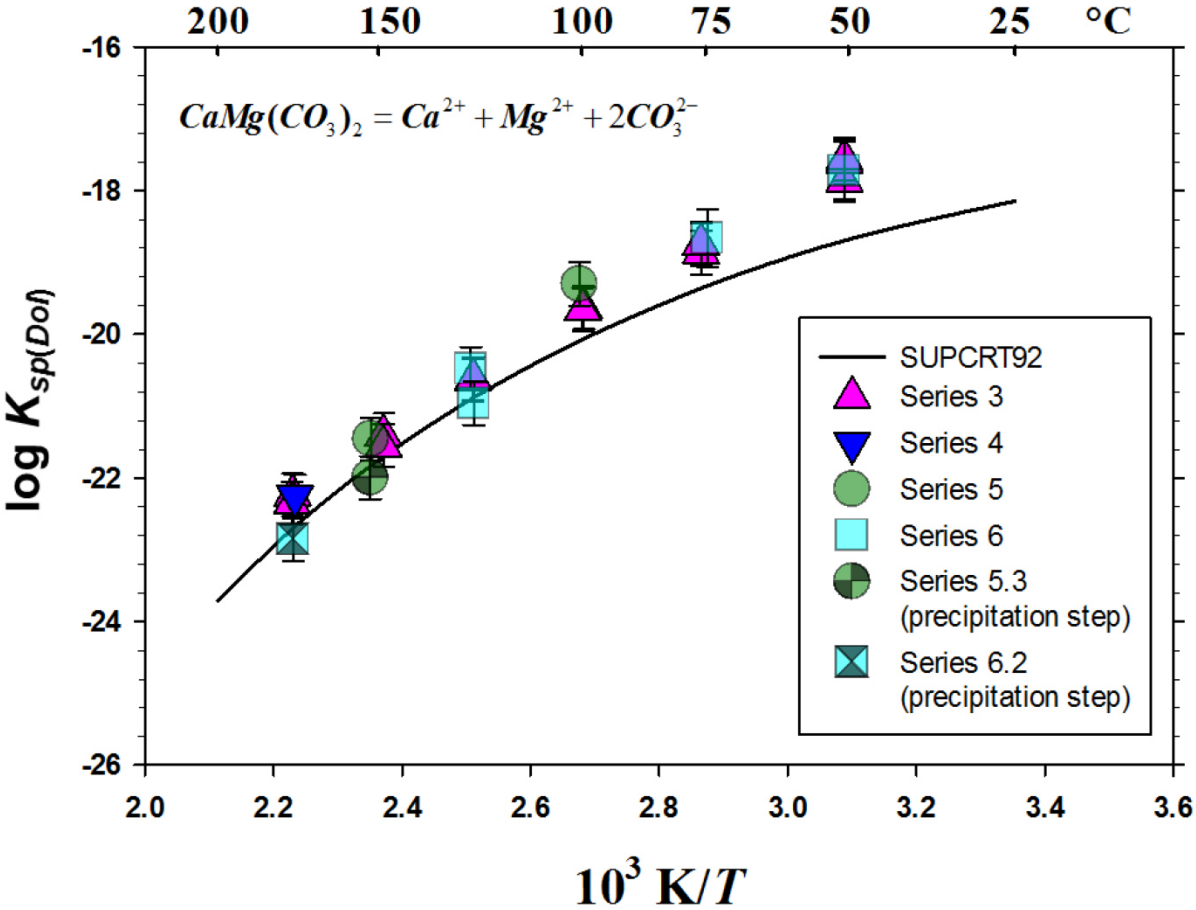


Figure 25: Values of dolomite solubility product obtained in this study plotted as a function of the reciprocal absolute temperature.

The composition of the dolomite precipitated during the experiments can be deduced from the temporal evolution of the reactive fluid composition. *Figure 26* shows the temporal evolution of TDIC and aqueous calcium and magnesium for experimental series 5. Note that the concentration of aqueous calcium is always higher than aqueous magnesium, but the concentration difference between both aqueous cations always stays rather constant during dissolution and precipitation. This demonstrates that a calcium to magnesium ratio close to

unity should be expected within the precipitated phase after the performed temperature jump. Similarly, the amount of TDIC which was released during the initial dissolution from 150 to 100 °C decreased back to its former concentration during the reprecipitation from 100 to 150 °C. These observations are consistent with stoichiometric dissolution and reprecipitation of dolomite during the experimental series.

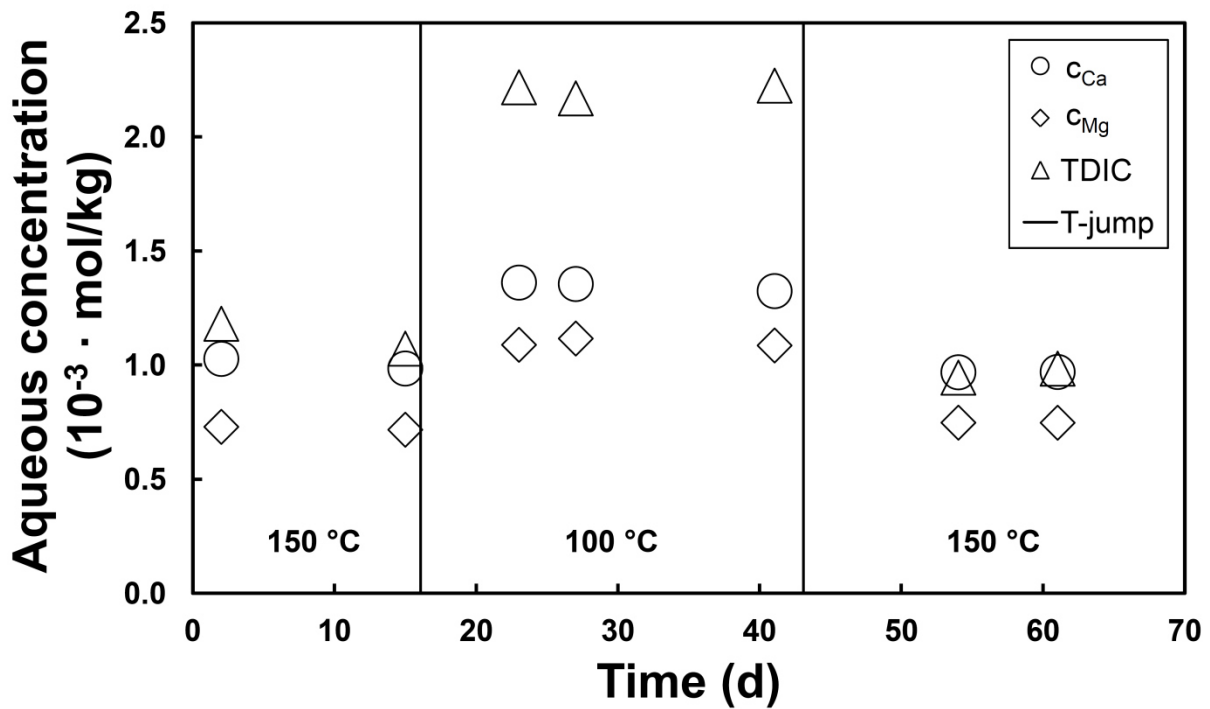


Figure 26: Temporal evolution of TDIC and aqueous calcium and magnesium concentration of experimental series 5. Uncertainties of the concentration measurements are within the size of the symbols. Note that the reactor temperature was first decreased from 150 to 100 °C (step 5.1 to 5.2 in *Tables 13* and *14*) and then increased back to 150 °C (step 5.2 to 5.3 in *Tables 13* and *14*) provoking dolomite precipitation.

5.4.2 Solid phase analyses on retrieved material after the experiments

Analyses performed on the solids recovered after all of the experimental series show that these samples are free of all carbonate phases other than of dolomitic composition. Electron

microprobe analyses performed on the solids recovered after experimental series 2 and 5 (dissolution and reprecipitation, respectively) show these to have an identical composition to that of the initial dolomite powder (see *Table 12*). Calculated growth layer thickness during the temperature jump between experiments 5.2 and 5.3 ranges between 8 and 20 nm using either the initial BET surface area or a simplified geometrical approach, respectively. The latter approach assumed the dolomite seeds to consist of cubes with an average diameter of 75 μm . For such a growth layer thickness electron microprobe should provide reliable results. X-ray diffraction (XRD) analysis of the solids recovered from series 5 revealed the presence of traces of phyllosilicates (muscovite and chlorite), a contamination which wasn't detected in the initial seed material. The presence of trace muscovite was also detected by energy-dispersive x-ray (EDX) spectroscopy in the solids recovered from experimental series 2. The presence of these trace impurities, however, has negligible influence on the solubility product constants measured in this study.

Scanning electron micrographs taken of the solids recovered after series 3 reveals some dissolution features including rounded grain edges (compare *Figures 23A* and *23B* with *23C* and *23D*). The quenched solid retrieved directly after experimental series 5 exhibits mineral growth on the dolomite seed material surfaces (see *Figures 23E* and *23F*). Electron backscattering verifies that these precipitates have the same chemical composition as the dolomite seed material (*Figure 27A*). However, high resolution scanning electron micrographs show that these precipitates lack a clear rhombohedral morphology even though they are intergrown with the seed crystal surfaces (*Figure 27B*).

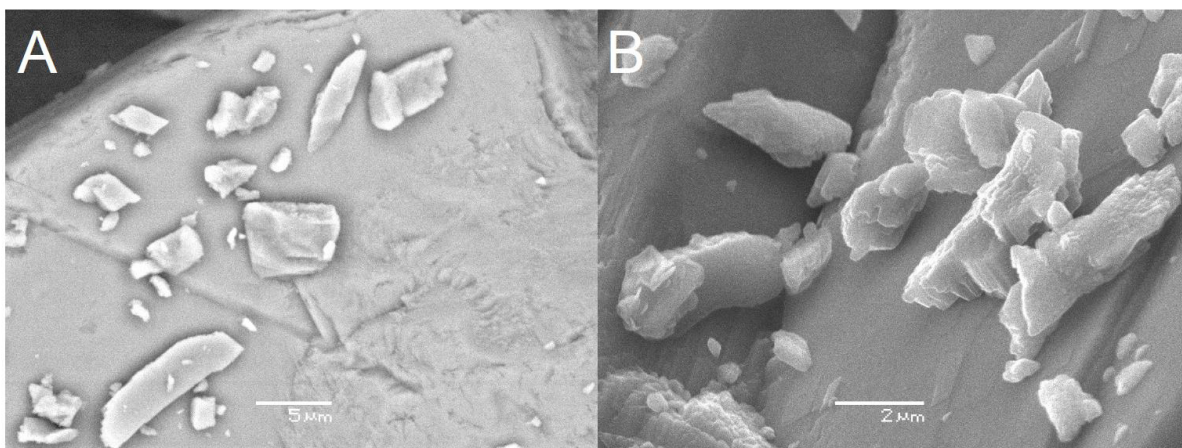


Figure 27: Scanning electron micrographs of the quenched sample after reprecipitation experiment 5.3 showing precipitates on the Sainte Colombe dolomite (A, B). Backscattered electron micrographs verify the identical chemical composition of the precipitates and the substrate (A). High magnification of these precipitates shows that they are intergrown with the substrate but do not show obvious rhombohedral morphologies (B).

To further investigate the surfaces of the dolomite samples x-ray photoelectron spectroscopy (XPS) analyses were performed on pristine Sainte Colombe dolomite powder, a synthetic Ca-rich protodolomite powder for comparison, and on the recovered solids from experimental series 5 and 6. The XPS analyses were performed with a $700 \times 300 \mu\text{m}$ spot size thus averaging the analysis over several grains. Atomic percentages at the outermost surface (*i.e.*, to $\sim 100 \text{ \AA}$ depth) derived from these measurements (*Table 15*) are in very good agreement with ion probe analysis revealing a calcium to magnesium ratio between 0.97 and 1.11 for both the solids recovered after series 5 and 6, respectively. However, one can observe a significant difference in the intensity ratios of the Mg 1s to Mg 2s peaks between the initial dolomite and the solids obtained from series 5 and to a lesser degree also from series 6. These ratios are 4.43, 5.93, and 5.27, respectively (see *Table 15*). Due to the lower kinetic energy of Mg 1s ($\sim 180 \text{ eV}$) compared to Mg 2s ($\sim 1400 \text{ eV}$) photoelectrons, Mg 1s photoelectrons are

less likely to escape from deeper regions of the solid than Mg 2s photoelectrons. Hence, the observed differences in these ratios could either mean a depletion of Mg²⁺ in the lower regions of the precipitated layer of series 5 and 6, an enrichment of Mg²⁺ in the uppermost layer, and/or a combination of both. Note that both series 5 and 6 solids underwent a precipitation leg but unlike series 5 the outermost surfaces of series 6 solids should be dissolution dominated.

Table 15: Atomic percentages from high resolution XPS.

	C (CO ₃)	C (adv. C)	Mg 2s	Ca 2p	O 1s	Ca/Mg	Mg 1s / Mg 2s
Initial dolomite	16.5	15.2	9.2	9.2	44.0	1.00	4.43
Post series 5	16.3	13.0	9.5	9.2	46.1	0.97	5.93
Post series 6						1.11	5.27
Protodolomite reference	18.4	4.0	14.2	8.1	50.0	0.57	5.89

Adv. C is organic carbon that we call adventitious carbon, which is carbon ‘contamination’ from air or solution, this value is normal. C (CO₃) is carbon from carbonate.

Significant differences are also evident in the binding energies (BE) and the full width half maximum (FWHM) values of C 1s, O 1s, Ca 2p_{3/2}, and Mg 2s photoemission peaks between the unreacted dolomite surface and the samples recovered after series 5 and again to a lesser degree of post series 6 solids (see *Table 16*). The binding energies of atoms present at the surface of the solids recovered after series 5 are slightly but systematically shifted to higher values indicating a distinct chemical environment and are similar to what is observed for protodolomite. The significantly higher FWHM values suggest that magnesium and calcium atoms are more randomly distributed and have an increased coordination in the solids recovered after series 5 compared to the initial dolomite.

Table 16: Binding energy (BE in eV) and full width half maximum (FWHM in eV) for C in CO₃, O in CO₃, Ca, and Mg.

	C 1s (CO ₃)		O 1s (CO ₃)		Ca 2p _{3/2}		Mg 2s	
	BE	FWHM	BE	FWHM	BE	FWHM	BE	FWHM
Initial dolomite	289.8	1.27	531.6	1.44	347.3	1.32	89.00	1.67
Post series 5	290.2	1.68	531.9	1.66	347.6	1.68	89.30	1.91
Post series 6	290.0	1.27			347.3	1.38	89.15	1.80
Proto-dolomite reference	290.3	1.60	532.1	1.74	347.6	1.70	89.60	2.12

XPS measurements revealed additional differences between the initial Sainte Colombe dolomite and the post series 5 samples, which were recovered directly after the precipitation leg. In contrast to the initial dolomite, the surfaces of the post series 5 solids were prone to increasing x-ray damage with increasing exposure time exemplified by the development of secondary Mg 2s peaks at higher binding energies and their increasing intensity with increasing x-ray exposure time. This increased fragility in response to x-ray exposure of the post series 5 samples may indicate some sort of lattice misfits of the grown phase.

A model explaining the nature and inner structure of the precipitated and quenched phase of experiment 5.3 would need to include 1) the overall stoichiometric decrease of aqueous calcium and magnesium concentration during the temperature jump between experiments 5.2 and 5.3, 2) the dolomitic composition (Ca/Mg = 0.97) of the overgrowths determined by XPS, 3) the XPS results demonstrating an enrichment of Mg²⁺ in the uppermost growth layer and/or a depletion of Mg²⁺ below, and 4) the lower apparent equilibrium constant determined during experiment 5.3. An initial precipitation layer enriched in Ca²⁺ followed by a slightly less reactive and possibly less soluble growth layer enriched in Mg²⁺ could satisfy these requirements. The initially faster adsorption of Ca²⁺ is supported by the higher water-exchange

rate of aqueous calcium compared to aqueous magnesium (Pokrovsky and Schott, 2002; Schott *et al.*, 2009). Experimental evidence for the enrichment of Ca^{2+} directly at the (104) dolomite cleavage surface after precipitation experiments at 25 °C, having equal Ca^{2+} and Mg^{2+} aqueous solution activities, was given by Hu *et al.* (2006) using XPS. Previous experiments with similar solution compositions performed with atomic force microscopy proved this growth to consist of only one atomic layer (Hu *et al.*, 2005). Berninger *et al.* (2016) demonstrated a strong preferential incorporation of aqueous calcium into magnesite at 100 °C indicating that this preferential uptake is not reduced at elevated temperatures in aqueous and mineralogical environments similar to our experimental conditions. According to this reasoning, the precipitation at 150 °C in experiment 5.3 would start with an initial enrichment of Ca^{2+} at the reprecipitate-dolomite interface followed by a growth successively depleted with respect to Ca^{2+} developing an overall dolomitic composition. The Mg-enriched outer rim of this growth layer might explain the determined lower apparent solubility of the re-precipitated dolomite.

This model is also capable of explaining the observations of the slightly more complex experimental series 6. Similarly, the Mg-enriched outermost surface would explain the observed lower apparent solubility of experiment 6.2 and 6.3 after the precipitation leg. However, due to the additional re-dissolution lag (step 6.2 to 6.3) before the quenching a reduced Mg 1s to Mg 2s ratio compared to the post series 5 solids and an increased calcium to magnesium ratio of 1.11 is observed (*Table 15*).

5.4.3 Determination of dolomite thermodynamic properties

Of all the temperature functions tested, the simplest equation giving a reliable fit of our data has the form shown in *Equation (28)*:

$$\log_{10} K_{sp(Dol)} = a + b/T + cT \quad (28)$$

where T refers to absolute temperature and a , b , and c are regression coefficients of this polynomial equation, which yields:

$$\Delta G_r^{\circ} = -R \ln(10) \{ aT + b + cT^2 \} \quad (29)$$

which can be differentiated with respect to T to obtain enthalpy and heat capacity of *Reaction (21)*:

$$\Delta H_r^{\circ} = R \ln(10) \{-b + cT^2\} \quad (30)$$

$$\Delta C_{p,r}^{\circ} = 2 RT \ln(10) c \quad (31)$$

A first fit of the solubility product constants with their respective errors are reported in *Table 17*, where the parameters and thermodynamic values obtained from this regression are reported as well. This regression yielded the dashed blue curve in *Figure 28* from 25 to 200 °C. A second fit was made by fixing $\log_{10} K_{sp(Dol)}$ at 25 °C to -17.2, a value which was obtained experimentally by Sherman and Barak (2000). The result of this second fit is shown as a dashed green curve in *Figure 28*. A third fit was made by fixing the heat capacity of *Reaction (21)*: $\Delta_r C_p^{\circ}$ (-789.832 J/mol/K at 298.15 K) consistent with the dolomite heat capacity ($C_p^{\circ}_{298.15} = 157.51$ J/mol/K) reported by Robie and Hemingway (1995) (see *Table 11*) and allowing the calculation of the parameter c (-0.06919 1/K) from *Equation (31)*. This fit generates the red dashed curve shown in *Figure 28*. The parameters corresponding to these 3 fits are listed in *Table 17*, which can be used together with *Equations (29) to (31)* to obtain the thermodynamic properties of *Reaction (21)* at 25 °C. Combining these values with the thermodynamic properties for Mg^{2+} , Ca^{2+} , and CO_3^{2-} from Shock *et al.* (1997) (see

Table 11), we obtained the dolomite thermodynamic properties at 25 °C and 1 bar as listed in Table 17.

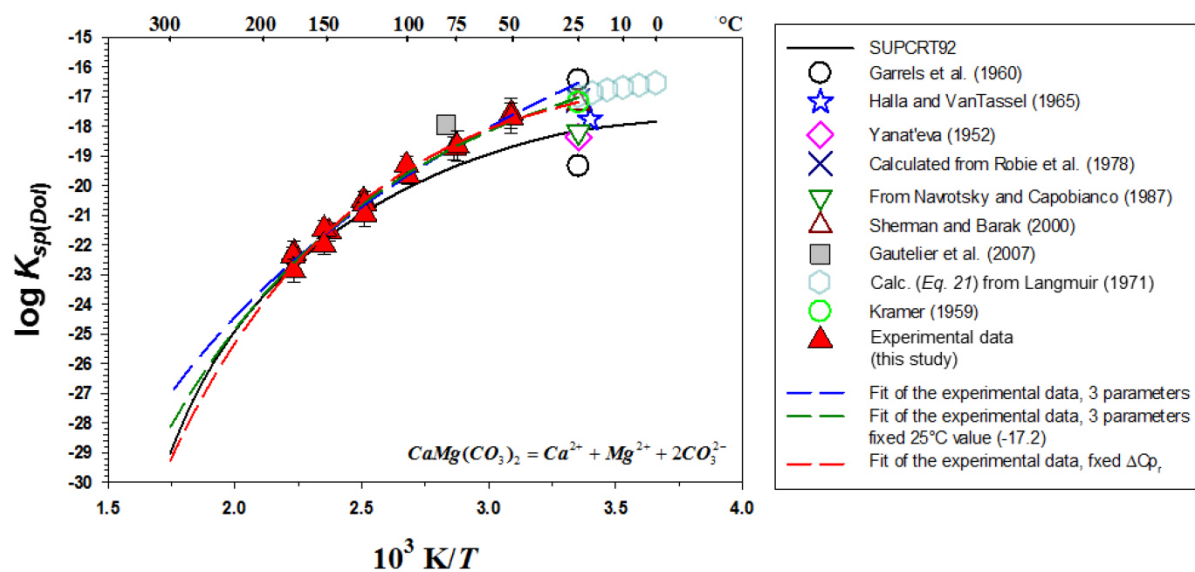


Figure 28: Summary of dolomite solubility products as a function of reciprocal temperature. Fits of the experimental data (see text) of this study are compared with literature values.

Table 17: Parameters deduced from the fitting Equation (28) and subsequently used in Equations (29) to (31) to retrieve the dolomite solubility product at 25 °C and the thermodynamic properties of dolomite.

$\text{Log}_{10} K_{sp}(\text{Dol})$ $= a + b/T + cT$	a	b	c	$\log_{10} K_{sp}(\text{Dol})$ 25 °C	$\Delta_f G_{298.15}^{\circ}$ (kJ/mol)	$\Delta_f H_{298.15}^{\circ}$ (kJ/mol)	$CP_{298.15}^{\circ}$ (J/mol/K)	$S_{298.15}^{\circ}$ (J/mol/K)
Fit of all the experimental data	-10.9079	1130.8997	-0.03157	-16.53*	-2157.07	-2284.15	-271.92	274.67
Fit of all the experimental data - fixed 25 °C	5.3474	-2020.9248	-0.05229	-17.20 (fixed) -17.02*	-2159.89	-2309.22	-35.39	200.00
Fit of all the experimental data - fixed	17.9109	-4313.0597	-0.06919	-17.18*	-2160.82	-2324.35	157.54	152.41
$\Delta C_{p,r}^{\circ}$								

In *italic*: fixed value in the fit

* Calculated using Equation (28) and the fitting parameters,

Bold: recommended fit

5.5 Discussion

This study is the first to systematically measure dolomite solubility at elevated temperatures. This was only possible due to the precise *in-situ* pH measurements made using the hydrogen electrode concentration cell. Furthermore, the reported experiments bracket equilibrated dolomite from both undersaturated and supersaturated conditions and thereby strongly constraining the equilibrium constants of *Reaction (21)*. The obtained equilibrium constants for temperatures above 125 °C are nearly identical to SUPCRT92, but then start to deviate from this database for lower temperatures amounting to about one order of magnitude difference at 50 °C.

This study suggests that the dolomite $\log_{10} K_{sp(Dol)}$ extrapolated to 25 °C can range from -16.5 to 17.4, depending upon the fitting procedure as reported in *Table 17*. However, the only fit giving a good set of thermodynamic data, compared with direct calorimetric measurements reported in the literature, is the one performed by fixing the heat capacity of dolomite given by Robie and Hemingway (1995). This fit gives a $\log_{10} K_{sp(Dol)}$ value at 25 °C of -17.18, in very good agreement with the experiments of Kramer (1959) and Sherman and Barak (2000), the latter performed experiments that lasted two years. Moreover, this value is very close to Hsu (1963), who reported a solubility product of $10^{-17.2}$ determined from the composition of groundwaters sampled from supposedly well equilibrated dolomite aquifers. Additionally, all these results are in good agreement with the thermodynamic data derived from solution calorimetry published by Robie *et al.* (1978).

5.6 Conclusion

The values of dolomite solubility have been controversial at room temperature and few dolomite solubility data are available at elevated temperature. This study was the first to

systematically measure dolomite solubility in a wide range of temperatures (50 to 175 °C). Equilibrium was approached both from undersaturation and supersaturation demonstrating its reversibility, at least at temperature starting from 150 °C. From the regression of our dolomite solubility products as a function of temperature, we have generated equations and parameters describing the dolomite solubility products from 25 to 300 °C from which we derived thermodynamic properties of dolomite. The calculated value at 25 °C is consistent with most of the previous data but significantly higher than that generated from SUPCRT92, or that calculated from the data reported by Stout and Robie (1963), in particular the estimates of Stout and Robie (1963) derived from decomposition phase equilibria of Graf and Goldsmith (1956).

This study greatly improves our knowledge on accurate thermodynamic calculations at ambient conditions and substantially contributes to a better assessment of the role of fluid-dolomite reactivity in a variety of natural and socially relevant processes. Application of these results will likely improve our ability to quantify subsurface carbon storage and provide insight into the origin of the dolomite problem. An eventual understanding of dolomite genesis at low temperatures is not unlikely, despite the still existing controversies at the present moment.

Chapter 6

ASSESSING DOLOMITE SURFACE REACTIVITY BY HYDROTHERMAL ATOMIC FORCE MICROSCOPY

Abstract

This study investigated dolomite reactivity on the (104) surface by hydrothermal atomic force microscopy at temperatures up to 100 °C, pH ranging from 4 to 8, and pressures up to 5 bars.

All dissolution experiments produced crystallographically well defined etch pits, consistent with the stoichiometric release of ordered lattice cations. Most of the growth experiments, however, led to growth of one or two layers of a carbonate (layer height $< 3 \text{ \AA}$) which morphologically reproduced the initial surface features, resembling a template effect. Growth on top of these layers was strongly inhibited and did not show any systematic crystallographically orientated growth morphologies. As such, this study shows that, while dissolution can readily release material from the dolomite surface to great depths, growth becomes sparingly slow after the first monolayer has been previously precipitated on its surface.

6.1 Introduction

Dolomite ($\text{CaMg}(\text{CO}_3)_2$) is the second most abundant carbonate mineral in the Earth's crust (*e.g.*, Warren, 2000). Knowledge of dolomite precipitation and dissolution rates is

essential for modeling major natural and industrial processes including the formation of sedimentary carbonates (Baker and Kastner, 1981), carbon capture and storage (Xu *et al.*, 2003; Moore *et al.*, 2005; Oelkers *et al.*, 2008; Wang *et al.*, 2013; Tutolo *et al.*, 2014), the preservation of paleoenvironmental signatures in carbonate rocks (Fantle and DePaolo, 2007; Fantle and Higgins, 2014; Fantle, 2015), secondary oil recovery (Wang *et al.*, 2013), and ocean chemistry (Mackenzie and Morse, 1992; Mackenzie and Andersson, 2013).

The formation of dolomite in natural and laboratory systems is, however, confounding (Arvidson and Mackenzie, 1999). Seawater is strongly oversaturated with respect to dolomite but there is no evidence of abiotic dolomite precipitation in modern marine depositional environments; in contrast, the ancient sedimentary record often contains dolomite (Tribble *et al.*, 1995; Hardie, 1996; Berner and Berner, 1996; Stanley and Hardie, 1999; Lowenstein *et al.*, 2001; Berner, 2004; Holland, 2005). Abiotic laboratory synthesis of dolomite generally requires hydrothermal conditions (Kessels *et al.*, 2000). The lack of abiotic low temperature (< 100 °C) dolomite formation has been interpreted as a kinetic limitation potentially due to the slow dehydration rates of the aqueous Mg²⁺ cation (Lippmann, 1973; Higgins and Hu, 2005; Saldi *et al.*, 2009).

Numerous laboratory studies suggested that microorganisms facilitate the formation of dolomite at low temperatures. Microbes that have been implicated in low temperature dolomite formation include sulfate-reducing bacteria (Vasconcelos *et al.*, 1995; Vasconcelos and McKenzie, 1997; Warthmann *et al.*, 2000; van Lith *et al.*, 2003; Wright and Wacey, 2005), sulfide oxidizers (Moreira *et al.*, 2004), and moderately halophilic aerobic heterotrophs (Sánchez-Román *et al.*, 2008). Many of these studies observe disordered or iron-rich dolomite forming on cell surfaces, raising the possibility that dolomite nucleation is surface-mediated rather than driven by metabolic processes.

This study was initiated to illuminate the processes and mechanisms responsible for the inhibition of abiotic dolomite precipitation at ambient conditions. Towards this goal the growth of dolomite from supersaturated aqueous solution was monitored on its surface using hydrothermal atomic force microscopy (HAFM) at temperatures from 40 to 100 °C. These temperatures were chosen for two reasons. First, dolomite is reported to precipitate at temperatures in excess of 140 °C (Rodriguez-Blanco *et al.*, 2015). Second, recent work on the anhydrous carbonate mineral magnesite shows that this mineral precipitates sufficiently fast at 80 to 120 °C to be measured directly using HAFM (Saldi *et al.*, 2009, 2012; Gautier *et al.*, 2015; Berninger *et al.*, 2016). This observation suggests that this method may also be applicable to quantify dolomite growth at these conditions. The purpose of this manuscript is to present the results of this HAFM study of dolomite growth and to use these results to improve our understanding of dolomite reactivity in natural systems.

6.2 Materials, chemical analysis, and experimental methods

6.2.1 Geochemical calculations

The standard state adopted in this study is that of unit activity for pure minerals and H₂O at any temperature and pressure. For aqueous species other than H₂O, the standard state is unit activity of the species in a hypothetical 1 molal solution referenced to infinite dilution at any temperature and pressure.

Dolomite precipitation or dissolution can be described using



In accord with the standard state, the law of mass action for *Reaction (21)* can be written

$$K_{sp(Dol)} = a_{eqCa^{2+}} a_{eqMg^{2+}} a_{eqCO_3^{2-}}^2 \quad (22)$$

where a_{eqi} refers to the activity of the subscripted aqueous species i at equilibrium and $K_{sp(Dol)}$ designates the equilibrium constant for *Reaction (21)*. The saturation state, Ω_{Dol} , of the aqueous fluid with respect to dolomite can then be written as

$$\Omega_{Dol} = \frac{a_{Ca^{2+}} a_{Mg^{2+}} a_{CO_3^{2-}}^2}{K_{sp(Dol)}} \quad (32)$$

where a_i refers to the activity of the subscripted aqueous species. All thermodynamic calculations reported in the present study were calculated using PHREEQC (Parkhurst and Appelo, 1999) assuming activity coefficients which can be described using the ‘b-dot’ activity model (Helgeson, 1969). The thermodynamic database used in these calculations was a slightly modified version of the Ilnl database. Much of data present in the Ilnl database of PHREEQC originates from SUPCRT92 (Johnson *et al.*, 1992). The Ilnl database was modified to include the equilibrium constants for Mg^{2+} hydrolysis and the carbonic acid dissociation reported by Brown *et al.* (1996) and Millero *et al.* (2007), respectively.

6.2.2 Hydrothermal atomic force microscopy (HAFM) experiments

Hydrothermal atomic force microscopy dolomite growth experiments were performed using an in-house constructed continuous-flow HAFM operating in contact mode fitted with uncoated silicon cantilevers purchased from Nanosensors. The system allows for *in-situ* visualization of relatively flat mineral surfaces at temperatures up to 150 °C and pressures up to 50 bars (*cf.*, Higgins *et al.*, 1998; Aldushin *et al.*, 2004; Jordan and Astilleros, 2006). The experiments in this study were performed at temperatures up to 100 °C with confining pressures of less than 5 bars. Experiments were not performed at higher temperature because

preliminary tests showed that it was not possible to obtain high quality images at such conditions due primarily to the dissolution of the cantilever in contact with the intended solution compositions. Experiments were performed by passing a reactive fluid over a cleaved dolomite grain orientated to expose its (104) surface. Inlet fluids were placed in Viton containers above the HAFM cell allowing gravitational fluid feed. Fluid flow rates were approximately 10 $\mu\text{g/s}$ allowing the rapid renewal of the fluid within the $\sim 500 \mu\text{L}$ reaction cell. Due to the rapid fluid renewal and a mineral surface area of only a few mm^2 , the chemical composition of the inlet fluid was negligibly affected by fluid-mineral reactions occurring in the reaction cell.

Experiments were performed on natural transparent dolomite single crystals from 1) Eugui, Spain (purchased from Fabre Minerals) and 2) Sunk, Austria (obtained from the Museum Reich der Kristalle in Munich, Germany). The composition of these dolomites were determined using a Cameca SX 100 electron microprobe; the results of these analyses are provided in *Table 18*. These dolomites contain slightly more calcium than magnesium due to the presence of $\sim 2\%$ Fe most likely at the magnesium site. The mineralogy of these solids were determined using an INEL CPS-120 diffractometer with Co K_{α} -radiation, $\lambda = 1.78897 \text{ \AA}$, and a graphite monochromator. X-ray diffraction was performed from 1 to $110^{\circ} 2\theta$ at $0.09^{\circ}/\text{min}$ and at a step size of 0.029° . Representative x-ray diffraction patterns are provided in *Figure 29*. These diffractograms show the initial solids to be pure dolomite. They also show strong superstructure reflections (*e.g.*, Lippmann, 1973) indicating that these dolomites are highly ordered. The crystals were cleaved with a scalpel immediately before being fixed in the HAFM cell orienting the (104) surface perpendicular to the tip of the cantilever. The (104) dolomite cleavage surface was chosen for this growth study 1) due to ease of preparation, and 2) that this surface contains equal amounts of calcium and

magnesium. The HAFM flow system was then pressurized and the cell heated to the desired temperature at the start of each experiment.

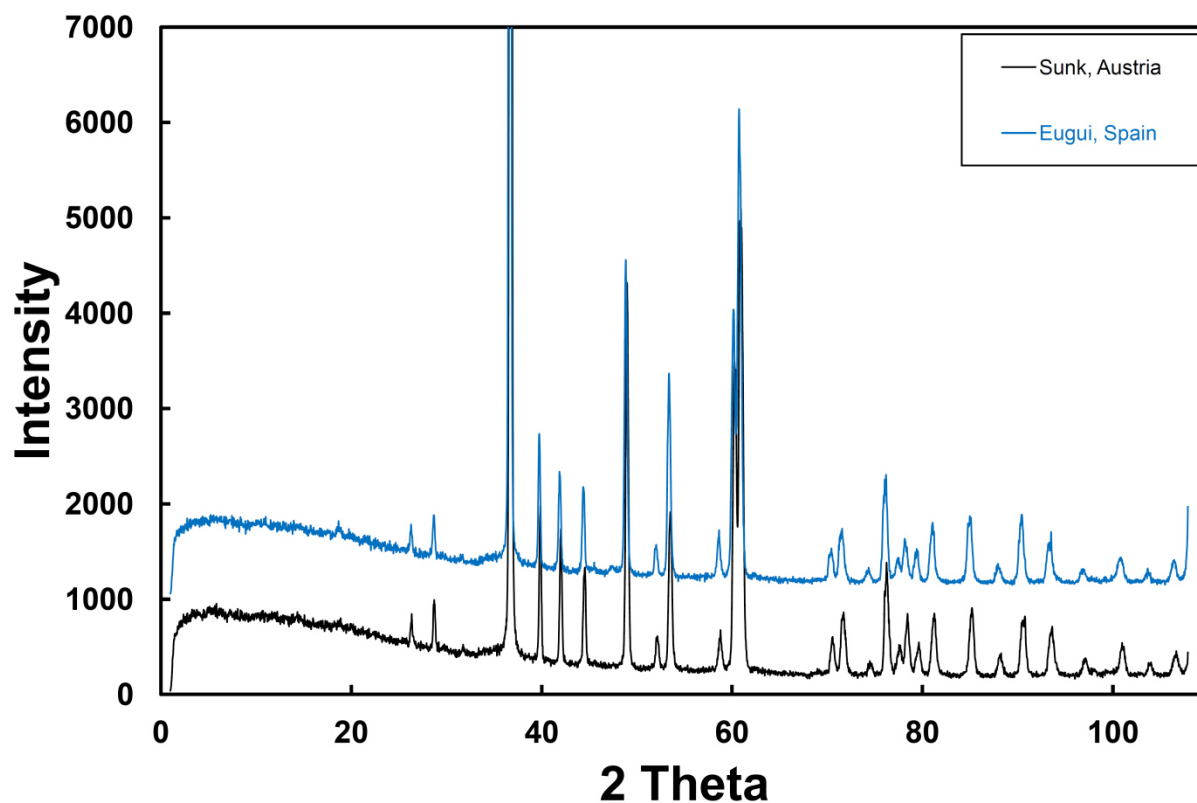


Figure 29: Powder x-ray diffractogram of dolomite from Eugui, Spain, and Sunk, Austria.

Table 18: Electron microprobe analyses of both dolomite single crystals used in this study.

	Eugui (single xtl)	Sunk (single xtl)
CaO	29.89	29.18
MgO	20.89	20.39
FeO	0.5568	0.9701
MnO	0.0807	0.1613
ZnO	0.0387	0.0346
CuO	0.0183	0.0238
calc. CO ₂	48.53	49.24
measured points	94	98
chem. formula based on six oxygens	Ca _{1.005} Mg _{0.977} Fe _{0.015} Mn _{0.002} Zn _{0.001} (CO ₃) ₂	Ca _{0.998} Mg _{0.971} Fe _{0.026} Mn _{0.004} Zn _{0.001} (CO ₃) ₂

6.2.3 Reactive fluids and their analysis

The inlet fluids of all experiments consisted of high purity deionized water (resistivity 18.2 MΩ cm), and reagent grade NaCl, 1N HCl, NaHCO₃, MgCl₂·6H₂O, and CaCl₂·2H₂O as well as dry ice purchased from Linde. The inlet fluid compositions for all experiments are summarized in *Table 19*.

Table 19: Summary of inlet solution compositions for hydrothermal atomic force microscopy (HAFM) experiments on dolomite.

Experiment	pH	c _{CaCl₂·2H₂O}	c _{MgCl₂·6H₂O}	Alkalinity	NaCl	1N HCl	CO ₂ saturation
		(mmol/kg)	(mmol/kg)	(meq/L)	(g/kg)	(mL/L)	(1 bar)
Eugui-01	6.59	0.606	57.4	45.9	0.2003	15.6	-
Eugui-02	6.32	0.535	48.5	30.0	0.0266	19.8	-
Eugui-03-A	6.59	0.286	54.9	45.9	0.1895	15.8	-
Eugui-03-B	6.59	0.286	54.9	45.9	0.1895	15.8	-
Eugui-04	7.86	0.501	0.502	0.986	5.6678	-	-
Eugui-06	7.86	0.590	0.555	0.987	5.6678	-	-
Eugui-08	8.30	0.0092	0.0101	100	0.0529	-	-
Sunk-01	6.53	4.68	5.21	1.98	4.0930	1.0	-
Sunk-02	6.43	10.4	16.0	1.63	0.8780	1.0	-
Sunk-03	6.13	8.20	10.4	1.49	1.9971	1.8	-
Sunk-04	5.95	9.73	12.3	1.57	1.2623	2.9	-
Sunk-05	6.15	8.29	10.5	1.57	1.9961	1.8	-
Sunk-06	6.12	9.52	12.2	1.58	1.3162	2.0	-
Sunk-07	6.10	6.34	24.6	2.60	0.2765	3.3	-
Sunk-08	6.15	24.2	6.06	0.763	0.4171	0.9	-
Sunk-09	6.19	5.94	25.3	2.17	0.3379	2.2	-
Sunk-10	6.18	24.4	6.02	0.947	0.4092	1.0	-
Sunk-11	5.67	50.0	50.5	2.01	-	5.0	-
Sunk-12	6.23	0.323	38.3	10.1	0.4198	8.8	-
Sunk-13	6.19	0.509	24.5	7.05	0.5052	7.4	-
Sunk-14	6.36	0.117	26.8	10.1	0.5236	7.0	-
Sunk-15	6.16	0.122	26.7	10.1	0.2828	11.2	-

Table 19: continued

Experiment	pH	c_{CaCl₂*2H₂O}	c_{MgCl₂*6H₂O}	Alkalinity	NaCl	1N HCl	CO₂ saturation
		(mmol/kg)	(mmol/kg)	(meq/L)	(g/kg)	(mL/L)	(1 bar)
Sunk-16	6.30	0.495	27.1	11.1	0.4212	8.8	-
Sunk-17	6.18	0.643	25.2	7.73	0.4559	8.2	-
Sunk-18	8.45	0.0088	0.0058	52.4	0.0445	-	-
Sunk-19	4.84	10.6	10.1	1.62	0.0952	38.4	-
Sunk-21	8.36	0.0198	0.102	5.59	-	-	-
Sunk-23	6.23	1.03	12.4	7.52	-	8.0	-
Sunk-24	5.51	48.5	56.9	9.99	-	-	saturated
Sunk-25	5.71	48.1	55.5	9.98	-	-	saturated
Sunk-26	5.77	52.4	58.0	4.98	-	-	saturated
Sunk-27	5.57	50.7	56.2	4.99	-	-	saturated
Sunk-28	5.66	49.4	55.9	7.49	-	-	saturated
Sunk-29	7.14	0.323	33.9	2.72	-	0.3	-
Sunk-30	7.06	0.0328	34.0	2.69	-	0.3	-
Sunk-31	7.10	0.178	34.0	2.71	-	0.3	-
Sunk-32	6.39	105	112	2.62	-	0.9	-
Sunk-33	6.42	10.6	10.1	1.32	-	0.9	-
Sunk-34	6.71	10.6	10.3	1.64	0.0265	0.5	-
Sunk-35	6.39	57.6	61.3	1.97	-	0.9	-
Sunk-36	6.41	0.0055	32.2	1.86	0.0209	1.1	-
Sunk-38	6.41	32.8	0.0010	1.86	0.0209	1.1	-
Sunk-39	6.55	32.4	0.0093	2.08	0.0337	0.9	-
Sunk-40	6.41	16.4	16.1	1.86	0.0209	1.1	-
Sunk-41	3.93	10.7	1.12	0.0048	-	30.0	-
Sunk-42	6.28	5.78	1.10	15.3	0.3113	14.7	-
Sunk-43	5.79	8.22	1.11	7.68	0.1108	22.3	-
Sunk-44	5.58	0.0071	51.8	10.0	-	-	saturated
Sunk-45	5.58	0.0099	51.8	10.0	-	-	saturated
Sunk-46	5.59	48.6	0.0022	10.1	-	-	saturated
Sunk-47	5.60	47.9	0.0044	10.1	-	-	saturated
Sunk-48-A	5.59	19.2	31.1	10.0	-	-	saturated
Sunk-48-B	5.59	19.2	31.1	10.0	-	-	saturated

Table 19: continued

Experiment	pH	c _{CaCl₂*2H₂O}	c _{MgCl₂*6H₂O}	Alkalinity	NaCl	1N HCl	CO ₂ saturation
		(mmol/kg)	(mmol/kg)	(meq/L)	(g/kg)	(mL/L)	(1 bar)
Sunk-49-A	5.59	17.6	29.4	10.1	-	-	saturated
Sunk-49-B	5.59	17.6	29.4	10.1	-	-	saturated
Sunk-50-A	5.38	22.1	27.0	6.24	-	-	saturated
Sunk-50-B	5.38	22.1	27.0	6.22	-	-	saturated
Sunk-51	7.08	0.0435	7.35	5.23	0.5370	0.8	-
Sunk-52	7.02	4.91	0.0007	0.796	0.5757	0.1	-
Sunk-53	6.76	10.8	0.0276	2.66	0.5350	0.8	-
Sunk-54	6.94	5.43	3.69	3.95	0.5360	0.8	-
Sunk-55	4.12	0.0137	521	0.673	-	-	saturated
Sunk-56	4.94	5.42	260	1.67	0.2922	5.0	saturated
Sunk-57	6.38	2.81	30.3	7.65	-	5.0	-
Sunk-59-A	6.38	1.08	32.5	7.71	-	5.0	-
Sunk-59-B	6.38	1.08	32.5	7.71	-	5.0	-
Sunk-61	6.38	1.93	29.8	7.68	-	5.0	-

Aqueous magnesium and calcium concentrations were measured by flame atomic absorption spectroscopy using a Perkin Elmer AAnalyst 400 Atomic Absorption Spectrometer with an uncertainty of $\pm 2\%$ and detection limits of 1×10^{-7} and 2×10^{-7} mol/kg, respectively. Alkalinity was determined by standard HCl titration using Schott TA 10plus with an uncertainty of $\pm 1\%$ and a detection limit of 2×10^{-5} eq/L. Reactive fluid pH measurements were performed at room temperature immediately before and after the performed experiments using a standard glass electrode, previously calibrated with 4.01, 6.86, and 9.18 NIST pH buffers. The uncertainty of these measurements is estimated to be ± 0.05 pH units. Fluid pH, speciation, and saturation state with respect to dolomite at the temperature of each experiment

were calculated by PHREEQC (Parkhurst and Appelo, 1999) using pH values and fluid compositions measured at 25 °C.

6.3 Results

In total of 67 HAFM experiments were performed in this study at temperatures ranging from 40 to 100 °C. Seven of these experiments were performed using Eugui dolomite and 60 on Sunk dolomite. A summary of the experimental conditions, measured reactive fluid chemistry, the saturation state of the fluid phase with respect to dolomite, and observed dolomite growth behavior is presented in *Table 20*. Several distinct behaviors were observed as described below.

Table 20: Summary of the results of hydrothermal atomic force microscopy (HAFM) experiments on dolomite (104) surfaces.

Experiment	Temp (°C)	pH _{calc}	Ionic strength	Ω_{Dol}	$a_{Ca^{+2}}$ (x 10 ⁻⁴)	$a_{Mg^{+2}}$ (x 10 ⁻⁴)	$a_{CO_3^{2-}}$ (x 10 ⁻⁷)	Observation
Eugui-01	40	6.50	0.217	220	1.65	176	48.6	1 layer
Eugui-02	40	6.23	0.183	26.4	1.60	162	17.9	1 layer
Eugui-03-A	40	6.50	0.209	103	0.787	170	49.2	1 layer
Eugui-03-B	60	6.47	0.207	336	0.746	161	54.5	1 layer
Eugui-04	100	7.50	0.099	10.7	1.71	1.86	16.3	no reaction
Eugui-06	100	7.49	0.100	13.6	2.01	2.05	16.1	no reaction
Eugui-08	100	8.10	0.101	49.6	0.0064	0.014	6667	1 layer
Sunk-01	100	6.51	0.101	41.6	15.9	19.3	3.26	1 layer*
Sunk-02	100	6.37	0.095	80.6	36.3	61.2	1.69	1 layer*
Sunk-03	100	6.09	0.091	11.5	28.9	40.1	0.883	1 layer
Sunk-04	100	5.91	0.090	7.4	34.5	47.5	0.594	1 layer
Sunk-05	100	6.11	0.092	14.3	29.1	40.4	0.976	1 layer
Sunk-06	100	6.08	0.089	15.7	33.8	47.1	0.880	1 layer
Sunk-07	100	6.04	0.100	38.5	21.6	92.1	1.23	1 layer
Sunk-08	100	6.09	0.098	4.2	84.1	23.1	0.410	no reaction

Table 20: continued

Experiment	Temp (°C)	pH_{calc}	Ionic strength	Ω_{Dol}	a_{Ca+2} ($\times 10^{-4}$)	a_{Mg+2} ($\times 10^{-4}$)	a_{CO3-2} ($\times 10^{-7}$)	Observation
Sunk-09	100	6.13	0.101	38.4	20.3	94.7	1.25	1 layer
Sunk-10	100	6.12	0.099	7.3	84.5	22.9	0.544	1 layer
Sunk-11	100	5.57	0.297	11.1	121	142	0.224	1 layer
Sunk-12	100	6.17	0.133	57.3	0.962	126	6.07	3 layers*
Sunk-13	100	6.14	0.093	39.3	1.72	89.9	4.47	3 layers*
Sunk-14	100	6.31	0.101	39.4	0.377	94.4	9.31	5 layers*
Sunk-15	100	6.11	0.100	16.6	0.394	94.1	5.92	3 layers*
Sunk-16	100	6.25	0.103	148	1.58	94.3	8.84	1 layer*
Sunk-17	100	6.13	0.096	56.2	2.14	91.5	4.75	2 layers*
Sunk-18	100	8.21	0.053	28.1	0.0086	0.011	4783	no reaction
Sunk-19	100	4.81	0.102	0.0	36.2	37.7	0.050	dissolution
Sunk-21	100	8.01	0.006	103	0.094	0.586	383	1 layer
Sunk-23	40	6.14	0.054	1.7	4.59	58.8	4.49	dissolution
Sunk-24	100	5.40	0.307	129	113	154	0.762	3 layers*
Sunk-25	100	5.61	0.302	324	113	151	1.22	3 layers*
Sunk-26	100	5.66	0.320	111	123	158	0.669	1 layer*
Sunk-27	100	5.46	0.310	44.1	120	155	0.432	1 layer*
Sunk-28	100	5.55	0.306	146	116	153	0.802	1 layer*
Sunk-29	100	6.94	0.102	157	1.09	126	9.46	1 layer
Sunk-30	100	6.89	0.101	12.6	0.111	127	8.36	1 layer
Sunk-31	100	6.91	0.102	76.7	0.601	127	8.89	1 layer
Sunk-32	100	6.22	0.614	575	203	262	0.920	1 layer*
Sunk-33	100	6.36	0.063	47.6	41.8	43.1	1.44	1 layer*
Sunk-34	100	6.63	0.064	243	41.7	43.6	3.24	1 layer*
Sunk-35	100	6.25	0.344	261	133	166	0.962	1 layer*
Sunk-36	100	6.33	0.097	0.1	0.019	122	1.69	dissolution
Sunk-38	100	6.34	0.100	0.0	112	0.0038	1.72	dissolution
Sunk-39	100	6.46	0.099	0.3	111	0.035	2.57	dissolution
Sunk-40	100	6.33	0.098	128	56.5	60.8	1.71	2 layers*
Sunk-41	100	3.93	0.065	0.0	42.2	4.75	0.00066	dissolution
Sunk-42	100	6.27	0.054	287	20.9	4.25	15.9	1 layer
Sunk-43	100	5.78	0.058	11.1	31.4	4.52	2.48	1 layer

Table 20: continued

Experiment	Temp (°C)	pH_{calc}	Ionic strength	Ω_{Dot}	a_{Ca+2} ($\times 10^{-4}$)	a_{Mg+2} ($\times 10^{-4}$)	a_{CO3-2} ($\times 10^{-7}$)	Observation
Sunk-44	100	5.51	0.154	0.1	0.020	166	1.22	dissolution
Sunk-45	100	5.50	0.154	0.1	0.028	166	1.21	dissolution
Sunk-46	100	5.53	0.149	0.0	140	0.0071	1.36	dissolution
Sunk-47	100	5.53	0.147	0.0	139	0.014	1.37	dissolution
Sunk-48-A	40	5.49	0.155	2.9	63.9	116	1.11	no reaction
Sunk-48-B	70	5.46	0.154	17.3	59.9	109	1.24	1 layer
Sunk-49-A	40	5.50	0.145	2.8	59.8	111	1.14	no reaction
Sunk-49-B	70	5.47	0.144	16.7	56.1	104	1.29	1 layer
Sunk-50-A	50	5.27	0.149	0.8	74.1	101	0.46	dissolution
Sunk-50-B	100	5.31	0.147	18.3	65.6	89.6	0.494	1 layer*
Sunk-51	70	6.97	0.036	9.9	0.204	36.4	27.9	no reaction
Sunk-52	70	6.90	0.025	0.0	26.1	0.0039	3.76	dissolution
Sunk-53	70	6.64	0.045	0.5	49.4	0.134	6.49	dissolution
Sunk-54	70	6.82	0.040	171	25.1	18.1	14.8	1 layer
Sunk-55	120	4.01	1.275	0.0	0.020	874	0.0008	dissolution
Sunk-56	120	4.81	0.705	0.1	9.24	522	0.015	dissolution
Sunk-57	40	6.28	0.108	13.0	10.4	123	5.63	no reaction
Sunk-59-A	40	6.29	0.110	5.4	4.00	132	5.67	no reaction
Sunk-59-B	100	6.31	0.107	234	3.49	115	6.75	2 layers*
Sunk-61	40	6.29	0.104	9.3	7.21	122	5.76	no reaction

* Growth seemed to continue but extremely slow.

In 14 experiments, the reactive fluid was undersaturated with respect to dolomite as indicated by a saturation index of < 1 in *Table 20*. Dolomite dissolution was also observed in experiment Sunk-23; the reactive fluid in this experiment was calculated to be slightly super-saturated with respect to dolomite. This ambiguity may be due to the uncertainties in the thermodynamic database at the conditions of this experiment at 40 °C. A representative example of observed dolomite dissolution behavior at 100 °C is shown in *Figure 30*. Well

defined etch pits that follow the crystallographic directions $[\bar{4}41]$ and $[48\bar{1}]$ of the dolomite substrate are observed to form. Dolomite step retreat velocities in these experiments were too rapid to obtain unambiguous retreat rates.

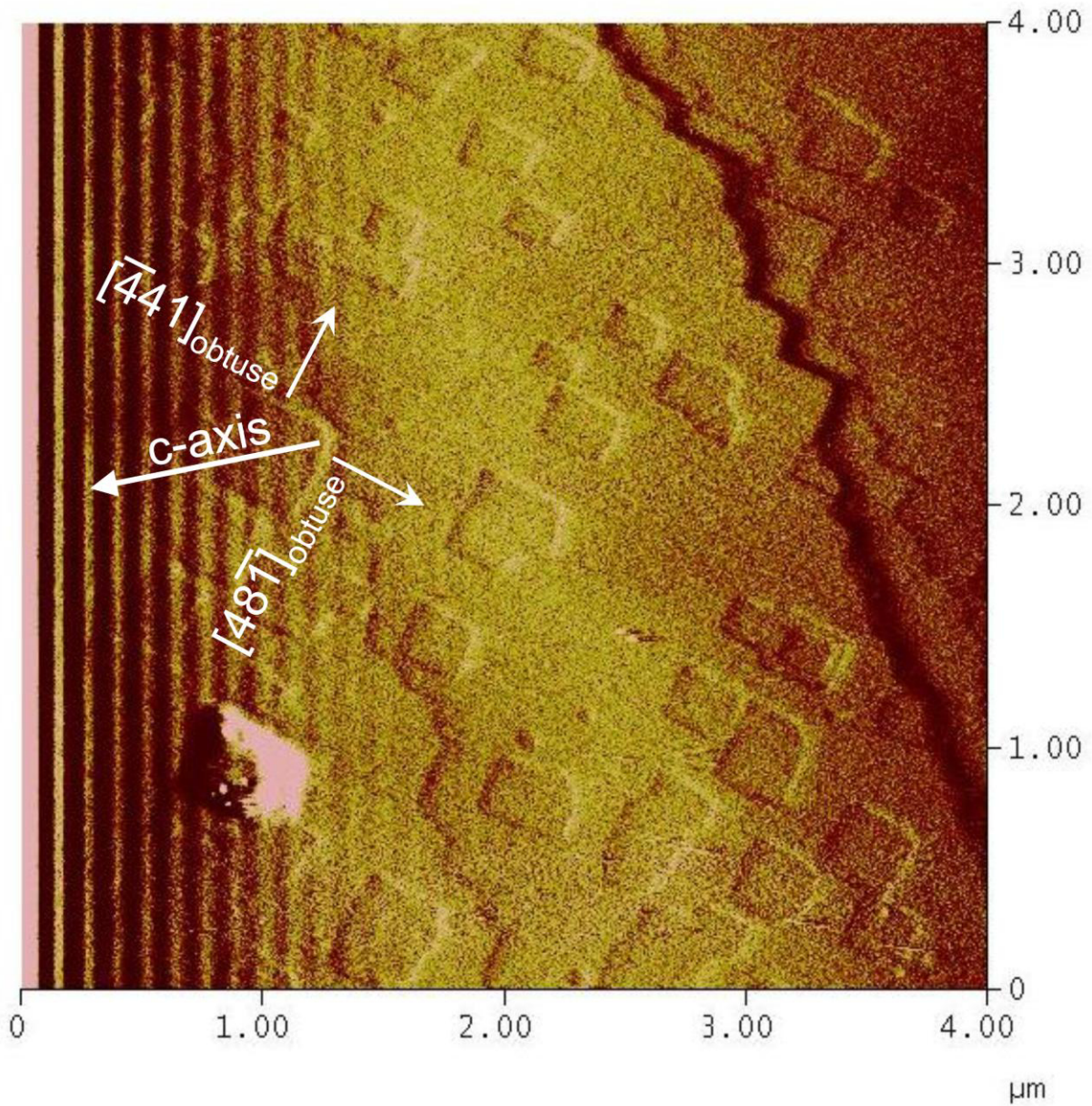


Figure 30: HAFM deflection image showing the development of etch pits during the very initial moment of dissolution at 100 °C (Sunk-19).

In 10 experiments no dolomite dissolution or precipitation was observed. The reactive fluid saturation state in these experiments ranged from 2.8 to 13.6, other than one experiment with a saturation index of 28.1; this latter experiment was that having the lowest reactive fluid divalent cation concentrations, aqueous Ca^{2+} and Mg^{2+} activities were calculated to be $\sim 9 \times 10^{-7}$ and $\sim 1 \times 10^{-6}$, respectively. The relatively high degree of saturation state of this experiment is due to the high reactive fluid alkalinity and comparatively high pH. A representative example of an unreacting dolomite surface during a representative experiment is shown in *Figure 31*.

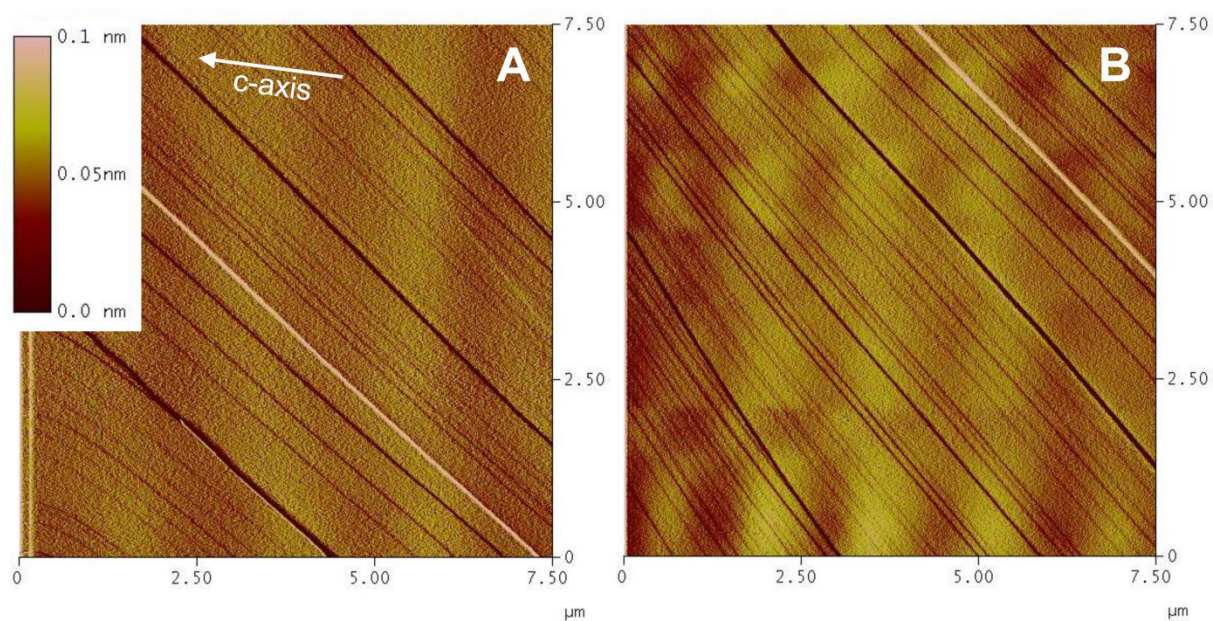


Figure 31: HAFM height images showing an inert (104) dolomite surface during more than 1 h 15 min of the growth experiment Sunk-48-A. The left image (A) was recorded more than 1 h and the right image more than 2 h 20 min after the start of the experiment; during all this time the surface didn't show any morphological change; the big cleavage step (white/rose diagonal feature) can serve as reference. Note that the whole scanning area is drifting to Northeast due to piezo creep.

In 33 experiments a single dolomite growth layer was observed to form. The saturation states of the reactive fluids with respect to dolomite in these experiments ranged from 7.3 to 336. The height of the observed growth layers is observed to be $< 3.0 \text{ \AA}$, consistent with the formation of a monolayer of carbonate. A representative example of such observations is shown in *Figure 32*. It can be seen in this figure that the first layer grows via step advancement to the point at which a full monolayer is completed after which growth is significantly inhibited. Thus, the step morphology of the starting surface is reproduced once the first layer is complete, similar to the results observed by Higgins and Hu (2005) for dolomite growth at 25 °C.

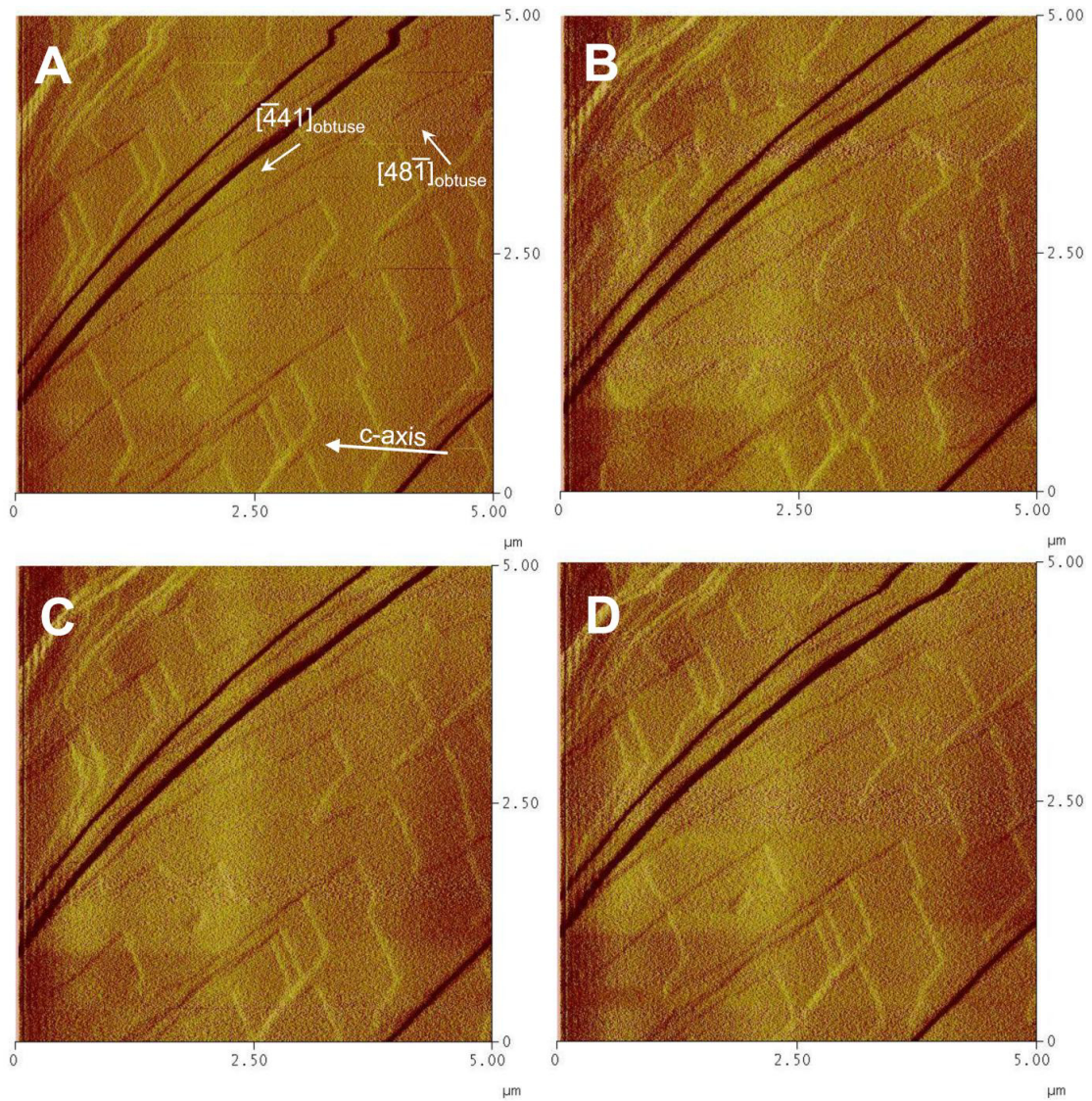


Figure 32: The development of a single layer template growth on a (104) surface of dolomite as recorded by HAFM deflection images (Sunk-09). The precipitation sequence starts on a surface which had been pre-cleaned in-situ via dissolution in MQ-water at 100 °C and monitored by HAFM (A). Pre-dissolution of some dolomite layers stopped just after developing a small etch pit in the lower left area of image A. As precipitation begins the surface is quickly covered by a $\sim 3 \text{ \AA}$ thick layer (B and C) which expands in obtuse step directions. Note steps are not propagating perpendicular to the initial step front but are rather curving forward (B) and do not close the tiny etch pit (which is atypical for layer-wise growth of carbonates) but grow around it (C). The precipitation seemingly stopped after the formation of one layer of carbonate was completed and the initial surface was reproduced (D).

In 9 experiments multiple layers of dolomite growth was observed. The saturation states of the reactive fluids with respect to dolomite in these experiments ranged from 16.6 to 324. A representative example of these observations can be seen in *Figure 33*. The growth of the first layer in these experiments is similar to that of the experiments exhibiting the growth of only a single layer. After this first layer forms, subsequent layers form slower. In contrast to this first growth layer, which follows the morphology of the dolomite substrate, the subsequent growth layers form more rounded ‘growth island morphologies’, each subsequent layer following less the original morphological form of the original dolomite substrate. In each case the continued growth of dolomite continued through the end of the experiment.

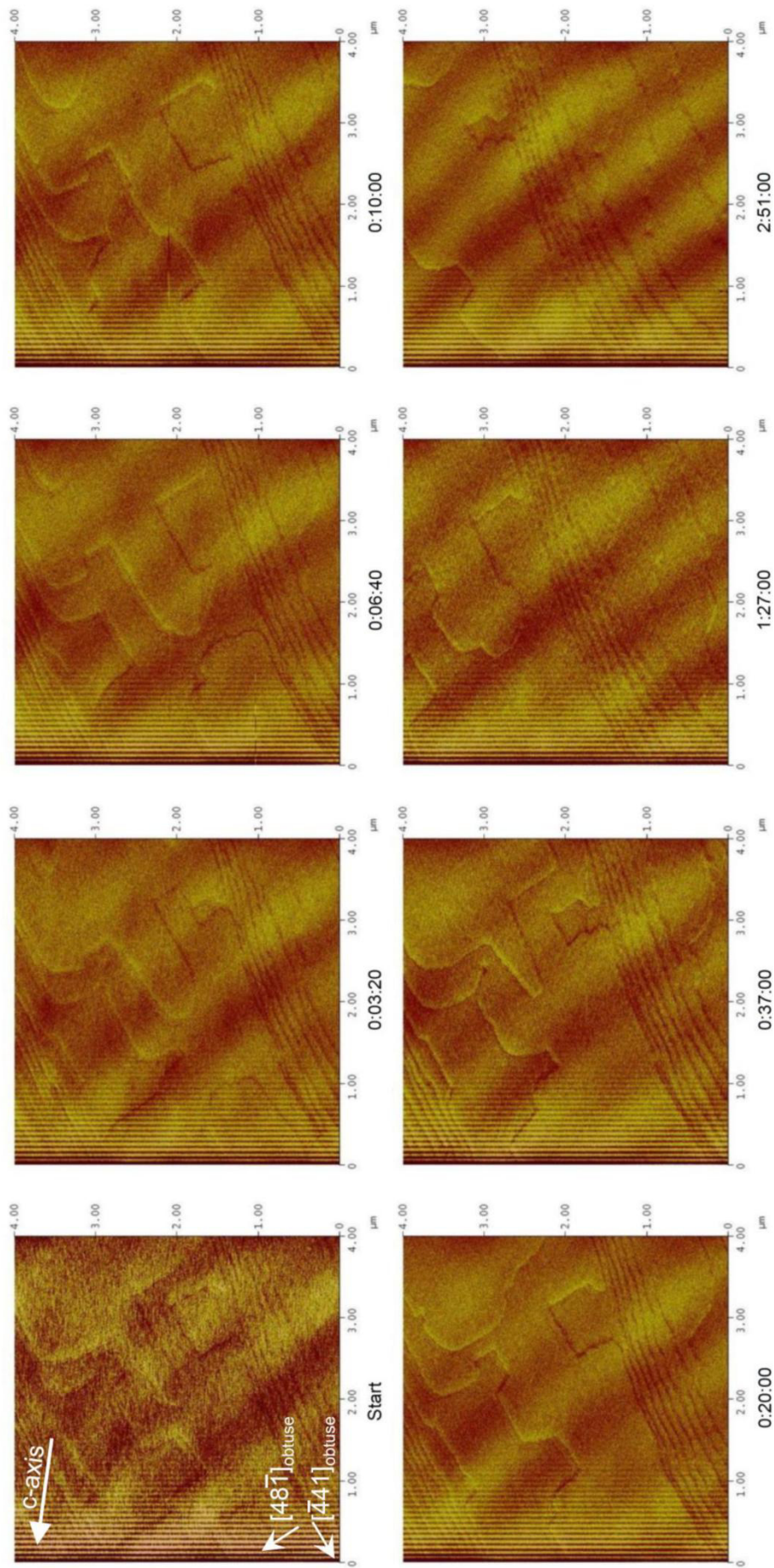


Figure 33: Sequence of deflection images on (104) dolomite at 100 °C and 2 bars showing a template effect during dolomite growth on a 4x4 μm scan area (Sunk-12). Growth continued very slowly after the first layer precipitated and is seemingly less confined to the initial surface morphology.

6.4 Discussion

6.4.1 Comparison with past results

A number of past studies have attempted to precipitate dolomite abiotically at temperatures less than 200 °C. Most, and perhaps all of these past attempts failed to precipitate stoichiometric, well crystallized dolomite. For example, Land (1998) failed to precipitate dolomite from supersaturated aqueous solutions at 25 °C despite a 32-year long experiment. Higgins and Hu (2005) and Hu *et al.* (2005) attempted to precipitate dolomite at 27 °C and monitoring the reaction progress using atomic force microscopy on the (104) dolomite surface. As was observed in the present study, a single layer of dolomite was rapidly formed on the existing dolomite surface but additional layers were strongly inhibited from growing. Arvidson and Mackenzie (1999) attempted to measure the precipitation rates of dolomite at temperatures of 100 to 200 °C in mixed-flow reactors but rather succeeded in measuring the steady-state precipitation rates of a calcium-rich protodolomite on the surface of dolomite seeds. These authors provided a rate equation to describe their protodolomite precipitation rates as a function of temperature and saturation state. Our results are largely consistent with these past observations as we observed the precipitation of a single dolomite layer on the original dolomite surface followed by a far slower growth of a poorly defined Mg-Ca-carbonate. In contrast, Rodriguez-Blanco *et al.* (2015) argued that they crystallized dolomite from aqueous solution at temperatures from 60 to 220 °C via a mechanism that transforms an originally precipitated amorphous calcium carbonate into crystalline stoichiometric dolomite via a protodolomite precursor. Only at temperatures > 140 °C they did no longer observe the formation of protodolomite as an intermediate step. It should be emphasized however that the evidence presented by these authors for the presence of an ordered dolomite in their experiments is based on the observations of superstructural reflections that may not have been significant considering their intensity compared with that of the background signal, indicating

a very low degree of ordering. It should also be noted that although numerous studies have argued that dolomite is readily formed biotically (*e.g.*, Warthman *et al.*, 2000), such conclusions have been questioned by Gregg *et al.* (2015) who reexamined published x-ray diffraction data concluding that dolomite synthesis in the laboratory under near-ambient conditions by microbial mediation are unsubstantiated.

6.4.2 What inhibits dolomite precipitation at temperatures ≤ 100 °C?

The results described above show that a single layer of carbonate is readily precipitated on the surface of dolomite. This first layer closely mimics the surface of the original dolomite consistent with epitaxial growth. In consequence, subsequent layers are more sluggish to form and do not follow the original surface structure. These subsequent layers tend to form as distinct growth islands on the surface of the first epitaxial growth layer. Such observations are similar to that observed by Higgins and Hu (2005). These previous authors suggested that this behavior stemmed from the likelihood that the first layer precipitated on the dolomite surface was non-stoichiometric and non-ordered due to the high affinity of calcium compared to magnesium for the dolomite surface. This non-stoichiometric, non-ordered layer then serves as a poor template for further growth because of its increased surface free energy. Note that as in the Higgins and Hu (2005) study, this study can neither determine the exact chemical composition of this first layer nor if it is ordered. Nevertheless x-ray photoelectron spectroscopy of the products of dolomite growth experiments described in *Chapter 5* of this thesis, performed in bulk chemical reactors, show that the composition of the precipitated surface layers is mildly enriched in magnesium at the outermost surface. In addition scanning electron microscope analysis of these grains show the development of distinct growth islands on the surface of the original seed crystals (*Figure 27B*). Taken together, these observations

suggest that dolomite growth starting from room temperature up to 100 °C is self-inhibited by the initial precipitation of a non-stoichiometric disordered Mg-Ca-carbonate which then disfavors the further epitaxial growth on this surface. Subsequent growth requires nucleation of new growth sites on the substrate. This is supported by the slow formation of growth islands after the first layer has formed. Due to the lack of surface templating, these growth islands are likely poorly ordered and non-stoichiometric, consistent with our observations.

6.4.3 Consequences for mineral carbonation

The possibility of storing carbon in the subsurface as dolomite is particularly attractive as it is highly stable and its formation can take advantage of large quantities of magnesium present in basalts and ultramafic rocks (*cf.*, Oelkers *et al.*, 2008; Kaszuba *et al.*, 2011). Moreover a number of geochemical modeling studies have suggested that dolomite is thermodynamically favored to precipitate during the injection of CO₂ into the subsurface as part of carbon capture and storage efforts (*e.g.*, Xu *et al.*, 2003; Gysi and Stefánsson, 2008). The results of this study illustrate that the precipitation of dolomite via abiotic processes is sluggish and/or not possible at temperatures up to 100 °C. As such it seems unlikely that dolomite would be an effective mineralogical carbon storage host in *in-situ* mineral carbonation systems at least at temperatures < 100 °C. It should be noted, however, that the results of Gysi and Stefánsson (2012) suggest that dolomite-ankerite solid solutions might readily form in these conditions providing the means to carbonate magnesium during subsurface carbon storage efforts.

6.5 Conclusion

The results summarized above provide further insight into the inhibition of abiotic dolomite growth in low temperature systems. Most notably these results support the hypothesis that the first dolomite growth layer formed on dolomite substrate poisons this surface, inhibiting further growth. The results show that this behavior is not just limited to room temperature but well extends into the mildly hydrothermal range. Additional growth appears to require surface nucleation and results in the formation of a somewhat non-stoichiometric and/or poorly ordered dolomite-like phase. As such it seems that the most likely route for the formation of dolomite in natural systems may be via the recrystallization of a poorly crystalline and/or non-stoichiometric and disordered protodolomite such as suggested by Kaczmarek and Sibley (2014) and Montes-Hernandez *et al.* (2014).

Chapter 7

CONCLUSIONS

The reported research in this thesis contains a systematic investigation of the reactivity of Mg-carbonates, specifically dissolution and precipitation kinetics of hydromagnesite, magnesite, and dolomite. Enabled by the collaboration of GET and LMU laboratories, these investigations on fluid-mineral interactions were performed with a suite of scale spanning techniques. Due to their different correlation lengths, macroscale and nanoscale investigations provide complementary insights into processes at the fluid-mineral interface. These complementary insights were used to further unravel the reactivity of Mg-carbonates in aqueous solutions - a system with important relevance in both nature and society. The results reported within this thesis considerably contribute to the understanding of the mechanisms and rates which control the formation of carbonates in sedimentary settings and in the context of CO₂ sequestration. Representative for hydrous Mg-carbonates, the precipitation kinetics of the most abundant natural hydrous Mg-carbonate phase hydromagnesite were investigated and reported in *Chapter 2*. Due to its rapid reaction rates, hydromagnesite quickly equilibrates with natural fluids at low and ambient temperatures. The fast precipitation rates suggest that hydromagnesite could be an efficient product phase for the *ex-situ* and *in-situ* sequestration of CO₂.

The results of *Chapter 3* demonstrated the rapid and efficient re-equilibration of isotopic signatures during fluid-mineral interaction. Such observations indicate that the accurate interpretation of isotopic signals recorded in the geological record cannot be assumed to be fixed during their original precipitation, and may likely reflect at least some resetting during

deposition and burial. This appears to be particularly the case for carbonate minerals and even more so for hydrous Mg-carbonates, which tend to react rapidly at ambient conditions. Similarly, as the isotopic composition of the fluid phase is rapidly and significantly influenced by its interaction with its coexisting minerals, it seems unlikely that natural fluids preserve pristine records of the origin of these fluids. In consequence, the novel approach of tracking the isotopic evolution even during chemical equilibrium of water-rock interactions certainly will have to be considered and implemented to water-rock models as well as it demonstrates the necessity for a whole suite of new experimental designs for future studies.

In *Chapter 4* macroscopic and microscopic experiments were performed to investigate the effect of competing aqueous ions for magnesite lattice sites during magnesite growth. This complementary approach yielded a robust validated rate equation which was tested up to very high degrees of supersaturation. The performed experiments and Raman spectroscopy showed that Ca^{2+} preferably incorporates into the magnesite structure despite high saturation states with respect to pure magnesite. This incorporation, however, does not affect significantly measured magnesite growth rates. This result contrasts greatly with the observed effect of aqueous magnesium on calcite growth kinetics at ambient temperatures. Such differences may stem from a number of factors including the high saturation state of the reactive fluid in this study, differences in the strength of the hydration shells of aqueous Mg^{2+} and Ca^{2+} , and the effect of increased temperature on the water exchange rate of these hydration shells. Nevertheless, the fact that the ubiquitous presence of aqueous calcium in geological settings does not substantially affect magnesite precipitation rates suggests that the presence of this cation and other analogous aqueous divalent metal ions do not impede the precipitation rate of carbonate minerals with calcite structure and, therefore, will not affect significantly mineral carbonation efforts in mafic or ultramafic rocks.

In *Chapter 5* the rock-forming Ca/Mg-carbonate dolomite was investigated. The values of dolomite solubility have been controversial at room temperature and few dolomite solubility data are available at elevated temperature. This study was the first to systematically measure dolomite solubility in a wide range of temperatures (50 to 175 °C). Equilibrium was approached both from undersaturation and supersaturation demonstrating its reversibility, at least at temperatures starting from 150 °C. From the regression of the obtained dolomite solubility products as a function of temperature, equations and parameters describing the dolomite solubility products from 25 to 300 °C were generated allowing the derivation of thermodynamic properties of dolomite. The calculated value at 25 °C is consistent with most of the previous data but significantly higher than that generated from SUPCRT92, or that calculated from the data reported by Stout and Robie (1963), in particular the estimates of Stout and Robie (1963) derived from decomposition phase equilibria of Graf and Goldsmith (1956).

This greatly improves our knowledge on accurate thermodynamic calculations at ambient conditions and substantially contributes to a better assessment of the role of fluid-dolomite reactivity in a variety of natural and socially relevant processes. Application of these results will likely improve our ability to quantify subsurface carbon storage and provide insight into the origin of the dolomite problem. An eventual understanding of dolomite genesis at low temperatures is not unlikely, despite the still existing controversies at the present moment.

The results of *Chapter 6* provide further insight into the inhibition of abiotic dolomite growth in low temperature systems. Most notably these results support the hypothesis that the first growth layer formed on dolomite substrates poisons the surfaces and inhibits further growth. Additional growth appears to require surface nucleation and results in the formation of a probably non-stoichiometric and/or poorly ordered dolomite-like phase. As such it seems that the most likely route for the formation of dolomite in natural systems may be via the

recrystallization of a poorly crystalline and/or non-stoichiometric and/or disordered protodolomite such as suggested by Kaczmarek and Sibley (2014) and Montes-Hernandez *et al.* (2014).

REFERENCES

- Aagaard P. and Helgeson H.C. (1982) Thermodynamic and kinetic constraints on reaction rates among minerals and aqueous solutions. I. Theoretical considerations. *American Journal of Science*, **282**, 237-285.
- Akao M., Marumo F. and Iwai S. (1974) The crystal structure of hydromagnesite. *Acta Crystallographica Section B*, **30**, 2670-2672.
- Aldushin K., Jordan G., Rammensee W., Schmahl W.W. and Becker H.-W. (2004) Apophyllite (001) surface alteration in aqueous solutions studied by HAFM. *Geochimica et Cosmochimica Acta*, **68**, 217-226.
- Alexander G., Maroto-Valer M.M. and Gafarova-Aksoy P. (2007) Evaluation of reaction variables in the dissolution of serpentine for mineral carbonation. *Fuel*, **86**, 273-281.
- Alfredsson H.A., Hardarson B.S., Franzson H. and Gislason S.R. (2008) CO₂ sequestration in basaltic rock at the Hellisheidi site in SW Iceland: Stratigraphy and chemical composition of the rocks at the injection site. *Mineralogical Magazine*, **72**, 1-5.
- Alkattan M., Oelkers E.H., Dandurand J.-L. and Schott J. (2002) An experimental study of calcite dissolution rates at acidic conditions and 25 °C in the presence of NaPO₃ and MgCl₂. *Chemical Geology*, **190**, 291-302.
- Andreani M., Luquot L., Gouze P., Godard M., Hoise E. and Gibert B. (2009) Experimental study of carbon sequestration reactions controlled by the percolation of CO₂-rich brine through peridotites. *Environmental Science & Technology*, **43**, 1226-1231.
- Antao S.M., Mulder W.H., Hassan I., Crichton W.A. and Parise J.B. (2004) Cation disorder in dolomite, CaMg(CO₃)₂, and its influence on the aragonite + magnesite ↔ dolomite reaction boundary. *American Mineralogist*, **89**, 1142-1147.
- Aradóttir E.S.P., Sonnenthal E.L., Björnsson G. and Jónsson H. (2012) Multidimensional reactive transport modeling of CO₂ mineral sequestration in basalts at the Hellisheidi geothermal field, Iceland. *International Journal of Greenhouse Gas Control*, **9**, 24-40.
- Archer D.G. (1992) Thermodynamic properties of the NaCl + H₂O system. II. Thermodynamic properties of NaCl(aq), NaCl·2H₂O(cr), and phase equilibria. *Journal of Physical & Chemical Reference Data*, **21**, 793-829.
- Arvidson R.S. and Mackenzie F.T. (1999) The dolomite problem: Control of precipitation kinetics by temperature and saturation state. *American Journal of Science*, **299**, 257-288.
- Arvidson R.S. and Mackenzie F.T. (2000) Temperature dependence of mineral precipitation rates along the CaCO₃-MgCO₃ join. *Aquatic Geochemistry*, **6**, 249-256.
- Astilleros J.M., Fernández-Díaz L. and Putnis A. (2010) The role of magnesium in the growth of calcite: An AFM study. *Chemical Geology*, **271**, 52-58.
- Astilleros J.M., Pina C.M., Fernández-Díaz L., Prieto M. and Putnis A. (2006) Nanoscale phenomena during the growth of solid solutions on calcite {10 $\bar{1}$ 4} surfaces. *Chemical Geology*, **225**, 322-335.

- Astilleros J.M., Pina C.M., Fernández-Díaz L. and Putnis A. (2003) Metastable phenomena on calcite {10 $\bar{1}$ 4} surfaces growing from Sr²⁺-Ca²⁺-CO₃²⁻ aqueous solutions. *Chemical Geology*, **193**, 93-107.
- Baker P.A. and Kastner M. (1981) Constraints on the formation of sedimentary dolomite. *Science*, **213**, 214-216.
- Ballirano P., De Vito C., Ferrini V. and Mignardi S. (2010) The thermal behaviour and structural stability of nesquehonite, MgCO₃·3H₂O, evaluated by in situ laboratory parallel-beam x-ray powder diffraction: New constraints on CO₂ sequestration within minerals. *Journal of Hazardous Materials*, **178**, 522-528.
- Barnes J. and Back W. (1964) Dolomite solubility in ground water. *United States Geological Survey Professional Paper*, **475-D**, 179-180.
- Béarat H., McKelvy M.J., Chizmeshya A.V.G., Gormley D., Nunez R., Carpenter R.W., Squires K. and Wolf G.H. (2006) Carbon sequestration via aqueous olivine mineral carbonation: Role of passivating layer formation. *Environmental Science & Technology*, **40**, 4802-4808.
- Beinlich A., Mavromatis V., Austrheim H. and Oelkers E.H. (2014) Inter-mineral Mg isotope fractionation during hydrothermal ultramafic rock alteration – Implications for the global Mg-cycle. *Earth & Planetary Science Letters*, **392**, 166-176.
- Bénézech P., Dandurand J.-L. and Harrichoury J.-C. (2009) Solubility product of siderite (FeCO₃) as a function of temperature (25-250 °C). *Chemical Geology*, **265**, 3-12.
- Bénézech P., Palmer D.A., Anovitz L.M. and Horita J. (2007) Dawsonite synthesis and reevaluation of its thermodynamic properties from solubility measurements: implications for mineral trapping of CO₂. *Geochimica et Cosmochimica Acta*, **71**, 4438-4455.
- Bénézech P., Saldi G.D., Dandurand J.-L. and Schott J. (2011) Experimental determination of the solubility product of magnesite at 50 to 200 °C. *Chemical Geology*, **286**, 21-31.
- Berger G., Cadore E., Schott J. and Dove P.M. (1994) Dissolution rate of quartz in lead and sodium electrolyte solutions between 25 and 300 °C: Effect of the nature of surface complexes and reaction affinity. *Geochimica et Cosmochimica Acta*, **58**, 541-551.
- Berman R.G. (1988) Internally consistent thermodynamic data for minerals in the system Na₂O-K₂O-CaO-MgO-FeO-Fe₂O₃-Al₂O₃-SiO₂-TiO₂-H₂O-CO₂. *Journal of Petrology*, **29**, 445-522.
- Berner E.K. and Berner R.A. (1996) *Global environment: Water, air, and geochemical cycles*. Prentice Hall, Englewood Cliffs, New Jersey. 376 pp.
- Berner R.A. (1975) The role of magnesium in the crystal growth of calcite and aragonite from seawater. *Geochimica et Cosmochimica Acta*, **39**, 489-504.
- Berner R.A. (2004) A model for calcium, magnesium and sulfate in seawater over Phanerozoic time. *American Journal of Science*, **304**, 438-453.
- Berninger U.-N., Jordan G., Lindner M., Reul A., Schott J. and Oelkers E.H. (2016) On the effect of aqueous Ca on magnesite growth – Insight into trace element inhibition of carbonate mineral growth. *Geochimica et Cosmochimica Acta*, **178**, 195-209.

- Berninger U.-N., Jordan G., Schott J. and Oelkers E.H. (2014) The experimental determination of hydromagnesite precipitation rates at 22.5 to 75 °C. *Mineralogical Magazine*, **78**, 1405-1416.
- Bischoff W.D., Sharma S.K. and Mackenzie F.T. (1985) Carbonate ion disorder in synthetic and biogenic magnesian calcites: A Raman spectral study. *American Mineralogist*, **70**, 581-589.
- Bock C.W. (1994) Coordination of water to magnesium cations. *Inorganic Chemistry*, **33**, 419-427.
- Bolou-Bi E.B., Vigier N., Brenot A. and Poszwa A. (2009) Magnesium isotope compositions of natural reference materials. *Geostandards & Geoanalytical Research*, **33**, 95-109.
- Bracco J.N., Grantham M.C. and Stack A.G. (2012) Calcite growth rates as a function of aqueous calcium-to-carbonate ration, saturation index, and inhibitor concentration: Insight into the mechanism of reaction and poisoning by strontium. *Crystal Growth & Design*, **12**, 3540-3548.
- Bracco J.N., Stack A.G. and Higgins S.R. (2014) Magnesite step growth rates as a function of the aqueous magnesium:carbonate ratio. *Crystal & Growth Design*, **14**, 6033-6040.
- Brown P.L., Drummond S.E. and Palmer D.A. (1996) Hydrolysis of magnesium (II) at elevated temperatures. *Journal of the Chemical Society-Dalton Transactions*, **1996**, 3071-3075.
- Brunauer S., Emmett P. and Teller E. (1938) Adsorption of gases in multimolecular layers. *Journal of the American Chemical Society*, **60**, 309-319.
- Bryan S.P. and Marchitto T.M. (2008) Mg/Ca-temperature proxy in benthic foraminifera: New calibrations from the Florida Straits and a hypothesis regarding Mg/Li. *Paleoceanography*, **23**, PA2220.
- Burton E.A. and Walter L.M. (1987) Relative precipitation rates of aragonite and Mg calcite from seawater: Temperature or carbonate ion control? *Geology*, **15**, 111-114.
- Case D.H., Wang F. and Giammar D.E. (2011) Precipitation of magnesium carbonates as a function of temperature, solution composition, and presence of a silicate mineral substrate. *Environmental Engineering Science*, **28**, 881-889.
- Chai L. and Navrotsky A. (1993) Thermochemistry of carbonate-pyroxene equilibria. *Contributions to Mineralogy & Petrology*, **114**, 139-147.
- Chen Z.Y., O'Connor W.K. and Gerdemann S.J. (2006) Chemistry of aqueous mineral carbonation for carbon sequestration and explanation of experimental results. *Environmental Progress*, **25**, 161-166.
- Chou L., Garrels R.M. and Wollast R. (1989) Comparative study of the kinetics and mechanisms of dissolution of carbonate minerals. *Chemical Geology*, **78**, 269-282.
- Coggon R.M., Teagle D.A.H., Smith-Duque C.E., Alt J.C. and Cooper M.J. (2010) Reconstructing past seawater Mg/Ca and Sr/Ca from mid-ocean ridge flank calcium carbonate veins. *Science*, **327**, 1114-1117.

- Compton R.G. and Brown C.A. (1994) The inhibition of calcite dissolution/precipitation: Mg^{2+} cations. *Journal of Colloid & Interface Science*, **165**, 445-449.
- Criss C.M. and Cobble J.W. (1964) The thermodynamic properties of high temperature aqueous solutions. V. The calculation of ionic heat capacities up to 200 °C. Entropies and heat capacities above 200 °C. *Journal of the American Chemical Society*, **86**, 5390-5393.
- Criss R.E. (1999) *Principles of stable isotope distribution*. Oxford University Press, New York, 254 pp.
- Curti E., Fujiwara K., Iijima K., Tits J., Cuesta C., Kitamura A., Glaus M.A. and Müller W. (2010) Radium uptake during barite recrystallization at 23 ± 2 °C as a function of solution composition: An experimental ^{133}Ba and ^{226}Ra tracer study. *Geochimica et Cosmochimica Acta*, **74**, 3553-3570.
- Daval D., Sissmann O., Menguy N., Saldi G.D., Guyot F., Martinez I., Crovixier J., Garcia B., Machouk I., Knauss K. and Hellmann R. (2011) Influence of amorphous silica layer formation on the dissolution rate of olivine at 90 °C and elevated pCO_2 . *Chemical Geology*, **284**, 193-209.
- Davis K.J., Dove P.M. and De Yoreo J.J. (2000) The role of Mg^{2+} as an impurity in calcite growth. *Science*, **290**, 1134-1137.
- Davis K.J., Dove P.M., Wasylenki L.E. and De Yoreo J.J. (2004) Morphological consequences of differential Mg^{2+} incorporation at structurally distinct steps on calcite. *American Mineralogist*, **89**, 714-720.
- Debure M., Frugier P., De Windt L. and Gin S. (2013) Dolomite effect on borosilicate glass alteration. *Applied Geochemistry*, **33**, 237-251.
- Declercq J., Bosc O. and Oelkers E.H. (2013) Do organic acids affect forsterite dissolution rates? *Applied Geochemistry*, **39**, 69-77.
- Deleuze M. and Brantley S. (1997) Inhibition of calcite crystal growth by Mg^{2+} at 100 °C and 100 bars: Influence of growth regime. *Geochimica et Cosmochimica Acta*, **61**, 1475-1485.
- De Yoreo J.J. and Vekilov P. (2003) Principles of crystal nucleation and growth. *Reviews in Mineralogy & Geochemistry*, **54**, 57-93.
- Dickson J.A.D. (2002) Fossil echinoderms as monitor of the Mg/Ca ratio of Phanerozoic oceans. *Science*, **298**, 1222-1224.
- Di Tommaso D. and de Leeuw N.H. (2010) Structure and dynamics of the hydrated magnesium ion and of the solvated magnesium carbonates: Insights from first principles simulations. *Physical Chemistry Chemical Physics*, **12**, 894-901.
- Druhan J.L., Steefel C.I., Williams K.H. and DePaolo D.J. (2013) Calcium isotope fractionation in groundwater: Molecular scale processes influencing field scale behavior. *Geochimica et Cosmochimica Acta*, **119**, 93-116.
- Duckworth O.W. and Martin S.T. (2004) Dissolution rates and pit morphologies of rhombohedral carbonate minerals. *American Mineralogist*, **89**, 554-563.

- Dufaud F., Martinez I. and Shilobeeva S. (2009) Experimental study of Mg-rich silicates carbonation at 400 and 500 °C and 1 kbar. *Chemical Geology*, **265**, 79-87.
- Elderfield H., Yu J., Anand P., Kiefer T. and Nyland B. (2006) Calibrations for benthic foraminiferal Mg/Ca paleothermometry and the carbonate ion hypothesis. *Earth & Planetary Science Letters*, **250**, 633-649.
- Fantle M.S. (2015) Calcium isotopic evidence for rapid recrystallization of bulk marine carbonated and implications for geochemical proxies. *Geochimica et Cosmochimica Acta*, **148**, 378-401.
- Fantle M.S. and DePaolo D.J. (2007) Ca isotopes in carbonate sediment and pore fluid from ODP Site 807A: The Ca²⁺(aq)-calcite equilibrium fractionation factor and calcite recrystallization rates in Pleistocene sediments. *Geochimica et Cosmochimica Acta*, **71**, 2524-2546.
- Fantle M.S. and Higgins J. (2014) The effects of diagenesis and dolomitization on Ca and Mg isotopes in platform carbonates: Implications for the geochemical cycles of Ca and Mg. *Geochimica et Cosmochimica Acta*, **142**, 458-481.
- Fantle M.S., Maher K.M. and DePaolo D.J. (2010) Ca isotopic approaches for quantifying rates of marine burial diagenesis. *Reviews of Geophysics*, **48**, RG3002.
- Felmy A.R., Qafoku O., Arey B.W., Hu J.Z., Hu M., Schaef H.T., Ilton E.S., Hess N.J., Pearce C.I., Feng J. and Rosso K.M. (2012) Reaction of water-saturated supercritical CO₂ with forsterite: Evidence for magnesite formation at low temperatures. *Geochimica et Cosmochimica Acta*, **91**, 271-282.
- Felmy A.R., Qafoku O., Arey B.W., Kovarik L., Liu J., Perea D. and Ilton E.S. (2015) Enhancing magnesite formation at low temperature and high CO₂ pressure: The impact of seed crystals and minor components. *Chemical Geology*, **395**, 119-125.
- Fiquet G. and Reynard B. (1999) High-pressure equation of state of magnesite: New data and a reappraisal. *American Mineralogist*, **84**, 856-860.
- Flaathen T.K., Oelkers E.H., Gislason S.R. and Aagaard P. (2011) The effect of dissolved sulphate on calcite precipitation kinetics and consequences for subsurface CO₂ storage. *Energy Procedia*, **4**, 5037-5043.
- Freij S.J., Putnis A. and Astilleros J.M. (2004) Nanoscale observations of the effect of cobalt on calcite growth and dissolution. *Journal of Crystal Growth*, **267**, 288-300.
- Frost R.L., Bahfenne S., Graham J. and Martens W.N. (2008) Thermal stability of artinite, dypingite and brugnatellite – Implications for the geosequestration of greenhouse gases. *Thermochimica Acta*, **475**, 39-43.
- Galy A., Bar-Matthews M., Halicz L. and O’Nions R.K. (2002) Mg isotopic composition of carbonate: Insight from speleothem formation. *Earth & Planetary Science Letters*, **201**, 105-115.
- Garcia B., Beaumont V., Perfetti E., Rouchon V., Blanchet D., Oger P., Dromart G., Huc A.-Y. and Haeseler F. (2010) Experiments and geochemical modelling of CO₂ sequestration by olivine: Potential, quantification. *Applied Geochemistry*, **25**, 1383-1396.

- Garrels R.M., Thompson M.E. and Siever R. (1960) Stability of some carbonates at 25 °C and one atmosphere total pressure. *American Journal of Science*, **258**, 402-418.
- Gautelier M., Schott J. and Oelkers E.H. (2007) An experimental study of dolomite dissolution rates at 80 °C as a function of chemical affinity and solution composition. *Chemical Geology*, **242**, 509-517.
- Gautier Q. (2012) *Cinétiques de précipitation de minéraux carbonatés magnésiens, influence de ligands organiques, et conséquences pour la séquestration minérale du CO₂*. Ph.D.-thesis at Université Paris-Est, 248 pp.
- Gautier Q., Bénézech P., Mavromatis V. and Schott J. (2014) Hydromagnesite solubility product and growth kinetics in aqueous solution from 25 to 75 °C. *Geochimica et Cosmochimica Acta*, **138**, 1-20.
- Gautier Q., Berninger U.-N., Schott J. and Jordan G. (2015) Influence of organic ligands on magnesite growth: A hydrothermal atomic force microscopy study. *Geochimica et Cosmochimica Acta*, **155**, 68-85.
- Gerdemann S.J., O'Connor W.K., Dahlin D.C., Penner L.R. and Rush H. (2007) Ex situ aqueous mineral carbonation. *Environmental Science & Technology*, **41**, 2587-2593.
- Geske A., Goldstein R.H., Mavromatis V., Richter D.K., Buhl D., Kluge T., John C.M. and Immenhauser A. (2015) The magnesium isotope ($\delta^{26}\text{Mg}$) signature of dolomites. *Geochimica et Cosmochimica Acta*, **149**, 131-151.
- Giammar D.E., Bruant R.G. and Peters C.A. (2005) Forsterite dissolution and magnesite precipitation at conditions relevant for deep saline aquifer storage and sequestration of carbon-dioxide. *Chemical Geology*, **217**, 257-276.
- Gislason S.R. and Oelkers E.H. (2014) Carbon storage in basalt. *Science*, **344**, 373-374.
- Gislason S.R., Wolff-Boenisch D., Stefánsson A., Oelkers E.H., Gunnlaugsson E., Sigurdardóttir H., Sigfússon G., Brocker W.S., Matter J., Stute M., Axelsson G. and Fridriksson T. (2010) Mineral sequestration of carbon dioxide in basalt: A pre-injection overview of the CarbFix project. *International Journal of Greenhouse Gas Control*, **4**, 537-545.
- Gledhill D.K. and Morse J.W. (2006) Calcite dissolution kinetics in Na-Ca-Mg-Cl brines. *Geochimica et Cosmochimica Acta*, **70**, 5802-5813.
- Graf D.L. and Goldsmith J.R. (1956) Some hydrothermal syntheses of dolomite and protodolomite. *Journal of Geology*, **64**, 173-186.
- Gregg J.M., Bish D.L., Kaczmarek S.E. and Machel H.G. (2015) Mineralogy, nucleation and growth of dolomite in the laboratory and sedimentary environment: A review. *Sedimentology*, **62**, 1749-1769.
- Gutjahr A., Dabringhaus H. and Lacmann R. (1996) Studies of growth and dissolution kinetics of the CaCO₃ polymorphs calcite and aragonite II. The influence of divalent cation additives on the growth and dissolution rates. *Journal of Crystal Growth*, **158**, 310-315.
- Gysi A.P. and Stefánsson A. (2008) Numerical modelling of CO₂-water-basalt interaction. *Mineralogical Magazine*, **72**, 55-59.

- Gysi A.P. and Stefánsson A. (2012) CO₂-water-basalt interaction. Low temperature experiments and implications for CO₂ sequestration into basalts. *Geochimica et Cosmochimica Acta*, **81**, 129-152.
- Hänchen M., Prigiobbe V., Baciocchi R. and Mazzotti M. (2008) Precipitation in the Mg-carbonate system-effects of temperature and CO₂ pressure. *Chemical Engineering Science*, **63**, 1012-1028.
- Hänchen M., Prigiobbe V., Storti G., Seward T.M. and Mazzotti M. (2006) Dissolution kinetics of fosteritic olivine at 90-150 °C including effects of the presence of CO₂. *Geochimica et Cosmochimica Acta*, **70**, 4403-4416.
- Halla V.F. and Van Tassel R. (1965) Auflösungserscheinungen bei Erdalkal karbonaten I. *Radex-Rundschau*, **4**, 595-599.
- Hardie L.A. (1996) Secular variation in seawater chemistry: An explanation for the coupled secular variation in the mineralogies of marine limestones and potash evaporates over the past 600 m.y. *Geology*, **24**, 279-283.
- Harouiya N., Chairat C., Köhler S.K., Gout R. and Oelkers E.H. (2007) The dissolution kinetics and apparent solubility of natural apatite in close system reactors at temperatures from 5 to 50 °C and pH from 1 to 6. *Chemical Geology*, **244**, 554-568.
- Healey S.L., Thunell R.C. and Corliss B.H. (2008) The Mg/Ca-temperature relationship of benthic foraminiferal calcite: New core-top calibrations in the < 4 °C temperature range. *Earth & Planetary Science Letters*, **272**, 523-530.
- Helgeson H.C. (1969) Thermodynamics of hydrothermal systems at elevated temperatures and pressures. *American Journal of Science*, **267**, 729-804.
- Helgeson H.C., Delaney J.M., Nesbitt H.W. and Bird D.K. (1978) Summary and critique of the thermodynamic properties of rock forming minerals. *American Journal of Science*, **278A**, 1-228.
- Hemingway B.S. and Robie R.A. (1994) Enthalpy and Gibbs energy of formation of dolomite, CaMg(CO₃)₂, at 298.15 K from HCl solution calorimetry. *United States Geological Survey, Open-File Report*, 94-575.
- Higgins J.A. and Schrag D.P. (2010) Constraining magnesium cycling in marine sediments using magnesium isotopes. *Geochimica et Cosmochimica Acta*, **74**, 5039-5053.
- Higgins J.A. and Schrag D.P. (2015) The Mg isotopic composition of Cenozoic seawater – evidence for a link between Mg-clays, seawater Mg/Ca, and climate. *Earth & Planetary Science Letters*, **416**, 73-81.
- Higgins S.R. and Hu X. (2005) Self-limiting growth on dolomite: Experimental observations with in situ atomic force microscopy. *Geochimica et Cosmochimica Acta*, **69**, 2085-2094.
- Higgins S.R., Eggleston C.M., Knauss K.G. and Boro C.O. (1998) A hydrothermal atomic force microscope for imaging in aqueous solution up to 150 °C. *Review of Scientific Instruments*, **69**, 2994-2998.

- Higgins S.R., Jordan G. and Eggleston C.M. (2002) Dissolution kinetics of magnesite in acidic aqueous solution: A hydrothermal atomic force microscopy study assessing step kinetics and dissolution flux. *Geochimica et Cosmochimica Acta*, **66**, 3201-3210.
- Hoefs J. (1973) *Stable isotope geochemistry*. Springer-Verlag, Berlin, 140 pp.
- Holland H.D. (2005) Sea level, sediments, and the composition of seawater. *American Journal of Science*, **305**, 220-239.
- Holland T.J.B. and Powell R. (1990) An enlarged and updated internally consistent thermodynamic dataset with uncertainties and correlations: The system $K_2O-Na_2O-CaO-MgO-MnO-FeO-Fe_2O_3-Al_2O_3-TiO_2-SiO_2-C-H_2-O_2$. *Journal of Metamorphic Geology*, **8**, 89-124.
- Hsu K.J. (1963) Solubility of dolomite and composition of Florida groundwaters. *Journal of Hydrology*, **1**, 288-310.
- Hu X., Grossie D.A. and Higgins S.R. (2005) Growth and dissolution kinetics at the dolomite-water interface: An in-situ scanning probe microscopy study. *American Mineralogist*, **90**, 963-968.
- Hu X., Joshi P., Mukhopadhyay S.M. and Higgins S.R. (2006) X-ray photoelectron spectroscopic studies of dolomite surfaces exposed to undersaturated and supersaturated aqueous solutions. *Geochimica et Cosmochimica Acta*, **70**, 3342-3350.
- Isshiki M., Irifune T., Hirose K., Ono S., Ohishi Y., Watanuki T., Nishibori E., Takata M. and Sakata M. (2004) Stability of magnesite and its high-pressure form in the lowermost mantle. *Nature*, **427**, 60-63.
- Johnson J.W., Oelkers E.H. and Helgeson H.C. (1992) SUPCRT92: A software package for calculating the standard molal properties of minerals gases, aqueous species and reactions among them from 1 to 5000 bars and 0 to 1000 °C. *Computers & Geosciences*, **18**, 899-947.
- Jordan G. and Astilleros J.M. (2006) In situ HAFM study of the thermal dehydration on gypsum (010) surfaces. *American Mineralogist*, **91**, 619-627.
- Jordan G., Higgins S.R., Egglestone C.M., Knauss K.G. and Schmahl W.W. (2001) Dissolution kinetics of magnesite in acidic aqueous solution, a hydrothermal atomic force microscopy (HAFM) study: Step orientation and kink dynamics. *Geochimica et Cosmochimica Acta*, **65**, 4257-4266.
- Jordan G., Pokrovsky O.S., Guichet X. and Schmahl W.W. (2007) Organic and inorganic ligand effects on magnesite dissolution at 100 °C and pH = 5 to 10. *Chemical Geology*, **242**, 484-496.
- Kaczmarek S.E. and Sibley D.F. (2014) Direct physical evidence of dolomite recrystallization. *Sedimentology*, **61**, 1862-1882.
- Kasemann S.A., Pogge von Strandmann P.A.E., Prave A.R., Fallick T.E., Elliott T. and Hoffmann K.-H. (2014) Continental weathering following Cryogenian glaciation: Evidence from calcium and magnesium isotopes. *Earth & Planetary Science Letters*, **396**, 66-74.

- Kaszuba J.P., Navarre-Sitchler A., Thyne G., Chopping C. and Meuzelaar T. (2011) Supercritical carbon-dioxide and sulfur in the Madison Limestone: A natural analog in southwest Wyoming for geologic carbon-sulfur co-sequestration. *Earth & Planetary Science Letters*, **309**, 131-140.
- Katz A.K., Glusker J.P., Beebe S.A. and Bock C.W. (1996) Calcium ion coordination: A comparison with that of beryllium, magnesium, and zinc. *Journal of the American Chemical Society*, **118**, 5752-5763.
- Kessels L.A., Sibley D.F. and Nordeng S.H. (2000) Nanotopography of synthetic and natural dolomite crystals. *Sedimentology*, **47**, 173-186.
- King H.E., Plümper O. and Putnis A. (2010) Effect of secondary phase formation on the carbonation of olivine. *Environmental Science & Technology*, **44**, 6503-6509.
- King H.E., Satoh H., Tsukamoto K. and Putnis A. (2013) Nanoscale observations of magnesite growth in chloride- and sulfate-rich solutions. *Environmental Science & Technology*, **47**, 8684-8691.
- Kramer J.R. (1959) Correction of some earlier data on calcite and dolomite in sea water. *Journal of Sedimentary Petrology*, **29**, 465-467.
- Krishnamurti D. (1956) Raman spectrum of magnesite. *Proceedings of the Indian Academy of Sciences Section A*, **43**, 210-212.
- Krupka K.M., Hemingway B.S., Robie R.A. and Kerrick D.M. (1985) High-temperature heat capacities and derived thermodynamic properties of anthophyllite, diopside, dolomite, enstatite, bronzite, talc, tremolite, and wollastonite. *American Mineralogist*, **70**, 261-271.
- Lackner K.S., Wendt C.H., Butt D.P., Joyce E.L. and Sharp D.H. (1995) Carbon dioxide disposal in carbonate minerals. *Energy*, **20**, 1153-1170.
- Lakshtanov L.Z. and Stipp S.L.S. (2010) Interaction between silica and calcium carbonate: 1. Spontaneous precipitation of calcium carbonate in the presence of dissolved silica. *Geochimica et Cosmochimica Acta*, **74**, 2655-2664.
- Land L.S. (1998) Failure to precipitate dolomite at 25 °C from dilute solution despite 1000-fold oversaturation after 32 years. *Aquatic Geochemistry*, **4**, 361-368.
- Langmuir D. (1964) *Stability of carbonates in the system CaO-MgO-CO₂-H₂O*. Ph.D.-thesis at Harvard University, 142 pp.
- Langmuir D. (1971) The geochemistry of some carbonate ground waters in central Pennsylvania. *Geochimica et Cosmochimica Acta*, **35**, 1023-1045.
- Lea D.W., Mashiotto T.A. and Spero H.J. (1999) Controls on magnesium and strontium uptake in planktonic foraminifera determined by live culturing. *Geochimica et Cosmochimica Acta*, **63**, 2369-2379.
- Lear C.H., Rosenthal Y. and Slowey N. (2002) Benthic foraminiferal Mg/Ca-paleothermometry: A revised core-top calibration. *Geochimica et Cosmochimica Acta*, **66**, 3375-3387.

- Li W., Beard B.L. and Johnson C.M. (2011) Exchange and fractionation of Mg isotopes between epsomite and saturated MgSO₄ solution. *Geochimica et Cosmochimica Acta*, **75**, 1814-1824.
- Li W., Beard B.L., Li C., Xu H. and Johnson C.M. (2014) Magnesium isotope fractionation between brucite (Mg(OH)₂) and Mg aqueous species: Implications for silicate weathering and biogeochemical processes. *Earth & Planetary Science Letters*, **394**, 82-93.
- Li W., Beard B.L., Li C., Xu H. and Johnson C.M. (2015) Experimental calibration of Mg isotope fractionation between dolomite and aqueous solution and its geological implications. *Geochimica et Cosmochimica Acta*, **157**, 164-181.
- Li W., Chakraborty S., Beard B.L., Romanek C.S. and Johnson C.M. (2012) Magnesium isotope fractionation during precipitation of inorganic calcite under laboratory conditions. *Earth & Planetary Science Letters*, **333-334**, 304-316.
- Lin Y.-P. and Singer P.C. (2009) Effect of Mg²⁺ on the kinetics of calcite crystal growth. *Journal of Crystal Growth*, **312**, 136-140.
- Lincoln S.F. and Merbach A.E. (1995) Substitution reactions of solvated metal ions. In: Sykes A.G. (ed.) *Advances in Inorganic Chemistry*, vol. 42, pp. 1-88, Academic Press, San Diego.
- Lippmann F. (1973) *Sedimentary carbonate minerals*. Springer-Verlag, New York, 228 pp.
- Liu F., Lu P., Zhu C. and Xiao Y. (2011) Coupled reactive flow and transport modeling of CO₂ sequestration in the Mt. Simon sandstone formation, Midwest U.S.A.. *International Journal of Greenhouse Gas Control*, **5**, 294-307.
- Lorens R.B. (1981) Sr, Cd, Mn and Co distribution coefficient in calcite as a function of calcite precipitation rate. *Geochimica et Cosmochimica Acta*, **45**, 553-561.
- Loring J.S., Thompson C.J., Zhang C., Wang Z., Schaefer H.T. and Rosso K.M. (2012) In situ infrared spectroscopic study of brucite carbonation in dry to water-saturated supercritical carbon dioxide. *Journal of Physical Chemistry A*, **116**, 4768-4777.
- Lowenstein T.K., Timofeeff M.N., Brennan S.T., Hardie L.A. and Demicco R.V. (2001) Oscillations in Phanerozoic seawater chemistry: Evidence from fluid inclusions. *Science*, **294**, 1086-1088.
- Machel H.G. (2004) Concepts and models of dolomitization: A critical reappraisal. In: Braithwaite *et al.* (eds.) *The geometry and petrogenesis of dolomite hydrocarbon reservoirs*, pp. 7-63, The Geological Society of London, Special Publication 235.
- Mackenzie F.T. and Andersson A.J. (2013) The marine carbon system and ocean acidification during Phanerozoic time. *Geochemical Perspectives*, **2**, 1-227.
- Mackenzie F.T. and Morse J.W. (1992) Sedimentary carbonates through Phanerozoic time. *Geochimica et Cosmochimica Acta*, **56**, 3281-3295.
- Marini L. (2007) *Geological sequestration of carbon dioxide: Thermodynamics, kinetics, and reaction path modeling*. Elsevier, Amsterdam, 470 pp.

- Maroto-Valer M.M., Fauth D.J., Kuchta M.E., Zhang Y. and Andresen J.M. (2005) Activation of magnesium rich minerals as carbonation feedstock materials for CO₂ sequestration. *Fuel Processing Technology*, **86**, 1627-1645.
- Matter J.M., Broecker W.S., Gislason S.R., Gunnlaugsson E., Oelkers E.H., Stute M., Sigurdardóttir H., Stefánsson A., Alfredsson H.A., Aradóttir E.S., Axelsson G., Sigfússon B. and Wolff-Boenisch D. (2011) The CarbFix Pilot Project – Storing carbon dioxide in basalt. *Energy Procedia*, **4**, 5579-5585.
- Matter J.M., Broecker W.S., Stute M., Gislason S.R., Oelkers E.H., Stefánsson A., Wolff-Boenisch D., Gunnlaugsson E., Axelsson G. and Björnsson G. (2009) Permanent carbon dioxide storage into basalt: The CarbFix pilot project, Iceland. *Energy Procedia*, **1**, 3641-3646.
- Mavromatis V., Bundeleva I.A., Shirokova L.S., Millo C., Pokrovsky O.S., Bénézech P., Ader M. and Oelkers E.H. (2015) The continuous re-equilibration of carbon isotope compositions of hydrous Mg carbonates in the presence of cyanobacteria. *Chemical Geology*, **404**, 41-51.
- Mavromatis V., Gautier Q., Bosc O. and Schott J. (2013) Kinetics of Mg partition and Mg stable isotope fractionation during its incorporation in calcite. *Geochimica et Cosmochimica Acta*, **114**, 188-203.
- Mavromatis V., Meister P. and Oelkers E.H. (2014a) Using stable Mg isotopes to distinguish dolomite formation mechanisms: A case study from the Peru Margin. *Chemical Geology*, **385**, 84-91.
- Mavromatis V., Pearce C.R., Shirokova L.S., Bundeleva I.A., Pokrovsky O.S., Bénézech P. and Oelkers E.H. (2012) Magnesium isotope fractionation during hydrous magnesium carbonate precipitation with and without cyanobacteria. *Geochimica et Cosmochimica Acta*, **76**, 161-174.
- Mavromatis V., Prokushkin A.S., Pokrovsky O.S., Viers J. and Korets M.A. (2014b) Magnesium isotopes in permafrost-dominated Central Siberian larch forest watersheds. *Geochimica et Cosmochimica Acta*, **147**, 76-89.
- McGrail B.P., Schaef H.T., Ho A.M., Chien Y.-J., Dooley J.J. and Davidson C.L. (2006) Potential for carbon dioxide sequestration in flood basalts. *Journal of Geophysical Research-Solid Earth*, **111**, B12201.
- Millero F., Huang F., Graham T. and Pierrot D. (2007) The dissociation of carbonic acid in NaCl solutions as a function of concentration and temperature. *Geochimica et Cosmochimica Acta*, **71**, 46-55.
- Montes-Hernandez G., Findling N., Renard F. and Auzende A.-L. (2014) Precipitation of ordered dolomite via simultaneous dissolution of calcite and magnesite: New experimental insights into an old precipitation enigma. *Crystal Growth & Design*, **14**, 671-677.
- Moore J., Adams M., Allis R., Lutz S. and Rauzi. S. (2005) Mineralogical and geochemical consequences of the long term presence of CO₂ in natural reservoirs: An example of the Springerville-St. Johns Field, Arizona and New Mexico. *Chemical Geology*, **201**, 365-385.

- Moreira N.F., Walter L.M., Vasconcelos C., McKenzie J.A. and McCall P.J. (2004) Role of sulfide oxidation in dolomitization: sediment and pore-water geochemistry of a modern hypersaline lagoon system. *Geology*, **32**, 701-704.
- Morse J.W. and Arvidson R.S. (2002) The dissolution kinetics of major sedimentary carbonate minerals. *Earth-Science Reviews*, **58**, 51-84.
- Morse J.W., Arvidson R.S. and Lüttge A. (2007) Calcium carbonate formation and dissolution. *Chemical Reviews*, **107**, 342-381.
- Mucci A. and Morse J.W. (1983) The incorporation of Mg^{2+} and Sr^{2+} into calcite overgrowths: Influences of growth rate and solution composition. *Geochimica et Cosmochimica Acta*, **47**, 217-233.
- Müller M.N., Kısakürek B., Buhl D., Gutperlet R., Kolevica A., Riesbesell U., Stoll H. and Eisenhauer A. (2011) Response of the coccolithophores *Emiliania huxleyi* and *Coccolithus braarudii* to changing seawater Mg^{2+} and Ca^{2+} concentrations: Mg/Ca, Sr/Ca ratios and $\delta^{44/40}Ca$, $\delta^{26/24}Mg$ of coccolith calcite. *Geochimica et Cosmochimica Acta*, **75**, 2088-2102.
- Naumov G.B., Ryzhenko B.N. and Khodakovskii I.L. (1974) *Handbook of thermodynamic data*. National Technical Information Service PB-226 722, United States Geological Survey Water-resources, 328 pp.
- Navrotsky A. and Capobianco C. (1987) Enthalpies of formation of dolomite and magnesian calcites. *American Mineralogist*, **75**, 782-787.
- Nielsen A.E. (1984) Electrolyte crystal growth mechanisms. *Journal of Crystal Growth*, **67**, 289-310.
- Nielsen L.C., De Yoreo J.J. and DePaolo D.J. (2013) General model for calcite growth kinetics in the presence of impurity ions. *Geochimica et Cosmochimica Acta*, **115**, 100-114.
- Oelkers E.H. (2001a) An experimental study of forsterite dissolution rates as a function of temperature and aqueous Mg and Si concentrations. *Chemical Geology*, **175**, 485-494.
- Oelkers E.H. (2001b) General kinetic description of multioxide silicate mineral and glass dissolution. *Geochimica et Cosmochimica Acta*, **65**, 3703-3719.
- Oelkers E.H. and Cole D.R. (2008) Carbon dioxide sequestration: A solution to a global problem. *Elements*, **4**, 305-310.
- Oelkers E.H. and Schott J. (1995) Experimental study of anorthite dissolution and the relative mechanism of feldspar hydrolysis. *Geochimica et Cosmochimica Acta*, **59**, 5039-5053.
- Oelkers E.H. and Schott J. (1999) Experimental study of kyanite dissolution rates as a function of chemical affinity and solution composition. *Geochimica et Cosmochimica Acta*, **63**, 785-797.
- Oelkers E.H. and Schott J. (2001) An experimental study of enstatite dissolution rates as a function of pH, temperature, and aqueous Mg and Si concentration, and the mechanism of pyroxene/pyroxenoid dissolution. *Geochimica et Cosmochimica Acta*, **65**, 1219-1231.

- Oelkers E.H. and Schott J. (2005) Geochemical aspects of CO₂ sequestration. *Chemical Geology*, **217**, 183-186.
- Oelkers E.H., Bénézech P. and Pokrovsky G.S. (2009) Thermodynamic databases for water-rock interaction. *Reviews in Mineralogy & Geochemistry*, **70**, 1-46.
- Oelkers E.H., Gislason S.R. and Matter J. (2008) Mineral carbonation of CO₂. *Elements*, **4**, 333-337.
- Oelkers E.H., Pogge von Strandmann P.A.E. and Mavromatis V. (submitted) The rapid resetting of the Ca isotopic signatures of calcite at ambient temperature via congruent dissolution, precipitation, and at equilibrium. *Geochimica et Cosmochimica Acta*, (2016).
- Oelkers E.H., Schott J. and Devidal J.-L. (1994) The effect of aluminum, pH, and chemical affinity on the rates of aluminosilicate dissolution reactions. *Geochimica et Cosmochimica Acta*, **58**, 2011-2024.
- Oskierski H.C., Dlugogorski B.Z. and Jacobsen G. (2013) Sequestration of atmospheric CO₂ in chrysotile mine tailings of the Woodsreef Asbestos Mine, Australia: Quantitative mineralogy, isotopic fingerprinting and carbonation rates. *Chemical Geology*, **358**, 156-169.
- Park A.H.A. and Fan L.S. (2004) CO₂ mineral sequestration: physically activated dissolution of serpentine and pH swing process. *Chemical Engineering Science*, **59**, 5241-5247.
- Parkhurst D.L. and Appelo C.A.J. (1999) *User's guide to PHREEQC (version 2) - A computer program for speciation, batch-reaction, one-dimensional transport, and inverse geochemical calculations*. United States Geological Survey Water-resources Investigation Report 99-4259, 312 pp.
- Patterson C.S., Busey R.H. and Mesmer R.E. (1984) Second ionization of carbonic acid in NaCl media to 250 °C. *Journal of Solution Chemistry*, **13**, 647-661.
- Patterson C.S., Slocum G.H., Busey R.H. and Mesmer R.E. (1982) Carbonate equilibria in hydrothermal systems: First ionization of carbonic acid in NaCl media to 300 °C. *Geochimica et Cosmochimica Acta*, **46**, 1653-1663.
- Pavlov M., Siegbahn P.E.M. and Sandstrom M. (1998) Hydration of beryllium, magnesium, calcium, and zinc ions using density functional theory. *Journal of Physical Chemistry A*, **102**, 219-228.
- Pearce C.R., Saldi G.D., Schott J. and Oelkers E.H. (2012) Isotopic fractionation during congruent dissolution, precipitation and at equilibrium: Evidence from Mg isotopes. *Geochimica et Cosmochimica Acta*, **92**, 170-183.
- Pina C. and Jordan G. (2010) Reactivity of mineral surfaces at nanoscale: kinetics and mechanisms of growth and dissolution. *EMU Notes in Mineralogy*, **10**, 43-64.
- Plummer L.N. and Busenberg E. (1982) The solubilities of calcite, aragonite and vaterite in CO₂-H₂O solutions between 0 and 90 °C, and an evaluation of the aqueous model for the system CaCO₃-CO₂-H₂O. *Geochimica et Cosmochimica Acta*, **46**, 1011-1040.

- Pogge von Strandmann P.A.E., Burton K.W., James R.H., van Calsteren P., Gislason S.R. and Sigfússon B. (2008) The influence of weathering processes on riverine magnesium isotopes in a basaltic terrain. *Earth & Planetary Science Letters*, **276**, 187-197.
- Pogge von Strandmann P.A.E., Forshaw J. and Schmidt D.N. (2014) Modern and Cenozoic records of seawater magnesium from foraminiferal Mg isotopes. *Biogeosciences*, **11**, 5155-5168.
- Pokrovsky B.G., Mavromatis V. and Pokrovsky O.S. (2011) Co-variation of Mg and C isotopes in late Precambrian carbonates of the Siberian platform: A new tool for tracing the change in weathering regime? *Chemical Geology*, **290**, 67-74.
- Pokrovsky O.S. and Schott J. (1999) Processes at the magnesium-bearing carbonate/solution interface. II. Kinetics and mechanism of magnesite dissolution. *Geochimica et Cosmochimica Acta*, **63**, 881-897.
- Pokrovsky O.S. and Schott J. (2000) Kinetics and mechanism of forsterite dissolution at 25 °C and pH from 1 to 12. *Geochimica et Cosmochimica Acta*, **64**, 3313-3325.
- Pokrovsky O.S. and Schott J. (2001) Kinetics and mechanism of dolomite dissolution in neutral to alkaline solutions revisited. *American Journal of Science*, **301**, 597-626.
- Pokrovsky O.S. and Schott J. (2002) Surface chemistry and dissolution kinetics of divalent metal carbonates. *Environmental Science & Technology*, **36**, 426-432.
- Pokrovsky O.S., Golubev S.V. and Schott J. (2005) Dissolution kinetics of calcite, dolomite and magnesite at 25 °C and 0 to 50 atm pCO₂. *Chemical Geology*, **217**, 239-255.
- Pokrovsky O.S., Golubev S.V., Schott J. and Castillo A. (2009) Calcite, dolomite and magnesite dissolution kinetics in aqueous solutions at acid to circumneutral pH, 25 to 150 °C and 1 to 55 atm pCO₂: New constraints on CO₂ sequestration in sedimentary basins. *Chemical Geology*, **265**, 20-32.
- Politi Y., Batchelor D.R., Zaslansky P., Chmelka B.F., Weaver J.C., Sagi I., Weiner S. and Addadi L. (2010) Role of magnesium ion in the stabilization of biogenic amorphous calcium carbonate: A structure-function investigation. *Chemistry of Materials*, **22**, 161-166.
- Power I.M., Wilson S.A., Harrison A.L., Dipple G.M., McCutcheon J., Southam G. and Kenward P.A. (2014) A depositional model for hydromagnesite-magnesite playas near Atlin, British Columbia, Canada. *Sedimentology*, **61**, 1701-1733.
- Power I.M., Wilson S.A., Thom J.M., Dipple G.M., Gabites J.E. and Southam G. (2009) The hydromagnesite playas of Atlin, British Columbia, Canada: A biogeochemical model for CO₂ sequestration. *Chemical Geology*, **260**, 286-300.
- Power I.M., Wilson S.A., Thom J.M., Dipple G.M. and Southam G. (2007) Biologically induced mineralization of dypingite by cyanobacteria from an alkaline wetland near Atlin, British Columbia, Canada. *Geochemical Transactions*, **8**, 13 pp.
- Prigione V. and Mazzotti M. (2013) Precipitation of Mg-carbonates at elevated temperature and partial pressure of CO₂. *Chemical Engineering Journal*, **223**, 755-763.

- Prigobbe V., Hänchen M., Werner M., Baciocchi R. and Mazzotti M. (2009) Mineral carbonation processes for CO₂ sequestration. *Energy Procedia*, **1**, 4885-4890.
- Pronost J., Beaudoin G., Tremblay J., Larachi F., Duchesne J., Hebert R. and Constantin M. (2011) Carbon sequestration kinetic and storage capacity of ultramafic mining waste. *Environmental Science & Technology*, **45**, 9413-9420.
- Robie R.A. and Hemingway B.S. (1972) The heat capacities at low-temperatures and entropies at 298.15 K of nesquehonite, MgCO₃·3H₂O, and hydromagnesite. *American Mineralogist*, **57**, 1768-1781.
- Robie R.A. and Hemingway B.S. (1973) The enthalpies of formation of nesquehonite, MgCO₃·3H₂O, and hydromagnesite, 5MgO·4CO₂·5H₂O. *Journal of Research of the United States Geological Survey*, **1**, 543-547.
- Robie R.A. and Hemingway B.S. (1995) Thermodynamic properties of minerals and related substances at 298.15 K and 1 bar (10⁵ Pa) pressure and at higher temperatures. *United States Geological Survey Bulletin*, **2131**, 461 pp.
- Robie R.A., Hemingway B.S. and Fisher J.R. (1978) Thermodynamic properties of minerals and related substances at 298.15 K and 1 bar (10⁵ Pascals) pressure and at higher temperatures. *United States Geological Survey Bulletin*, **1452**, reprinted with corrections 1979.
- Rock P.A., Mandell G.K., Casey W.H. and Walling E.M. (2001) Gibbs energy of formation of dolomite from electrochemical cell measurements and theoretical calculations. *American Journal of Science*, **301**, 103-111.
- Rodriguez-Blanco J.D., Shaw S. and Benning L.G. (2011) The kinetics and mechanism of amorphous calcium carbonate (ACC) crystallization to calcite. *Nanoscale*, **3**, 265-271.
- Rodriguez-Blanco J.D., Shaw S. and Benning L.G. (2015) A route for direct crystallization of dolomite. *American Mineralogist*, **100**, 1172-1181.
- Ruiz-Agudo E., Kudlacz K., Putnis C.V., Putnis A. and Rodriguez-Navarro C. (2013) Dissolution and carbonation of portlandite (Ca(OH)₂) single crystals. *Environmental Science & Technology*, **47**, 11342-11349.
- Saenger C. and Wang Z.R. (2014) Magnesium isotope fractionation in biogenic and abiogenic carbonates: Implications for paleo environmental proxies. *Quaternary Science Reviews*, **90**, 1-21.
- Saldi G.D., Daval D., Morvan G. and Knauss K.G. (2013) The role of Fe and redox conditions in olivine carbonation rates: An experimental study of the rate limiting reactions at 90 and 150 °C in open and closed systems. *Geochimica et Cosmochimica Acta*, **118**, 157-183.
- Saldi G.D., Jordan G., Schott J. and Oelkers E.H. (2009) Magnesite growth rates as a function of temperature and saturation state. *Geochimica et Cosmochimica Acta*, **73**, 5646-5657.
- Saldi G.D., Schott J., Pokrovsky O.S., Gautier Q. and Oelkers E.H. (2012) An experimental study of magnesite precipitation rates at neutral to alkaline conditions and 100-200 °C as a function of pH, aqueous solution composition and chemical affinity. *Geochimica et Cosmochimica Acta*, **83**, 93-109.

- Saldi G.D., Schott J., Pokrovsky O.S. and Oelkers E.H. (2010) An experimental study of magnesite dissolution rates at neutral to alkaline conditions and 150 and 200 °C as a function of pH, total dissolved carbonate concentration, and chemical affinity. *Geochimica et Cosmochimica Acta*, **74**, 6344-6356.
- Sánchez-Román M., Vasconcelos C., Schmid T., Dittrich M., McKenzie J.A., Zenobi R. and Rivadeneyra M.A. (2008) Aerobic microbial dolomite at the nanometer scale: Implications for the geologic record. *Geology*, **36**, 879-882.
- Sayles F.L. and Fyfe W.S. (1973) The crystallization of magnesite from aqueous solution. *Geochimica et Cosmochimica Acta*, **37**, 87-96.
- Schaefer H.T., McGrail B.P. and Owen A.T. (2010) Carbonate mineralization of volcanic province basalts. *International Journal of Greenhouse Gas Control*, **4**, 249-261.
- Schaefer H.T., McGrail B.P. and Owen A.T. (2011a) Basalt reactivity variability with reservoir depth in supercritical CO₂ and aqueous phases. *Energy Procedia*, **4**, 4977-4984.
- Schaefer H.T., Windisch C.F. and McGrail B.P. (2011b) Brucite [Mg(OH)₂] carbonation in wet supercritical CO₂: An in situ high pressure x-ray diffraction study. *Geochimica et Cosmochimica Acta*, **75**, 7458-7471.
- Schott J. and Oelkers E.H. (1995) Dissolution and crystallization rates of silicate minerals as a function of chemical affinity. *Pure & Applied Chemistry*, **67**, 903-910.
- Schott J., Oelkers E.H., Bénézech P., Goddérès Y. and François L. (2012) Can accurate kinetic laws be created to describe chemical weathering? *Comptes Rendus Geoscience*, **344**, 568-585.
- Schott J., Pokrovsky O.S. and Oelkers E.H. (2009) The link between mineral dissolution/precipitation kinetics and solution chemistry. *Reviews in Mineralogy & Geochemistry*, **70**, 207-258.
- Seifritz W. (1990) CO₂ disposal by means of silicates. *Nature*, **345**, 486.
- Sethmann I., Wang J., Becker U. and Putnis A. (2010) Strain-induced segmentation of magnesian calcite thin films growing on a calcite substrate. *Crystal Growth & Design*, **10**, 4319-4326.
- Sherman L.A. and Barak P. (2000) Solubility and dissolution kinetics of dolomite in Ca-Mg-HCO₃/CO₃ solutions at 25 °C and 0.1 MPa carbon dioxide. *Soil Science Society of America Journal*, **64**, 1959-1968.
- Shiraki R. and Brantley S.L. (1995) Kinetics of near-equilibrium calcite precipitation at 100 °C: An evaluation of elementary-reaction based and affinity-based rate law. *Geochimica et Cosmochimica Acta*, **59**, 1457-1471.
- Shirokova L.S., Mavromatis V., Bundelova I.A., Pokrovsky O.S., Bénézech P., Gerard E., Pearce C.R. and Oelkers E.H. (2013) Using Mg isotopes to trace cyanobacterially mediated magnesium carbonate precipitation in alkaline lakes. *Aquatic Geochemistry*, **19**, 1-24.

- Shirokova L.S., Mavromatis V., Bundeleva I., Pokrovsky O.S., Bénézeth P., Pearce C., Gerard E., Balor S. and Oelkers E.H. (2011) Can Mg isotopes be used to trace cyanobacteria-mediated magnesium carbonate precipitation in alkaline lakes? *Biogeosciences Discussions*, **8**, 6473-6517.
- Shock E.L. and Helgeson H.C. (1988) Calculation of the thermodynamic and transport properties of aqueous species at high pressures and temperatures: Correlation algorithms for ionic species and equation of state predictions to 5 kb and 1000 °C. *Geochimica et Cosmochimica Acta*, **52**, 2009-2036.
- Shock E.L., Sassani D.C., Willis M. and Sverjensky D.A. (1997) Inorganic species in geologic fluids: Correlations among standard molal thermodynamic properties of aqueous ions and hydroxide complexes. *Geochimica et Cosmochimica Acta*, **61**, 907-950.
- Sissmann O., Brunet F., Martinez I., Guyot F., Verlaquet A., Piquier Y. and Daval D. (2014) Enhanced olivine carbonation within a basalt as compared to single-phase experiments: Reevaluating the potential of CO₂ mineral sequestration. *Environmental Science & Technology*, **48**, 5512-5519.
- Skorodumova N.V., Belonoshko A.B. and Huang L. (2005) Stability of the MgCO₃ structures under lower mantle conditions. *American Mineralogist*, **90**, 1008-1011.
- Southard I.C. (1941) A modified calorimeter for high temperatures. The heat content of silica, wollastonite and thorium dioxide above 25 °C. *Journal of the American Chemical Society*, **63**, 3142-3146.
- Stanley S.M. and Hardie L.A. (1999) Hypercalcification: Paleontology links plate tectonics and geochemistry to sedimentology. *GSA Today*, **9**, 2-7.
- Steeffel C.I., Druhan J.L. and Maher K. (2014) Modeling coupled chemical and isotopic equilibration rates. *Procedia Earth & Planetary Science*, **10**, 208-217.
- Stout J.W. and Robie R.A. (1963) Heat capacity from 11 to 300 K, entropy, and heat of formation of dolomite. *Journal of Physical Chemistry*, **67**, 2248-2252.
- Talman S.J., Wiwchar B., Gunter W.D. and Scarge C.M. (1990) Dissolution kinetics of calcite in the H₂O–CO₂ system along the steam saturation curve to 210 °C. *Fluid-Mineral Interactions: A Tribute to HP Eugster*, 41-55.
- Teir S., Eloneva S., Fogelholm C.-J. and Zevenhoven R. (2009) Fixation of carbon dioxide by producing hydromagnesite from serpentinite. *Applied Energy*, **86**, 214-218.
- Teir S., Kuusik R., Fogelholm C.-J. and Zevenhoven R. (2007) Production of magnesium carbonates from serpentinite for long-term storage of CO₂. *International Journal of Mineral Processing*, **85**, 1-15.
- Temkin M.I. (1963) The kinetics of stationary reactions. *Doklady Akademii Nauk SSSR*, **152**, 782-785.
- Teng H.H., Dove P.M. and De Yoreo J.J. (2000) Kinetics of calcite growth: Surface processes and relationships to macroscopic rate laws. *Geochimica et Cosmochimica Acta*, **64**, 2255-2266.

- Tesoriero A.J. and Pankow J.F. (1996) Solid solution partitioning of Sr^{2+} , Ba^{2+} and Cd^{2+} to calcite. *Geochimica et Cosmochimica Acta*, **60**, 1053-1063.
- Tipper E.T., Galy A. and Bickle M.J. (2008) Calcium and magnesium isotope systematics in rivers draining the Himalaya-Tibetan plateau region: Lithological or fractionation control? *Geochimica et Cosmochimica Acta*, **72**, 1057-1075.
- Tipper E.T., Galy A., Gaillardet J., Bickle M.J., Elderfield H. and Carder E.A. (2006) The magnesium isotope budget of the modern ocean: Constrains from riverine magnesium isotope ratios. *Earth & Planetary Science Letters*, **250**, 241-253.
- Tribble J.S., Arvidson R.S., Lane M. and Mackenzie F.T. (1995) Crystal chemistry, and thermodynamic and kinetic properties of calcite, dolomite, apatite, and biogenic silica: Applications to petrographic problems. *Sedimentary Geology*, **95**, 11-51.
- Turchyn A.V. and DePaolo D.J. (2011) Calcium isotope evidence for suppression of carbonate dissolution in carbonate-bearing organic-rich sediments. *Geochimica et Cosmochimica Acta*, **75**, 7081-7098.
- Tutolo B.M., Luhman A.J., Kong X.-Z., Saar M.O. and Seyfried W.E. (2014) Experimental observation of permeability changes in dolomite at CO_2 sequestration conditions. *Environmental Science & Technology*, **48**, 2445-2452.
- Uzdowski E. (1994) Synthesis of dolomite and geochemical implications. In: Purser *et al.* (eds.) *Dolomites: A volume in honour of Dolomieu*, pp. 345–360, Blackwell Science Publication, Oxford.
- van Lith Y., Warthmann R., Vasconcelos C. and McKenzie J.A. (2003) Sulphate-reducing bacteria induce low-temperature Ca-dolomite and high Mg-calcite formation. *Geobiology*, **1**, 71-79.
- Vasconcelos C. and McKenzie J.A. (1997) Microbial mediation of modern dolomite precipitation and diagenesis under anoxic conditions, Lagoa Vermelha, Rio de Janeiro, Brazil. *Journal of Sedimentary Research*, **67**, 378-390.
- Vasconcelos C., McKenzie J.A., Bernasconi S., Grujic D. and Tien A.J. (1995) Microbial mediation as a possible mechanism for natural dolomite formation at low temperatures. *Nature*, **377**, 220-222.
- Wagman D.D., Evans W.H., Parker V.B., Schumm R.H., Halow I., Bailey S.M., Churney K.L. and Nuttall R.L. (1982) The NBS tables of chemical thermodynamic properties, selected values for inorganic and C_1 and C_2 organic substances in SI units. *Journal of Physical and Chemical Reference Data*, **11**, Suppl. 2, 392 pp.
- Wang X.Y., Alvarado V., Swoboda-Colberg N. and Kazszuba J.P. (2013) Reactivity of dolomite in water-saturated supercritical carbon-dioxide: Significance for carbon capture and storage and for enhanced oil and gas recovery. *Energy Conversion & Management*, **65**, 564-573.
- Warren J. (2000) Dolomite: Occurrence, evolution and economically important associations. *Earth Science Reviews*, **52**, 1-81.

- Warthmann R., van Lith Y., Vasconcelos C., McKenzie J.A. and Karpoff A.M. (2000) Bacterially induced dolomite precipitation in anoxic culture experiments. *Geology*, **28**, 1091-1094.
- Wasylenki L.E., Dove P.M. and De Yoreo J.J. (2005) Effects of temperature and transport conditions on calcite growth in the presence of Mg^{2+} : Implications for paleothermometry. *Geochimica et Cosmochimica Acta*, **69**, 4227-4236.
- Watson B.E. (2004) A conceptual model for near-surface kinetic controls on the trace-element and stable isotope composition of abiogenic calcite crystals. *Geochimica et Cosmochimica Acta*, **68**, 1473-1488.
- White W.B. (1974) The carbonate minerals. In: Farmer V.C. (ed.) *The infrared spectra of minerals*, p. 227-284, Mineralogical Society Monograph 4.
- White W.P. (1919) Silicate specific heats; second series. *American Journal of Science*, XLVII, 1-43.
- Wilson S.A., Dipple G.M., Power I.M., Thom J.M., Anderson R.G., Raudsepp M., Gabites J.E. and Southam G. (2009) Carbon dioxide fixation within mine wastes of ultramafic-hosted ore deposits: Examples from the Clinton Creek and Cassiar chrysotile deposits, Canada. *Economic Geology*, **104**, 95-112.
- Wimpenny J., Burton K.W., James R., Gannoun A., Mokadem F. and Gislason S.R. (2011) The behaviour of magnesium and its isotopes during glacial weathering in an ancient shield terrain in West Greenland. *Earth & Planetary Science Letters*, **304**, 260-269.
- Wogelius R.A. and Walther J.V. (1991) Olivine dissolution at 25 °C: Effects of pH, CO₂ and organic acids. *Geochimica et Cosmochimica Acta*, **55**, 943-954.
- Wolf G.H., Chizmeshya A.V.G., Diefenbacher J. and McKelvy M.J. (2004) In-situ observation of CO₂ sequestration reactions using a novel microreaction system. *Environmental Science & Technology*, **38**, 932-936.
- Wombacher F., Eisenhauer A., Heuser A. and Weyer S. (2009) Separation of Mg, Ca and Fe from geological reference materials for stable isotope ratio analyses by MC-ICP-MS and double-spike TIMS. *Journal of Analytical Atomic Spectrometry*, **24**, 627-636.
- Wright D.T. and Wacey D. (2005) Precipitation of dolomite using sulphate-reducing bacteria from the Coorong Region, South Australia: Significance and implications. *Sedimentology*, **28**, 987-1008.
- Xu J., Yan C., Zhang F., Konishi H., Xu H. and Teng H.H. (2013) Testing the cation-hydration effect on the crystallization of Ca-Mg-CO₃ systems. *Proceedings of the National Academy of Science of the United States of America*, **110**, 17750-17755.
- Xu M. and Higgins S.R. (2011) Effects of magnesium ions on near-equilibrium calcite dissolution: Step kinetics and morphology. *Geochimica et Cosmochimica Acta*, **75**, 719-733.
- Xu T.F., Apps J.A. and Pruess K. (2003) Reactive geochemical transport simulation to study mineral trapping for CO₂ disposal in deep arenaceous formation. *Journal of Geophysical Research-Solid Earth*, **108**, 2071.

- Xu T.F., Apps J.A. and Pruess K. (2005) Mineral sequestration of carbon dioxide in a sandstone-shale system. *Chemical Geology*, **217**, 295-318.
- Yanat'eva O.K. (1952) Solubility of dolomite in water salt solutions. *Izvestiya Sektora FkhA Akademii Nauk SSSR*, **20**, 252-268.
- Young E.D. and Galy A. (2004) The isotope geochemistry and cosmochemistry of magnesium. *Reviews in Mineralogy & Geochemistry*, **55**, 197-230.
- Zhang F.F., Yan C., Teng H.H., Roden E.E. and Xu H.F. (2013) In situ AFM observation of Ca-Mg carbonate crystallization catalyzed by dissolved sulfide: Observations for sedimentary dolomite formation. *Geochimica et Cosmochimica Acta*, **105**, 44-55.
- Zhang R., Hu S., Zhang X. and Yu W. (2007) Dissolution kinetics of dolomite in water at elevated temperatures. *Aquatic Geochemistry*, **13**, 309-338.
- Zhang Y. and Dawe R.A. (2000) Influence of Mg^{2+} on the kinetics of calcite precipitation and calcite crystal morphology. *Chemical Geology*, **163**, 129-138.
- Zhao L., Sang L., Chen J., Ji J. and Teng H.H. (2009) Aqueous carbonation of natural brucite: relevance to CO_2 sequestration. *Environmental Science & Technology*, **44**, 406-411.
- Zhu C., Lu P., Zheng Z. and Ganor J. (2010) Coupled alkali feldspar dissolution and secondary mineral precipitation in batch systems: 4. Numerical modeling of kinetic reaction paths. *Geochimica et Cosmochimica Acta*, **74**, 3963-3983.
- Zimmermann H. (2000) Tertiary seawater chemistry – Implications from primary fluid inclusions in marine halite. *American Journal of Science*, **300**, 723-767.
- Zuddas P. and Mucci A. (1998) Kinetics of calcite precipitation from seawater: II Influence of the ionic strength. *Geochimica et Cosmochimica Acta*, **62**, 757-766.